UNIVERSITY OF IOANNINA
SCHOOL OF NATURAL SCIENCE
PHYSICS DEPARTMENT

Modern Theoretical Cosmological Models and their Observational Predictions

Ioannis Chr. Antoniou
Physicist

PHD THESIS

IOANNINA 2019

ΠΑΝΕΠΙΣΤΗΜΙΟ ΙΩΑΝΝΙΝΩΝ
ΣΧΟΛΗ ΘΕΤΙΚΩΝ ΕΠΙΣΤΗΜΩΝ
ΤΜΗΜΑ ΦΥΣΙΚΗΣ

Σύγχρονα Θεωρητικά Κοσμολογικά Μοντέλα και οι Παρατηρησιακές τους Προβλέψεις

Ιωάννης Χρ. Αντωνίου
Φυσικός

ΔΙΔΑΚΤΟΡΙΚΗ ΔΙΑΤΡΙΒΗ

ΙΩΑΝΝΙΝΑ 2019

"*If you can't explain it simply, you don't understand it well enough.*"
Albert Einstein

"*Dedicated to my daughters, Christina and Spyridoula*"

Three-member advisory committee:

1. Leandros Perivolaropoulos (Supervisor) - Professor, Physics Department, University of Ioannina

2. Panagiota Kanti - Professor, Physics Department, University of Ioannina

3. Theocharis Kosmas - Professor, Physics Department, University of Ioannina

Seven-member PhD thesis examination committee:

1. Leandros Perivolaropoulos (Supervisor) - Professor, Physics Department, University of Ioannina

2. Panagiota Kanti - Professor, Physics Department, University of Ioannina

3. Theocharis Kosmas - Professor, Physics Department, University of Ioannina

4. Georgios Leontaris - Professor, Physics Department, University of Ioannina

5. Spyros Basilakos - Director of the Institute for Astronomy, Astrophysics, Space Applications and Remote Sensing (IAASARS) at the National Observatory of Athens.

   Director of Research, Research Center for Astronomy and Applied Mathematics Academy of Athens, Greece.

6. Christos Tsagas - Professor, Department of Physics, Aristotle University of Thessaloniki

7. Dimitris Papadopoulos - Professor, Department of Physics, Aristotle University of Thessaloniki

Ακαδημαϊκό έτος 2018 - 2019

ΠΑΝΕΠΙΣΤΗΜΙΟ ΙΩΑΝΝΙΝΩΝ
ΤΜΗΜΑ ΦΥΣΙΚΗΣ
Π.Μ.Σ. ''Φυσικής''

ΠΡΑΚΤΙΚΟ

ΔΗΜΟΣΙΑΣ ΠΑΡΟΥΣΙΑΣΗΣ ΕΞΕΤΑΣΗΣ ΚΑΙ ΑΞΙΟΛΟΓΗΣΗΣ ΔΙΔΑΚΤΟΡΙΚΗΣ ΔΙΑΤΡΙΒΗΣ

Σήμερα, Πέμπτη **23 Μαΐου 2019**, **ώρα 12:00,** στην αίθουσα Σεμιναρίων του Τμήματος Φυσικής (Αναγνωστήριο, κτίριο Φ2, 3ος όροφος) στη Πανεπιστημιούπολη, πραγματοποιήθηκε η διαδικασία της δημόσιας παρουσίασης, εξέτασης και αξιολόγησης, ενώπιον της Επταμελούς Εξεταστικής Επιτροπής, της Διδακτορικής Διατριβής που εκπόνησε ο υποψήφιος διδάκτορας κ**. Ιωάννης Αντωνίου** στα πλαίσια του Προγράμματος Μεταπτυχιακών Σπουδών **«Φυσικής»** του Τμήματος Φυσικής του Πανεπιστημίου Ιωαννίνων.

Την 7-μελή Εξεταστική Επιτροπή, που όρισε με σχετική απόφασή της η Γενική Συνέλευση Ειδικής Σύνθεσης του Τμήματος Φυσικής (κατά τη συνεδρίασή της με αριθμό 516/01-04-2019), αποτελούν τα ακόλουθα μέλη:

1) **Βασιλάκος Σπύρος**, Διευθυντής του Ινστιτούτου Αστρονομίας, Αστροφυσικής, Διαστημικών Εφαρμογών και Τηλεπισκόπησης (IAASARS) στο Εθνικό Αστεροσκοπείο Αθηνών. Διευθυντής Ερευνών, Κέντρο Ερευνών Αστρονομίας και Εφαρμοσμένων Μαθηματικών της Ακαδημίας Αθηνών, Ελλάδα.
2) **Καντή Παναγιώτα**, Καθηγήτρια, Τμήμα Φυσικής Παν/μιο Ιωαννίνων (μέλος τριμελούς συμβουλευτικής επιτροπής)
3) **Κοσμάς Θεοχάρης**, Ομότιμος Καθηγητής, Τμήμα Φυσικής Παν/μιο Ιωαννίνων (μέλος τριμελούς συμβουλευτικής επιτροπής)
4) **Λεοντάρης Γεώργιος**, Καθηγητής, Τμήμα Φυσικής Παν/μιο Ιωαννίνων
5) **Παπαδόπουλος Δημήτρης**, Καθηγητής, Τμήμα Φυσικής Α.Π.Θ.
6) **Περιβολαρόπουλος Λέανδρος**, Καθηγητής, Τμήμα Φυσικής Παν/μιο Ιωαννίνων (Επιβλέπων)
7) **Τσάγκας Χρήστος**, Καθηγητής, Τμήμα Φυσικής Α.Π.Θ.

Στην παρουσίαση δεν ήταν παρών ο κος Σπύρος Βασιλάκος λόγω εκτάκτου περιστατικού για το οποίο ειδοποίησε τηλεφωνικά.

Ο υποψήφιος παρουσίασε και υποστήριξε δημόσια ενώπιον των παρόντων μελών της Εξεταστικής Επιτροπής και του ακροατηρίου την διδακτορική διατριβή που εκπόνησε με τίτλο: **"Σύγχρονα θεωρητικά κοσμολογικά μοντέλα και οι παρατηρησιακές τους προβλέψεις**".

Μετά την ολοκλήρωση της δημόσιας προφορικής διαδικασίας, αποχώρησαν το ακροατήριο και ο υποψήφιος και παρέμειναν μόνο τα μέλη της Εξεταστικής Επιτροπής, τα οποία μετά από συζήτηση κατέληξαν στα ακόλουθα συμπεράσματα:

Τα μέλη της Επιτροπής συμφώνησαν ότι η διδακτορική διατριβή που εκπόνησε ο κ. Αντωνίου είναι πρωτότυπη επιστημονική εργασία για την οποία ο υποψήφιος εργάστηκε με συνέπεια. Το θέμα της διατριβής απαιτεί γνώσεις σε ένα ευρύ φάσμα των θεωρητικών μοντέλων της Κοσμολογίας και αναφέρεται κυρίως στον έλεγχο της εγκυρότητας του καθιερωμένου μοντέλου (ΛCDM) και στην ανίχνευση πιθανών αποκλίσεων από αυτό. Ταυτόχρονα γίνεται μελέτη σύγχρονων και επίκαιρων θεμάτων, όπως η επίδραση ισχυρών βαρυτικών πεδίων που υπόκεινται σε διαστολή του χώρου, στα χαρακτηριστικά ενός βαρυτικού κύματος. Επίσης, αντιμετωπίστηκαν και θέματα, όπως η κίνηση σωματιδίων με σπιν σε περιβάλλον με ισχυρή βαρύτητα και διαστελλόμενο υπόβαθρο. Ο υποψήφιος έδειξε ότι μελέτησε συστηματικά και κατανόησε σε σημαντικό βαθμό τις σχετικές έννοιες, ενώ

παράλληλα κάλυψε την σχετική βιβλιογραφία με ικανοποιητικό βαθμό πληρότητας, τόσο όσο αφορά θεμελιώδεις παλαιότερες εργασίες, αλλά και πρόσφατες εξελίξεις.

Η ολοκλήρωση της διατριβής απαίτησε την χρήση υπολογιστικών κωδίκων οι οποίοι αποτελούν σύγχρονα εργαλεία, καθώς και την ανάπτυξη νέων κωδίκων, κυρίως με την χρήση της Mathematica, στην οποία ο υποψήφιος επέδειξε ικανοποιητική πρωτοβουλία.

Τα παραπάνω κύρια συμπεράσματα της διατριβής μαζί με άλλα παρόμοια νέα αποτελέσματα είναι επίκαιρα και παρουσιάστηκαν σε 7 ερευνητικές εργασίες. Η πλειονότητά τους έχει δημοσιευθεί σε διεθνή κορυφαία επιστημονικά περιοδικά (οι 4 έχουν δημοσιευθεί στο Physical Review D, 1 στο Journal of Cosmology and Astroparticle Physics και 1 στο Classical and Quantum Gravity). Η έβδομη δημοσίευση αφορά μία μονογραφία του υποψηφίου που δημοσιεύτηκε στο περιοδικό Gravitation and Cosmology. Αναλυτικά, οι εργασίες οι οποίες μέχρι σήμερα έχουν περισσότερες από 100 ετεροαναφορές, είναι:

1) **Searching for a Cosmological Preferred Axis: Union2 Data Analysis and Comparison with Other Probes**
I. Antoniou, L. Perivolaropoulos (Ioannina U.). Jul 2010. 8 pp.
Published in JCAP 1012 (2010) 012 DOI: 10.1088/1475-7516/2010/12/012

2) **Dilatonic Topological Defects in 3+1 Dimensions and their Embeddings**
Nikos Platis, Ioannis Antoniou, Leandros Perivolaropoulos (Ioannina U.). Jun 3, 2014. 13 pp.
Published in Phys.Rev. D89 (2014) no.12, 123510 DOI: 10.1103/PhysRevD.89.123510

3) **Geodesics of McVittie Spacetime with a Phantom Cosmological Background**
Ioannis Antoniou, Leandros Perivolaropoulos (Ioannina U.). Mar 6, 2016. 10 pp.
Published in Phys.Rev. D93 (2016) no.12, 123520 DOI: 10.1103/PhysRevD.93.123520

4) **Propagation of gravitational waves in an expanding background in the presence of a point mass**
I. Antoniou (Ioannina U.), D. Papadopoulos (Aristotle U., Thessaloniki), L. Perivolaropoulos (Ioannina U.). Jul 27, 2016. 10 pp. Published in Phys.Rev. D94 (2016) no.8, 084018 DOI: 10.1103/PhysRevD.94.084018

5) **Constraints on spatially oscillating sub-mm forces from the Stanford Optically Levitated Microsphere Experiment data**
Ioannis Antoniou (Ioannina U.), Leandros Perivolaropoulos (Patras U.). Aug 7, 2017. 14 pp.
Published in Phys.Rev. D96 (2017) no.10, 104002 DOI: 10.1103/PhysRevD.96.104002

6) **Constraints on scalar coupling to electromagnetism**
Ioannis Antoniou. Aug 5, 2015. 11 pp. Published in Grav.Cosmol. 23 (2017) 171
DOI: 10.1134/S0202289317020025

7) **Spinning particle orbits around a black hole in an expanding background**
I. Antoniou (Ioannina U.), D. Papadopoulos (Aristotle U., Thessaloniki), L. Perivolaropoulos (Ioannina U.). Mar 9, 2019. 15 pp. Published in Class.Quant.Grav. 36 (2019) no.8, 085002
DOI: 10.1088/1361-6382/ab0fc1

Η παρουσίαση της διατριβής από τον υποψήφιο και η ικανοποιητική αντιμετώπιση των ερωτήσεων που υποβλήθηκαν κατέδειξε κατανόηση των εννοιών και της βιβλιογραφίας από τον υποψήφιο, καθώς και καλή γνώση των τεχνικών που χρησιμοποίησε.

Κατά την αξιολόγηση της διατριβής τα μέλη της Επιτροπής έκριναν ότι η διδακτορική διατριβή του κ. Αντωνίου είναι πρωτότυπη και συμβάλλει στην προαγωγή της επιστήμης, αποφάσισε δε ομόφωνα να

εισηγηθεί την απονομή στον κ. Αντωνίου του τίτλου του διδάκτορα του Τμήματος Φυσικής του Πανεπιστημίου Ιωαννίνων με βαθμό " **Άριστα**".

Σύμφωνα με τα προηγούμενα, η Επιτροπή παρακαλεί να κινηθούν οι νόμιμες διαδικασίες για την αναγόρευση του κ. **Ιωάννη Αντωνίου** σε διδάκτορα του Τμήματος Φυσικής.

Τα μέλη της Εξεταστικής Επιτροπής

Βασιλάκος Σπύρος, Διευθυντής του Ινστιτούτου Αστρονομίας, Αστροφυσικής, Διαστημικών Εφαρμογών και Τηλεπισκόπησης (IAASARS) στο Εθνικό Αστεροσκοπείο Αθηνών. Διευθυντής Ερευνών, Κέντρο Ερευνών Αστρονομίας και Εφαρμοσμένων Μαθηματικών της Ακαδημίας Αθηνών, Ελλάδα.

(απών λόγω εκτάκτου περιστατικού)

Καντή Παναγιώτα, Καθηγήτρια, Τμήμα Φυσικής Παν/μιο Ιωαννίνων

Κοσμάς Θεοχάρης, Ομότιμος Καθηγητής, Τμήμα Φυσικής Παν/μιο Ιωαννίνων

Λεοντάρης Γεώργιος, Καθηγητής, Τμήμα Φυσικής Παν/μιο Ιωαννίνων

Παπαδόπουλος Δημήτρης, Καθηγητής, Τμήμα Φυσικής Α.Π.Θ.

Περιβολαρόπουλος Λέανδρος, Καθηγητής, Τμήμα Φυσικής Παν/μιο Ιωαννίνων (Επιβλέπων)

Τσάγκας Χρήστος, Καθηγητής, Τμήμα Φυσικής Α.Π.Θ.,

Contents

Acknowledgments

First of all, I wish to express my sincerest appreciation to my Supervisor Professor Leandros Perivolaropoulos for his continuous guidance and support throughout the years that I have tried to complete my doctoral studies. I am truly grateful for all that I have learnt from him. I would also like to praise his understanding and patience with me because the daily available time I have had for studying was limited due to professional and family responsibilities.

Furthermore, I would like to thank my postgraduate professors who encouraged me to continue my studies in order to obtain my doctoral degree (PhD). I must also thank the advisor committee without whose invaluable comments and insights this thesis would be undoubtedly poorer.

During my doctoral education, I have been extremely happy to acquire two lovely daughters. My beloved wife and children have been deprived of my presence and I promise that in the future I shall compensate for lost time.

Finally, I would like to refer to my parents who have always stood by me since the beginning of my school years, supporting me and my personal choices. With their altitude, they have always pointed the way.

List of Publications

Within the context of my PhD studies, seven peer-reviewed articles have been produced. They are listed here for reference in descending chronological order.

1. **Searching for a Cosmological Preferred Axis: Union2 Data Analysis and Comparison with Other Probes**,
   I. Antoniou, L. Perivolaropoulos [1]

2. **Dilatonic Topological Defects in 3+1 Dimensions and their Embeddings**,
   Nikos Platis, Ioannis Antoniou, Leandros Perivolaropoulos [2]

3. **Constraints on scalar coupling to electromagnetism**,
   Ioannis Antoniou [3]

4. **Geodesics of McVittie Spacetime with a Phantom Cosmological Background**,
   Ioannis Antoniou, Leandros Perivolaropoulos [4]

5. **Propagation of gravitational waves in an expanding background in the presence of a point mass**,
   I. Antoniou, D. Papadopoulos, L. Perivolaropoulos [5]

6. **Constraints on spatially oscillating sub-mm forces from the Stanford Optically Levitated Microsphere Experiment data**,
   Ioannis Antoniou, Leandros Perivolaropoulos [6]

7. **Spinning particle orbits around a black hole in an expanding background**,
   I. Antoniou, D. Papadopoulos, L. Perivolaropoulos [7]

Abstract

My thesis deals with modern cosmological models and their observational predictions. Nowadays, Cosmology is one of the most interesting branch of Physics due to many significant recent discoveries and challenges in this area of science. Its evolution over the past 100 years has been very fast. We are interested in the study of the Universe and more specifically, where it came from, how it evolves, which will be its fate. This purpose demands a theory which can describe the Universe and fit the observational data from small to large scales. Also, we want to respond to modern cosmological questions, which arise through the cosmological observations and probes.

The most prevalent theory for the beginning of the Universe is the Big Bang theory, which included in the Standard Model (the most acceptable cosmological model) and explains very accurately the current cosmological observations. After this point, the Universe has begun to expand with different rhythm during the cosmological epochs. Almost two decades ago, it was observed that the expansion of the Universe is accelerating. Observations of the expansion rate are made from supernova explosions, from fluctuations in cosmic microwave background CMB radiation (remnant of the Big Bang) and from baryon acoustic oscillations (BAO).

The most likely cause for the accelerating expansion is the Dark Energy, which is about 70% of the Universe, or extensions and modifications of the theory of General Relativity, while Dark Matter appears to play an important role, such as in the formation of the structures in the Universe or in the rotational motion of stars in galaxies. The Dark Energy is probably induced due to the cosmological constant which acts as a repulsive force (Einstein had introduced it in his equations in order to describe a static Universe, but later abandoned it), or due to scalar fields which are subject to coupling with gravity. Dark matter consists of particles such as WIMPs or axions and the scientific community seeks through experiments to detect them. Recently, the detection of gravitational waves has attracted the interest of scientists, since their existence was predicted by the Theory of General Relativity.

The fate of the Universe depends mostly on the percentage of its components (visible matter, Dark matter and Dark energy) and there are three basic possibilities/theories. The first theory predicts that the Universe in the future will expand rapidly and will tear apart (known as *Big Rip* singularity). The second theory predicts that the Universe will begin to shrink until it crashes (known as *Big Chill* or *Big Crunch* singularity), while the third theory predicts that the Universe will continue to expand at a similar rate as today (is called *de Sitter* Universe).

The main objective of the present Thesis is to explore the modern and more acceptable cosmological models and their observational predictions. We investigate with details the ΛCDM model and we focus on deviations from this model. Since the accuracy of the cosmological data increases, occur statistically significant deviations from the ΛCDM model, such as the Hubble tension. Also, our purpose is the study of the Universe and more specifically, where it came from, how it evolves, which will be its fate. Finally, we want to response to many modern cosmological questions, such as the ones we have mentioned above.

In Chapter 1, we describe analytically the current status in Cosmology. More precisely, we begin from the Einstein field equations and we end up with alternative theories of ΛCDM model (*Concordance model*). In this Chapter, we describe the features of the components of the Universe, the observational expansion of the Universe, the acceptable and non acceptable cosmological models and the methods to measure distances in Cosmology. Also, we present a thorough guide for the accelerating expansion, which we observe today and the possible interpretations of this kind of expansion. Finally, we address

the formation of gravitational waves, as tensor perturbations, since the recent discovery of the existence of gravitational waves, an issue which is a milestone in modern Cosmology, gives a new observational instrument and opens a new window to explore the Universe.

In Chapter 2, we test the isotropy of the Universe through the data of the Union2 Supernova Ia (SnIa) compilation. Using the hemisphere comparison method, we have found that the distribution of Union2 data have a preferred axis in the Universe. We have indications that there is a preferred cosmological axis of maximum asymmetry, since many other cosmological observations such as CMB multipoles, quasar alignment and velocity flows indicate almost the same direction as SnIa Union2 compilation and we have checked how possible this evidence is to be random with statistical methods.

In Chapter 3, we investigate the stability of the 't Hooft-Polyakov monopoles with a dilatonic coupling to electromagnetism in the presence of a magnetic field and the consequences of their possible existence in Cosmology. Monopoles are a kind of topological defect (the others are cosmic strings, textures and domain walls), which were formed during the expansion of the early Universe, when a symmetry broke up. In particular, monopoles can play a role in variation of fundamental constants, such as the fine structure constant.

In Chapter 4, we explore signatures of a scalar particle which is known as axion like particle from experiments which try to detect it. Possibly, this particle interacts with photons and theoretically the interaction is described through a coupling to electromagnetism. No experiment has detected this particle and thus the researchers estimate an upper bound for the energy (or mass) of this particle. Similar experiments aiming to detect chameleons, which are candidate scalar particles as components of dark energy, but the results until now are not satisfactory. Through these experiments the research teams estimate bounds for the energy of the chameleons.

In Chapter 5, we process the data from Stanford optically levitated experiment. They include distance and interaction (force) in a very small distance scale (bellow mm). We have a significant signal that the sub-mm forces obey oscillating form with characteristic wavelength, thus the Newtonian gravity seems to be modified in small scales or this signal may come from the Dark energy density scale. Also, we propose a chameleon model as a possible explanation of this signal, since the hypothetical fifth force can be mediated by the chameleons.

In Chapter 6, we explore the effects on the behavior of gravitational waves in the vicinity of a large mass, where the gravity is strong, such as a black hole or a neutron star. We solve the wave equation and we investigate the changes in the characteristics of the wave due to the presence of the mass. We found that the amplitude and the period increase as the wave approaches the mass. The increasing of the period is a well known effect, the *gravitational time dilation*. Also, the power spectrum which contains the contribution of each frequency in the waveform changes (if we compare it with the wave which has been propagated in empty space).

In Chapter 7, we estimate the time of dissociation of bound systems in a phantom cosmological background. We solve the geodesic equations taking into account relativistic effects and we compare the time of dissociation (Big Rip) with the corresponding well known Newtonian time of dissociation. For large and massive cosmological structures the dissociation occurs earlier in the relativistic consideration.

In Chapter 8 we deal with the influence of spin on the orbits of spinning particles in a curved spacetime around a much bigger mass, such as a black hole. We consider the Mathisson-Papapetrou equations and we solve these equations for a spinning particle in a static and an expanding Universe, when the geometry of the background is the post-Newtonian limit of McVittie spacetime. For any spinning particle the orbits deviate from geodesics, due to the coupling between spin and curvature which induces repulsive or attractive force in the particle. In the absence of expansion the spinning particle orbits between a minimum and a maximum radius, depending on the magnitude and the orientation of the spin, but in most cases it remains bounded. If the radius of the orbit becomes less than $3R_s$ which is the innermost stable circular orbit (ISCO), the particle begins to merge with the black hole. In an expanding Universe the orbits are affected by the rate of the expansion and the orientation of the spin angular momentum.

In Chapter 9, we summarize the main results and the extracted conclusions of the present Thesis and we discuss further the applications and the cosmological consequences. Our present results offer significant contribution to deeply understand the fundamental Physics of our observable Universe.

Εκτεταμένη Περίληψη

Η Κοσμολογία είναι μία επιστήμη που η απαρχή της βρίσκεται στα βάθη των αιώνων. Οι πρώτες παρατηρήσεις του σύμπαντος προέρχονται από τους αρχαίους Αιγύπτιους και αργότερα από τους αρχαίους Έλληνες. Τότε εμφανίστηκαν και οι πρώτες θεωρίες που προέβλεπαν ποια θα μπορούσαν να είναι τα συστατικά του σύμπαντος. Στο κέντρο του τότε γνωστού σύμπαντος, οι αστρονόμοι της εποχής είχαν τοποθετήσει την Γη (γεωκεντρικό σύστημα), αν και ο Πτολεμαίος είχε διαφορετική απόψη θεωρώντας πως το κέντρο του σύμπαντος είναι ο Ήλιος (ηλιοκεντρικό σύστημα). Η άποψη του Πτολεμαίου έμεινε στο παρασκήνιο μέχρι την εποχή του Τύχο Μπραχέ και του Κοπέρνικου.

Οι συστηματικές, για πρώτη φορά, παρατηρήσεις του Κοπέρνικου, οι νόμοι του Κέπλερ, οι απόψεις του Γαλιλαίου για την κίνηση της Γης και ο νόμος της βαρύτητας του Νεύτωνα αντικατέστησαν τις εσφαλμένες θεωρίες του παρελθόντος και έβαλαν τις βάσεις για την δημιουργία της σύγχρονης Κοσμολογίας. Στις αρχές του εικοστού αιώνα η Ειδική και Γενική θεωρία της Σχετικότητας του Αϊνστάιν οδήγησαν στα πρώτα σύγχρονα κοσμολογικά μοντέλα.

Η παρούσα διδακτορική διατριβή διαπραγματεύεται τα πιο μοντέρνα, ελπιδοφόρα και σύγχρονα κοσμολογικά μοντέλα καθώς και τις παρατηρησιακές τους προβλέψεις. Η Κοσμολογία αποτελεί έναν από τους πιο ενδιαφέροντες κλάδους της Φυσικής εξαιτίας της ραγδαίας εξέλιξής της τα τελευταία 100 χρόνια, των πολύ σημαντικών ανακαλύψεων των τελευταίων ετών και των προκλήσεων που αυτές δημιουργούν. Οι αναζητήσεις του ανθρώπου για το ¨τι υπάρχει εκεί επάνω' ξεκινούν από την εμφάνιση του ανθρώπινου είδους, αλλά μόνο την τελευταία εκατονταετία μπορούν να δοθούν πολλές απαντήσεις στα ερωτήματα αυτά. Μας ενδιαφέρει η μελέτη του σύμπαντος και πιο συγκεκριμένα από πού προήλθε, πως εξελίχθηκε και ποια θα είναι η τύχη του (το πιθανό του μέλλον), ποια είναι τα συστατικά του, πως αλληλεπιδρούν μεταξύ τους, πως τα ανιχνεύουμε και πως αυτά καθορίζουν την κίνηση των σωμάτων. Επίσης, θέλουμε να απαντήσουμε και σε άλλα σύγχρονα κοσμολογικά ερωτήματα που προκύπτουν κατά την μελέτη των κοσμολογικών συστημάτων και των ιδιοτήτων τους.

Η επικρατέστερη θεωρία για την δημιουργία του σύμπαντος είναι η Μεγάλη Έκρηξη, που εξηγεί με μεγάλη ακρίβεια και απλότητα τις περισσότερες από τις σημερινές κοσμολογικές παρατηρήσεις. Εδώ και σχεδόν δύο δεκαετίες παρατηρήθηκε από την μελέτη υπερκαινοφανών αστέρων πως η διαστολή του Σύμπαντος είναι επιταχυνόμενη, μία παρατήρηση που άλλαξε εντελώς τον τρόπο προσέγγισης της μελέτης του Σύμπαντος, μιας και μέχρι τότε οι επιστήμονες πίστευαν πως η διαστολή του Σύμπαντος, που ξεκίνησε με την Μεγάλη Έκρηξη ήταν επιβραδυνόμενη λόγω της καταλυτικής παρουσίας της βαρύτητας. Μέχρι σήμερα, οι παρατηρήσεις του ρυθμού διαστολής γίνονται από εκρήξεις σουπερνόβα ή από διαταραχές στην κοσμική μικροκυματική ακτινοβολία υποβάθρου (απομεινάρι από την μεγάλη έκρηξη).

Οι πιο πιθανές αιτίες για την επιταχυνόμενη διαστολή είναι η ύπαρξη της σκοτεινής ενέργειας που αποτελεί περίπου το 70% του Σύμπαντος ή επεκτάσεις και τροποποιήσεις της Γενικής Θεωρίας της Σχετικότητας, ενώ σημαντικό ρόλο στη διαστολή φαίνεται να διαδραματίζει και η σκοτεινή ύλη. Η σκοτεινή ενέργεια πιθανόν να οφείλεται στην κοσμολογική σταθερά που λειτουργεί ως απωστική δύναμη και την είχε εισάγει ο Einstein στις εξισώσεις του αλλά την απέρριψε αργότερα γιατί δεν οδηγούσε σε στατικό Σύμπαν όπως πίστευε ο ίδιος πως είναι το Σύμπαν, ή σε βαθμωτά πεδία όπως τα σωματίδια χαμαιλέοντες που υπόκεινται σε σύζευξη με την βαρύτητα. Η σκοτεινή ύλη αποτελείται από σωματίδια που η επιστημονική κοινότητα έχει υποθέσει πως υπάρχουν και ψάχνει αποδείξεις μέσω πειραμάτων για την ύπαρξή τους. Τέτοια σωματίδια μπορεί να είναι τα αξιόνια, τα ασθενώς αλληλεπιδρώντα μαζικά σωματίδια (WIMP) και πολλά άλλα.

Πρόσφατα, η ανίχνευση των βαρυτικών κυμάτων έχει προσελκύσει το ενδιαφέρον των επιστημόνων, μιας και η ύπαρξή τους προβλεπόταν από την Γενική Θεωρία της Σχετικότητας. Προς το παρόν, λόγω της περιορισμένης ευαισθησίας των ανιχνευτικών διατάξεων, μπορούμε να ανιχνεύσουμε βαρυτικά κύματα που παράγονται από την συγχώνευση δύο μελανών οπών ή αστέρων νετρονίων. Οι αναζητήσεις για συνεχή βαρυτικά κύματα από αστέρες νετρονίων που έχουν ελλειπτική περιστροφή δεν είχαν επιτυχές αποτέλεσμα. Οι συγχωνεύσεις αστέρων νετρονίων διαρκούν αρκετά δευτερόλεπτα, ενώ των μαύρων τρυπών μερικά κλάσματα του δευτερολέπτου. Αρκετές συγχωνεύσεις αστέρων νετρονίων συνοδεύονται από έκλυση ηλεκτρομαγνητικής ακτινοβολίας. Τα βαρυτικά κύματα προσφέρουν ένα ακόμη παρατηρησιακό εργαλείο για το Σύμπαν, μέσω του οποίου μπορούμε να υπολογίσουμε διάφορα μεγέθη, όπως μάζα, διαστάσεις, απώλεια ενέργειας κτλ του σώματος που τα εκπέμπει.

Η μελλοντική εξέλιξη του Σύμπαντος εξαρτάται σε μεγάλο βαθμό από το ποσοστό του κάθε συστατικού του (ορατή ύλη, σκοτεινή ύλη και σκοτεινή ενέργεια). Από τους κοσμολόγους έχουν αναπτυχθεί πρόσφατα τρεις βασικές θεωρίες για το πως θα εξελιχθεί το Σύμπαν μας στο μέλλον. Η πρώτη προβλέπει ότι το Σύμπαν κάποια στιγμή στο μέλλον θα διασταλεί απότομα και θα διαλυθεί (γνωστή ως μεγάλο σχίσιμο ή Big Rip). Η δεύτερη θεωρία προβλέπει ότι το Σύμπαν δεν θα διαστέλεται για πάντα αλλά από ένα σημείο και μετά θα αρχίσει να συρρικνώνεται μέχρι να συνθλιβεί (γνωστή ως μεγάλη ψύξη ή Big Crunch), ενώ η τελευταία θεωρία προβλέπει πως το Σύμπαν θα συνεχίσει να διαστέλλεται με παρόμοιο ρυθμό όπως και σήμερα (αποκαλείται Σύμπαν de Sitter). Στην παρούσα κοσμολογική χρονική περίοδο βρισκόμαστε πάνω στο μεταίχμιο του χωροχρόνου από το οποίο διέρχονται τα τρία πιθανά σενάρια, συνεπώς δεν μπορούμε να ξεχωρίσουμε ποιό είναι το επικρατέστερο. Εν κατακλείδι και τα τρία μοντέλα είναι αποδεκτά και αυτό το γεγονός μας οδηγεί σε ένα μεγάλο πλήθος θεωρητικών κυρίως επιστημονικών εργασιών.

Στόχος της παρούσας διδακτορικής διατριβής είναι η περαιτέρω διερεύνηση και απάντηση μερικών από τα συγχρονα κοσμολογικά προβλήματα. Από την στιγμή που το καθιερωμένο κοσμολογικό μοντέλο έχει εδραιωθεί ως η βάση της σύγχρονης Κοσμολογίας, το ενδιαφέρον επικεντρώνεται στην αναζήτηση πιθανών αποκλίσεων από αυτό. Με την πάροδο του χρόνου οι κοσμολογικές παρατηρήσεις γίνονται με μεγαλύτερη ακρίβεια και τα σφάλματα μειώνονται. Έτσι οι έλεγχοι για πιθανές ανωμαλίες ή αποκλίσεις γίνονται πιο ακριβείς.

Στο κεφάλαιο 1, γίνεται μία εκτενής αναφορά στην σύγχρονη Κοσμολογία και τις βασικές έννοιές της. Ξεκινάμε από τις εξισώσεις πεδίου του Einstein ο οποίος υπέδειξε ότι η βαρύτητα δεν είναι ιδιότητα των σωμάτων, αλλά ιδιότητα του χώροχρόνου. Η παρουσία ενός σώματος καμπυλώνει τον χωροχρόνο και αυτή η καμπύλωση επηρεάζει την κίνηση των γειτονικών σωμάτων και όσων πλησιάζουν σε κοντινή απόσταση. Η βασική αρχή για το Σύμπαν είναι η *κοσμολογική αρχή* δηλαδή η υπόθεση πως το Σύμπαν είναι ομογενές και ισότροπο, η οποία έχει ελεγχθεί επιτυχώς με πάρα πολλά πειράματα.

Οι τροχιές που ακολουθούν τα σώματα όταν δέχονται μόνο την βαρυτική αλληλεπίδραση των άλλων σωμάτων λέγονται γεωδαισιακές. Στην Νευτώνεια Φυσική η τροχιά αυτή είναι ευθεία γραμμή, αλλά σε έναν καμπύλο χωροχρόνο η γεωδαισιακή μπορεί να έχει οποιοδήποτε σχήμα. Λόγω της διαστολής του Σύμπαντος, η ακτινοβολία που φτάνει στη Γη από κάθε ουράνιο σώμα είναι μετατοπισμένη προς μεγαλύτερα μήκη κύματος. Έτσι για κάθε σώμα ορίζουμε την *ερυθρή μετατόπιση* που εκφράζει την απόστασή του από εμάς. Η ερυθρή μετατόπιση συνδέεται με τον παράγοντα κοσμικής διαστολής που δείχνει τον ρυθμό διαστολής του Σύμπαντος σε κάθε κοσμολογική εποχή. Η μέτρηση των αποστάσεων στην Κοσμολογία γίνεται με διάφορους τρόπους και ανάλογα με τον ορισμό της απόστασης έχουμε και διαφορετική πληροφορία για το ουράνιο σώμα.

Σήμερα είναι ευρέως αποδεκτό πως το Σύμπαν είναι γεμάτο με ένα ρευστό άγνωστης σύστασης που αποκαλείται κοσμολογικό ρευστό, ενώ οι ιδιότητες του ρευστού αυτού περιγράφονται από τον τανυστή ενέργειας-ορμής. Η ενέργεια του Σύμπαντος είναι σταθερή, δηλαδή ισχύει η διατήρησή της. Επίσης, η πίεση και η πυκνότητα του ρευστού συνδέονται με μία καταστατική εξίσωση, όπου τα μεγέθη αυτά είναι ανάλογα. Το Σύμπαν χαρακτηρίζεται από έναν αριθμό κοσμολογικών παραμέτρων, όπως η παράμετρος πυκνότητας ενέργειας, η σταθερά Hubble ή η χωρική καμπυλότητα, οι οποίες προσδιορίζουν τις ιδιότητές του. Οι παράμετροι αυτές γενικά δεν είναι σταθερές και μπορεί να εξελίσσονται με τον χρόνο.

Έπειτα από την διατύπωση της θεωρίας της Σχετικότητας (Ειδικής και Γενικής) εμφανίστηκαν και τα πρώτα απλά κοσμολογικά μοντέλα, όπως το μοντέλο του Einstein, του de Sitter και πολλών άλλων. Αρκετά από αυτά είναι βιώσιμα, δηλαδή μπορούν να υποστηρίξουν τις τιμές των κοσμολογικών παραμέτρων που προσδιορίζουμε μέσω παρατηρήσεων, ενώ άλλα έχουν μόνο θεωρητικό και ιστορικό ενδιαφέρον. Ένα από

τα πιο σημαντικά μοντέλα που εμφανίστηκαν στα πρώτα χρόνια είναι το μοντέλο του Friedmann, το οποίο θεωρεί ότι το Σύμπαν αποτελείται από ύλη και ακτινοβολία. Το μοντέλο αυτό προβλέπει την ύπαρξη της Μεγάλης Έκρηξης και ένα τέτοιο Σύμπαν θα μπορούσε να είναι ανοιχτό, κλειστό ή επίπεδο. Βέβαια, σχεδόν όλες οι παρατηρησιακές ενδείξεις οδηγούν στο συμπέρασμα πως το Σύμπαν στο οποίο ζούμε είναι *επίπεδο ή σχεδόν επίπεδο*.

Σε αντίθεση με το κοσμολογικό μοντέλο του Friedmann το κοσμολογικό μοντέλο του Lemaitre που αποτελεί γενίκευση του μοντέλου του Friedmann, ενσωματώνει την κοσμολογική σταθερά Λ. Το μοντέλο de Sitter είναι μία ειδική περίπτωση του μοντέλου Lemaitre και θεωρεί πως μοναδικό συστατικό του Σύμπαντος είναι η κοσμολογική σταθερά. Λόγω αυτής της ιδιαιτερότητας δεν είναι βιώσιμο και το μελετάμε κυρίως για την σύνδεσή του με τον *κοσμικό πληθωρισμό* (ένα στάδιο πολύ έντονης διαστολής του χωροχρόνου στο πολύ αρχικό Σύμπαν) και για ιστορικούς λόγους. Ένα ακόμη μοντέλο που αναφέρουμε στο κεφάλαιο 1 είναι το μοντέλο του Einstein το οποίο είναι στατικό, προβλέπει την τιμή της κοσμολογικής σταθεράς αρκετά κοντά στα απαιτούμενα από τις παρατηρήσεις όρια, αλλά είναι ασταθές. Οποιαδήποτε προσθήκη μάζας μπορεί να το αποσταθεροποιήσει.

Το πιο ευρέως αποδεκτό κοσμολογικό μοντέλο από το επιστημονικό κόσμο είναι το ΛCDM επειδή είναι εξαιρετικά απλό αλλά ταυτόχρονα μπορεί να υποστηρίξει τις περισσότερες κοσμολογικές παρατηρήσεις. Αποδέχεται πως τα συστατικά του Σύμπαντος είναι ψυχρή μη σχετικιστική σκοτεινή ύλη, ορατή ύλη και σκοτεινή ενέργεια που εκφράζεται μέσω της κοσμολογικής σταθεράς. Πολύ συχνά αναφέρεται και ως *πρότυπο μοντέλο* (standard model) ή μοντέλο αρμονίας (concordance model) επειδή ερμηνεύει πολλές ιδιότητες του Σύμπαντος, όπως την ύπαρξη και δομή της κοσμικής ακτονοβολίας υποβάθρου, την κατανομή των γαλαξιών σε μεγάλη κλίμακα, την αφθονία του υδρογόνου, του ηλίου και του λιθίου καθώς και την επιταχυνόμενη διαστολή του Σύμπαντος. Επίσης προβλέπει με πολύ μεγάλη ακρίβεια την ηλικία του Σύμπαντος, η οποία είναι περίπου 13.7 δισεκατομμύρια χρόνια.

Το μοντέλο αυτό αποδέχεται την ομοιογένεια και ισοτροπία του χωροχρόνου, καθώς και την επιπεδότητά του. Προσθέτοντας διάφορα συστατικά όπως κοσμικό πληθωρισμό ή πεμπτουσία, το ΛCDM μοντέλο μπορεί να επεκταθεί στην κατεύθυνση ερμηνείας και άλλων κοσμολογικών ιδιοτήτων, που μέχρι σήμερα παραμένουν αναπάντητες. Ταυτόχρονα, όπως σε κάθε θεωρία, έχουν προταθεί εναλλακτικές προτάσεις που μπορούν να αντικαταστήσουν ή να επεκτείνουν το ΛCDM μοντέλο. Στις προτάσεις αυτές περιλαμβάνονται τροποποιημένες θεωρίες βαρύτητας, θεωρίες μεγάλης κλίμακας μεταβολών στην πυκνότητα ύλης του Σύμπαντος, αναλλοίωτη κλίμακα του κενού χώρου και τροποποιημένες Νευτώνειες δυναμικές (MOND).

Στο τέλος του κεφαλαίου γίνεται αναφορά στον συνδετικό κρίκο των ενοτήτων της παρούσας διατριβής. Ο συνδετικός κρίκος δεν είναι άλλος από την *αναζήτηση πιθανών αποκλίσεων από το καθιερωμένο μοντέλο* και ο στατιστικός έλεγχος των βασικών υποθέσεων του μοντέλου αυτού. Επίσης γίνεται μελέτη των βαρυτικών κυμάτων, που παρότι δεν αποτελούν απόκλιση από το καθιερωμένο μοντέλο, είναι ένα εξαιρετικά επίκαιρο και ενδιαφέρον θέμα. Μέσω των βαρυτικών κυμάτων μπορεί να γίνει έλεγχος για πιθανές αποκλίσεις από το καθιερωμένο μοντέλο μιας και μπορούμε να μετρήσουμε τον ρυθμό διάσπασης του Σύμπαντος, να ελέγξουμε τον βαθμό ισοτροπίας και να τεστάρουμε την Γενική Σχετικότητα σε περιοχές με ισχυρή βαρύτητα, όπως είναι το περιβάλλον μιας μελανής οπής. Στο ίδιο πλαίσιο με τα βαρυτικά κύματα εντάσσεται και η μελέτη τροχιών σωματιδίων με σπιν γύρω από μία κατανομή μάζας σε διαστελλόμενο σύμπαν, η οποία παρουσιάζεται στο προτελευταίο κεφάλαιο της διατριβής.

Στο κεφάλαιο 2, ελέγχουμε την ισοτροπία του Σύμπαντος με δεδομένα από εκρήξεις υπερκαινοφανών αστέρων τύπου Ια, οι οποίοι θεωρούνται στην Κοσμολογία ως πρότυπα κεριά. Παράγουν την ίδια σχεδον φωτεινότητα όταν εκρήγνυνται και για τον λόγο αυτό χρησιμοποιούνται για την μέτρηση αποστάσεων στο Σύμπαν. Από τις υπάρχουσες συλλογές υπερκαινοφανών Ια επιλέξαμε την συλλογή Union2 που περιέχει 557 υπερκαινοφανείς και αποτελούσε τη μεγαλύτερη συλλογή όταν αρχίσαμε την μελέτη μας. Σήμερα υπάρχει η συλλογή PANTHEON που περιέχει 1048 υπερκαινοφανείς. Χρησιμοποιήσαμε την μέθοδο σύγκρισης ημισφαιρίων, κατά την οποία χωρίσαμε τους υπερκαινοφανείς σε δύο ουράνια ημισφαίρια, το ΄πάνω΄ και το ΄κάτω΄ και υπολογίσαμε την διεύθυνση στην οποία η κατανομή τους παρουσιάζει τη μέγιστη επιτάχυνση.

Η μελέτη μας οδήγησε στο συμπέρασμα πως το Σύμπαν είναι ομογενές ως προς την κατανομή των υπερκαινοφανών, αλλά η κατανομή των υπερκαινοφανών δείχνει μία προτιμητέα διεύθυνση στην οποία παρουσιάζουν μέγιστη ανισοτροπία και μέγιστη επιτάχυνση. Σε γαλαξιακές συντεταγμένες, η διεύθυνση της μέγιστης ανισοτροπίας είναι $(l, b) = (309°, 18°)$. Για τον έλεγχο του μεγέθους της ανισοτροπίας

χρησιμοποιήσαμε την μέθοδο Μόντε Κάρλο, συγκρίνοντας τα δεδομένα από την συλλογή Union2 με ισοτροπικά δεδομένα που παράγει τυχαία η μέθοδος αυτή. Βρήκαμε ότι το επίπεδο της ανισοτροπίας είναι κάτω από 1σ, γεγονός που υποδεικνύει πως είναι στατιστικά αμελητέο, χωρίς περαιτέρω ενδιαφέρον. Συνεπώς δεν εντοπίσαμε κάποια απόκλιση από το καθιερωμένο μοντέλο.

Διεύθυνση μέγιστης ανισοτροπίας στην κατανομή τους δεν παρουσιάζουν μόνο οι υπερκαινοφανείς, αλλά όπως συλλέξαμε από την βιβλιογραφία και άλλες κοσμικές δομές όπως η διπολική, τετραπολική και οκταπολική ροπή της κοσμικής μικροκυματικής ακτινοβολίας υποβάθρου, ο άξονας περιστροφής των κβάζαρ (πολύ ενεργοί γαλαξίες) στο χώρο και η ταχύτητα με την οποία ρέουν στο κοσμικό ρευστό οι δομές του σύμπαντος, όπως οι γαλαξίες. Η ταχύτητα αυτή δεν σχετίζεται με την διαστολή του σύμπαντος. Παρατηρώντας πως αυτές οι διευθύνσεις είναι σχετικά κοντά στην ουράνια σφαίρα, εκτιμήσαμε πόσο πιθανό είναι αυτό το φαινόμενο να είναι τυχαίο. Χρησιμοποιήσαμε πάλι αντίστοιχη μέθοδο Μόντε Κάρλο και εκτιμήσαμε πως η πιθανότητα να είναι τυχαίο το φαινόμενο αυτό είναι περίπου 1%. Αν αγνοήσουμε τις πολυπολικές ροπές της κοσμικής ακτινοβολίας υποβάθρου μιας και αναφέρονται στο ίδιο φαινόμενο, τότε η πιθανότητα σύμπτωσης γίνεται 7%, αλλά και πάλι είναι πολύ χαμηλή. Συνεπώς, μία τόσο μεγάλη συμφωνία στην κατανομή τους είναι φυσικό να μας οδηγεί στο να σκεφτούμε πως κάποια άγνωστη μέχρι σήμερα φυσική σχέση υπάρχει μεταξύ τους.

Στο κεφάλαιο 3, ασχοληθήκαμε με τις τοπολογικές ανωμαλίες και τον ρόλο που μπορεί να έχουν στην μεταβολή σταθερών της Φυσικής, όπως η σταθερά της λεπτής υφής η οποία σύμφωνα με αρκετές παρατηρήσεις μεταβάλλεται χρονικά και χωρικά. Στις τοπολογικές ανωμαλίες ανήκουν οι κοσμικές χορδές, τα μονόπολα και άλλες μορφές οι οποίες παράγονται κατά την διαστολή του Σύμπαντος, όταν σπάνε συμμετρίες και ενδεχομένως αποτελούν συστατικά της σκοτεινής ύλης. Το Σύμπαν αρχικά ήταν υπερσυμμετρικό, αλλά μέχρι σήμερα από εκείνες τις συμμετρίες έχουν μείνει ελάχιστες. Τοπολογικές ανωμαλίες δεν έχουν παρατηρηθεί εώς τώρα σε πειράματα ή σε φυσικά κοσμικά συστήματα. Η ανίχνευσή τους είναι μία ακόμη πρόκληση για την σύγχρονη Κοσμολογία.

Ειδικότερα, τα μονόπολα όταν υπόκεινται σε σύζευξη με τον ηλεκτρομαγνητικό τανυστή, αυτή εκφράζεται στην Λαγκρατζιανή με μία συνάρτηση σύζευξης. Επιλέξαμε μία γραμμική συνάρτηση που περιγράφει την παραπάνω σύζευξη ως την πιο απλή περίπτωση, χρησιμοποιήσαμε κατάλληλο δυναμικό και υπολογίσαμε την ενέργεια που περικλείει ένα τέτοιο μονόπολο. Ελαχιστοποιώντας την ενέργεια, υπολογίσαμε τα πεδία-σωμάτια που σχετίζονται με το βαθμωτό και το ηλεκτρομαγνητικό πεδίο. Στην συνέχεια εξάγαμε τα αντίστοιχα αποτελέσματα σε εκθετική συνάρτηση σύζευξης. Τα πεδία αυτά σχετίζονται με την μεταβολή θεμελιωδών σταθερών της Φυσικής και προβλέψαμε τον βαθμό που μπορούν να επηρεάσουν τις σταθερές αυτές. Εάν το μονόπολο εισαχθεί σε χωροχρόνο με επιπλέον συμμετρία και ύπαρξη μαγνητικού πεδίου, τότε καθίστανται ασταθές για όλες τις παραμέτρους, ενώ οι κοσμικές χορδές εξακολουθούν να είναι σταθερές.

Στο κεφάλαιο 4, μελετήσαμε δεδομένα από πειράματα που έχουν γίνει και γίνονται σε διάφορα εργαστήρια ανά τον κόσμο και επιδιώκουν την ανίχνευση βαθμωτών σωματιδίων που σχετίζονται με την σκοτεινή ύλη και σκοτεινή ενέργεια. Μέχρι σήμερα έχουν εκτελεστεί πολλά πειράματα που στοχεύουν στην ανίχνευση τέτοιων σωματιδίων που εικάζεται πως αλληλεπιδρούν πολύ ασθενικά με την ύλη. Επίσης σχεδιάζονται και άλλα πειράματα για το μέλλον με όργανα που θα έχουν βελτιωμένη ανιχνευτική ικανότητα σε σχέση με την σημερινή. Στα σωματίδια αυτά ανήκουν βαθμωτά πεδία που συμπεριφέρονται ως αξιόνια και έχουν πάριτυ περιττό αριθμό (ALPs) και σχετίζονται με την σκοτεινή ύλη και τα σωματίδια χαμαιλέοντες που σχετίζονται με την σκοτεινή ενέργεια. Τα σωματίδια αυτά αλληλεπιδρούν με τα φωτόνια και προκαλούν διάφορα οπτικά φαινόμενα στο φως όπως οπτική περιστροφή, διχρωισμό, ελλειπτικότητα και διπλή διάθλαση. Πάνω σε αυτά τα φαινόμενα στηρίζονται τα πειράματα ανίχνευσης που γίνονται από διάφορες ερευνητικές ομάδες σε όλο τον κόσμο, ενώ η ύπαρξη τους δεν προβλέπεται από την γενική θεωρία της σχετικότητας. Συνεπώς, αποτελούν μία ακόμη πιθανή απόκλιση από το καθιερωμένο μοντέλο.

Ειδικότερα για την ανίχνευση των σωματιδίων που συμπεριφέρονται ως αξιόνια και είναι βαθμωτά, στα πειράματα γίνεται υπόθεση πως ένα ζεύγος φωτονίων αλληλεπιδρά και υπάρχει πιθανότητα, μικρή ή μεγάλη να παραχθεί ένα βαθμωτό σωμάτιο. Στην συνέχεια, αυτό το σωμάτιο λόγω αστάθειας διασπάται σε δύο νέα φωτόνια (αναγέννηση φωτονίων) που πιθανόν έχουν κάποια διαφορετική οπτική ιδιότητα σε σχέση με τα αρχικά φωτόνια. Δυστυχώς μέχρι σήμερα δεν έχει ανιχνευτεί κάποιο σωματίδιο και κάθε πείραμα με βάση τις ανιχνευτικές του δυνατότητες θέτει κάποιο άνω όριο για την ενέργεια-μάζα αυτού του σωματιδίου. Τα πιο αυστηρά όρια προέρχονται από πειράματα που σχετίζονται με την πέμπτη δύναμη και τα οποία είναι πολύ μακριά από τις ανιχνευτικές δυνατότητες των οργάνων των εργαστηρίων στη Γη.

Στην συνέχεια του κεφαλαίου αυτού παρουσιάσαμε τα ενεργειακά όρια που έχουν τεθεί από πειράματα ανίχνευσης σωματιδίων χαμαιλεόντων, των οποίων η μάζα εξαρτάται από την πυκνότητα της μάζας του περιβάλλοντος χώρου. Μέσω ενός μηχανισμού που αποκαλείται μηχανισμός-χαμαιλέων, τα σωμάτια αυτά σε περιοχές με μεγάλη πυκνότητα έχουν μεγάλη μάζα, ενώ σε περιοχές με μικρή πυκνότητα συμβαίνει το αντίστροφο. Αυτή η ιδιότητα καθιστά την ανίχνευσή τους εξαιρετικά δύσκολη. Έτσι, τα πειράματα ανίχνευσης γίνονται σε συνθήκες κενού και δεν στηρίζονται στο φαινόμενο της αναγέννησης φωτονίων, αλλά στο φαινόμενο της αναπήδησης. Κατά το φαινόμενο αυτό τα σωμάτια χαμαιλέοντες παράγονται από ταλαντώσεις φωτονίων, παγιδεύονται σε κενό δοχείο και καθώς ανακλώνται στα τοιχώματά του, αναπηδούν (μετατρέπονται) πάλι σε φωτόνια. Στην περίπτωση αυτή, όπως και στα βαθμωτά σωμάτια η σύζευξη με τον ηλεκτρομαγνητισμό γίνεται με μία συνάρτηση γραμμική ή εκθετική. Τα πειράματα αυτά όπως και τα προηγούμενα, δεν οδήγησαν στην ανίχνευση των σωματιδίων που αναζητούσαν οι ερευνητικές ομάδες. Όμως απέκλεισαν κάποιες περιοχές ενέργειας στις οποίες θα μπορούσε να βρίσκεται η μάζα ηρεμίας του σωματιδίου χαμαιλέοντας. Παρ΄όλα αυτά, η αναζήτηση συνεχίζεται μιας και η ύπαρξη των σωματιδίων αυτών μπορεί να υποστηρίξει την πυκνότητα ενέργειας της σκοτεινής ενέργειας, αφού αναμένεται να έχουν την ίδια τάξη μεγέθους.

Η συνάρτηση σύζευξης που χρησιμοποιήσαμε παραπάνω, μπορεί να εμφανιστεί ως επέκταση στην εξέλιξη του πεδίου πεμπτουσίας, μέσω μίας σύζευξης με τον ηλεκτρομαγνητικό τανυστή στην Λαγκρατζιανή. Σε αυτό το κοσμολογικό μοντέλο προβλέπεται πως όταν το δυναμικό είναι γραμμικό, το βαθμωτό πεδίο αυξάνει σταδιακά με τον χρόνο αλλά από ένα σημείο και μετά υπόκειται σε βίαιη αύξηση. Αντίστοιχα, ο παράγοντας κοσμικής διαστολής αυξάνει αλλά όταν το πεδίο αυξηθεί απότομα, τότε αυτός μειώνεται ραγδαία μέχρι που μηδενίζεται. Το φαινόμενο αυτό αποκαλείται μεγάλο σπάσιμο (Big Crunch) ή μεγάλο πάγωμα (Big Freeze) γιατί στην ουσία το Σύμπαν θα συρρικνωθεί σε μία μοναδικότητα (ένα σημείο). Ορίσαμε την ηλεκτρομαγνητική παράμετρο (ζ_m) ως τον λόγο της ηλεκτρομαγνητικής ενεργειακής πυκνότητας του χώρου προς την πυκνότητα ύλης του, η οποία εκφράζει το ποσοστό της ηλεκτρομαγνητικής ενέργειας σε σχέση με την πυκνότητα ύλης στο σύμπαν. Σε κάθε περίπτωση η πυκνότητα ύλης παραμένει κυρίαρχη. Μελετήσαμε την περίπτωση που στο χώρο κυριαρχεί η ηλεκτροστατική ενέργεια ($\zeta_m > 0$) και όχι η μαγνητοστατική ($\zeta_m < 0$). Καθώς αυξάνει η ηλεκτροστατική ενέργεια του χώρου μέσω της παραμέτρου ζ_m, το βαθμωτό πεδίο απειρίζεται σε μεταγενέστερη χρονική στιγμή και το μεγάλο πάγωμα εμφανίζεται επίσης πιο αργά. Αυτό σημαίνει πως το σύστημά μας, λόγω της συνεχώς αυξανόμενης ηλεκτροστατικής ενέργειας έναντι της μη σχετικιστικής ύλης που εξακολουθεί να είναι κυρίαρχη, αποκτά σταθερότητα για μεγαλύτερο χρονικό διάστημα. Το μεγάλο σπάσιμο καθυστερεί να συμβεί και τα κοσμικά συστήματα έχουν μεγαλύτερη διάρκεια ζωής.

Στη συνέχεια υπολογίσαμε τον τρόπο μεταβολής της παραμέτρου w της καταστατικής εξίσωσης σε συνάρτηση με τον χρόνο. Διαπιστώσαμε πως αυτό το μοντέλο αντιστοιχεί στο κοσμολογικό μοντέλο της πεμπτουσίας, αφού η τιμή της παραμέτρου καταστατικής εξίσωσης είναι ελάχιστα πάνω από την τιμή $w = -1$, αλλά με πολύ μικρή μεταβολή. Μάλιστα, όταν περάσει αρκετά μεγάλο χρονικό διάστημα, φαίνεται ότι η τιμή της ηλεκτρομαγνητικής παραμέτρου ζ_m, δεν επηρεάζει ιδιαίτερα την τιμή της παραμέτρου καταστατικής εξίσωσης. Παρόμοια συμπεράσματα εξάγονται και από την μεταβολή της παραμέτρου της καταστατικής εξίσωσης σε σχέση με την μετατόπιση στο ερυθρό. Αμελητέες διακυμάνσεις παρατηρούνται, λίγο πάνω από την τιμή $w = -1$.

Οι μεταβολές στην τιμή της σταθεράς λεπτής υφής α μπορούν να περιγραφούν και μέσω της σταθεράς σύζευξης g που προσπαθούν να ανιχνεύσουν και να μετρήσουν τα προαναφερθέντα πειράματα με βαθμωτά σωματίδια ή χαμαιλέοντες. Η ύπαρξη ενός θετικού σήματος θα μας επιτρέψει να ελέγξουμε αν οι σημερινές παρατηρούμενες μεταβολές στην σταθερά λεπτής υφής, θα μπορούσαν να οφείλονται σε βαθμωτά σωματίδια ή σωματίδια-χαμαιλέοντες (η μεταβολή των σταθερών της Φυσικής, δεν αποτελεί μέρος του κοσμολογικού μοντέλου) . Στο τέλος αυτού του κεφαλαίου συλλέξαμε αρκετά όρια για την σταθερά σύζευξης g από παρατηρήσεις στον μακρόκοσμο και τον μικρόκοσμο και τα συγκρίναμε με τις θεωρητικές τιμές των πειραμάτων, εκτιμώντας ότι οι ενδείξεις συσχέτισης θεωρίας και παρατηρήσεων είναι αξιοσημείωτες και ελπιδοφόρες.

Υπάρχουν ισχυρές ενδείξεις πως οι αλληλεπιδράσεις των σωμάτων σε πολύ μικρές αποστάσεις (κάτω από 1 χιλιοστό) δεν ακολουθούν τον νόμο της βαρύτητας του Νεύτωνα (νόμος αντιστρόφου τετραγώνου) αλλά έχουν ταλαντωτική μορφή. Αυτό μας οδηγεί στην σκέψη πως ο νόμος του Νεύτωνα ίσως χρειάζεται κάποια τροποποίηση, ή μπορεί να μην ισχύει σε τόσο μικρή απόσταση. Πολύ πιθανόν είναι επίσης, αυτή η συμπεριφορά να αποτελεί σημάδι εμφάνισης κάποιας νέας αλληλεπίδρασης και το μήκος κύματος που εμφανίζεται στην

ταλάντωση να σχετίζεται με την ενέργεια του νέου σωματίου, που είναι φορέας αυτής της δύναμης. Σε κάθε περίπτωση, αν τα πράγματα έχουν έτσι όπως εκτιμάμε, μιλάνε για ενδείξεις νέας Φυσικής σε πολύ μικρές αποστάσεις. Στο κεφάλαιο 5, προσπαθήσαμε να ανιχνεύσουμε ένα τέτοιο μήκος κύματος χρησιμοποιώντας δεδομένα απόστασης και δύναμης από ένα πείραμα με αιωρούμενες μικρόσφαιρες που έγινε στο πανεπιστήμιο του Stanford και είχε ως στόχο την ανίχνευση νέων αλληλεπιδράσεων. Η διάταξη που χρησιμοποιήθηκε έχει τέτοια ευαισθησία ώστε μπορεί να μετρήσει δυνάμεις αρκετά μικρότερες από 10^{-18}N, ενώ στο πείραμα χρησιμοποιήθηκαν 3 πανομοιότυπες μικρόσφαιρες.

Ορίσαμε ως υπόλοιπο δύναμης την διαφορά του ηλεκτροστατικού υποβάθρου από την μετρούμενη δύναμη για τις μικρόσφαιρες και με την μέθοδο ελαχίστων τετραγώνων εκτιμήσαμε το πλάτος, το μήκος κύματος και την αρχική φάση υιοθετώντας ταλαντωτικό μοντέλο για το υπόλοιπο δύναμης. Στην συνέχεια ελέγξαμε στατιστικά το αποτέλεσμα με δύο διαφορετικούς τρόπους. Αρχικά συγκρίναμε το αποτέλεσμα με την περίπτωση να μην υπάρχουν καθόλου υπόλοιπα δύναμης και αποδείξαμε με αρκετά μεγάλο βαθμό αξιοπιστίας πως αυτή η υπόθεση δεν είναι σωστή. Έπειτα, με την μέθοδο Μόντε Κάρλο επιλέξαμε τυχαία υπόλοιπα δύναμης που ακολουθούν κανονική κατανομή με μέση τιμή μηδέν και βρήκαμε πως μόνο σε ένα μικρό ποσοστό της τάξης του 5% μπορεί να εμφανιστεί ένα τέτοιο σήμα. Συνεπώς, το επίπεδο σημαντικότητας του σήματος που βλέπουμε στα δεδομένα είναι στα 2σ και θεωρείται αρκετά ισχυρό.

Το σήμα που εντοπίσαμε στα δεδομένα έχει μήκος κύματος $\lambda \simeq 35\mu m$ και θα μπορούσε να ερμηνευτεί ως ένδειξη για νέα αλληλεπίδραση (γνωστή ως πέμπτη δύναμη) που συνδέεται με τροποποιημένες θεωρίες βαρύτητας ή να σχετίζεται με την σκοτεινή ενέργεια. Μπορεί όμως και να οφείλεται σε συστηματικό σφάλμα του πειράματος, κάτι που θεωρεί πιθανότερο η ερευνητική ομάδα του Stanford. Η εκτίμηση αυτή διατυπώθηκε έπειτα από επικοινωνία μαζί τους. Στην περίπτωση που αυτή η ερμηνεία είναι σωστή, εκτιμήσαμε ένα άνω όριο για το πλάτος της αλληλεπίδρασης και αποκλείσαμε το ενδεχόμενο η δύναμη να είναι βαρυτική. Δοκιμάσαμε να προσαρμόσουμε και άλλες παραμετροποιήσεις στα δεδομένα, όπως πολυωνυμική ή Yukawa αλλά τα αποτελέσματα ήταν αποτρεπτικά, μιας και το αντίστοιχο σήμα ήταν αμελητέο. Η ερευνητική ομάδα, που εκτέλεσε το πείραμα, προσάρμοσε στα δεδομένα ένα μοντέλο που αντιστοιχεί σε δυναμικό που θα μπορούσαν να ακολουθούν τα σωματίδια χαμαιλέοντες.

Σε θεωρητικό επίπεδο αυτές οι αποκλίσεις είναι ενδείξεις για ένα μεγάλο εύρος επεκτάσεων της Γενικής Θεωρίας της Σχετικότητας όπως θεωρίες f(R), μοντέλα συμπιεσμένων επιπλέον διαστάσεων, συμπαγείς βαθμοτανυστικές θεωρίες Brans-Dicke και μη τοπικές θεωρίες βαρύτητας. Οι τρεις πρώτες θεωρίες περιέχουν αστάθειες. Αντίθετα, οι μη τοπικές θεωρίες βαρύτητας, έχουν αρκετά πλεονεκτήματα μιας και δεν έχουν αστάθειες ή μοναδικότητες, δεν χρειάζονται την κοσμολογική σταθερά για την ερμηνεία κοσμολογικών παρατηρήσεων και προκύπτουν με φυσικό τρόπο από το κβαντικό επίπεδο.

Στο κεφάλαιο 6, μελετήσαμε τις επιπτώσεις στη συμπεριφορά των βαρυτικών κυμάτων όταν πλησιάζουν ένα συμπαγές αστρικό αντικείμενο, όπως μία μελανή οπή ή έναν αστέρα νετρονίων όπου το βαρυτικό πεδίο είναι ισχυρό. Αρχικά εξαγάγαμε την κυματική εξίσωση, εισάγοντας διαταραχές με την μορφή συναρτήσεων στην μετρική FRW σε καρτεσιανές συντεταγμένες. Στην περίπτωση αυτή, η διαφορική εξίσωση που έχει ως λύση την κυματοσυνάρτηση, λύνεται αναλυτικά. Στην συνέχεια, θέλοντας να επεκτείνουμε την ήδη γνωστή λύση, εισάγαμε την μετρική McVittie που περιγράφει τον καμπύλο χωροχρόνο γύρω από μία μεγάλη μάζα, στο Νευτώνειο όριό της (ασθενής βαρύτητα, μικρές ταχύτητες). Στην περίπτωση αυτή η κυματική εξίσωση δεν λύνεται αναλυτικά, αλλά μόνο αριθμητικά. Για να ελέγξουμε την ορθότητα του φορμαλισμού μας λύσαμε την εξίσωση αυτή απουσία μάζας και διαπιστώσαμε πως είναι ακριβώς ίδια με την γνωστή λύση σε FRW χωροχρόνο. Αυτή η ταύτιση αποτέλεσε ένα κριτήριο ορθότητας της ανάλυσής μας.

Καθώς το επίπεδο βαρυτικό κύμα πλησιάζει μία μεγάλη μάζα, κάποια από τα χαρακτηριστικά του κύματος αλλάζουν λόγω της έντονης καμπύλωσης του χωροχρόνου. Συγκεκριμένα, η περίοδος ταλάντωσης αυξάνει και αυτή η αύξηση είναι αναμενόμενη, καθώς αντιστοιχεί σε ένα γνωστό κοσμολογικό φαινόμενο που ονομάζεται *βαρυτική χρονική καθυστέρηση*, αλλά είναι η πρώτη φορά που προβλέπεται θεωρητικά σε βαρυτικό κύμα. Προφανώς η συχνότητα του κύματος μειώνεται μιας και τα βαρυτικά κύματα διαδίδονται με σταθερή ταχύτητα, ίση με την ταχύτητα του φωτός. Επίσης, το πλάτος ταλάντωσης αυξάνει που σημαίνει πως η ενέργεια που μεταφέρει το κύμα αυξάνει. Η αύξηση ενέργειας πιθανόν να οφείλεται στην μεταφορά ενέργειας από τον χωροχρόνο στο κύμα με μηχανισμό που είναι άγνωστος μέχρι σήμερα. Η αύξηση που παρατηρούμε είναι σχετικά μικρή, αλλά μεγαλώνει με την αύξηση της καμπυλότητας του χωροχρόνου. Ακόμη βρήκαμε πως το φάσμα συχνοτήτων του κύματος αλλοιώνεται με την παρουσία της μάζας, καθώς συμετέχουν περισσότερο οι

χαμηλές αρμονικές και λιγότερο οι υψηλές στη διαμόρφωση του κύματος, σε σχέση με το κύμα που διαδίδεται σε κενό χώρο.

Από τα παραπάνω φαινόμενα που περιγράψαμε, εκείνο που μπορούμε να δούμε σε κοσμολογικές παρατηρήσεις είναι οι αλλαγές στο φάσμα συχνοτήτων. Στο ηλιακό μας σύστημα, όσον αφορά την μεταβολή της περιόδου είναι πολύ μικρή, άρα πολύ δύσκολα μετρήσιμη. Αντίθετα, σε γαλαξιακή κλίμακα, το φαινόμενο είναι αρκετά πιο ισχυρό, συνεπώς πιο εύκολα ανιχνεύσιμο. Τέλος, στα δεδομένα μας φαίνεται να υπάρχει μία συσχέτιση μεταξύ της πυκνότητας ενέργειας του κύματος και του πλάτος του κύματος, όπου η πυκνότητα είναι ανάλογη με το τετράγωνο του πλάτους.

Οι γεωδαισιακές αποτελούν τροχιές σωματιδίων ή φωτονίων υπό την επίδραση μόνο της βαρυτικής αλληλεπίδρασης. Είναι τροχιές που αντιστοιχούν στην μικρότερη χρονική απόσταση δύο σημείων σε έναν χωροχρόνο. Σε έναν κοσμολογικό χωροχρόνο, που η παράμετρος της καταστατικής εξίσωσης w είναι μικρότερη από -1, αν προσεγγίσουμε το φαινόμενο μη σχετικιστικά, οι γεωδαισιακές τροχιές των σωματιδίων σε κάποια χρονική στιγμή υφίστανται διάλυση και το σύστημα διασπάται. Το φαινόμενο αυτό είναι γνωστό ως *Μεγάλο Σχίσιμο* και όσο μεγαλύτερη είναι η κοσμική δομή σε μάζα και διαστάσεις, τόσο νωρίτερα προβλέπεται να συμβεί το φαινόμενο αυτό. Πρώτα προβλέπεται να διαλυθούν τα σμήνη γαλαξιών, μετά οι γαλαξίες και στην συνέχεια τα πλανητικά συστήματα.

Στο κεφάλαιο 7, μελετήσαμε το φαινόμενο διαχωρισμού των δέσμιων συστημάτων γύρω από μία μεγάλη μάζα όπως μαύρη τρύπα, επιβάλλοντας σχετικιστική προσέγγιση. Συγκεκριμένα θεωρήσαμε, όπως είναι ευρέως αποδεκτό, ότι ένας τέτοιος χωροχρόνος περιγράφεται ακριβέστερα με την μετρική McVittie. Ως κριτήριο διάσπασης του συστήματος ορίσαμε τη χρονική στιγμή που φτάνει σε μέγεθος αυξημένο κατά 20% σε σχέση με το αρχικό του ακτινικό μέγεθος. Ο χρόνος αποχωρισμού των συστημάτων εξαρτάται από το μέγεθός τους, αλλά και από την ταχύτητα περιστροφής.

Αν δύο συστήματα έχουν ίδια γωνιακή ταχύτητα περιστροφής, τότε αυτό που έχει το μεγαλύτερο μέγεθος θα διασπαστεί πιο γρήγορα. Διαπιστώσαμε πως σε σχέση με την Νευτώνεια προσέγγιση του φαινομένου ο χρόνος πραγματοποίησης της διάσπασης είναι μικρότερος αν το φαινόμενο μελετηθεί σχετικιστικά. Μάλιστα, όσο μεγαλύτερο είναι το μέγεθος, τόσο πιο γρήγορα γίνεται ο διαχωρισμός. Για συστήματα που έχουν το ίδιο μέγεθος, όταν αυξάνει η γωνιακή ταχύτητα περιστροφής, παρατείνεται η σταθερότητα του συστήματος, οπότε αργεί ο διαχωρισμός. Γενικά, για να είναι ένα σύστημα σταθερό για μεγάλο χρονικό διάστημα θα πρέπει να έχει μικρό μέγεθος και μεγάλη γωνιακή ταχύτητα περιστροφής. Στο τέλος εκτιμήσαμε για διάφορα κοσμικά συστήματα, όπως το ηλιακό σύστημα και τον γαλαξία μας, την χρονική διαφορά στην εμφάνιση του διαχωρισμού μεταξύ Νευτώνειας και σχετικιστικής θεώρησης. Εδώ πρέπει να τονίσουμε πως οι χρονικές διαφορές είναι πολύ μικρές και έχουν ουσιαστικό ενδιαφέρον όταν αναφέρονται σε μεγάλα και εκτενή κοσμολογικά συστήματα, όπως υπερσμήνη γαλαξιών.

Στο Κεφάλαιο 8, ασχοληθήκαμε με τις τροχιές που ακολουθεί ένα σώμα όταν περιστρέφεται γύρω από μία μεγάλη μάζα όπου η βαρύτητα είναι ισχυρή, όπως μία μαύρη τρύπα ή έναν αστερα νετρονίων και το οποίο έχει ιδιοπεριστροφή (σπιν), θεωρώντας ότι ο χωροχρόνος περιγράφεται από την μετρική McVittie στο μετα-Νευτώνειο όριο. Η περιστροφή μιας μάζας (που έχει και ιδιοπεριστροφή) γύρω από μία πολύ μεγαλύτερη περιγράφεται από τις εξισώσεις Mathisson-Papapetrou (MP) και έχει μελετηθεί πλήρως σε χωροχρόνο Schwarzschild όπως και σε άλλους χωροχρόνους. Το σώμα όταν έχει σπιν δεν κινείται σε γεωδαισιακή τροχιά, λόγω της επιπλέον δύναμης που προκαλείται από την ύπαρξη του σπιν, αλλά σε μία κοσμική γραμμή. Λόγω της σύζευξης μεταξύ σπιν και ταχύτητας του σωματιδίου, αυτή η δύναμη μπορεί να είναι ελκτική ή απωστική, ανάλογα με την φορά περιστροφής του σωματιδίου.

Το σύστημα των MP εξισώσεων έχει άπειρες λύσεις αφού οι άγνωστοι είναι περισσότεροι από τις εξισώσεις. Για να έχει το σύστημα μοναδική λύση εισάγουμε στο σύστημα μία συμπληρωματική συνθήκη που προσδιορίζει το κεντροειδές του συστήματος (το σημείο αναφοράς για την μέτρηση του σπιν). Επιλέξαμε την Τ συνθήκη, η οποία περιγράφει με πιο φυσικό τρόπο το σύστημα και χρησιμοποιείται ευρέως στην βιβλιογραφία. Λόγω αυτής της συνθήκης, το σπιν του σώματος διατηρείται σταθερό σε όλη τη διάρκεια της κίνησης. Επίσης, κατά την κίνηση του σώματος διατηρείται η συνολική στροφορμή, ενώ θεωρήσαμε πως η κίνηση πραγματοποιείται στο ισημερινό επίπεδο. Υποθέτοντας πως το περιστρεφόμενο σώμα έχει στροφορμή μόνο σε έναν άξονα, που είναι παράλληλος προς τον άξονα του σπιν, τα αποτελέσματα έδειξαν ότι οι τροχιές των σωματιδίων εξαρτώνται από τον παράγοντα κοσμικής διαστολής που ακολουθεί το κοσμολογικό υπόβαθρο, τις τιμές που μπορεί να πάρει το σπιν, την φορά ιδιοπεριστροφής του σώματος (δεξιόστροφη ή

αριστερόστροφη) καθώς και από την ακτίνα του κεντρικού σώματος.

Στην δική μας μελέτη, υιοθετήσαμε την μετρική McVittie στο μέτα-Νευτώνειο όριο και λάβαμε υπόψιν την διαστολή του Σύμπαντος με διάφορους ρυθμούς. Όταν το Σύμπαν είναι στατικό και το σώμα δεν έχει σπιν, θα εκτελεί συνεχώς κυκλική τροχιά. Όταν όμως εισάγουμε την ύπαρξη σπιν, τότε οι κυκλικές τροχιές διαταράσσονται και το σώμα πλησιάζει το κεντρικό σώμα όταν το σπιν είναι ομόρρροπο με την γωνιακή ταχύτητα περιστροφής ή απομακρύνεται από αυτό όταν το σπιν είναι αντίρροπο από την γωνιακή ταχύτητα περιστροφής (παραμένοντας δέσμιο του κεντρικού σώματος), γιατί η σύζευξη σπιν και ταχύτητας δημιουργεί ελκτική ή απωστική δύναμη αντίστοιχα. Αν η ακτίνα της τροχιάς γίνει μικρότερη από τρεις ακτίνες Schwarzschild που είναι το εσωτερικότερο όριο σταθερής τροχιάς, τότε το σώμα συλλαμβάνεται από την ισχυρή βαρύτητα του πεδίου και συγχωνεύεται με την μαύρη τρύπα.

Στην περίπτωση που η διαστολή του κοσμικού υποβάθρου είναι επιβραδυνόμενη, το σώμα για μικρές τιμές του σπιν πλησιάζει το κεντρικό σώμα και συλλαμβάνεται από αυτό, ενώ για μεγαλύτερες τιμές απομακρύνεται. Τέλος, στην περίπτωση που η διαστολή είναι επιταχυνόμενη όπως το Σύμπαν de Sitter, το περιστρεφόμενο σώμα σε όλες σχεδόν τις περιπτώσεις που μελετήσαμε απομακρύνεται από το κεντρικό σώμα, έχοντας κυρίως μεταφορική ταχύτητα, χωρίς να περιστρέφεται σημαντικά. Εξαίρεση αποτελεί η περίπτωση ελκτικής δύναμης λόγω της σύζευξης του σπιν στην περίπτωση που το σπιν έχει πολύ μεγάλες τιμές. Η ελκτική δύναμη κυριαρχεί της απωστικής διαστολής και το σώμα οδηγείται στην μαύρη τρύπα. Στο τέλος αυτού του κεφαλαίου εκτιμήσαμε το χρονικό διάστημα που απαιτείται σε ένα κοσμολογικό σύστημα ώστε να γίνουν αντιληπτά τα φαινόμενα διαστολής στις τροχιές των περιστρεφόμενων σωματιδίων. Ο χρόνος αυτός μπορεί να είναι από μερικά χρόνια (ηλιακό σύστημα) μέχρι μερικά εκατομμύρια χρόνια (σμήνος γαλαξιών). Σε περιβάλλον μαύρης τρύπας ο χρόνος αυτός είναι ακόμη μεγαλύτερος, λόγω της πολύ ισχυρής βαρύτητας.

Στο Κεφάλαιο 9, που αποτελεί και το τελευταίο κεφάλαιο του παρόντος πονήματος, παραθέτουμε τα σημαντικότερα συμπεράσματα που εξάχθηκαν από την έρευνα που πραγματοποιήθηκε στο πλαίσιο της παρούσας Διδακτορικής Διατριβής. Επιπλέον παραθέτουμε τις βασικές προοπτικές επέκτασης και εξέλιξης των υπό θεωριών που μελετήθηκαν, τα οποία ενθαρρύνονται από την υλοποίηση της παρούσας εργασίας, περιλαμβάνοντας ενδιαφέροντα ανοιχτά θέματα των συναφών αντικειμένων της εκπονηθείσας έρευνας.

Κλείνοντας, στα Παραρτήματα περιέχονται συμπληρωματικές πληροφορίες, απαραίτητες για την πλήρη κατανόηση των θεμάτων που αναπτύχθηκαν σε αυτό το πόνημα, όπως μερικοί υπολογιστικοί κώδικες, πειραματικά δεδομένα, ο τανυστής Riemann και τα σύμβολα Christoffel που απαιτούνται για τον προσδιορισμό των τροχιών των σωματίων με σπιν. Τέλος, παρατίθεται μία σύγχρονη και εκτεταμένη Βιβλιογραφία που αναφέρεται σε όλα τα θέματα που μελετήσαμε, η οποία αποτέλεσε το βασικό υπόβαθρο καθώς και το κίνητρο της Διδακτορικής Διατριβής.

List of Figures

List of Tables

Chapter 1

Introduction

1.1 The first steps of Modern Cosmology

At the beginning of twentieth century, the publication of the theory of General Relativity (GR) by Albert Einstein putt the foundations of the Modern Cosmology. It is important to underline that, according to this theory, the gravity is not a property of each mass, but a geometric property of the space. A large concentration of mass, such as the Earth, significantly distorts space-time in its vicinity. Bodies moving through a region of distorted spacetime move differently from the way they would have moved in an undisturbed spacetime. The central ideas of GR have been neatly summarized by the American physicist John Archibald Wheeler. In his famous phrase, Wheeler said

```
'Matter tells space how to curve. Space tells matter how to move.'
```

In contrast, the previous Newtonian theory of gravity, which considers the gravity as an interaction between the masses, is summarized in the words

```
'Matter tells matter how to move'
```

General relativity is a field theory of gravity. Until today, all astronomical and cosmological observations such as the light bending towards a big mass or the existence of gravitational waves show that the theory is correct. At its heart there is a set of equations called the Einstein field equations and if we use 'natural' units with $\hbar = c = k_B = 1$, they have the compact form

$$\boxed{G_{\mu\nu} \equiv R_{\mu\nu} - \frac{1}{2} g_{\mu\nu} R + g_{\mu\nu}\Lambda = 8\pi G T_{\mu\nu}} \tag{1.1}$$

The Einstein's tensor $G_{\mu\nu}$, which describes the geometry of spacetime, is proportional to the energy momentum tensor $T_{\mu\nu}$ that provides the matter distribution at each event in spacetime. The tensor $g_{\mu\nu}$ denotes the metric of the spacetime, $R_{\mu\nu}$ stands for the Ricci tensor and R is the Ricci scalar. Also, G is the Gravitational constant and Λ is the cosmological constant, first introduced by Einstein. The indices μ, ν are the coordinates of the spacetime, namely t, x, y, z in Cartesian system or 0,1,2,3 respectively. If in Eq. (1.1), the tensors are diagonal (the non diagonal terms are equal to zero), then only four field equations remain. Every solution of the system of equations (1.1) potentially is a cosmological model.

In order to calculate for a chosen metric the Ricci tensor and the Ricci scalar for any line element, one must begin from the Christoffel symbols

$$\boxed{\Gamma^a_{bc} = \frac{1}{2} g^{ad} \Big(\partial_b g_{dc} + \partial_c g_{bd} - \partial_d g_{bc} \Big)} \tag{1.2}$$

then, one must calculate the components of the Ricci tensor [1]

$$\boxed{R_{ab} \equiv R^{c}_{abc} = \partial_b \Gamma^{i}_{ai} - \partial_i \Gamma^{i}_{ab} + \Gamma^{j}_{ai}\Gamma^{i}_{jb} - \Gamma^{j}_{ab}\Gamma^{i}_{ji}} \tag{1.3}$$

and finally one obtains the Ricci scalar (curvature scalar)

$$\boxed{R \equiv g^{ab} R_{ab} = R^{a}_{a}} \tag{1.4}$$

which is a construction of the Ricci tensor.

In a homogeneous and isotropic universe, which is filled with a perfect fluid [2] with density ρ and pressure P, we consider the Friedmann-Robertson-Walker (FRW) metric (in spherical coordinates) and the line element

$$\boxed{ds^2 = -dt^2 + a^2(t)\left(\frac{dr^2}{1-kr^2} + r^2 d\theta^2 + r^2 \sin^2\theta d\phi^2\right)} \tag{1.5}$$

The non vanishing components of the metric tensor are

$$g_{00} = -1, \quad g_{11} = \frac{a^2(t)}{1-kr^2}, \quad g_{22} = a^2(t) r^2, \quad g_{33} = a^2(t) r^2 \sin^2\theta$$

A very important quantity which is connected with the geometry of the spacetime is the spatial curvature k which determines the shape of the universe. A maximally symmetric space is specified by just one number (the curvature k), which is independent of the coordinates. There are three allowable values for the spatial curvature which correspond to different shape of the universe

1. $k = -1$ which corresponds to an open hyperboloid shape,
2. $k = 0$ which describes a flat universe (i.e. Euclidean space)
3. $k = +1$ for a closed 3-sphere universe

The vast majority of the cosmological observations indicates that, the shape of our universe is flat. Thus, I adopt this evidence and assume $k = 0$, except the present Chapter, dealing with general Introduction of Cosmology.

When $k = \pm 1$, the coefficient of dr^2 in FRW metric (1.5) becomes singular as $r \to 1$. Thus, in order to remove the singularity, it is convenient to introduce a function $r = S(\chi)$, defined as

$$S(\chi) = \begin{cases} \sin\chi, & \text{if } k = +1, \\ \chi, & \text{if } k = 0, \\ \sinh\chi, & \text{if } k = -1, \end{cases} \tag{1.6}$$

In this case, the FRW metric takes the more convenient form

$$\boxed{ds^2 = -dt^2 + a^2(t)\left(d\chi^2 + S^2(\chi) d\theta^2 + S^2(\chi)\sin^2\theta d\phi^2\right)} \tag{1.7}$$

[1] The Riemann, or curvature tensor is defined as

$$R^{d}_{abc} = \partial_b \Gamma^{d}_{ac} - \partial_c \Gamma^{d}_{ab} + \Gamma^{e}_{ac}\Gamma^{d}_{eb} - \Gamma^{e}_{ab}\Gamma^{d}_{ec}$$

[2] A perfect fluid is defined as one for which there are no forces between the particles, and no heat conduction or viscosity in the inertial rest frame.

1.1.1 Cosmological Principle

A basic assumption of the theory of GR is the *Cosmological Principle*, which states that, the universe is homogeneous and isotropic to a high level of accuracy. Homogeneity demands that all points on a particular spacelike hypersurface are equivalent, whereas isotropy demands that all directions on the hypersurface are equivalent for fundamental observers [3]. Thus, at any particular time the universe looks the same from all positions in space at a particular time and all directions in space at any point are equivalent. The Cosmological Principle

- is motivated by extending the Copernican principle to the whole universe
- is the simplest principle in order to solve Einstein's equations
- is initially supported by few observations due to limitations in observational instruments

The acceptable theory for the origin of the universe is the Big Bang (a singularity with infinite density and temperature) which took place before almost 13.7 billion years. The universe started to expand and the temperature to decrease. The degree of expansion depends on the components of the universe. Today we know that the universe consists of ordinary (baryonic) visible matter ($\sim 5\%$), dark matter (almost 25%) which is invisible and dark energy (roughly 70%) whose origin and composition is unknown.

1.2 Geodesics

Geodesic is the trajectories followed by a particle in the absence of any forces, i.e. that experiencing only the 'background' gravitational field of the cosmological fluid. Examples of such particles might include a projectile shot out of a galaxy or a photon travelling through intergalactic space. When the particle has some mass the geodesic is called *timelike*, while for massless particles such as photons, the geodesic is called *null*. Also, geodesic is defined as the path of shortest distance between two points, or a line along which the tangent vector is parallel transported. The tangent vector to a path $x^\mu(\lambda)$ is defined as $\frac{dx^\mu}{d\lambda}$. In Newtonian Physics the geodesics are straight lines. Geodesics generalize the notion of a "straight line" to curved spacetime.

In General Relativity, where generally the spacetime is curved and the line element is

$$ds^2 = \sum_{\mu,\nu=0}^{3} g_{\mu\nu} dx^\mu dx^\nu \tag{1.8}$$

the geodesic equations correspond to particle's motion which interacts only gravitationally. It can be derived from the minimization of the action as

$$\boxed{\frac{d^2x^\mu}{d\lambda^2} + \Gamma^\mu_{\alpha\beta} \frac{dx^\alpha}{d\lambda} \frac{dx^\beta}{d\lambda} = 0} \tag{1.9}$$

where λ is a parameter which monotonically increases along the particle's path. For timelike geodesics, λ is called affine parameter and it is actually the proper time τ (the time which is measured by the moving particle). In that case, the path $x^\mu(\tau)$ is the worldline and the tangent vector is the 4-velocity

$$\boxed{u^\mu \equiv \frac{dx^\mu}{d\tau}} \tag{1.10}$$

[3] An observer is called fundamental when is assumed to have no motion in relation to the overall cosmological fluid. It is common practice to identify fundamental observers with individual galaxies (that are assumed to be pointlike). However, we must neglect the small peculiar velocities of real individual galaxies.

Thus, the worldlines $x^\mu(\tau)$ are geodesics and hence can describe particles (observers) moving only under the influence of gravity. A significant part of my thesis deals with geodesics in an expanding universe (specifically in McVittie spacetime). It is useful to rewrite the Eq. (1.9) in the form

$$\boxed{\frac{du_\mu}{d\tau} = \frac{1}{2}\Big(\partial_\mu g_{ab}\Big)u^a u^b} \tag{1.11}$$

which shows, as expected, that if the metric is independent of a particular coordinate x^μ, then $\frac{du_\mu}{d\tau} = 0$. Consequently, the corresponding velocity u^μ is conserved along the geodesic.

1.3 Scale factor and expansion

In 1929, Edwin Hubble discovered that distant galaxies are in fact receding from us and their velocity increases with distance. In an expanding universe the physical distance $R(t)$, where t is the cosmic time and the comoving distance r (distance without expansion) between two galaxies, are related as

$$\boxed{R(t) = a(t)r} \tag{1.12}$$

The degree of expansion is determined by the scale factor $a(t)$. In the absence of any peculiar velocity which means $\dot{r} = 0$ the differentiation of Eq. (1.12) gives $\dot{R} = \dot{a}r$, where dot stands for cosmic time derivative. Since $\dot{R}$ is the relative velocity υ of the galaxies, we conclude that $\dot{R} = \frac{\dot{a}}{a}ar = H(t)R$, where

$$\boxed{H(t) = \frac{\dot{a(t)}}{a(t)}} \tag{1.13}$$

is the Hubble rate. Thus, we derive the Hubble law in the form

$$\boxed{\upsilon = H(t)R} \tag{1.14}$$

The Hubble law indicates that the relative velocity of celestial objects is proportional to their distance from us. Also, it implies that the universe started off at high density at some finite time in the past (prediction for the existence of Big Bang singularity). Edwin Hubble in his work plotted the velocity of a few decades of nearby galaxies as a function of their distance from us, the corresponding diagram is called the *Hubble diagram* (see Fig. 1.1) and constitutes historically a first proof that the universe is expanding.

1.3.1 Redshift

Another way to observe the expansion of the universe is through the spectroscopy with the aid of Doppler effect. When a celestial body emits light with wavelength λ_e, due to expansion, when this light arrives to our detectors we observe a wavelength λ_o which is bigger, or in other words red shifted (see Fig. 1.2). Thus, for any celestial body which emits electromagnetic waves, we define the *redshift* z through the simple relation

$$\boxed{1 + z = \frac{\lambda_o}{\lambda_e} = \frac{f_e}{f_o}} \tag{1.15}$$

It is clear that the redshift is a stretching factor. Actually, the redshist expresses the distance of any celestial body which emits any kind of electromagnetic radiation. When the redshift is bigger, the body is farther. For an expanding universe the photon is redshifted by an amount z, for a static universe there is no frequency shift, while if the universe were contracting, the photon would be blueshifted.

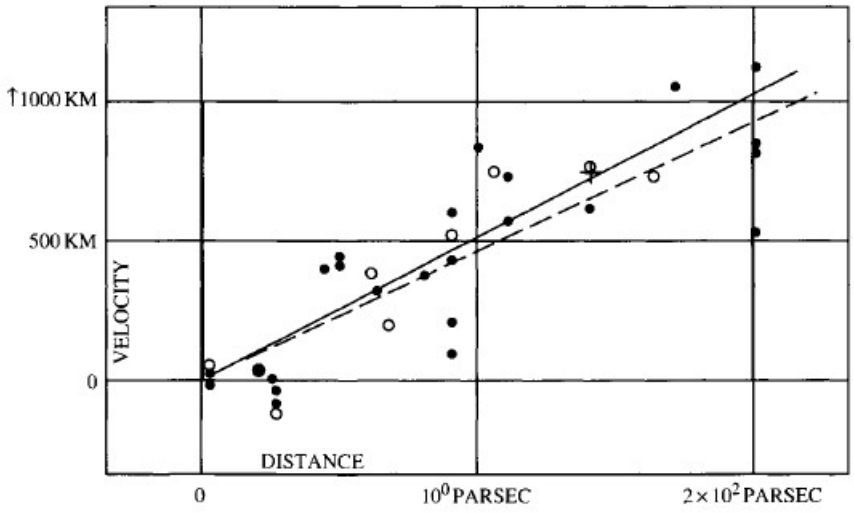

Figure 1.1: The Hubble diagram which presents the velocities of distant galaxies vs their distance (units should be Mpc). Solid (dashed) line is the best fit to the filled (open) points which are corrected (uncorrected) for the sun's motion. Adopted from [8].

The scale factor is connected with the redshift of the light emitting bodies, atoms or molecules, through the simple relation

$$\boxed{a(t) = \frac{a(t_0)}{1+z} = \frac{1}{1+z}} \tag{1.16}$$

where t_0 is the present time and for simplicity reasons, we normalize the scale factor setting $a(t_0) = 1$ by definition. We can prove the formula (1.16) if we set the distances equally [10], which we will describe right now. If an emitter sends a photon at time t_e which is received at time t_o the distance between emitter and observer is

$$\int_{t_e}^{t_o} \frac{dt}{a(t)}$$

Now, if the emitter sends a second light pulse at time $t_e + \delta t_e$, which is received at time $t_o + \delta t_o$, then the second photon travels the same distance as the first, so

$$\int_{t_e+\delta t_e}^{t_o+\delta t_o} \frac{dt}{a(t)} = \int_{t_e}^{t_o} \frac{dt}{a(t)} \Rightarrow$$

$$\int_{t_e+\delta t_e}^{t_e} \frac{dt}{a(t)} + \int_{t_e}^{t_o} \frac{dt}{a(t)} + \int_{t_o}^{t_o+\delta t_o} \frac{dt}{a(t)} = \int_{t_e}^{t_o} \frac{dt}{a(t)} \Rightarrow$$

$$\int_{t_o}^{t_o+\delta t_o} \frac{dt}{a(t)} = \int_{t_e}^{t_e+\delta t_e} \frac{dt}{a(t)}$$

Assuming that δt_o and δt_e are small, so that $a(t)$ can be taken as constant in both integrals, we have

$$\frac{1}{a(t_o)} \int_{t_o}^{t_o+\delta t_o} dt = \frac{1}{a(t_e)} \int_{t_e}^{t_e+\delta t_e} dt \Rightarrow \boxed{\frac{\delta t_o}{a(t_o)} = \frac{\delta t_e}{a(t_e)}}$$

Considering the successive pulses to be wavecrests of an electromagnetic wave, we conclude that

$$\boxed{1 + z = \frac{f_e}{f_o} = \frac{\delta t_o}{\delta t_e} = \frac{a(t_o)}{a(t_e)}} \tag{1.17}$$

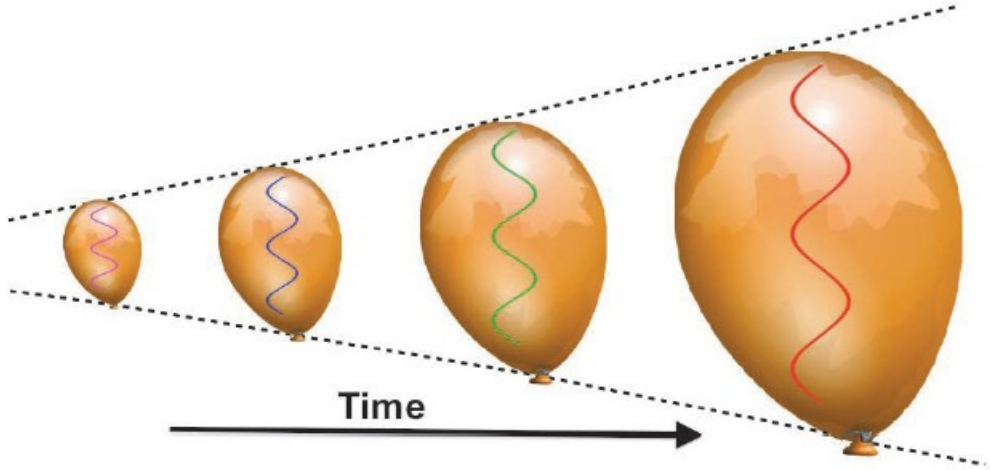

Figure 1.2: As universe expands, the spacetime which is presented as a balloon, stretches and the density goes down. Also, the wavelength of light increases and hence it is redshifted. Note that there is no single point on the balloon's surface that is the "center", but rather all points see the same thing: all the other points recede from them, with the far distant points receding faster. Adopted from [9].

The original Hubble diagram contains only nearby galaxies. In order to check the Hubble law at bigger distances, we must extend the Hubble diagram at bigger redshifts. For this reason, we use data from observations of type Ia Supernova. Type Ia Supernovae are known as standard candles due to their same intrinsic brightness. If two Supernova Ia have different brightness, this means that they are located at different distances. Also, the extension of the Hubble diagram is necessary in order to estimate with great precision the present value of Hubble rate H_0.

Since the redshift is an observable quantity, it is useful to derive general expressions for the look-back time interval $dt = t_0 - t$ (t is the time of emission from a galaxy or a particle and t_0 the time of arrival). First, we calculate the time interval dt as a function of interval dz. We have,

$$dz = d(1+z) = d\left(\frac{1}{a(t)}\right) = -\frac{\dot{a}(t)}{a^2(t)}dt = -(1+z)H(z)dt \Rightarrow$$

$$\boxed{dt = -\frac{dz}{(1+z)H(z)}} \tag{1.18}$$

Since t_0 corresponds to $z = 0$ and t to z, we can write the look-back time as

$$\boxed{t_0 - t = \int_t^{t_0} dt = \int_0^z \frac{dz}{(1+z)H(z)}} \tag{1.19}$$

and the χ coordinate of the galaxy, which is a function of the redshift z as

$$\chi = \int_t^{t_0} \frac{dt}{a(t)} = \int_0^z (1+z)\frac{dz}{(1+z)H(z)} \Rightarrow \boxed{\chi = \int_0^z \frac{dz}{H(z)}} \tag{1.20}$$

The Cosmic Microwave Background (CMB) radiation is the remnant of the Big Bang, the point which our universe began to expand. This radiation is (to a very high degree of accuracy) uniformly distributed throughout the universe and has a blackbody form. The energy of the photons is proportional to temperature ($E \sim k_B T$) and inversely proportional to wavelength ($E = \frac{hc}{\lambda}$). If we equate these energies

and take into account the redshift of the wavelength from Eq. (1.15) we conclude that the temperature of the plasma is inversely proportional to the scale factor as

$$\boxed{T(t) = \frac{T_0}{a(t)} = (1+z)T_0} \tag{1.21}$$

where $T_0 \simeq 2.725K$ is the present temperature of the CMB radiation. The Planck missions include observations of temperature and polarization anisotropies of the CMB radiation. The latest estimation [12] for the present value $H_0 \equiv H(t_0)$ of the Hubble rate is

$$H_0 = (67.8 \pm 0.9)\ Km\ sec^{-1}\ Mpc^{-1} \tag{1.22}$$

We must notice that as results from (1.14), the Hubble 'constant' has the dimensions of inverse time. For this reason, the quantity $1/H_0$ gives the age of the universe within a factor of order unity.

1.3.2 Energy-momentum tensor

The dynamics of the spacetime geometry is characterized entirely by the scale factor $a(t)$, which can be determined if we solve the gravitational field equations in the presence of matter. In order to solve the equations (1.1), we need a model for the energy–momentum tensor $T_{\mu\nu}$ of the matter that fills the universe. We shall consider that this matter is a perfect fluid, which is characterized at each point by its density ρ and the pressure P. In this formulation the energy momentum tensor $T^{\mu\nu}$ is given by the formula

$$\boxed{T^{\mu\nu} = (\rho + P)u^\mu u^\nu + Pg^{\mu\nu}} \tag{1.23}$$

The density ρ and pressure P must be functions of cosmic time t only, so that the solutions will describe a homogeneous and isotropic universe.

We adopt the FRW metric (1.5) with comoving coordinates (t, r, θ, ϕ), in order to simplify the required algebra. The 4-velocity of the cosmic fluid is now

$$[u^\mu] = (-1, 0, 0, 0) \tag{1.24}$$

The non-vanishing components of the Ricci tensor are

$$R_{tt} = -\frac{3\ddot{a}}{a}$$
$$R_{rr} = \frac{a\ddot{a} + 2\dot{a}^2 + 2k}{1 - kr^2}$$
$$R_{\theta\theta} = (a\ddot{a} + 2\dot{a}^2 + 2k)r^2$$
$$R_{\phi\phi} = (a\ddot{a} + 2\dot{a}^2 + 2k)r^2 \sin^2\theta$$

while the Ricci scalar R reads

$$R = 6\left(\frac{\ddot{a}}{a} + \frac{\dot{a}^2}{a^2} + \frac{k}{a^2}\right)$$

Combining these expressions with those for the components of the energy momentum tensor, we expect to derive four equations ($\mu = \nu = t, r, \theta, \phi$). Nevertheless, due to the homogeneity and isotropy of the FRW metric, the spatial equations are equivalent and thus the extracted equations are

$$\boxed{\frac{\dot{a}^2}{a^2} = \frac{8\pi G}{3}\rho - \frac{k}{a^2} + \frac{1}{3}\Lambda} \tag{1.25}$$

and

$$\boxed{\frac{\ddot{a}}{a} = -\frac{4\pi G}{3}\left(\rho + 3P\right) + \frac{1}{3}\Lambda} \tag{1.26}$$

These differential equations are known as the *Friedmann–Lemaitre equations* and their solution is the time evolution of the scale factor $a(t)$. If we set $\Lambda = 0$, they are often called the *Friedmann equations*, since in the Friedmann cosmological model the cosmological term is absent.

1.3.3 Cosmological parameters

It is common practice to rewrite the above equations (1.25) and (1.26) in terms of the Hubble rate and its first derivative with respect to coordinate time. Thus, the Friedmann equation (1.25), which defines the way that the energy of the universe determines the rhythm of expansion takes the form

$$\boxed{H^2 = \frac{8\pi G}{3}\rho - \frac{k}{a^2}} \tag{1.27}$$

while the Friedmann acceleration equation (1.26) becomes

$$\boxed{\dot{H} + H^2 = -\frac{4\pi G}{3}\Big(\rho + 3P\Big)} \tag{1.28}$$

The above equations (1.27) and (1.28) are independent. The Friedmann equation can be derived from the 00 (or tt) component of the Einstein equations (1.1) as we saw above, or by the fundamental Newtonian gravity.

We consider a spherical distribution mass M where the fundamental law of gravity is

$$\frac{d^2R}{dt^2} = \frac{GM}{R^2} \tag{1.29}$$

with $R(t) = a(t)r$ and $M = \frac{4\pi}{3}R^3\rho$. By replacing these quantities in Eq. (1.29) we derive the Eq. (1.27) for a flat universe ($k = 0$). Also, the acceleration equation can be derived from the Friedmann equation if we use the trace of Einstein's field equations during the procedure.

The energy density ρ, which appears in the Friedmann equations, is composed of a matter part ρ_m, a radiation part ρ_r and an energy density $\rho_\Lambda \equiv \frac{\Lambda}{8\pi G}$ due to the presence of the cosmological constant Λ, which was first introduced by Einstein in the theory of GR. If the above energy density components do not interact [4] except through their mutual gravitation, the multicomponent fluid can itself be modelled as a single perfect fluid with density

$$\boxed{\rho = \sum_i \rho_i = \rho_r + \rho_m + \rho_\Lambda} \tag{1.30}$$

and pressure

$$\boxed{P = \sum_i P_i} \tag{1.31}$$

The matter density $\rho_m(t)$ consists of ordinary baryonic matter (such as protons and neutrons) with density $\rho_b(t)$ and invisible dark matter $\rho_{dm}(t)$, which interacts only electromagnetically and very weakly. Dark matter may be relativistic and is called *hot dark matter* (HDM), or non-relativistic and it is called *cold dark matter* (CDM). Thus, the sum

$$\rho_m(t) = \rho_b(t) + \rho_{dm}(t)$$

represents the total matter density at any particular cosmic time t. Since matter density represents energy per volume and the volume is proportional to R^3, or equivalently to $a^3(t)$, the matter density in terms of the redshift scales as

$$\boxed{\rho_m(t) = \rho_{0m}\Big(1+z\Big)^3} \tag{1.32}$$

where $\rho_{0m} = \rho_m(t_0)$ is the present value of the matter density ($z = 0$). It is clear that the matter density at earlier times was smaller and as the time evolves it gets bigger.

[4] although matter and radiation did interact in the early universe, this is a reasonable approximation.

The radiation energy consists of photons which mainly make up the cosmic microwave background but also other particles with very small or zero rest masses, for example neutrinos, which they move relativistically today. The sum of the photon $\rho_\gamma(t)$ and neutrino $\rho_\nu(t)$ energy density contributions represents the total radiation density in the universe at some cosmic time t

$$\rho_r(t) = \rho_\gamma(t) + \rho_\nu(t)$$

The energy of the photons is proportional to their temperature ($E \sim k_B T$). Since temperature is inversely proportional to the scale factor (see Eq. (1.21)), the radiation density in terms of the redshift z scales as

$$\boxed{\rho_r(t) = \rho_{0r}\Big(1+z\Big)^4} \tag{1.33}$$

where $\rho_{0r} = \rho_r(t_0)$ is the present value of the radiation density. If we take into account the Eq. (1.21), it is easy to conclude that the radiation density is proportional to T^4 ($\rho_r(t) \propto T^4$) from which we derive that the universe must have not only been denser in the past, but also 'hotter'.

The last, but not least component of the universe is the Dark Energy, which is suggested from observations from distant supernovae. The modern interpretation of Λ is in terms of the energy density of the vacuum, which may also be modelled as a perfect fluid with negative pressure. With a great possibility, dark energy is constant with time, that's why we set $\rho_{\Lambda 0} = \rho_\Lambda = \frac{\Lambda}{8\pi G}$. Taking into account the above consideration, the Eq. (1.30) takes the form

$$\boxed{\rho = \rho_\Lambda + \frac{\rho_{0m}}{a^3} + \frac{\rho_{0r}}{a^4}} \tag{1.34}$$

From expression (1.34) it is clear that the relative contributions of matter, radiation and the vacuum to the total density vary as the universe evolves. During the expansion of the universe, the radiation energy density decreases more quickly than matter. Due to this reason, after some cosmological time, the matter becomes the dominant component. The epoch which radiation and matter density were equal is called *recombination epoch*. Finally, if the universe continues to expand, then the matter density dies away and the vacuum ultimately dominates the energy density.

From the Friedmann equation (1.27) we can define the *critical density* ρ_{crit} as

$$\boxed{\rho_{crit}(t) = \frac{3H^2(t)}{8\pi G}} \tag{1.35}$$

which is the required energy density for a flat universe. Generally, critical density changes with time. However, it is common to define ρ_{crit} to be a constant, because it evolves negligible with time. The present value of the critical density is

$$\rho_{crit,0} = \frac{3H_0^2}{8\pi G} \approx 9 \times 10^{-27} Kg/m^3$$

and determines the shape of the Universe. For example, if the present value of the matter density is equal to the critical density ($\rho_0 = \rho_{crit,0}$), the spacetime is flat. Most of the cosmological observations converge to this scenario. Nevertheless, the present critical density corresponds to $\rho_{crit,0} \approx 5.5 protons/m^3$, which is extremely low by laboratory standards.

It is common and useful in cosmology to express the energy densities in dimensionless quantities, which are usually called density parameters and are defined as

$$\Omega_i(t) \equiv \frac{8\pi G}{3H^2(t)}\rho_i(t) \tag{1.36}$$

Also, the density parameters Ω_i can be derived if we divide each energy density with the critical density. Thus, for the dark energy we have $\Omega_\Lambda = \frac{\rho_\Lambda}{\rho_{crit}}$, for the matter component $\Omega_m = \frac{\rho_m}{\rho_{crit}}$, while for the

radiation $\Omega_r = \frac{\rho_r}{\rho_{crit}}$. The total density parameter Ω_0 is defined as $\Omega_0 = \frac{\rho}{\rho_{crit}}$ and thus the Eq. (1.30) is modified as

$$\boxed{\Omega_0 = \Omega_\Lambda + \Omega_m + \Omega_r} \tag{1.37}$$

The entire history of the universe is determined by a few cosmological parameters. If we specify these parameters at some particular cosmic time, then we can determine the scale factor $a(t)$ at all cosmic times. The best naturally choice is this time to be the present time and the needed parameters are the below energy densities

$$\rho_{0m}, \qquad \rho_{0r} \qquad \text{and} \qquad \rho_{0\Lambda}$$

or equivalently the energy parameters and the Hubble rate

$$\boxed{\Omega_{0m}, \qquad \Omega_{0r}, \qquad \Omega_{0\Lambda} \qquad \text{and} \qquad H_0} \tag{1.38}$$

The density parameter of each component is estimated by cosmological observations and the present acceptable rate for the radiation is $\Omega_r \approx 5 \times 10^{-5}$, for the baryonic and dark matter $\Omega_m \approx 0.3$, for the dark energy $\Omega_\Lambda \approx 0.7$, while the Hubble rate is $H_0 \approx 70\ km\ sec^{-1}\ Mpc^{-1}$ or $H_0 \approx 2.2 \times 10^{-18}\ sec^{-1}$. Also, cosmological observations suggest that the present density parameter of the baryonic matter is $\Omega_{0b} \approx 0.05$, of the dark matter is $\Omega_{0dm} \approx 0.25$, while of the neutrinos is $\Omega_{0\nu} \approx 0$. For determining the overall expansion history of the universe however, only the quantities (1.38) need to be specified.

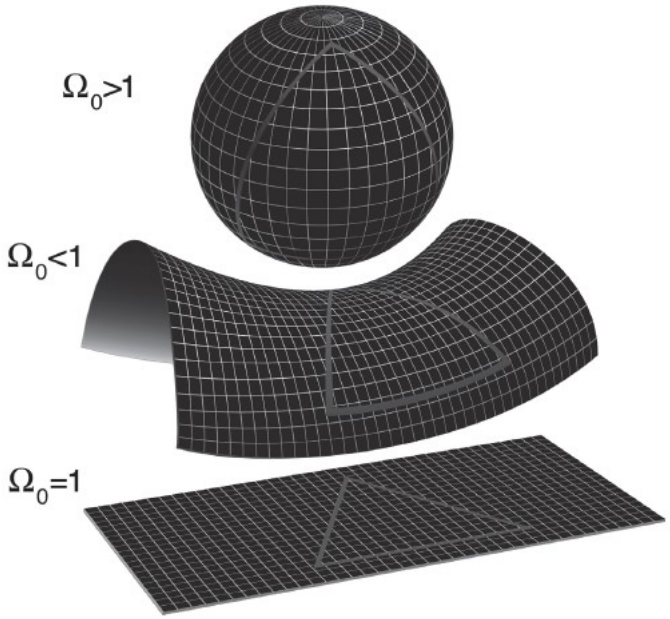

Figure 1.3: The possible rates of the spatial curvatures of the universe. Positive curvature (top), negative curvature (center), and a flat, zero-curvature Universe (bottom) correspond to different evolution of the universe (recollapsing, expanding forever, and a critical Universe, respectively), but also lead to different geometries, which can be measured. Adopted from [9].

In addition, we can express the total energy parameter Ω_i through the Friedmann equation (1.27). Dividing by H^2 we find that

$$\boxed{\Omega_m + \Omega_r + \Omega_\Lambda - \frac{k}{a^2 H^2} = 1} \tag{1.39}$$

where, for notational simplicity we have dropped the explicit time dependence of the variables. It is clear that the last term on the left hand side is an energy density parameter, which is known as the *curvature*

density parameter $\Omega_k(t)$

$$\Omega_k(t) \equiv -\frac{k}{a^2 H^2} \tag{1.40}$$

Consequently, the Eq. (1.39) becomes

$$\boxed{\Omega_m + \Omega_r + \Omega_\Lambda + \Omega_k = 1} \tag{1.41}$$

and with the aid of Eq. (1.37) it is easy to conclude that

$$\Omega_0 = 1 - \Omega_k$$

It should be noted that Ω_k is positive in cosmological models with negative spatial curvature. The parameters Ω_m and Ω_r are always positive, while Ω_Λ may be positive or negative (it depends on the sign of Λ). Also, the sum $\Omega_m + \Omega_r + \Omega_\Lambda$ cannot change sign, which means that the universe cannot evolve from one form of the FRW geometry to another. It will be closed or open or flat throughout the cosmic time. The universe has, in the entire time, the same sign of curvature. For the geometry of the universe, we distinguish the following cases

$$\Omega_m + \Omega_r + \Omega_\Lambda > 1 \quad \Leftrightarrow \quad k = +1 \quad \Leftrightarrow \text{closed universe}$$

$$\Omega_m + \Omega_r + \Omega_\Lambda < 1 \quad \Leftrightarrow \quad k = -1 \quad \Leftrightarrow \text{open universe}$$

$$\Omega_m + \Omega_r + \Omega_\Lambda = 1 \quad \Leftrightarrow \quad k = 0 \quad \Leftrightarrow \text{flat universe}$$

as someone can notice in Fig. 1.3.

These three cases correspond to three different shapes for the fabric of spacetime and determines when the gravity dominates expansion and when expansion dominates gravity. The first case, where gravitation wins and the universe recollapses in a Big Crunch, corresponds to a closed universe with positive curvature, similar to the surface of a sphere. The second case, where the expansion wins and continues forever, culminating in a Big Freeze, corresponds to an open universe with negative curvature, similar to the surface of a saddle, which curves downwards along a horse's flanks but upwards along a horse's spine. And the final case, the critical, or "Goldilocks" case, corresponds to a flat universe, with exactly zero curvature.

1.3.4 Conservation of energy

The conservation of energy is a general principle which is valid in every field of Physics. In General Relativity, it is expressed through the zeroing of the covariant derivative of the energy momentum tensor $T_{\mu\nu}$. Assuming energy–momentum tensor conservation, the covariant derivative must be equal to zero, namely

$$T^{\nu}_{\mu;\nu} = 0$$

From this formula it is easy to obtain through the time component, the continuity equation

$$\boxed{\dot{\rho} + 3H\big(\rho + P\big) = 0} \tag{1.42}$$

We can trivially obtain the condition for energy and momentum conservation in arbitrary coordinates replacing ∂_μ by ∇_μ, so we conclude that

$$\boxed{\nabla_\mu T^{\mu\nu} = 0} \tag{1.43}$$

If we replace the energy momentum tensor (1.23), the equation (1.43) gives

$$\nabla_\mu(\rho u^\mu) + P\nabla_\mu u^\mu = 0 \Rightarrow$$

$$(\partial_\mu \rho)u^\mu + (\rho + P)(\partial_\mu u^\mu + \Gamma^\mu_{\nu\mu} u^\nu) = 0$$

Since the density is a function of time alone, only the value $\mu = 0$ is acceptable and we end up in the continuity equation (1.42).

Although, in Minkowski spacetime Eq. (1.43) represents the conservation of energy and momentum, in a curved spacetime the situation is quite different. Energy and momentum of the matter alone is not conserved. In this case, Eq. (1.43) represents the equation of motion of the matter under the influence of the gravitational field.

Moreover, we can prove the density functions through the energy momentum tensor. Since we are assuming that the fluid components are non-interacting, conservation of energy and momentum requires that the condition

$$\nabla_\mu (T^{\mu\nu})_i = 0$$

holds separately for each component. If the equation of state is $w_i = P_i/\rho_i$ for each component, the continuity equation gives

$$\rho_i \propto a^{-3(1+w_i)}$$

Setting the values of w, we can find each density component as a function of the scale factor, or the redshift z.

1.3.5 Equation of state

The isotropic pressure and the energy density are the only variables of a perfect fluid which fills the spacetime and they are connected through the equation of state

$$\boxed{P = w\rho} \tag{1.44}$$

where w is constant [5] and characteristic for different cosmic fluids. Some representative values of the parameter w are the following:

- $w = -1$, for cosmological constant Λ (dark energy), or vacuum energy
- $w = -\frac{2}{3}$, for domain walls which are a class of topological defects
- $w = -\frac{1}{3}$, for cosmic stings which are another class of defects or 'curvature'
- $w = 0$, for pressureless dust (a set of massive particles with negligible relative velocities)
- $w = \frac{1}{3}$, for radiation, or relativistic matter
- $w = 1$, for stiff fluid

In this chapter, we will refer to quintessence models where $-1 < w < -1/3$ and phantom cosmological models with $w < -1$.

For a universe which is dominated by a single form of perfect fluid energy, where w is constant, the speed of sound c_s in the fluid is defined through the formula $c_s = \sqrt{\frac{\partial P}{\partial \rho}} = \sqrt{w}$. In many cases ($w < 0$), the sound speed becomes imaginary. This effect may exist only on small scales and may not affect the large scale nature of the universe. Also, in phantom cosmologies a phenomenological problem occurs, the speed of sound is unphysically greater than the speed of light.

[5] In more exotic cosmological models one sometimes allows w to be a function of redshift z such as the Chevallier-Polarski-Linder (CPL) parametrization

$$w = w_0 + w_a \frac{z}{1+z}$$

where w_0 and w_a are parameters which must be determined from cosmological data.

1.3.6 Evolution of the scale factor

The system of equations (1.27), (1.28) and (1.42) implies three unknown variables (a(t), ρ and P), but these equations are not all linearly independent, just two of them. The system, in order to give a physical solution, closes with the equation of state (1.44). As a first step, it is easy to solve the Eq. (1.42) which determines the energy density as a function of time. When $w \neq 1$, the result is

$$\boxed{\rho(t) = \rho_* a(t)^{-3(1+w)}} \tag{1.45}$$

If $w = -1$, which corresponds to the de Sitter model (we will describe this model below), the energy density scales as

$$\boxed{\rho(t) = \rho_{**} e^{Ht}} \tag{1.46}$$

with $H = \sqrt{\frac{\Lambda}{3}}$. The quantities ρ_* and ρ_{**} are constants of integration. From the Friedmann equation (1.27), it is easy to derive the scale factor as a function of time and of the parameter w_i

$$\boxed{a(t) = \pm\left(\frac{3}{2}(1+w_i)\sqrt{\Omega_{0i}}\right)^{\frac{2}{3(1+w_i)}} t^{\frac{2}{3(1+w_i)}} = a_* t^{\alpha}} \tag{1.47}$$

where the plus and minus signs correspond to the Big Bang and Big Crunch respectively, $\alpha = \frac{2}{3(1+w_i)}$ and $a_* = \pm\left(\frac{3}{2}(1+w_i)\sqrt{\Omega_{0i}}\right)^{\frac{2}{3(1+w_i)}}$.

1.3.7 Observation of Expansion

Soon after the expansion of the universe was firmly established, observational cosmologists were already trying to detect a modification of the expansion speed as a function of redshift. They were so confident that the expansion had to decelerate due to gravitational interaction of galaxies that they introduced the so-called *deceleration parameter* q, which thought to be positive. The expansion of the universe is said to be "accelerating" if $\ddot{a} > 0$ (recent measurements suggest that), and in this case the deceleration parameter will be negative. The deceleration parameter is defined as [13]

$$\boxed{q(z) \equiv -\frac{\ddot{a}a}{\dot{a}^2} = \frac{1}{2}\sum_i \Omega_i(z)\Big(1 + 3w_i(z)\Big)} \tag{1.48}$$

where $\Omega_i(z)$ is the fraction of critical density of component i at redshift z and $w_i(z) = \frac{P_i(z)}{\rho_i(z)}$ the equation of state of component i at redshift z.

With the aid of equation of state (1.44) we write the Eq. (1.28) in the form

$$\frac{\ddot{a}}{a} = -\frac{4\pi G}{3}(1+3w)\rho$$

and the Eq. (1.48) can be rewritten as

$$\boxed{q = \frac{1}{2}(1+3w)\left(1 + \frac{k}{a^2H^2}\right)} \tag{1.49}$$

For some time, the main cosmological parameters accessible to measurement were the deceleration parameter q and the present value of the Hubble rate H_0. Nowadays, one prefers to describe the variation of the expansion of the universe in terms of the energy density of its constituents and their equation of state. First expansion tests involved measuring brightness of galaxies, but astronomers started looking

for a better standard candle because the brightness of galaxies evolves quickly. These standard candles are the supernova Ia, which have almost the same brightness and they are a pure geometrical test of expansion.

The deceleration parameter can be extracted in terms of the density parameters Ω_i, from Eq. (1.48). We consider the corresponding parameter w for each component of the universe and thus,

$$q = \frac{1}{2}\Big(\Omega_m(1+3\times 0) + \Omega_r(1+3\frac{1}{3}) + \Omega_\Lambda(1+3(-1))\Big)$$

$$\boxed{q = \frac{1}{2}\Big(\Omega_m + 2\Omega_r - 2\Omega_\Lambda\Big)} \tag{1.50}$$

where, the density parameters as a function of cosmic time are

$$\Omega_i = \Omega_{0i}\left(\frac{H_0}{H}\right)^2 a^{-3(1+w)} \tag{1.51}$$

Generally, this equation holds for matter, radiation and vacuum. In conclusion, the Eq. (1.50) and the Hubble rate as a function of the scale factor $a(t)$

$$\boxed{H(a) = H_0\sqrt{\Omega_{0m}a^{-3} + \Omega_{0r}a^{-4} + \Omega_{0\Lambda} + \Omega_{0k}a^{-2}}} \tag{1.52}$$

or a function of the redshift z

$$\boxed{H(z) = H_0\sqrt{\Omega_{0m}(1+z)^3 + \Omega_{0r}(1+z)^4 + \Omega_{0\Lambda} + \Omega_{0k}(1+z)^2}} \tag{1.53}$$

are important field equations for the investigation of the universe.

1.3.8 Evolution of the density parameters

Although we usually consider that the energy parameters are stable, it is clear from Eq. (1.36) that they evolve with time. Thus, the time derivative of the energy densities is

$$\dot{\Omega}_i = \frac{8\pi G}{3H^2}\left(\dot{\rho}_i - \frac{2\dot{H}}{H}\rho_i\right)$$

Then, with the aid of energy conservation equation, we substitute the term $\dot{\rho}_i$, while we replace the fraction of the last term through the deceleration parameter as

$$\frac{\dot{H}}{H^2} = \frac{a\ddot{a}}{\dot{a}^2} - 1 = -q - 1$$

and the time derivative $\dot{\Omega}_i$ reads

$$\dot{\Omega}_i = -\Omega_i H\Big(3 + 3w_i - 2(q+1)\Big)$$

Finally, using Eq. (1.50) we derive the final differential equation

$$\boxed{\dot{\Omega}_i = \Omega_i H\Big(\Omega_m + 2\Omega_r - 2\Omega_\Lambda - 1 - 3w_i\Big)} \tag{1.54}$$

for $i = m, r, \Lambda$. For example, in the case of matter, Eq. (1.54) reads

$$\dot{\Omega}_m = \Omega_m H\Big(\Omega_m + 2\Omega_r - 2\Omega_\Lambda - 1\Big)$$

1.3.9 Evolution of the spatial curvature

The curvature density parameter is a function of time (1.39), even if we usually consider it to be constant. The time derivative $\dot{\Omega}_k$ can be easily derived from the Eq. (1.39) as

$$\boxed{\dot{\Omega}_k = 2\Omega_k H q = \Omega_k H \Big(\Omega_m + 2\Omega_r - 2\Omega_\Lambda \Big)} \tag{1.55}$$

We must distinguish the cases with $\Omega_\Lambda = 0$ and $\Omega_\Lambda \neq 0$. The first case refers to the absence of the cosmological term (the Friedmann models). In this case, the right hand side of Eq. (1.55) is always positive, which means that Ω_k grows with time. In early cosmic time, if Ω_k is not equal to zero, then the spatial curvature evolves away from the flat universe. In second case, the cosmological term is present (Lemaitre models) and the behaviour of Ω_k is very different. The term $2\Omega_\Lambda$ dominates at some cosmic time and Ω_k tends to zero, indicating flat geometry. This is a more interesting case than the first, since our universe is filled with vacuum energy ($\Lambda > 0$) which can give an explanation why the universe is close to spatially flat at the present epoch.

It is more convenient to derive the curvature density as a function of the redshift z, because the cosmological observations often include the redshift of the celestial object. From Eq. (1.39) we have that $\Omega_{0k} = -\frac{k}{H_0^2}$ and if we replace the parameter k in Eq. (1.39) we find that

$$\boxed{\Omega_k(z) = \left(\frac{(1+z)H_0}{H(z)} \right)^2 \Omega_{0k}} \tag{1.56}$$

where $H(z)$ is given by Eq. (1.53). The final form which describes the evolution of the curvature density parameter in terms of redshift z and the current energy density parameters Ω_{0i} is

$$\boxed{\Omega_k(z) = \frac{\Omega_{0k}}{\Omega_{0m}(1+z) + \Omega_{0r}(1+z)^2 + \Omega_{0\Lambda}(1+z)^{-2} + \Omega_{0k}}} \tag{1.57}$$

In the distant past or at high redshift, since the denominator of Eq. (1.57) gets to infinity, $\Omega_k(z)$ was almost equal to zero with small deviations. Modern cosmological measurements determine the value of the curvature density parameter in the range

$$-0.5 < \Omega_{0k} < 0.5$$

which means that at very early epochs Ω_k must have been very finely tuned to near zero. Generally, some of the initial conditions of the universe appear to be fine-tuned to very 'special' values and that small deviations from these values would have extreme effects on the appearance of the universe at the current time. This fine tuning of the initial conditions of the universe constitutes the famous *flatness problem* in cosmology (how the initial curvature density parameter came to be so closely fine-tuned to this 'special' value;) and there has not been a solution within standard cosmological models. The problem was first mentioned by Robert Dicke in 1969. The most commonly accepted solution among cosmologists is cosmic inflation, the idea that the universe went through a brief period of extremely rapid expansion in the first fraction of a second after the Big Bang.

1.3.10 Basic cosmological models

The general dynamical behaviour of the universe and the spatial geometry can be determined by the field equations (1.50) and (1.52) for any set of the cosmological parameters Ω_{0m}, Ω_{0r} and $\Omega_{0\Lambda}$. The observations suggest that the radiation density is significantly smaller than the matter and vacuum densities. It is therefore natural to neglect the radiation density Ω_{0r} so, we parametrise the universe in terms of Ω_{0m} and $\Omega_{0\Lambda}$, since we can substitute Ω_{0k} from Eq. (1.41). In Fig. 1.4 we summarize the

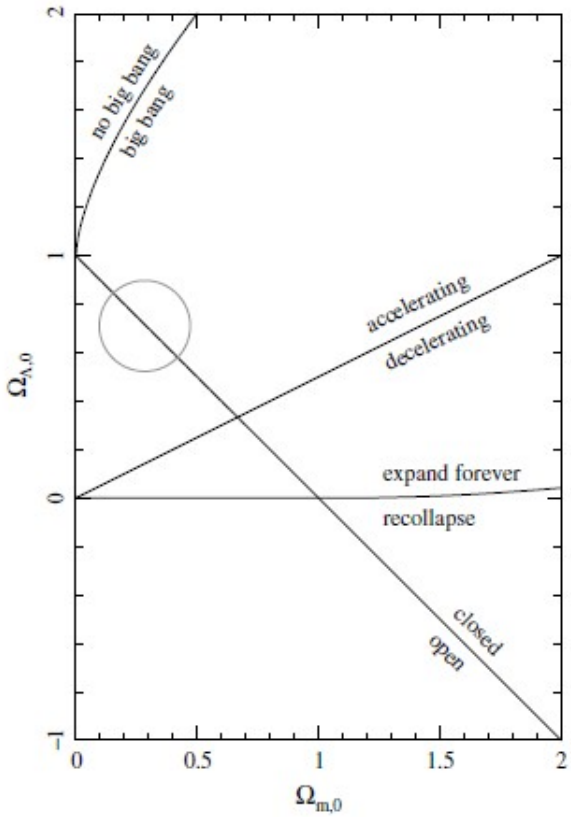

Figure 1.4: The parameter space (Ω_{0m},$\Omega_{0\Lambda}$) describes the dynamic of the universe for any given present value of the parameters Ω_{0m} and $\Omega_{0\Lambda}$. The circle is centred on the spatially flat model (0.3,0.7), consistent with recent cosmological observations and excludes the possibility of a zero cosmological constant Λ at high significance. Adopted from [10].

properties of FRW universes for any given value of Ω_{0m} and $\Omega_{0\Lambda}$ as a function of its position in parameter space (Ω_{0m},$\Omega_{0\Lambda}$). These universes are known as *Lemaitre models*.

As a next step, we aim to explain how we can determine the dividing lines between the various regions of Fig. 1.4. This may be realized through the Eqs. (1.41), (1.50) and (1.52).

- The 'open–closed' line can be derived from Eq. (1.41) if we set Ω_{0k} equal to zero. We end up in the linear relationship
$$\Omega_{0\Lambda} = 1 - \Omega_{0m}$$
which is plotted in Fig. 1.4 (the straight line with negative slope).

- The 'accelerating–decelerating' line can be derived from Eq. (1.50) if we erase the deceleration parameter q at the present cosmic time. We find that
$$\Omega_{0\Lambda} = \frac{1}{2}\Omega_{0m}$$
which describes a proportional relationship between $\Omega_{0\Lambda}$ and Ω_{0m}. The present energy destiny parameter is half of the present matter density parameter. Along the line, the acceleration is equal to zero.

- The 'expand-forever–recollapse' line and the 'big-bang–no-big-bang' line can be derived from Eq. (1.52) with a more complicated way, where we must distinguish the following cases.

1. $\Omega_{0\Lambda} < 0$

   In this case the deceleration parameter q of Eq. (1.50) is always positive which means that the $a(t)$ graph is always convex, because $\ddot{a} < 0$. Since at the present epoch we observe redshifts which correspond to $\dot{a} > 0$, we conclude that the universe started with a big bang at $a = 0$. As the universe expands the term Ω_Λ dominates on the right hand side of Eq. (1.50) and the deceleration parameter takes the approximate form $q \simeq -\Omega_\Lambda$. Since $\ddot{a}$ doesn't tend to zero, the universe must eventually recollapse in a *Big Crunch* singularity as $a \to 0$ once more.

2. $\Omega_{0\Lambda} = 0$

   In this case there is a single turning point for which $H(a) = 0$ at some cosmic time t. At this point the scale factor becomes

   $$a_* = \frac{\Omega_{0m}}{\Omega_{0m} - 1}$$

   which is not physically meaningful when $\Omega_{0m} < 1$, since $a(t)$ is negative. Therefore, over this range, the 'expand-forever–recollapse' line is simply given by $\Omega_{0\Lambda} = 0$.

3. $\Omega_{0\Lambda} > 0$

   In this case the detection of the turning point can be determined if we require $H(a) = 0$ and $H'(a) = 0$. There is a single positive turning point at

   $$a_* = \left(\frac{\Omega_{0m}}{2\Omega_{0\Lambda}}\right)^{1/3}$$

   which may be bigger or less that 1. Since the universe is expanding, if $a_* < 1$ it corresponds to a turning point in the past (i.e. no big bang) whereas $a_* > 1$ corresponds to a turning point in the future (i.e. recollapse).

Summarizing, it is worth mentioning that when $\Omega_{0\Lambda} = 0$, there is a direct correspondence between the geometry of the universe and its eventual fate (open universe expands forever, while closed universe recollapses). When $\Omega_{0\Lambda} \neq 0$ any combination of spatial geometry and eventual fate is possible. However, the recent cosmological observations indicate that $\Omega_{0m} \simeq 0.3$ and $\Omega_{0\Lambda} \simeq 0.7$. This region is shown in Fig. 1.4 with a circle, which corresponds to a universe with acceleration and excludes the possibility of a zero cosmological constant at high significance. It also requires the universe to have been started at a big bang at some finite cosmic time in the past and to expand forever in the future.

1.4 The Friedmann-Lemaitre cosmological models

Now, we will discuss the way to find the form of the scale factor curve in any cosmic time for a given set of (present-day) cosmological parameter values. This behaviour is entirely determined by the cosmological field equation (1.52) if we rewrite it in the form

$$\boxed{\left(\frac{da}{dt}\right)^2 = H_0^2\left(\Omega_{0m}a^{-1} + \Omega_{0r}a^{-2} + \Omega_{0\Lambda}a^2 + 1 - \Omega_{0m} - \Omega_{0r} - \Omega_{0\Lambda}\right)} \tag{1.58}$$

Generally, this equation can be solved numerically. However, for some particular simple values of the density parameters Ω_{0i} can be solved analytically. Some of these cases, each of them corresponding to a particular cosmological model, will be presented bellow.

1.4.1 The Friedmann models

We call Friedmann models the cosmological models with a zero cosmological constant i.e. $\Omega_\Lambda = 0$ and strictly a non-zero matter or/and radiation density. These models have the general following features:

1. they have a big-bang origin at a finite cosmic time in the past.

2. the age of the universe must be less than the Hubble time, i.e.

$$t_0 < H_0^{-1}$$

3. The evolution of the scale factor $a(t)$ depends crucially on the curvature density parameter

$$\Omega_{0k} = 1 - \Omega_{om} - \Omega_{0r}$$

and hence on the sign of the curvature parameter k so, we can distinguish the cases $\Omega_{0k} = 0$, $\Omega_{0k} > 0$ and $\Omega_{0k} < 0$ (for details, one can see Fig. 1.5).

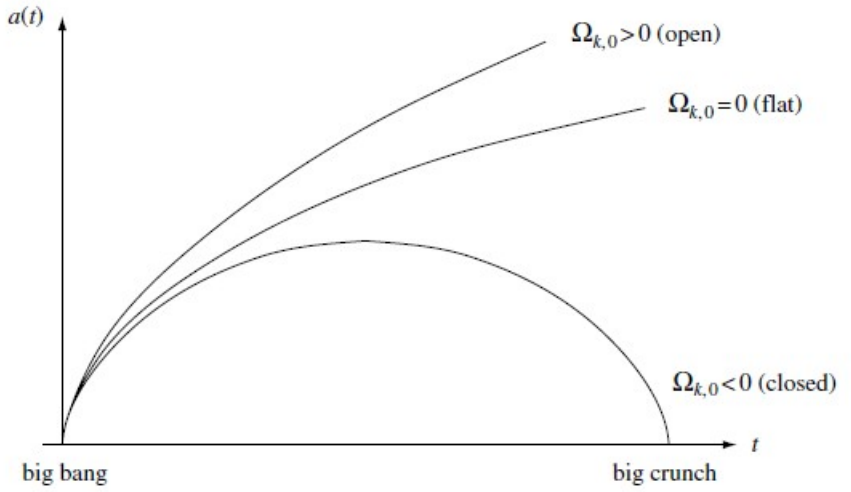

Figure 1.5: The evolution of the scale factor in closed, open and spatially flat Friedmann models ($\Omega_{0\Lambda} = 0$). Note that, each model begins from the big bang singularity, but the evolution of the universe depends on its geometry. Adopted from [10].

It is obvious from Fig. 1.5 that the dynamics of the universe is directly linked to its geometry. For example, the Friedmann models have the origin at the big bang singularity, but if the universe is closed (with $k = +1$), the evolution of the universe drives to the *Big Crunch* at some cosmic time in the future. For a flat or open universe, the expansion is perpetual.

As a next step, we investigate some particular cases of Friedmann cosmological models and we derive the function of the corresponding scale factor in a spatially flat universe.

- *Dust only universe*

  In this case we apply the condition $\Omega_{0r} = 0$, the Eq. (1.58) can be integrated for flat, open or closed universe and if $\Omega_{0m} = 1$ the scale factor is

$$a(t) = \left(\frac{3}{2} H_0 t\right)^{2/3}$$

  This particular case is known as the *Einstein–de-Sitter* model. In each case one can also obtain expressions for $\rho_m(t)$, $H(t)$ and $\Omega_m(t)$.

- *Radiation only universe*

  In this case the Friedmann universe is empty of matter ($\Omega_{0m} = 0$) and the Eq. (1.58) can be integrated for each value of the radiation density. If the universe is assumed spatially flat ($k = 0$), the radiation density is equal to unit and the scale factor evolves as

$$a(t) = \left(2H_0 t\right)^{1/2}$$

  In each case one may also obtain expressions for $\rho_r(t)$, $H(t)$ and hence $\Omega_r(t)$.

- *Spatially flat Friedmann models*

  In the final case, we consider both matter and radiation as components of the Friedmann universe, but we demand that $\Omega_{0m} + \Omega_{0r} = 1$. Integrating Eq. (1.58) we derive the function $t(a)$ as

$$t = \frac{2}{3H_0\Omega_{0m}^2}\left((\Omega_{0m}a + \Omega_{0r})^{1/2}(\Omega_{0m}a - 2\Omega_{0r}) + 2\Omega_{0r}^{3/2}\right)$$

  Unfortunately, this expression cannot be easily inverted to give the function $a(t)$, but agrees with the previous results when the universe is filled only with matter ($\Omega_{0r} = 0$), or only with radiation ($\Omega_{0m} = 0$).

1.4.2 The Lemaitre models

The generalization of the Friedmann models with non-zero cosmological constant are known as *Lemaitre models*. For simplicity, we will consider the case where the universe is empty of radiation ($\Omega_{0r} = 0$) and we will focus on determining the scale factor $a(t)$ in models that have a big-bang origin and will expand forever. We begin by considering the general case of arbitrary spatial curvature and then specialize to the spatially flat case.

- *Matter-only Lemaitre models with arbitrary spatial curvature*

  In this case we assume that the radiation density is equal to zero. For small $a(t)$ the first term on the right-hand side of Eq. (1.58) dominates and the equation is easily integrated. Thus

$$a(t) = \left(\frac{3}{2}H_0 t\sqrt{\Omega_{0m}}\right)^{2/3} \qquad \text{(for small t)}$$

  However, as the universe expands, the matter energy density decreases and the vacuum energy eventually dominates. Once again the equation is then easily integrated to give

$$a(t) \propto e^{\left(H_0 t\sqrt{\Omega_{0\Lambda}}\right)} \qquad \text{(for large t)}$$

  Since the early universe was decelerating while for long time it is accelerating, there must be some time in the past where this transition took place. This occurs when $\frac{d^2a}{dt^2} = \ddot{a} = 0$, in the turning point of the scale factor. If we differentiate Eq. (1.58) we can easily derive that at the point of inflection the scale factor was

$$a_* = \left(\frac{\Omega_{0m}}{2\Omega_{0\Lambda}}\right)^{1/3}$$

- *Spatially flat matter-only Lemaitre models*

  In this case we assume that the universe is filled with matter and vacuum energy the sum of which is equal to unit ($\Omega_{0m} + \Omega_{0\Lambda} = 1$), while the radiation energy is absent ($\Omega_{0r} = 0$). This model of sort appears to provide a reasonable description of our own universe, if one neglects its radiation energy density. The Eq. (1.58) may be integrated analytically and the result is

$$t = \frac{2}{3H_0\sqrt{|\Omega_{0\Lambda}|}} \begin{cases} \sinh^{-1}\left(\sqrt{\frac{a^3\Omega_{0\Lambda}}{1-\Omega_{0\Lambda}}}\right), & \text{if } \Omega_{0\Lambda} > 0 \\ \sin^{-1}\left(\sqrt{\frac{a^3|\Omega_{0\Lambda}|}{1-\Omega_{0\Lambda}}}\right), & \text{if } \Omega_{0\Lambda} < 0 \end{cases}$$

  which may be inverted to give the scale factor $a(t)$ in each case. Then, one can extract the functions of $\rho_m(t)$, $H(t)$ and the energy densities $\Omega_m(t)$ and $\Omega_\Lambda(t)$.

1.4.3 The de Sitter model

A particular case of Lemaitre models is the de Sitter model, where we assume that the universe is filled only with vacuum energy ie $\Omega_{0\Lambda} = 1$ and $\Omega_{0m} = \Omega_{0r} = 0$. It constitutes a model which describes a flat universe, but due to the above assumptions is not a real cosmological model. However, it is interesting in its own right both for historical reasons and of its close connection with the theory of inflation. Locally, it is possible that cosmological backgrounds exist and are filled with dark energy. The scale factor is derived from Eq. (1.58) as

$$a(t) = e^{H_0 t}$$

where $H_0 = \sqrt{\frac{\Lambda}{3}}$ is the present value of the Hubble rate. The scale factor increases exponentially, but this model has no big bang origin at a finite time in the past.

1.4.4 Einstein's static universe

Einstein presented his static model ($\dot{a} = 0$ and $\ddot{a} = 0$) well before the discovery of the expansion of the universe and he was worried that he could not find static cosmological solutions. For this reason, he introduced the cosmological term in the field equations (1.1) in order to balance the gravity. From the field equations we conclude that

$$4\pi G\rho_{0m} = \Lambda$$

which means that $\rho_{0m} = 2\rho_{0\Lambda}$. The parameters of this model do not fit well with cosmological observations, since it has matter density two orders of magnitude bigger than the observed matter density. From the matter density we estimate the size of the universe approximately at $6000Mpc$. However, the estimated value of the cosmological constant is $\Lambda = 2.5 \times 10^{-53}m^{-2}$ which is in the expected region, as it can be arisen by cosmological observations. Thus, the Einstein static universe was not immediate and obviously wrong.

Aside from the fact that the model disagreed with later observations indicating an expanding universe, the great disadvantage of Einstein's static universe is the feature of being unstable. The cosmological constant must be fine-tuned to match the density of the universe. With addition or subtraction of each massive particle such as a proton in this universe, we destroy the balance between gravity and cosmological term and the universe will begin to expand or contract.

1.5 Age of the universe

A very important parameter for the cosmological models, whose origin is the big bang singularity is the time interval between the point when $a(t) = 0$ and the present epoch $t = t_0$ which is actually the *age of the universe*. It is a look back time (1.19) from $t = 0$ until $t = t_0$, or in terms of the redshift the

time interval between $z \to \infty$ (big bang) until $z = 0$ (present epoch). If we assume the radiation density negligible, Eq. (1.19) with the aid of equation (1.53) reads

$$t_0 = \frac{1}{H_0} \int_0^\infty \frac{dz}{(1+z)\sqrt{\Omega_{0m}(1+z)^3 + \Omega_{0\Lambda} + \Omega_{0k}(1+z)^2}} \tag{1.59}$$

and it is of order of the Hubble time $1/H_0$. The result depends on the values of model parameters Ω_{0i}, but since the age of the oldest stars in globular clusters is

$$t_{stars} \approx (11.5 \pm 1.3)\ Gyrs$$

one requires $t_0 > t_{stars}$ for a viable cosmology.

Previously, we investigated some cosmological models (Friedmann and Lemaitre) for several values of the parameters Ω_{0i}. For each of them with a Big Bang origin, for which we have derived analytical form for the scale factor $a(t)$, or the inverse function $t(a)$, we can estimate the age of the universe by setting $a = 1$ and $t = t_0$. For example, the age of Einstein–de-Sitter universe is $t_0 = \frac{2}{3H_0}$. This would be a criterion for the rejection of a cosmological model, if it can not support the observed limit of the age of universe.

1.6 Distances

The measure of *distances* in Cosmology is of great significance in order to complete the cosmological observations and to estimate cosmological parameters which are part of the corresponding cosmological models [14]. The unifying aspect is that all distance measures somehow measure the separation between events on radial null trajectories, i.e. trajectories of photons which terminate at the observer. In an expanding universe there are two possible ways to measure distances. The first is the comoving distance which remains fixed despite the expansion of the universe (we consider the same peculiar velocity for every cosmological object). The second is the physical distance which takes into account the expansion and thus always grows. In this case Earth-bound observers look back in time as they look out in distance.

Important comoving distance is the distance between a distant cosmological object or event at redshift z and us. The *comoving distance* $S(\chi)$ as it has been defined in Eq. (1.6), remains constant with epoch if the two objects are comoving with the Hubble flow. Only for these observers in comoving coordinates the universe is isotropic. From the definition of $\chi(z)$ (see Eq. (1.20)) we must replace the Hubble rate as a function of the redshift z. When the cosmological fluid contains matter, radiation, curvature and vacuum the Hubble rate as a function of the redshift z is given by Eq. (1.53).

Each of the components of the universe decreases during the expansion of the universe (decreasing redshift), except the dark energy term. Physicists use the values of these cosmological parameters to determine the acceleration of the universe. As it will be shown below, other distances are quite simply derived in terms of the comoving distance $r = S(\chi)$ and in some sense $S(\chi)$ is the fundamental distance in cosmography.

1.6.1 Angular diameter distance

When a distant object has physical transverse size l and angular size in radians $\Delta\theta$, we can define the *angular diameter distance* in a static universe as

$$d_A = \frac{l}{\Delta\theta}$$

where, we use the approximation $\tan \Delta\theta \simeq \Delta\theta$ because $\Delta\theta \to 0$. For a better understanding, one can see the geometrical definition in Fig. 1.6. This distance is used to convert angular separations in telescope images into proper separations at the source.

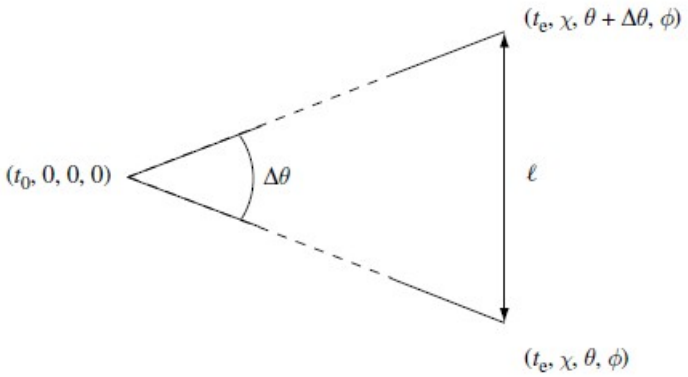

Figure 1.6: Specification of the coordinates in the definition of angular diameter distance. Since $\Delta\theta \to 0$, we can define the angular diameter distance as $d_A = \frac{l}{\Delta\theta}$. Adopted from [10].

If we take into account the expansion of the Universe, where $\Delta\theta = \frac{l}{a(t_e)S(\chi)}$, the above definition of d_A in a FRW spacetime takes the form

$$\boxed{d_A = \frac{S(\chi)}{1+z}} \tag{1.60}$$

In Fig. 1.7 we present a geometrical definition of the angular diameter distance. The size of the object ℓ looks larger at the time of light emission (t_e) than the time of observation (t_0), since the universe expands. Also, it is obvious that the expansion increases the distance between the observer and the emitter, since the worldlines of the emitter and the observer diverge.

At low redshift, where $a \simeq 1$, or $z \ll 1$ the comoving and angular diameter distance are equal, but at larger redshifts the comoving distance is bigger. At high redshift, the angular diameter distance is such that 1 *arcsec* is on the order of 5 *kpc*.

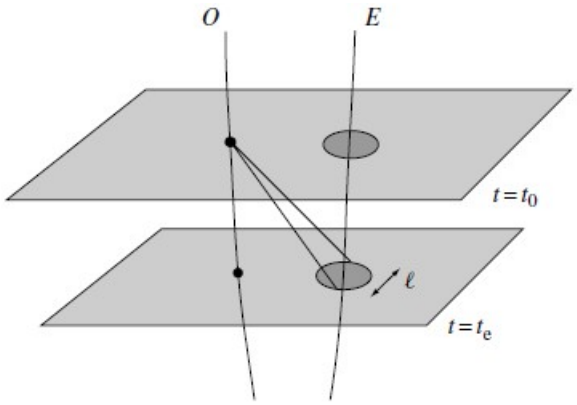

Figure 1.7: The geometrical definition of angular diameter distance d_A with one spatial dimension suppressed, for a cosmological object with size ℓ. It is obvious that the expansion increases the distance between the observer and the emitter, since the worldlines of the emitter and the observer diverge. Adopted from [10].

1.6.2 Luminosity distance

We can also measure distances through the flux-luminosity relationship whose definition for a static universe is

$$\boxed{d_L = \left(\frac{L}{4\pi F}\right)^{1/2}} \tag{1.61}$$

where F is the observed flux from a source with known luminosity L, which is constant in a spherical shell with radius the *luminosity distance* d_L. In an expanding universe, since the luminosity is smaller by a factor of a^2, the flux we observe in a comoving spherical shell with radius $S(\chi)$ is

$$F = \frac{La^2}{4\pi S^2(\chi)}$$

If we replace the flux F in Eq. (1.61) it is easy to conclude that the luminosity distance [6] in an expanding universe is given by the relation

$$\boxed{d_L = S(\chi)(1+z)} \tag{1.62}$$

which describes an increasing cosmological distance as a function of the redshift.

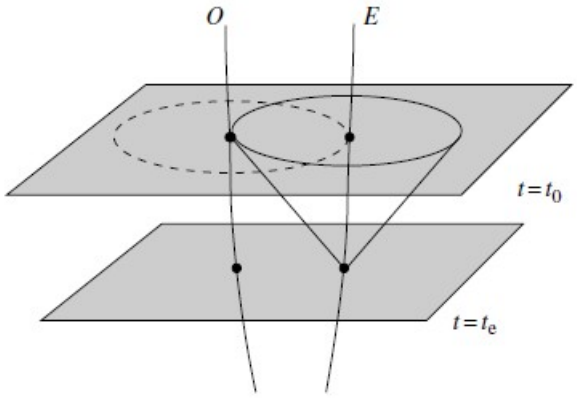

Figure 1.8: The geometrical definition of the luminosity distance d_L with one spatial dimension suppressed between an observer O and an emitter E. It is clear that as the universe expands, the luminosity distance increases, since $d_L(t_0) > d_L(t_e)$. The worldlines of the emitter and the observer diverge. Adopted from [10].

This is an important relation which can be used practically, but note that it depends on the time history of the scale factor through the dependence on χ. Therefore, we can find the luminosity distance d_L if we multiply the angular diameter distance d_A by a factor of $(1+z)^2$, or

$$d_L = d_A(1+z)^2$$

[6] The comoving distance in a curved universe with density parameter $\Omega_k = 1 - \Omega_0$, where Ω_0 is the ratio of total to critical distance today and measures the "curvature of space" is

$$d_A = \frac{1}{(1+z)H_0\sqrt{\Omega_k}} \sinh\left(\sqrt{\Omega_k} H_0 \chi\right), \qquad \Omega_k > 0$$

or

$$d_A = \frac{1}{(1+z)H_0\sqrt{-\Omega_k}} \sin\left(\sqrt{-\Omega_k} H_0 \chi\right), \qquad \Omega_k < 0$$

emphasizing again that 'distance' depends on definition. The latter is known as the *distance duality relation*. The luminosity distance and the angular diameter distance measures form the basis for observational tests of the geometry of the universe.

A very high redshift galaxy looks large, dim and ghostly in the sky. This is expected, since the observed light from the galaxy has been emitted when the universe was younger. This reason, coupled with gravitational focussing of the light rays by the intervening matter in the universe, means that the galaxy looks bigger. Geometry associated with the definition of luminosity distance with one spatial dimension suppressed, is presented in Fig. 1.8.

In order to test the relation between the luminosity distance $d_L(z)$ and the angular diameter distance $d_A(z)$, we need a standard candle (to test the $d_L(z)$ function) which is a sample of supernova type Ia and a standard ruler (to test the $d_A(z)$ function) which are anisotropies on the cosmic microwave background radiation. Almost all the cosmological observations indicate that we live in a flat universe, the components of which are $\approx 70\%$ vacuum energy and $\approx 30\%$ matter.

The luminosity distance $d_L(z)$ and the angular diameter distance $d_A(z)$ depend on the cosmological model which we have adopted. Different values of the energy densities Ω_{0i} give a different value of $S(\chi)$ and consequently different distances for the same comoving celestial object. Thus, it is of extremely importance to determine through observations the exact value of each energy density Ω_{0i}.

We can also define the luminosity distance in terms of the relationship between the absolute magnitude M and apparent magnitude m of an astronomical object, such as supernova or a quasar. Absolute magnitude is a measure (with a volometer) of the luminosity of a celestial object, which is defined to be equal to the apparent magnitude that the object would have if it were viewed from a distance of exactly 10 *parsecs* (this was once thought to be the distance to star Vega), while the apparent magnitude is a number that is a measure of its brightness as seen by an observer on Earth.

The measurement of apparent magnitude or brightness of a celestial object is known as photometry, quantifies the brightness of sources at ultraviolet, visible, and infrared wavelengths and is usually measured in a specific passband corresponding to some photometric system. The relationship between apparent and absolute magnitude is

$$\boxed{m - M = 5\log_{10}\left(\frac{d_L}{10pc}\right) + C} \tag{1.63}$$

where C is a correction term for the shifting of the spectrum due to expansion.

1.6.3 Cosmological horizons

Any comoving observer at a particular cosmic time has a viable region. The extent of this region depends on its definition and is called horizon [15]. Someone, can distinguish two different horizons, the *particle horizon* and the *event horizon*.

First, we will define the *comoving distance light* which determines the χ coordinate of the *particle horizon*. It is the distance which a photon could have traveled (with $c = 1$) from the big bang (where we assume $t = 0$) to a time t, the particle horizon, so is therefore

$$\chi_p(t) \equiv \int_0^t \frac{dt'}{a(t')} \tag{1.64}$$

The importance of the particle horizon $\chi_p(t)$ is the fact that, under the standard cosmological model, the portions of the sky on our comoving horizon which are separated by more than $\chi_p(t)$, are not causally connected. As every distance can be expressed in units of time, the comoving distance light corresponds to comformal time, which is useful in perturbation theory and in the formulation of gravitational waves. The corresponding proper distance to the particle horizon is

$$d_p(t) = a(t)\chi_p(t)$$

Any universe with continually decelerating expansion up to cosmic time t has a finite particle horizon at that time. Finite particle horizon also exists in other cosmological models, such as the Friedmann

models or in the flat Lemaitre model with $\Omega_{0\Lambda} \approx 0.7$ and $\Omega_{0m} \approx 0.3$. These parameter values seems to provide a reasonable description of our universe. The time derivative of the particle horizon is equal to $\dot{\chi}_p(t) = 1/a$, always positive, which means that increases with time. Also, the particle horizon at any given cosmic time is the surface of infinite redshift ($z \to \infty$) beyond which we cannot see, but once an object lies within an observer's particle horizon it remains so.

In some cosmological models it is easy from Eq. (1.64) to derive the particle horizon. For example, in a matter dominated model at early time the scale factor obeys the relation $a(t) \sim t^{2/3}$, which means that the particle horizon is $d_p(t) = 3t$. Also, in a radiation dominated model with $a(t) \sim t^{1/2}$, the corresponding particle horizon is $d_p(t) = 2t$.

The *horizon problem* is another cosmological fine-tuning problem within the Big Bang model of the universe. It arises due to the difficulty in explaining the observed homogeneity, such as nearly uniform temperature of the CMB, of causally disconnected regions of space in the absence of a mechanism that sets the same initial conditions everywhere. It was first pointed out by Wolfgang Rindler in 1956. This problem, like the flatness problem, is an important challenge to standard cosmology, that can only be resolved by invoking the theory of inflation.

In Cosmology, the *event horizon*, or commonly cosmic event horizon, of the observable universe is the largest comoving distance from which light emitted now can reach the observer in the future. This definition differs from the concept of particle horizon, which represents the largest comoving distance from which light emitted in the past could have reached the observer at a given time. It is a region in spacetime beyond which events cannot affect an outside observer (we never see them). In the case where the integral of Eq. (1.64) converses, the event horizon is defined as

$$\chi_e(t) \equiv \int_{t_1}^{t_{max}} \frac{dt'}{a(t')} \tag{1.65}$$

where t_1 is the time at which the light is emitted and t_{max} is the infinity or the time where the scale factor gets equal to zero (the time of Big Crunch). Examples of cosmological models without an event horizon are universes which are dominated by matter or by radiation. An example of a cosmological model with an event horizon is a universe which is dominated by the cosmological constant (a de Sitter universe).

An event horizon is commonly associated with black holes, but differs from the event horizon which we discussed earlier. Light which is emitted from inside the event horizon of a black hole can never reach the outside observer. Likewise, any object approaching the horizon from the observer's side appears to slow down and never quite pass through the horizon with its image becoming more and more redshifted as time elapses. This means that the wavelength of the light which is emitted from the object is getting longer as the object moves away from the observer. The travelling object however, experiences no strange effects and does, in fact, pass through the horizon in a finite amount of proper time.

Extremely important distance in cosmology is the *Hubble distance*

$$d_H(t) = H^{-1}(t) \tag{1.66}$$

since it represents the typical length scale at a cosmic time t. The Hubble distance would be the distance between the Earth and the galaxies which are currently receding from us at the speed of light. We can also define the *comoving Hubble distance* as

$$\chi_H(t) = \frac{d_H(t)}{a(t)} = \frac{1}{\dot{a}(t)}$$

Some characteristic properties of the Hubble distance are

1. in this length scale the relativistic effects become important, so we can not ignore them.
2. in standard cosmological models it is of the same order as the particle horizon $d_p(t)$. They differ significantly in inflationary cosmologies.
3. an object can be within an observer's Hubble distance at one time, lie outside it at some later time and even come back within it, at a far later epoch.

1.7 Accelerating Expansion

At the end of twentieth century (1998), the observation that the universe appears to be expanding at an increasing rate is a milestone of modern Cosmology. It is one of the most profound discoveries, pointing to a universe in which $\sim 70\%$ of the mass-energy density has an unknown form spread uniformly across the universe. Cosmologists at that time, expected that the expansion would be decelerating due to the gravitational attraction of the matter in the universe. Two independent projects, the Supernova Cosmology Project [16] and the High-z Supernova Search Team [17], which both used distant type Ia supernovae (SNe Ia) to measure the acceleration, discovered the accelerating expansion. Using SNe Ia as standard candles, they measured the distance of the supernovae through their brightness, and they compared the result with the distance from redshift, which measures how fast the supernovae are receding from us. Both teams independently determined that high-redshift SNe were fainter than expected in a matter-dominated universe, implying the need for a cosmological constant or more generally the need of dark energy to accelerate the expansion of the universe. Later, the accelerating expansion was confirmed from baryon acoustic oscillations (BAO) and from temperature fluctuations in CMB.

The main challenge of modern cosmology is the understanding of the nature of cosmic late-time acceleration, which has been confirmed by a large number of observations [18] such as

- measurements of Type Ia supernovae (SNe Ia) distances,
- peaks of baryon acoustic oscillations (BAO) in the large-scale correlation function of galaxies,
- studies of the weak lensing signal for source galaxies binned by photometric redshift (one can probe the history of structure growth)
- analyses of the clustering of galaxies
- the power spectrum of fluctuations in the cosmic microwave background (CMB), and
- the detection of gravitational waves of a binary neutron star inspiral

Up to now, to describe this accelerated mechanism theoretical physicists propose two main classes of models, i.e.,

1. the so-called **dark energy (DE)**, which maintains the correctness of the general relativity and introduces an exotic matter source in the Einstein equations or
2. **modified theories of gravity**, which modify the standard Lagrangian of GR based on some reasonable physical consideration.

1.8 Dark Energy

A crucial question in modern Cosmology is what induces the accelerating expansion which, until now is an open question. Cosmic acceleration could arise from the repulsive gravity of dark energy, the quantum energy of the vacuum, or it may be a signal that General Relativity breaks down on cosmological scales and must be replaced. Dark energy has a negative pressure with w less than $-1/3$. According to indications and theories, the dark energy dominated era begun since almost 5 billion years. The simplest explanation for the dark energy is the consideration of a positive cosmological constant Λ. While, as we will see below, there are alternative possible explanations, this description for dark energy is used in the current standard model of cosmology, which also includes cold dark matter (CDM) and is known as the Lambda-CDM model (ΛCDM) [19].

The nature of dark energy is more hypothetical than that of dark matter, and many things about it remain matters of speculation [19]. Dark energy is thought to be very homogeneous and not very dense, and is not known to interact through any of the fundamental forces other than gravity. It is very difficult to be detectable in laboratory experiments, since the dark energy density is very small ($\sim 10^{-27} kg/m^3$).

Dark energy (as well as dark matter) is identified via gravitational probes, such as data from distant supernova Ia, density fluctuations of CMB or the growth rate of cosmological perturbations on a range of redshifts and scales. The measurements of the growth rate are determined by the product

$$\boxed{f(a)\sigma_8(a)} \tag{1.67}$$

where a is the scale factor,

$$f(a) = \frac{d\ln\delta(a)}{d\ln a}$$

is the growth rate of cosmological perturbations, $\delta(a) = \delta\rho/\rho$ is the linear matter overdensity growth factor and σ_8 is the matter power spectrum normalization on scales of $8\ h^{-1}\ Mpc$.

Independently of its actual nature, dark energy would need to have a strong negative pressure (repulsive action), to explain the observed acceleration of the expansion of the universe. According to general relativity, the pressure within a substance contributes to its gravitational attraction for other objects just as its mass density does. In the FLRW metric, it can be shown that a strong constant negative pressure, which fills the universe, causes an acceleration in the expansion if the universe is already expanding, or a deceleration in contraction if the universe is already contracting. This accelerating expansion effect is sometimes labeled as "gravitational repulsion".

There are many suggested proposals about the nature of dark energy. The models for dark energy range from a cosmological constant (Λ) term to quintessence, Chaplygin gas, topological defects, chameleon particles, etc. Subsequently, first we will mention the basic triumphs and challenges of the ΛCDM model and then we will discuss in brief the most important of the alternative suggestions about the nature of dark energy. The biggest part of the present thesis deals with these model aspects about the dark energy.

1.9 ΛCDM model: triumphs and challenges

A large and diverse variety of cosmological observations during the past twenty years have established a standard cosmological model (ΛCDM) which is based on the cosmological principle (homogeneity, isotropy, general relativity, cold dark matter and baryonic matter), flatness of space, the existence of a cosmological constant and Gaussian scale invariant matter perturbations generated during inflation.

Parameter	Symbol	Value
Physical baryon density parameter	$\Omega_b h^2$	0.02230 ± 0.00014
Physical dark matter density parameter	$\Omega_c h^2$	0.1188 ± 0.0010
Scalar spectral index	n_s	0.9667 ± 0.0040
Reionization optical depth	τ	0.066 ± 0.012
Age of the universe	t_0	$(13.799 \pm 0.021) \times 10^9$ years
Curvature fluctuation amplitude, $k_0 = 0.002 Mpc^{-1}$	Δ^2_R	$2.441^{+0.088}_{-0.092} \times 10^{-9}$

Table 1.1: The simplest viable cosmological model is the ΛCDM model. It is based on 6 independent or free cosmological parameters, which are presented in this Table. The values have been estimated by the Planck Collaboration [12]. The independent parameters of this model have been pinned down to extraordinary accuracy by the Planck mission.

The ΛCDM is the simplest cosmological model, which is consistent with current cosmological observations. It includes only 6 independent parameters, which are presented in Table 1.1. These parameters are the physical baryon density parameter ($\Omega_b h^2$), the physical dark matter density parameter ($\Omega_c h^2$), the age of the universe (t_0), the scalar spectral index (n_s), the curvature fluctuation amplitude (Δ^2_R) and the reionization optical depth (τ). The symbol h denotes the reduced Hubble constant. The ΛCDM model

includes fixed parameters, such as the equation of state w or the total density Ω_0 and calculated parameters, such as the critical density ρ_{crit}, or the Hubble constant H_0. The observed accelerating expansion of the universe is attributed to a cosmological constant which introduces repulsive properties to gravity at large distances [20–25]. Crucial assumptions of this model are the validity of GR on cosmological scales, flatness, homogeneity, isotropy and the invariance of dark energy, both space and time (cosmological constant). The independent parameters of this model have been pinned down to extraordinary accuracy by the Planck mission [12]. The model uses the Friedmann–Lemaître–Robertson–Walker metric, the Friedmann equations and the cosmological equations of state to describe the observable universe from right after the inflationary epoch to present and future. The cosmological constant may be described as a homogeneous dark energy perfect fluid with constant energy density, negative pressure and constant equation of state parameter

$$w = \frac{P}{\rho} = -1. \tag{1.68}$$

This cosmological model makes clear and well defined predictions which have withstood the continuous and rapid improvement of cosmological observational tests. It is frequently referred to as the standard model of Big Bang cosmology because it is the simplest model that provides a reasonably good account of many properties of the cosmos. Prominent successes of the standard cosmological model include the following:

- The Cosmic Microwave Background (CMB) angular power spectrum of perturbations [26] is overall in excellent agreement with the predictions of the standard model (existence and structure of CMB). However, a few issues related to the orientation and magnitude of low multipole moments (CMB anomalies) constitute remaining puzzles for the standard model [27–34].
- The statistics of the CMB temperature perturbation maps [35] are consistent with the prediction of gaussianity of the standard model.
- Observations of the recent accelerating expansion history of the universe [36] in the light from distant galaxies and supernovae are consistent with the existence of a cosmological constant. Despite of the continuously improved data no need has appeared for more complicated models based on dynamical dark energy or modified gravity. The likelihood of the cosmological constant vs more complicated models has been continuously increasing during the past decade [37].
- Observations of large scale structure are in good agreement with ΛCDM [38] (basic statistics such as the distribution of galaxies [39], or halo power spectrum [40]).
- The predicted abundances of hydrogen (including deuterium), helium and lithium during the Big Bang (also known as primordial) nucleosynthesis are in excellent agreement with the cosmological observations.

Despite of the above major successes, the standard model is challenged by a few puzzling large scale cosmological observations [41] which may hint towards required modifications of the model. These challenges of ΛCDM may be summarized as follows:

1. *Large Scale Velocity Flows*

   ΛCDM predicts significantly smaller amplitude and scale of flows than what observations indicate. It has been found that the dipole moment (bulk flow) of a combined peculiar velocity sample extends [42] on scales up to 100 $h^{-1}Mpc$ ($z \leq 0.03$) with amplitude larger than 400 km/sec. The direction of the flow has been found approximately in the direction $l \simeq 282°$, $b \simeq 6°$. Other independent studies have also found large bulk velocity flows on similar directions [43] on scales of about 100 $h^{-1}Mpc$ or larger [44]. The expected root mean square (rms) bulk flow in the context of ΛCDM normalized with WMAP5 $(\Omega_{0m}, \sigma_8) = (0.258, 0.796)$ on scales larger than 50 $h^{-1}Mpc$ is approximately 110 km/sec. The probability that a flow of magnitude larger than 400 km/sec is realized in the context of the above ΛCDM normalization (on scales larger than 50 $h^{-1}Mpc$) is less

than 1%. A possible connection of such large scale velocity flows and cosmic acceleration may be found in Ref. [45].

2. *Alignment of low multipoles in the CMB angular power spectrum*

   The normals to the octopole and quadrupole planes are aligned with the direction of the cosmological dipole at a level inconsistent with Gaussian random, statistically isotropic skies at 99.7% [28]. The corresponding directions are: octopole plane normal $(l, b) = (308°, 63°)$ [27, 46], quadrupole plane normal $(l, b) = (240°, 63°)$ [27, 47], CMB dipole moment $(l, b) = (264°, 48°)$ [48]. A related effect has also been recently observed [49] by considering the temperature profile of 'rings' in the WMAP temperature fluctuation maps. It was found that there is a ring with anomalously low mean temperature fluctuation with axis in the direction $(l, b) = (276°, -1°)$ which is relatively close to the above directions (particularly that corresponding to the bulk velocity flows).

3. *Large scale alignment in the Quasi-stellar objects (QSOs) or quasars optical polarization data*

   Quasar polarization vectors are not randomly oriented over the sky with a probability often in excess of 99.9%. The alignment effect seems to be prominent along a particular axis in the direction $(l, b) = (267°, 69°)$ [50].

4. *Profiles of Cluster Haloes:* ΛCDM predicts shallow low concentration and density profiles in contrast to observations which indicate denser high concentration cluster haloes [51, 52].

5. *Missing power on the low l multipoles of the CMB angular power spectrum*

   which leads to a vanishing correlation function $C(\theta)$ on angular scales larger than 60° [28, 33, 53]

In addition to the above large scale effects there are issues on galactic scales (missing satellites problem [54–56] and the cusp/core nature of the central density profiles of dwarf galaxies [57–60]).

The ΛCDM model can be extended by adding cosmological inflation, quintessence and other elements that are current areas of speculation and research in cosmology. Some alternative models challenge the assumptions of the ΛCDM model. Examples of these are modified Newtonian dynamics, modified gravity, theories of large-scale variations in the matter density of the universe and scale invariance of empty space [61].

1.9.1 Evidence for a preferred cosmological axis

Three of the above five large scale puzzles are large scale effects related to preferred cosmological directions (CMB multipole alignments, QSO polarization alignment [62] and large scale bulk flows) which appear to be not far from each other. Their direction is approximately normal to the axis of the ecliptic poles $(l, b) = (96°, 30°)$ and lies close to the ecliptic plane and the equinoxes. This coincidence has triggered investigations for possible systematic effects related to the CMB preferred axis but no significant such effects have been found [28].

Thus, unless there is a hidden common systematic [63], the existence of a cosmological preferred axis may be attributed to physical effects. An incomplete list of these effects is the following:

- An anisotropic dark energy equation of state [64–66] due perhaps to the existence of vector fields [67, 68].
- Dark Energy and/or Dark matter perturbations on scales of the order of the horizon scale [69, 70]. For example an off center observer in a 1 *Gpc* void would experience the existence of a preferred cosmological axis through the Lematre-Tolman-Bondi metric [71–75].
- Deviations from the isotropic cosmic expansion rate are induced by a fundamental violation of the cosmological principle eg through a multiply connected non-trivial cosmic topology [76, 77], rotating universe coupled to an anisotropic scalar field [78], non-commutative geometry [79] or simply a fundamental anisotropic curvature [80].

- Statistically anisotropic primordial perturbations [81–83], such as inflationary perturbations induced by vector fields [84–87]. Note, however, that inflationary models with vector fields usually suffer from instabilities due to the existence of ghosts. [88–90]
- The existence of a large scale primordial magnetic field [91–93]. Evidence for such a magnetic field has recently been found in CMB maps [94].

Some anomalies in the background radiation (CMB) have been reported which are aligned with the plane of the Solar System, which contradicts the Copernican principle by suggesting that the Solar System's alignment is special. Specifically, with respect to the ecliptic plane the "bottom half" of the CMB is slightly hotter than the "top half". Also, the quadrupole and octupole axes are only a few degrees apart, and these axes are aligned with the top/bottom divide. Land and Magueijo in 2005 dubbed this alignment the "*axis of evil*", although several later studies have shown systematic errors in the collection of that data and the way it has been processed.

1.10 Topological Defects

A few moments after the big bang singularity the universe was super-symmetric, but as it was expanded these symmetries gradually broke through phase transitions. In the context of standard cosmology, *topological defects* are stable configurations of matter which are formed at phase transitions in the very early universe through the Kibble mechanism. These configurations are in the original, symmetric or old phase, but nevertheless they persist after a phase transition to the asymmetric or after a new phase is completed. In a symmetry breaking phase transition, different regions of the universe will choose to fall into different minima in the set of possible states (this set is known as the vacuum manifold) and topological defects are the boundaries between these regions. Spontaneous symmetry breaking is induced by an order parameter ϕ, which is usually a scalar field. Scalar fields participate at phase transitions and contain vacuum energy. A plethora of scalar fields survive until today, but they are 'inactive'. A typical symmetry breaking potential, which is known as the Mexican hut is of the form

$$\boxed{V(\phi) = \frac{1}{4}\lambda\left(\phi^2 - \eta^2\right)^2} \tag{1.69}$$

where λ is a positive coupling constant very close to zero and $\eta > 0$ is the symmetry breaking scale. When the temperature of the cosmic plasma is above the critical value $T_c \sim \eta$, the symmetry is unbroken because the minimum $\phi = 0$ is stable, but as the universe cools below the critical value, the symmetry breaks since the point $\phi = 0$ becomes unstable.

We consider the existence of the following types of topological defects, although they have not been observed directly until today

- **monopoles:** they are zero dimensional (point-like) objects which are formed when a spherical symmetry is broken. It seems to be supermassive, but their existence is one of the puzzles of the standard cosmology, which is known as the *monopole problem*.
- **cosmic strings:** they are objects with one dimension and they are formed when an axial or cylindrical symmetry is broken. They are very thin and may stretch across the visible universe.
- **domain walls:** they are two dimensional objects that are formed when a discrete symmetry is broken at a phase transition. They have some strange properties, such as the gravitational field of a domain wall which is repulsive rather than attractive.
- **textures:** they are formed when larger more complicated symmetry groups are completely broken.

Theories giving rise to domain walls are ruled out by cosmological constraints, since they are cosmologically catastrophic. Those producing cosmic strings, monopoles and textures are quite attractive,

since they can crucially affect the evolution of the universe. If the scale of symmetry breaks, at which the defects that are produced is about $10^{16}\ GeV$, then defects can act as the seeds that led to the formation of the large-scale structures we observe today, as well as the anisotropies in the CMB. Also, topological defects may play a crucial role in baryogenesis. Finally, they could be at the origin of some of the 'dark matter' of the universe. In conclusion, topological defects can be connected with many cosmological theories and observations.

1.11 Chameleons

The existence of chameleons [95–98] could support the accelerating expansion of the universe (as a component of dark energy) and the time evolution of the fine structure constant α. Time-variation of coupling constants are generally modeled with rolling scalar fields and the recent evidence for a time-varying α requires the mass of the corresponding scalar field to be of order H_0 [11]. Chameleons are scalar particles [99, 100] the effective mass of which is a function of its local environment. Just like a chameleon changes color in different environments, the magnitude of the mass of a cosmological chameleon particle depends on the density of the location. In regions with high density, such as Earth, the mass is large in order to evade the fifth force searches, which are excluded by experiments on a wide range of scales. In regions with low density, such as our solar system, the mass is lower and in cosmological scales is of order of the present Hubble value [101, 102]. The chameleon screening mechanism lies in the fact that the effective mass m_{eff} of the scalar field is calculated at the minimum value ϕ_{min} of the potential $V_{eff}(\phi)$ by evaluating the second derivative of the potential as

$$\boxed{m_{eff} \equiv \sqrt{\frac{d^2 V_{eff}}{d\phi^2}\bigg|_{\phi_{min}}}} \tag{1.70}$$

where V_{eff} is the effective potential which contains terms of chameleon, matter and radiation potential, as

$$V_{eff}(\phi, \vec{x}) = V(\phi) + e^{\frac{\beta_m \phi}{M_{Pl}}} \rho_m(\vec{x}) + e^{\frac{\beta_\gamma \phi}{M_{Pl}}} \rho_\gamma(\vec{x}) \tag{1.71}$$

where β_m and β_γ are parameters which describe the strength of the chameleon to matter and radiation coupling respectively.

It is clear that, the effective mass depends on the electromagnetic fields and the local matter density [103], since the effective potential depends on the matter density of the environment (see Fig. 1.9). The convexity of the curve V_{eff} when the density is small (right panel), is less than the curve of the potential which describes region with large density (left panel). Thus, the second derivative of V_{eff}, which is proportional to $(m_{eff})^2$, is smaller. A possible potential for chameleons is the Ratra-Peebles inverse power-law form potential

$$\boxed{V(\phi) = M^4\big(1 + \frac{M^n}{\phi^n}\big)} \tag{1.72}$$

where n is an integer and $M = \frac{M_{Pl}}{\beta}$ is a model parameter (in the case of dark matter, $M \simeq 3\ meV$). The term $\frac{1}{\phi^n}$ is responsible for the non-linear scalar interactions which are required for the chameleon mechanism to be operational while the constant piece can drive cosmic acceleration at the present time [104]. When the local matter density is high, the chameleon becomes invisible due to its mixing with the environment in order to evade current constraints on equivalence principle violations and fifth force. For this reason experiments, which have the purpose to detect chameleons in laboratory are performed in almost absolute vacuum where the chameleons have interesting cosmological effects.

Chameleons can couple to all forms of matter and can also couple to photons [105]. Coupling to matter leads to fifth force which acts only on large scales and is negligible on small scales. We have not observed any fifth force or modification of gravity in the laboratory or in the Solar System. The

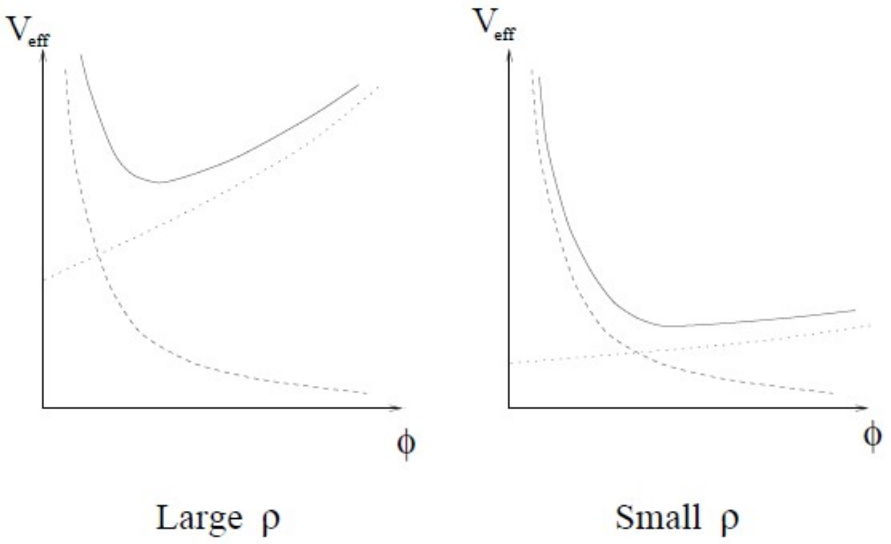

Figure 1.9: The effective potential as a function of the scalar field (chameleon) in regions with large density and small density. It is obvious that the denser the environment, the more massive the chameleon. Larger values of ρ correspond to smaller ϕ_{min} and larger m_{eff}. Adopted from [11].

chameleon mechanism has exactly the above properties, because it suppresses the fifth force mediated by the new degree of freedom without killing the modification on all scales. The environment dependent mass (1.70) is enough to hide the fifth force in dense media such as the atmosphere. The chameleon force [11, 106] is only sourced by a thin shell near the surface of dense objects, which reduces its magnitude significantly. In other words, in chameleon-type models the scalar field acquires a very large mass within a massive object and consequently decouples due to the Yukawa suppression. Thus, essentially only a fraction of the total mass (in circumference) contributes to the fifth force.

1.12 Modified Theories of Gravity

Alternatives to general relativity are physical theories that attempt to describe the gravitation in competition to Einstein's theory of general relativity. Thus, once one meets difficulties in the explanation of dark energy, it is a natural idea to step back and question if the current gravity theory can be applied to cosmological scales (or even galactic scales). A vast range of modified theories now exists in literature. Some of these have extra scalar, vector or tensor fields in their gravitational sector, variation of the Newton constant G_{eff} as a function of the scale factor or the redshift.

Measurements of the growth of structure (1.67) at redshifts of $z \simeq 0.8$ can be used as a test key for a plethora of modified theories of gravity. With these measurements one can test and reject, a large number of proposals for modified gravity. This work carefully considers the impact of modifications to gravity on the CMB, weak lensing and a variety of other cosmological probes. As a result, testing gravity has become one of the core tasks of many current and future cosmological missions and surveys.

1.13 Extended to ΛCDM models: quintessence and phantom cosmology

Extended models allow one or more of the fixed parameters of ΛCDM model to vary, in addition to the basic six parameters. So these models join smoothly to the basic six-parameter model in the limit

that the additional parameter(s) approach the default values. For example, possible extensions of the simplest ΛCDM model allow for spatial curvature (Ω_0 may be different from 1) or quintessence rather than a cosmological constant where the parameter of equation of state of dark energy is allowed to differ from the value $w = -1$. Also, cosmic inflation predicts tensor fluctuations which are the origin of gravitational waves. Their amplitude is parameterized by the tensor-to-scalar ratio which is determined by the unknown energy scale of inflation. Allowing additional variable parameter(s) will generally increase the uncertainties in the standard six parameters quoted in Table 1.1 and may also shift the central values slightly.

In physics, *quintessence* is a hypothetical form of dark energy, more precisely a scalar field ϕ postulated as an explanation of the observation of an accelerating expansion of the universe. The first example of this scenario was proposed by Ratra and Peebles (1988). The concept was expanded to more general types of time-varying dark energy and the term "quintessence" was first introduced in a paper by Caldwell, Dave and Steinhardt [107]. It has been proposed by some physicists to be a fifth fundamental force. Quintessence differs from the cosmological constant explanation of dark energy in that it is dynamic. That is, it changes over time, unlike the cosmological constant which by definition, does not change. It is suggested that quintessence can be either attractive or repulsive depending on the ratio of its kinetic and potential energy. Those working with this postulate believe that quintessence became repulsive about ten billion years ago, almost 3.7 billion years after the Big Bang. Many models of quintessence have a tracker behavior, which partly solves the cosmological constant problem.

The pressure of the quintessence fluid is given by the relation $P = \frac{1}{2}\dot{\phi}^2 - V(\phi)$, while the density is defined as $\rho = \frac{1}{2}\dot{\phi}^2 + V(\phi)$. The first term is the kinetic energy and the second term is the potential energy. The parameter of equation of state, which differs from $w = -1$ since $V(\phi) \neq 0$, is

$$\boxed{w = \frac{\frac{1}{2}\dot{\phi}^2 - V(\phi)}{\frac{1}{2}\dot{\phi}^2 + V(\phi)}} \tag{1.73}$$

A special case of quintessence models is the *phantom energy*, where the kinetic energy is negative. The parameter of equation of state is $w < -1$ and if this type of energy existed, it would cause a Big Rip singularity. In this scenario the scale factor increases rapidly and the bound systems get dissociated due to the growing energy density of dark energy which would cause the expansion of the universe to increase at a faster than exponential rate. This acceleration passes the speed of light, since it involves expansion of the universe itself, not particles moving within it. As a result, more and more objects leave our observable universe faster than the expansion and will be unable to interact with each other via fundamental forces. Eventually the expansion will prevent any action of forces between any particles, even within atoms.

1.14 Gravitational waves

The theoretical prediction of gravitational waves (GWs) originated in 1893 when Heaviside first discussed the possibility of their existence. More than 100 years ago, Einstein predicted that something special happens when two bodies, such as planets or stars, orbit each other [108, 109]. He believed that this kind of movement could cause ripples in space. These ripples would spread out like the ripples in a pond when a stone is tossed in and these ripples are called *space gravitational waves*. GWs are invisible and incredibly fast, since they travel at the speed of light. Also, GWs transport energy as gravitational radiation, a form of radiant energy similar to electromagnetic radiation and squeeze and stretch anything in their path as they pass by.

The most powerful GWs are created when massive objects move at very high speeds. Some examples of events that could cause a GW are the following

- when a star explodes asymmetrically (such as supernova)
- when two big stars (such as neutron stars) orbit each other and merge

- when two black holes orbit each other and merge

Since these types of objects that create GWs are far away and sometimes, these events only cause small, weak gravitational waves, the waves are then very weak by the time they reach Earth. This feature makes GWs incredibly hard to detect. Nonetheless, until now 11 events of detection of GW have been announced (10 from merge of black holes and 1 from merge of neutron stars).

In theoretical level, in the linearized weak-field approximation, Einstein found that his equations had transverse wave solutions travelling at the speed of light [110] produced by the time dependence of the mass quadrupole moment of the source [111]. He realized that GW amplitudes would be small and up until 1957, there had been a debate about the physical relevance of their existence [112].

Nevertheless, the discovery of the binary pulsar system PSR B1913+16 by Hulse and Taylor [113] and subsequent observations of its energy loss by Taylor and Weisberg [114] demonstrated indirectly the existence of GWs. This discovery, along with subsequent related analysis [115] led to the recognition that a possible direct detection and analysis of GWs could reveal interesting properties of various relativistic systems and could also provide new tests of general relativity, especially in the strong-field regime.

Recently, Abbot et al [116, 117] have reported the first direct detection of GWs emitted by a binary black hole (BBH) system merging to form a single black hole (BH). Their observation provides a direct window to the properties of space time in the strong-field limit and is consistent with predictions of GR for the nonlinear dynamics of highly disturbed BHs. The announced beautiful discovery is the result of great efforts for a century by several scientists [117] (and references therein). It is a great investigation, because it constitutes one more window to the Universe and one more confirmation of the theory of GR. Such GW observations can be used to check many cosmological indications and observations, such as

- to test the equivalence principle [118–121]
- to test the propagation of GWs [121–128]
- to test the validity of general relativity [129–131]
- to constrain early cosmological phase transitions [132, 133]
- to probe the quantum structure of black holes [134]
- to probe the connection between dark matter and primordial black holes [135–137]
- signatures from evolving scalar fields in GR and in Modified Gravity [138].

For these reasons, during the last years the Gravitational-wave astronomy has been developed, which uses gravitational waves to collect observational data about sources of detectable gravitational waves such as binary star systems which are composed of white dwarfs, neutron stars and black holes. Also, uses events such as supernovae and the formation of the early universe shortly after the Big Bang.

1.15 Deviations from the ΛCDM Standard Model

The flat ΛCDM model (the Standard model of the Big Bang cosmology) is the most acceptable cosmological model, since it is very simple and many cosmological observations can be supported theoretically from this model. Some basic components of this model are the cosmological constant Λ, the law of gravity which is Einstein's General Relativity and the cosmological principle. In the course of this Chapter we are discussing its defining principles and the possible ways that these principles can be evaded in the context of various extended models. Such deviations constitute the main focus of this thesis. Despite the large increase in data volume and accuracy, the ΛCDM model seems to be extremely successful at describing all these data and provide us with a better understanding of the Universe. Although it is considered a successful model, there are some observations which indicate deviations from the ΛCDM model. As data has been improved, some inconsistencies or deviations from the ΛCDM model have been appeared, which do not seem to be statistically significant, since the level of these deviations is at $\simeq 2\sigma$ [139].

Results from Planck satellite mission of the European Space Agency (ESA) [140], demonstrate that the Standard model of cosmology remains an excellent description of the Universe. However, when the Planck data are combined with other astronomical observations, several deviations emerge. The most significant deviation is the *Hubble tension* [141] which refers to one detail in the current model for the evolution of the universe that has not been resolved: the rate at which the universe is expanding. Scientists can arrive at the rate of expansion H_0 in two different ways and the two techniques result in slightly different rates. Local measurements of the Hubble parameter, from supernovae [142] and lensing time delays [143], disagree with the value inferred from a ΛCDM fit to the cosmic microwave background [140], with local measurements suggesting a higher value [7]. The uncertainties in both the supernova and CMB measurements are small enough that the disagreement between the two is statistically significant. This long-standing deviation has become stronger with time and is currently at 4.4σ [144]. The authors of Ref. [141] suggest that an exotic form of dark energy which is known as early dark energy is responsible for the Hubble tension, the discrepancy between the predicted and measured rates of universe expansion. Early dark energy behaves like a cosmological constant at early times and then decays away like radiation or faster at later times. Further studies must determine whether these anomalies are due to measurement uncertainties or undiscovered physical correlations, which would also challenge Einstein's theory of gravitation. The lack of a fully satisfactory model gives rise to alternatives to the cosmological Standard model.

In the present Thesis we look beyond the Standard model and we test the existence of possible deviations from the ΛCDM model. If the concordance model is correct, then these tests will provide a useful way to quantify how confident we are in a more absolute way than we can at present. On the other hand, possible deviations for any of these tests, will help point us in other directions. The bulk of the present thesis is devoted to the study of gravity theories, which mainly are based on *deviations from ΛCDM model*. In particular, these issues are

1. The Standard model of Cosmology is based on the cosmological principle, which states that our observational location in the universe is not unusual or special. On a large enough scale, the universe looks the same in all directions (isotropy) and from every location (homogeneity). In Chapter 2, we test the validity of the cosmological principle through the Union2 dataset of Supernova Ia, searching for deviations. Also, we search for a preferred cosmological axis in this dataset, which is the direction of maximum acceleration (the direction of the minimum value of Ω_{0m}).

2. The standard model assumes that all fundamental constants do not change in time and space. Also it assumes that no topological defects are present. In Chapter 3, we promote the fine structure constant to a scalar field and discuss its effects on the stability of particular types of topological defects (dilatonic gauged monopoles). Monopoles can affect the formation of the large scale structure or the anisotropies of the CMB. Since the Planck data predict some deviations from the ΛCDM model, especially in the low multipole moments of the CMB, it is important to study some properties of these monopoles. In Chapter 3, we investigate the stability of monopoles in the case of a coupling to electromagnetism and the consequences of their possible existence in Cosmology. In particular, we focus our interesting on the role of monopoles in some physical effects, such as the variation of the fine structure constant.

3. Scalar particles are an enigma from the point of view of General Relativity. In Cosmology, some scalar particles can contribute to dark matter. A cosmological classical background due to a scalar field can cause maximally positive or negative pressure. A negative pressure is most probably responsible for the present observed acceleration of the expansion of the universe. This approach for the interpretation of the observed type of expansion consists a deviation from the ΛCDM model. In Chapter 4, we explore signatures of some scalar particles which are known as axion like particles and chameleons, from experiments which try to detect them. Axion like particles are connected with

[7] Scientists who infer the rate of expansion from observations of the cosmic microwave background, conclude that we're expanding at a rate of $H_0 = 67.7 \frac{Km}{sec\ Mpc}$ which is approximately 3 million light-years. Those who observe stellar explosions, or supernovae, in the nearby universe and study how they move in relation to Earth come up with $H_0 = 73.5 \frac{Km}{sec\ Mpc}$

dark matter, while chameleons are connected with dark energy. Possibly, these particles interact with photons and the interaction is described through a coupling to electromagnetism. Until now, no experiment has detected these particles and for this reason, bounds have been estimated for the energy (or mass) of the corresponding particles. Also, we focus on a case of quintessence models where scalar fields which couple to electromagnetism can stabilize the cosmological structures for longer time than the ΛCDM model.

4. The ΛCDM model is based on the validity of General Relativity and thus the Newtonian law of gravity at all distance scales. However, there are indications that at sub-mm scale, appear deviations from the Newtonian gravity. For this reason, we need to perform a detailed check on experimental data which contain interactions below mm. In Chapter 5, we analyze data from an experiment which took place at the University of Stanford. According to our analysis, oscillating model for the residual force fits the data better than other models. This could be an indication for deviations from the law of gravity. However, most probably, this signal is due to systematic errors of the experiment.

5. The spacetime in the flat ΛCDM model is described by the FRW metric. In the vicinity of a mass concentration, this expanding background gets modified to different types of metrics. One of them is the McVittie metric which contains expansion and describes an expanding spacetime around a mass concentration, such as a black hole, where the gravity is strong. In such background, it is important to investigate the geodesics or the behaviour of a gravitational wave. In Chapter 6, we adopt the Newtonian limit of a McVittie spacetime and we focus on the evolution of a gravitational wave in the vicinity of a point mass and the corresponding effects, while in 7 we focus on geodesics in a phantom cosmological background in the presence of a mass concentration.

6. One of the basic concepts of the ΛCDM model is that the accelerating expansion is due to the presence of the cosmological constant Λ, where the equation of state parameter w is equal to -1. However, cosmological models with different values of the parameter w have been proposed as deviations from the concordance model, aiming to improve the understanding of cosmos and to describe the cosmological observations with a better way than the ΛCDM model. In phantom cosmology we have $w < -1$, while in quintessence models $w > -1$. In Chapter 7, we focus on geodesics of bound systems in a phantom cosmological background which is described by the McVittie metric. In this case the bound systems get dissociated in the future, since the scale factor becomes infinite. This singularity is known as Big Rip.

7. Chapter 8 is distinct from the other chapters since we do not consider deviations from the standard model. Instead we stay in the context of General Relativity and we focus on the effects of spin on the trajectories of particles in the vicinity of black holes. If we consider the spin of the particle, since many astrophysical systems have spin, the motion is described by the MP equations and the orbits are not geodesics, since the existence of spin induces an additional interaction. In Chapter 8, we consider the Mathisson Papapetrou Dixon equations in the post Newtonian limit of McVittie metric and we focus on the orbits of a particle in such a spacetime, where the gravitational effects are strong. We are interested in the deviations of the orbits which are circular in a static universe for a spinless particle. Deviations appear due to spin-orbit coupling and due to expanding background.

In conclusion, the principle that unifies and connects most of the contents of this thesis is the directions of deviation from the standard ΛCDM model. In this subsection we kept the exposition of the material of the present Thesis brief and focused onto the introduction of notions which are relevant to the subsequent chapters of this Thesis.

Chapter 2

Testing the isotropy of the Universe with Union2 data.

One of the most profound discoveries in Modern Cosmology is that the universe appears to be expanding at an increasing rate. Thus, the Universe either it is dominated by dark energy which is gravitationally repulsive, or General Relativity is inadequate and needs to be replaced by a modified theory of gravity. This discovery was made through the investigation of distant type Ia supernovae (SNe Ia), which are used as standard candles. In the upcoming decade, with improved distance precision, SNe Ia will provide measurements of the inhomogeneous motions of structures in the Universe that will provide an unmatched test of whether dark energy or modified gravity is responsible for the accelerating expansion of the Universe.

The cosmological principle which includes isotropy and homogeneity is a basic component of the ΛCDM model. Since it constitutes an assumption, it is tested by many cosmological observations. These observations come from the cosmic microwave background radiation [145–147], from the distribution of supernovae type Ia [1, 148, 149], using photometric and spectroscopic data [150], from highest energy cosmic rays [151] or from large scale structures [152–154]. The tests are carried out from data in local universe and large scales. Although the results are consistent with the cosmological principle, there are some indications for possible deviations (anomalies) from this principle in local and in large scales [1, 28, 152, 155].

In the course of this Chapter we estimate the cosmological parameter Ω_{0m} through the Union2 dataset of Supernova Ia. We search for possible deviations from the isotropy and homogeneity through the Union2 dataset and we prove that it is consistent with the Cosmological principle. Using the hemisphere comparison method, we find that this dataset has a direction with maximum acceleration, which corresponds to the minimum value of the parameter Ω_{0m}. As pointed out in section 1.15 such a study is one of the main directions of deviations from the ΛCDM standard model and is the one of the main focuses of this thesis. Since there are some different cosmological observations, such as CMB low multipole moments, quasar alignment, supernova Ia and bulk velocity flow of galaxies with a preferred cosmological axis in the same region of the celestial sphere, we estimate how possible is this coincidence to be random. The probability that the above independent six axes directions would be so close in the sky is less than 1%. Thus, either the relative coincidence is a very large statistical fluctuation or there is an underlying physical or systematic reason that leads to their correlation.

A type Ia supernova (SnIa) occurs in binary systems (two stars orbiting one another) in which one of the stars is a white dwarf with mass below the Chandrasekhar limit ($1.44 M_{\odot}$). The other star can be anything from a giant star to an even smaller white dwarf. When a slowly-rotating white dwarf accretes matter from the companion, it can exceed the Chandrasekhar limit, beyond which it can no longer support its gravity with electron degeneracy pressure. Then, the white dwarf explodes causing the companion star to be ejected away. This type Ia category of supernovae produces consistent peak

luminosity because of the uniform mass of white dwarfs that explode via the accretion mechanism. The stability of this value allows these explosions to be used as *standard candles* to measure the distance to their host galaxies because, as we can see from Eq. (1.63), the visual magnitude of the supernovae depends primarily on the distance.

Until today, have emerged many compilations of supernova Ia datasets, such as Constitution, Union, Union2 and Union 3, ESSENCE, SNLS, Gold06, SDSS-II and most recently Pantheon (Pan-STARRS1 Medium Deep Survey). More analytically, type Ia supernovae are used as standard candles

- to check the isotropy of the universe,
- to search for hints of existence of preferred axes in cosmos
- to investigate the recent expansion history of the universe.

Most previous studies searching for anisotropies in SnIa datasets have found no statistically significant evidence for anisotropies [156–161]. The authors of Ref. [157] used the Union2 dataset [36] consisting of 557 SnIa, to derive the angular covariance function of the standard candle magnitude fluctuations searching for angular scales where the covariance function deviates from null in a statistically significant manner. No such angular scale was found. However, this is a useful and ambitious approach which aims at identifying not only the existence of a possible anisotropy but also, its detailed angular scale dependence despite of relatively small number of data in most angular scales considered.

An alternative approach is found in Ref. [162] where a statistically significant preferred axis was detected using the hemisphere comparison method. This method amounts to fitting the ΛCDM parametrization for Ω_{0m} on several pairs of opposite hemispheres and comparing the maximally asymmetric pair with the corresponding maximally asymmetric pair of isotropized similar datasets. The advantage of this method is that it optimizes the statistics since there is a large number of SnIa in each hemisphere. This is achieved at the cost of loosing all information about the detailed structure of the anisotropy.

The method was applied to four SnIa datasets [162]. The most prominent axis of maximal hemispheric asymmetry $(l, b) = (123°, 27°)$ was found to be close to the axis of the equatorial poles $(l, b) = (96°, 30°)$. This alignment between maximally asymmetric hemispheric Hubble diagrams and the equatorial frame was attributed to a systematic error by the authors of Ref. [162]. A second direction of maximum asymmetry $(l, b) = (235°, 15°)$ in one of the datasets (the Gold04 [163]) was considered in Ref. [162] which was closer to the preferred axes of other observations discussed above but it was also discarded because the maximum asymmetry between the hemispheres coincided with the maximal asymmetry in the number of degrees of freedom.

In this Chapter we apply a variation of the hemisphere comparison method to the Union2 dataset. Our aim is to identify the direction of the axis of maximal asymmetry for the Union2 dataset [36] (directions to the SnIa provided in Ref. [157]) and evaluate its statistical significance by comparing with a large number of similar Monte Carlo isotropized datasets. We also compare the obtained direction of maximal asymmetry axis with the directions of preferred axes obtained from other cosmological observations discussed in Chapter 1. In particular, we estimate the probability these axes would have the observed angular separation if they are uncorrelated.

2.1 Hemisphere comparison method

The Union2 SnIa dataset [36] is a sample consisting of 557 SNe Ia covering the redshift range $z = [0.015, 1.400]$. It extends the Union dataset [164] by adding SnIa data at low and intermediate redshifts discovered by the CfA3 [165] and SDSS-II Supernova Search [166], respectively. It also includes six new SnIa discovered by the Hubble Space Telescope at high z. In this Chapter we use the directions to the SnIa provided in Ref. [157]. The angular distribution of the Union2 dataset in galactic coordinates is shown in Figure 2.1. The color of each point provides information about the redshift according to the legend on the right.

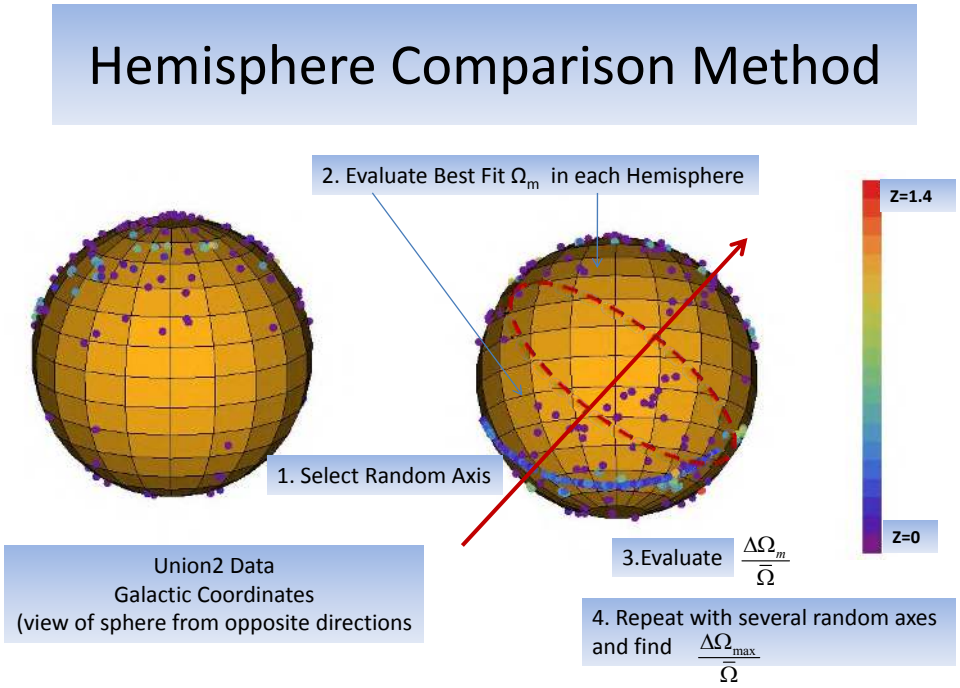

Figure 2.1: The Union2 data in galactic coordinates and the Hemisphere Comparison Method in four steps. The color of each datapoint provides information about the redshift according to the legend on the right. Two opposite hemispheres are shown. The viewpoints are along the axis of maximum asymmetry which we discuss in this Chapter.

The Union2 data along with directions as presented in Ref. [157] include the name of the SnIa, the redshift in the CMB rest frame, the distance modulus and its uncertainties (which include both the observational and the intrinsic magnitude scatter). They also include the equatorial coordinates (right ascension and declination) of each SnIa. It is straightforward to convert these coordinates to galactic coordinates or to usual spherical coordinates (θ, ϕ) in the equatorial or galactic systems [167]. This dataset may be analyzed in the usual manner by applying the maximum likelihood method. The apparent magnitude $m(z)$ is related to the Hubble-free luminosity distance $D_L(z)$ through

$$m_{th}(z, \Omega_{0m}) = \bar{M}(M, H_0) + 5log_{10}\Big(D_L(z)\Big) \tag{2.1}$$

where, in a flat cosmological model

$$D_L(z) = (1+z)\int_0^z dz' \frac{H_0}{H(z'; \Omega_{0m})} \tag{2.2}$$

is the Hubble-free luminosity distance assumed here to be parameterized by ΛCDM as

$$\boxed{H(z)^2 = H_0^2\Big(\Omega_{0m}(1+z)^3 + (1-\Omega_{0m})\Big)} \tag{2.3}$$

Also $\bar{M}$ is the magnitude zero point offset which depends on the absolute magnitude M and on the present Hubble parameter $H_0 = 100h\frac{km}{sec\ Mpc}$ as

$$\bar{M} = M + 5log_{10}(\frac{H_0^{-1}}{Mpc}) + 25 = M - 5log_{10}h + 42.38 \tag{2.4}$$

The parameter M is the absolute magnitude which is assumed to be constant. The data points of the Union2 compilation are given in terms of the distance modulus

$$\mu_{obs}(z_i) \equiv m_{obs}(z_i) - M \tag{2.5}$$

The theoretical model parameter (Ω_{0m}) is determined by minimizing the quantity $\chi^2(\Omega_{0m}, \mu_0)$, which is defined as

$$\boxed{\chi^2(\Omega_{0m}, \mu_0) = \sum_{i=1}^{N} \frac{\Big(\mu_{obs}(z_i) - \mu_{th}(z_i, \Omega_{0m}, \mu_0)\Big)^2}{\sigma^2_{\mu\, i}}} \tag{2.6}$$

where $\sigma^2_{\mu\, i}$ are the distance modulus uncertainties which include both the observational and the intrinsic magnitude scatter. These uncertainties are assumed to be Gaussian and uncorrelated (we assume a diagonal covariance matrix and ignore systematics). The theoretical distance modulus is defined as

$$\mu_{th}(z_i, \Omega_{0m}, \mu_0) \equiv m_{th}(z_i, \Omega_{0m}) - M = 5log_{10}\Big(D_L(z)\Big) + \mu_0 \tag{2.7}$$

where

$$\mu_0 = 42.38 - 5log_{10}h \tag{2.8}$$

As a test we have checked that our full sky analysis reproduces the results of Ref. [36] for the cases of no systematics. For example we obtain a full sky best fit value $\Omega_{0m} = 0.27$ which is almost, the current acceptable rate for the visible and dark matter and we reproduce the contour Fig. 10a of Ref. [36].

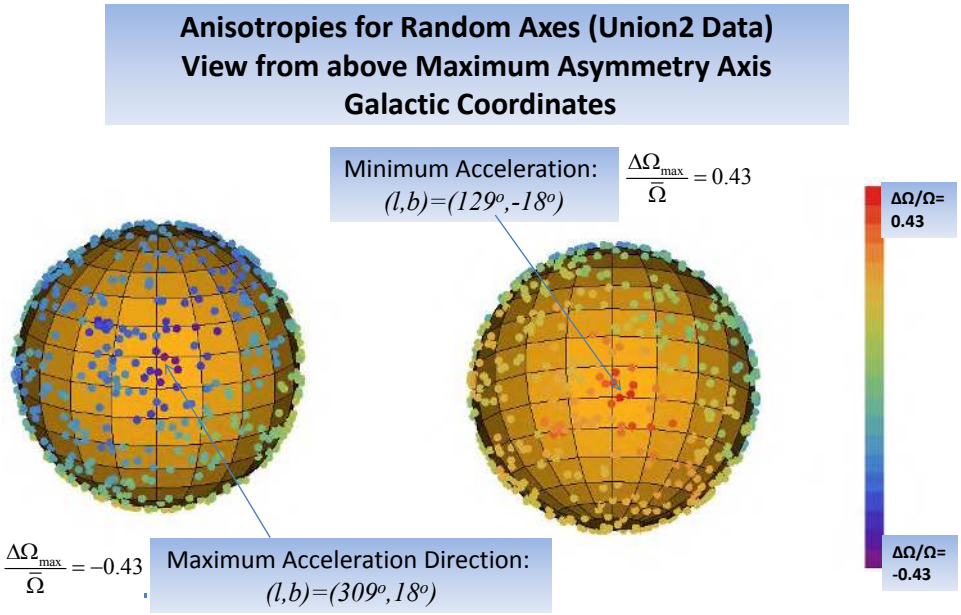

Figure 2.2: The directions of the random axes considered are shown as dots on the unit sphere colored according to the sign and magnitude of the anisotropy level $\left(\frac{\Delta\Omega_{0m}}{\bar{\Omega}_{0m}}\right)^{U2}$. The hemisphere shown on the left (right) is the one corresponding to maximum (minimum) acceleration. The corresponding best fit values of Ω_{0m} are $\Omega_{0m} = 0.19$ with $(l, b) = (309°, 18°)$ and $\Omega_{0m} = 0.30$ with $(l, b) = (129°, -18°)$.

The hemisphere comparison method, which implemented in this Chapter and in Fig. 2.1 involves the following steps [162]:

1. Generate a random direction in the celestial concave with the aid of the unit vector

$$\hat{r}_{rnd} = (\cos\phi\ \sqrt{1-u^2}, \sin\phi\ \sqrt{1-u^2}, u) \tag{2.9}$$

where $\phi \in [0, 2\pi)$ and $u \in [-1, 1]$ are random numbers with uniform probability distribution.

2. Split the dataset under consideration into two subsets according to the sign of the inner product $\hat{r}_{rnd} \cdot \hat{r}_{dat}$ where $\hat{r}_{dat}$ is a unit vector describing the direction of each SnIa in the dataset. Thus, one subset corresponds to the hemisphere in the direction of the random vector (defined as 'up') while the other subset corresponds to the opposite hemisphere (defined as 'down').

3. Find the best fit values on Ω_{0m} in each hemisphere ($\Omega_{0m,u}$ and $\Omega_{0m,d}$) and use these values to obtain the anisotropy level quantified through the normalized difference

$$\boxed{\frac{\Delta\Omega_{0m}}{\bar{\Omega}_{0m}} \equiv 2\frac{\Omega_{0m,u} - \Omega_{0m,d}}{\Omega_{0m,u} + \Omega_{0m,d}}} \tag{2.10}$$

4. Repeat for 400 random directions $\hat{r}_{rnd}$ and find the maximum standardized difference for the Union2 data

$$\left(\frac{\Delta\Omega_{0m,max}}{\bar{\Omega}_{0m}}\right)^{U2}$$

We also obtain the corresponding direction of maximum anisotropy.

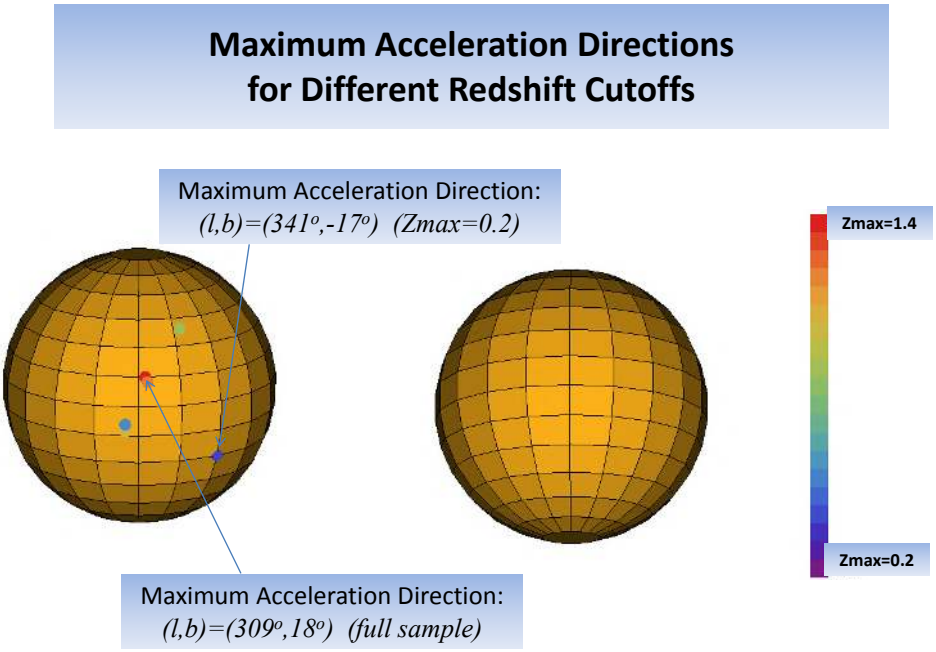

Figure 2.3: The directions of maximum acceleration which correspond to the redshift cutoffs of Table 1.

Instead of the above algorithm involving random directions of the axes, we could have implemented a uniform coverage of the sphere, utilizing equal area pixels along the lines of Healpix [168]. In that

case each axis would have a fixed direction in the center of each equal area pixel. However, we find the use of axes with random directions simpler to implement in practice without any specific disadvantage compared to the Healpix approach. In order to maximize efficiency, the number of axes should be approximately equal to the number of data points (SnIa) on each hemisphere. The reason for this is that changing the direction of an axis, does not change the corresponding $\frac{\Delta\Omega_{0m,max}}{\bar{\Omega}_{0m}}$ until a data point is crossed by the corresponding equator line. Such a crossing is expected to occur when the direction of an axis changes by approximately the mean angular separation between data points. Thus, using more axes than the number of datapoints in a hemisphere does not improve the accuracy of the determination of the maximum anisotropy direction. Given that the number of datapoints per hemisphere for the Union2 dataset is about 280 it becomes clear that using 280 test axes is close to the optimal number of axes to use. We have used 400 axes in our analysis, well above the value of 280.

In order to derive the 1σ error in the maximum anisotropy direction, we first obtain the 1σ error $\sigma_{\Delta\Omega}$ associated with $\frac{\Delta\Omega_{0m,max}}{\Omega_m}$. This is of the form

$$\boxed{\sigma_{\Delta\Omega} = \frac{\sqrt{\sigma^2_{\Omega_{0m,u}} + \sigma^2_{\Omega_{0m,d}}}}{\Omega_{0m,u} + \Omega_{0m,d}} = 0.06} \tag{2.11}$$

Notice that this is the error due to the uncertainties of the supernova distance moduli propagated to the best fit Ω_{0m} on each hemisphere and thus to $\frac{\Delta\Omega_{0m,max}}{\Omega_m}$. Then, we identify the test axes that correspond to an anisotropy level within 1σ from the maximum anisotropy level i.e.

$$\frac{\Delta\Omega_{0m}}{\bar{\Omega}_{0m}} = \frac{\Delta\Omega_{0m,max}}{\bar{\Omega}_{0m}} \pm \sigma_{\Delta\Omega}$$

These axes apparently cover an angular region corresponding to the 1σ range of the maximum anisotropy direction.

2.2 Axis of maximum asymmetry

Using a run with 400 test axes we find the 1σ angular region for the hemisphere of maximum acceleration is in the direction

$$\left(l = 309^{\circ}{}^{+23^{\circ}}_{-3^{\circ}}, \qquad b = 18^{\circ}{}^{+11^{\circ}}_{-10^{\circ}}\right)$$

and the best fit value is $\Omega_{0m} = 0.19$, while the hemisphere with the minimum acceleration is in the opposite direction

$$\left(l = 129^{\circ}{}^{+3^{\circ}}_{-23^{\circ}}, \qquad b = -18^{\circ}{}^{+10^{\circ}}_{-11^{\circ}}\right)$$

with best fit value $\Omega_{0m} = 0.30$. The corresponding maximum anisotropy level is

$$\boxed{\left(\frac{\Delta\Omega_{0m,max}}{\bar{\Omega}_{0m}}\right)^{U2} = 0.43 \pm 0.06} \tag{2.12}$$

Our results are shown in Fig. 2.2 where we present the directions of the random axes considered as dots on the unit sphere colored according to the sign and magnitude of the anisotropy level $\left(\frac{\Delta\Omega_{0m}}{\bar{\Omega}_{0m}}\right)^{U2}$. The view point is on top of the hemisphere of maximum (left) and minimum (right) acceleration.

In an effort to identify possible redshift dependence of the above anisotropy, we have implemented a redshift tomography of the Union2 data and have identified the maximum anisotropy directions (with their errors) for the following redshift ranges: $(0-0.2)$, $(0-0.4)$, $(0-0.6)$, $(0-0.8)$, $(0-1.0)$, $(0-1.2)$,

$(0-1.4)$. This tomography presented in Table 2.1 and Fig. 2.3. We have found that with the exception of the nearest supernovae $(0-0.2$ redshift range) whose maximum anisotropy direction is about 40° away from the maximum anisotropy direction of the full dataset, all the other redshift ranges have an anisotropy direction which is within about 20° from the anisotropy direction of the full Union2 dataset.

2.2.1 Maximum anisotropy level and cosmological isotropy

Subsequently, we wish to address the question whether the maximum anisotropy level (2.12) for the Union2 data is consistent with statistical isotropy. In order to address this question we have constructed simulated isotropic datasets by replacing the i^{th} distance modulus of the Union2 dataset by a random number with a Gaussian distribution with mean value and standard deviation determined by the best fit value of $\mu_{th}(z_i, \Omega_{0m}, \mu_0)$ (Eq. (2.7) with the best fit values $\Omega_{0m} = 0.27$, $\mu_0 = 43.16$) and by $\sigma_{\mu\, i}$ of the corresponding Union2 data-point respectively. We then compare a simulated isotropic dataset with the real Union2 dataset by splitting each dataset into hemisphere pairs using 10 random directions. This part of the present analysis is not aimed at identifying the maximum anisotropy direction neither at comparing with the result of the search in N=400 directions. Instead, it only aims at comparing the real data with the isotropic simulated data with respect to the level of anisotropy.

In the context of this comparison, it is not important to identify the level of absolute maximum anisotropy. What is more important is to repeat the comparison a relatively large number of times (40 in our case) in order to have acceptable statistics. Given the limitations of computing time we had to reduce the number of axes directions (10) in order to increase the number of Monte Carlo experiments performed. Clearly the level of anisotropy identified in this case ($\frac{\Delta\Omega_m}{\Omega_m} \simeq 0.29$) is significantly smaller compared to the case of 400 axes directions ($\frac{\Delta\Omega_m}{\Omega_m} \simeq 0.43$) but this is not important for our purposes which do not include in this case the identification of the maximum anisotropy. Then we find the maximum levels of anisotropy $\left(\frac{\Delta\Omega_{0m,max}}{\bar{\Omega}_{0m}}\right)^{U2}$ (Union2) and $\left(\frac{\Delta\Omega_{0m,max}}{\bar{\Omega}_{0m}}\right)^{I}$ (Isotropic) and compare them. We repeat this comparison experiment 40 times with different simulated isotropic data and axes each time. We found the following results:

- In about 1/3 of the numerical experiments (14 times out of 40) we have that

$$\left(\frac{\Delta\Omega_{0m,max}}{\bar{\Omega}_{0m}}\right)^{I} > \left(\frac{\Delta\Omega_{0m,max}}{\bar{\Omega}_{0m}}\right)^{U2}$$

  i.e. the anisotropy level was larger in the isotropic simulated data. In the rest 2/3 of the numerical experiments the anisotropy level was larger in the Union2 data. This is a clear indication that the anisotropy level, which found in the Union2 data, is not significant and it is consistent with statistical isotropy.

- The mean value and standard deviation of the maximum anisotropy level for the Union2 data are

$$\left(\frac{\Delta\Omega_{0m,max}}{\bar{\Omega}_{0m}}\right)^{U2} = 0.29 \pm 0.05 \tag{2.13}$$

  and for the simulated isotropic data

$$\left(\frac{\Delta\Omega_{0m,max}}{\bar{\Omega}_{0m}}\right)^{I} = 0.24 \pm 0.07 \tag{2.14}$$

  The error region which is described by equation (2.13) is not the error associated with the uncertainties of the supernova magnitudes as are the error regions of the 4^{th} and 5^{th} columns of Table 2.1. It corresponds to the range of the anisotropy level obtained when using 10 test axes to find the maximum anisotropy. Given the relatively small number of axes directions (10) considered in this

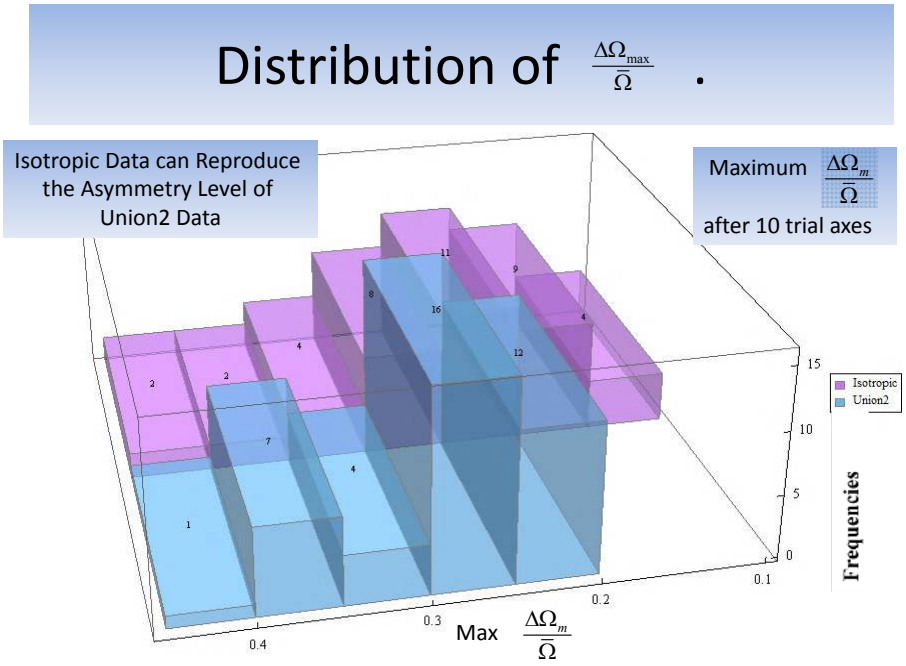

Figure 2.4: The distribution of the anisotropy levels $\left(\frac{\Delta\Omega_{0m,max}}{\bar{\Omega}_{0m}}\right)$ in the Union2 (front histogram) and simulated Isotropic datasets (back) using 10 random directions in each dataset. They show significant overlap which is a sign of consistency of the Union2 data with statistical isotropy.

part of the analysis, there is a significant variation of the level of maximum anisotropy identified in each run. This variation is described by the result of Eq. (2.13). In this case what we call 'the error' corresponds to the range of values $\frac{\Delta\Omega_{0m,max}}{\Omega_m}$ that is expected to be obtained in about 68% of the trials when our approach is implemented using 10 axes with random directions. In view of the fact that this variation is large enough to overlap significantly with the corresponding results obtained with the isotropic Monte Carlo data, it becomes clear that the anisotropy of the real data is consistent with statistical isotropy. It is clear from Eqs. (2.13) and (2.14) that there is a clear overlap at the 1σ level which also implies that the maximum anisotropy level of the Union2 data is consistent with statistical isotropy.

- The histograms indicating the distribution of $\frac{\Delta\Omega_{0m,max}}{\Omega_m}$ in each case are shown in Fig. 2.3 and they clearly show a significant overlap confirming also the consistency of the Union2 data with statistical isotropy.

Thus we have identified a direction of maximum anisotropy in the Union2 data and the level of this anisotropy is larger than about 70% of isotropic simulated datasets. However this level is clearly not enough to indicate inconsistency with statistical isotropy. Signals bellow 2σ are statistically negligible.

2.3 Preferred Axes from Other Observations and correlation

In this section we proceed to compare the direction of the identified maximum anisotropy with corresponding directions obtained with different, independent cosmological observations. The potential consistency among these independent anisotropy directions can dramatically increase the statistical significance of

Redshift Range	l	b	$\left(\frac{\Delta\Omega_{0m,max}}{\bar{\Omega}_{0m}}\right)^{U2}$	$\left(\frac{\Delta\Omega_{0m,max}}{\bar{\Omega}_{0m}}\right)^{I}$
0-0.2	$341^{\circ}{}^{+9}_{-22}$	$-17^{\circ}{}^{+28}_{-6}$	2.08 ± 0.22	4.28 ± 0.22
0-0.4	$301^{\circ}{}^{+16}_{-2}$	$-1^{\circ}{}^{+21}_{-15}$	1.81 ± 0.27	1.23 ± 0.15
0-0.6	$301^{\circ}{}^{+43}_{-14}$	$-4^{\circ}{}^{+23}_{-26}$	0.6 ± 0.1	0.48 ± 0.08
0-0.8	$327^{\circ}{}^{+22}_{-21}$	$37^{\circ}{}^{+4}_{-19}$	0.46 ± 0.07	0.36 ± 0.06
0-1.0	$301^{\circ}{}^{+35}_{-0}$	$-4^{\circ}{}^{+31}_{-0}$	0.45 ± 0.07	0.35 ± 0.06
0-1.2	$310^{\circ}{}^{+8}_{-4}$	$16^{\circ}{}^{+16}_{-11}$	0.43 ± 0.07	0.35 ± 0.06
0-1.4 (all data)	$309^{\circ}{}^{+23}_{-3}$	$18^{\circ}{}^{+11}_{-10}$	0.43 ± 0.06	0.36 ± 0.06

Table 2.1: Directions of maximum anisotropy for several redshift ranges of the Union2 data (see also Fig. 2.3). The level of maximum anisotropy for a typical isotropic simulated dataset is also shown in the 5^{th} column. The asymmetry of errors is largely due to the non-uniform distribution of the SnIa on the sky.

each one of them. In what follows we focus only on the kind of anomalies that appear to be related with the possible existence of a preferred axis. It is possible, a single mechanism could be responsible for seemingly unrelated anomalies. After all, before inflation it would be hard to imagine that the same mechanism could be responsible for both the generation of primordial fluctuations on all scales and for the horizon problem (two seemingly unrelated issues).

As discussed in the Chapter 1, there is a range of independent cosmological observations which indicate the existence of anisotropy axes. The consistency of these directions may be interpreted as a hint of the existence of an underlying physical or systematic cause which is common in all of these apparently independent axes. These cosmological observations along with their preferred directions and the corresponding references are summarized in Table 2.2. In what follows we focus on the preferred axes and ignore the information about the directionality of each axis. Had we considered also information about the directionality of axes the likelihood of the observed coincidence would be even smaller given that the directions of the bulk velocity flow, faster accelerating expansion and CMB dipole all appear to be towards the North Galactic Hemisphere.

Cosmological Obs.	l	b	**Reference**
SnIa Union2	309°	18°	This Study
CMB Dipole	264°	48°	[48]
Velocity Flows	282°	6°	[169] [42]
Quasar Alignment	267°	69°	[50]
CMB Octopole	308°	63°	[46]
CMB Quadrupole	240°	63°	[47] [46]
Mean	$278^{\circ} \pm 26^{\circ}$	$45^{\circ} \pm 27^{\circ}$	-

Table 2.2: Directions of Preferred axes from different cosmological observations.The precise directions may vary by a few degrees across the literature but our results are insensitive to such small variations.

The six axes corresponding to the observations of Table 2.2 are shown in Fig. 2.5 in galactic coordin-

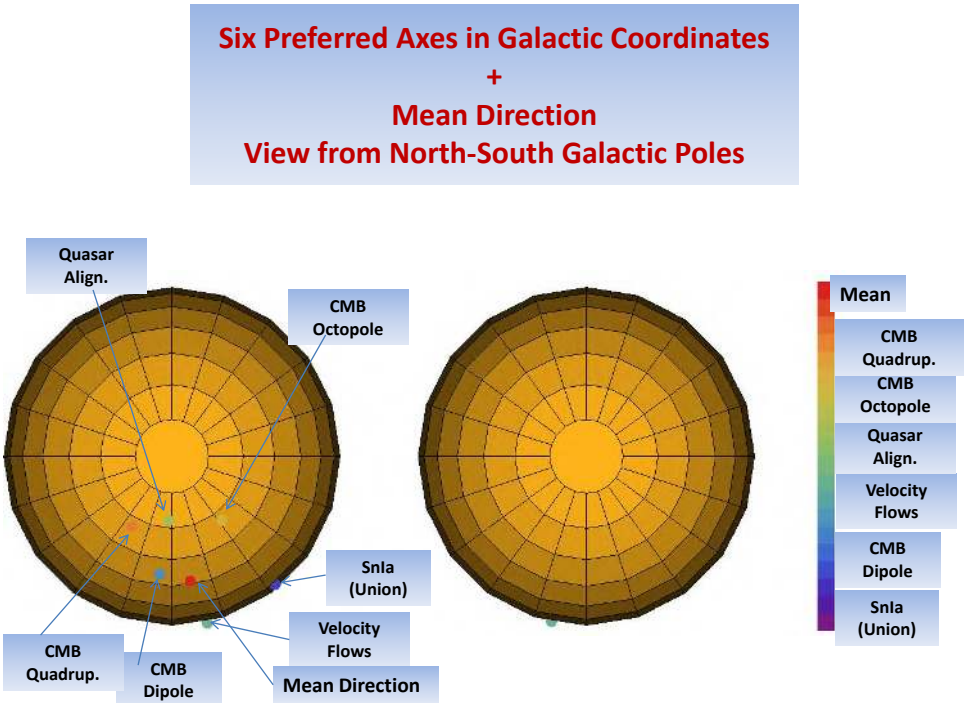

Figure 2.5: The coordinates of the preferred axes of Table 2.2 are located in a region less than a quarter of the North Galactic Hemisphere (left). The south galactic hemisphere (right) is also shown for completeness. The bulk flow direction is also visible in the south galactic hemisphere because it is close to the equator. The mean direction obtained in Table 2.2 with coordinates $(l, b) = (278°, 44°)$ is also shown.

ates. Clearly all coordinates are located in a relatively small part of the North Galactic Hemisphere (less than a quarter of it). It is straightforward to estimate the probability that six random points would lie in such a small region on a hemisphere. To obtain this estimate we evaluate the mean value of the inner product between all pairs of unit vectors corresponding to the preferred directions of Table 2.2 and compare with the corresponding mean value of six random directions on a hemisphere.

Thus we evaluate the quantity

$$< |cos\theta_{ij}| >=< |\hat{r}_i \cdot \hat{r}_j| >= \sum_{i,j=1,j\neq i}^{N} \frac{|\hat{r}_i \cdot \hat{r}_j|}{N(N-1)} \tag{2.15}$$

where in our case $N = 6$ and we take the absolute value in order to ignore the directionality of the axes. We apply Eq. (2.15) to both the real data of Table 2.2 and to 1000 realizations of six random points on the sphere obtained using Eq. (2.9). For the real data we find

$$< |\cos\theta_{ij}| >= 0.72 \tag{2.16}$$

while from the Monte Carlo uncorrelated data we obtain

$$< |\cos\theta_{ij}| >= 0.5 \pm 0.072 \tag{2.17}$$

Clearly, the value of $< |\cos\theta_{ij}| >$ of the real data is about 3σ away from the expected value if there were no correlation among the axes of Table 2.2. This is also seen in Fig. 2.6 which shows a histogram of the distribution of $< |\cos\theta_{ij}| >$ as obtained from the Monte Carlo data superposed with the value obtained

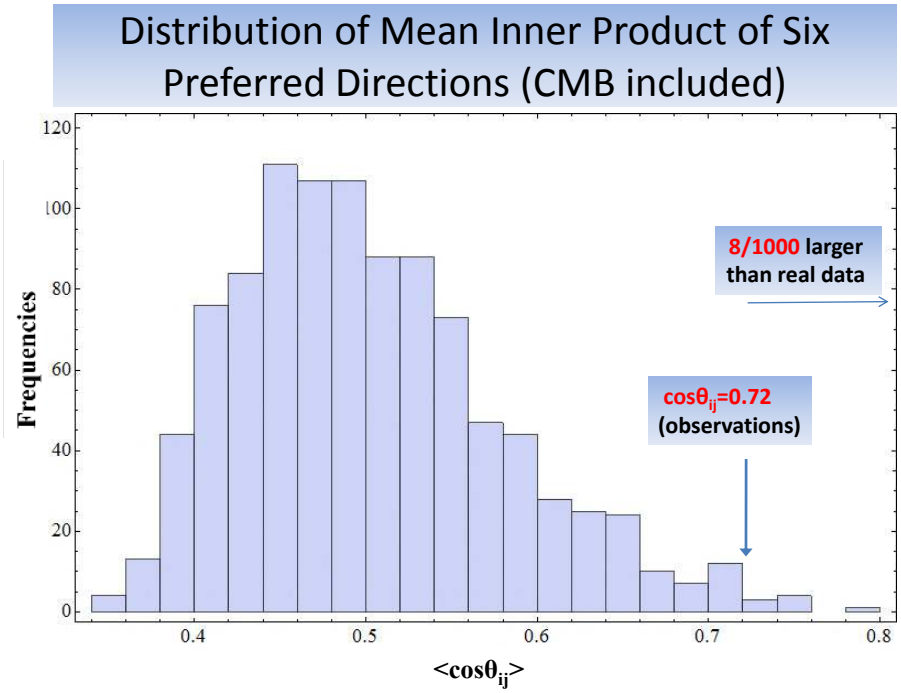

Figure 2.6: A histogram of the distribution of $< |cos\theta_{ij}| >$ as obtained from the Monte Carlo data, superposed with the value obtained from the real data of Table 2.2 (Eq. (2.16)). Less than 1% of the Monte Carlo data exceed the value corresponding to the real data.

from the real data (Eq. (2.16)). Clearly, less than 1% (0.8%) of the simulated data exceed the value of $< |cos\theta_{ij}| >$ obtained with the real data. Thus, the coincidence of these independent preferred axes in such a small angular region is a highly unlikely event.

Even if we ignore the axes related to the CMB, the coincidence of the three remaining axes in such a small angular region is still a relatively unlikely event with probability about 7% (Fig. 2.7). In fact for the three remaining axes of Table 2.2 we find

$$< |cos\theta_{ij}| >= 0.76 \tag{2.18}$$

while the Monte Carlo simulation gives

$$< |cos\theta_{ij}| >= 0.5 \pm 0.16 \tag{2.19}$$

i.e. the real data are about 1.5σ away from the Monte Carlo mean value.

Therefore, we conclude that even though each of the axes of Table 2.2 does not by itself constitute statistically significant evidence for a cosmological anisotropy, their coexistence in a relatively small angular region is a very unlikely event which is most probably attributed to either an undiscovered physical effect or to a common basic systematic error that has so far escaped attention.

2.4 Conclusions

The main conclusions of the study in this Chapter may be summarized as follows:

- The hemisphere of maximum accelerating expansion of the universe according to the Union2 data has a pole in the direction $(l, b) = (309^{\circ}{}^{+23}_{-3}, 18^{\circ}{}^{+11}_{-10})$ while the hemisphere of minimum acceleration is in the opposite direction.

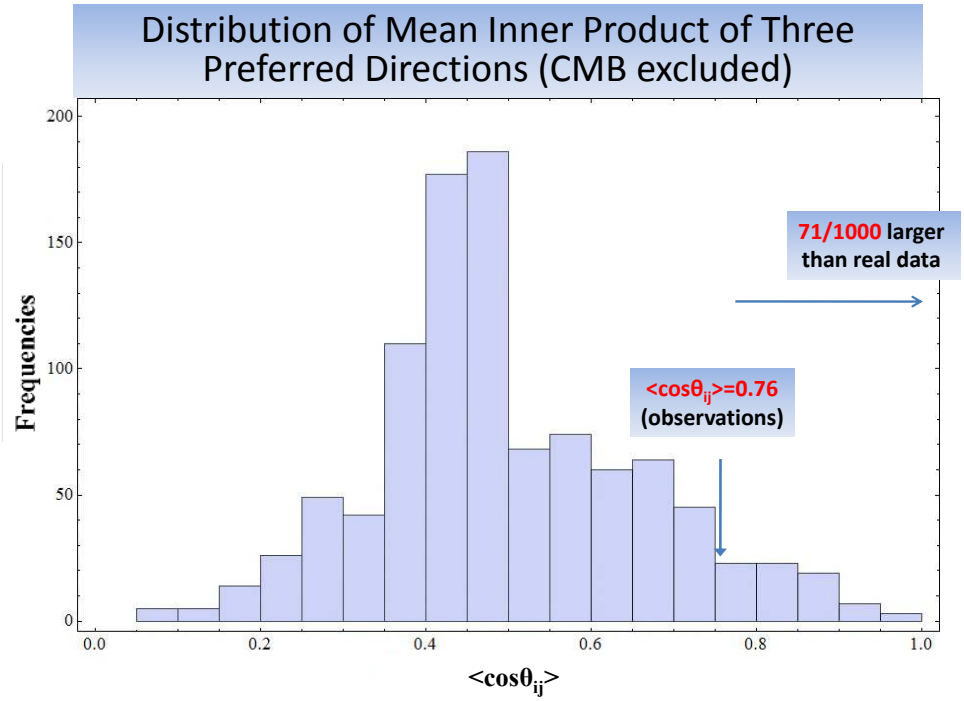

Figure 2.7: A histogram of the distribution of $< |cos\theta_{ij}| >$ as obtained from the Monte Carlo data, superposed with the value obtained from the real data of Table 2.2 excluding the axes related to the CMB (Eq. (2.18)). About 7% of the Monte Carlo data exceed the value corresponding to the real data.

- The level of anisotropy of the Union2 dataset is larger than about 70% of simulated datasets but it is still consistent with statistical isotropy.
- The coincidence of the anisotropy axes of Table 2.2 in a relatively small angular region is statistically a highly unlikely event that hints towards a physical or systematic connection among the axes of Table 2.2.

The combination of these cosmological observations may involve some a posteriori reasoning in the sense that there are other observations that show no hint of a preferred axis. However, most large scale cosmological observations may be analyzed in the context of a monopole, a dipole term (and higher moments) even if the significance level of a preferred direction is low and consistent with statistical isotropy. A real a posteriori reasoning would select some of these observations and points out that they point in similar directions. On the other hand, we have analyzed all large scale cosmological observations that we could find in the literature which involve a preferred cosmological direction (even if it is of low significance by itself) and point out that these directions are abnormally close to each other.

The confirmation of the existence of a cosmological preferred axis would constitute a breakthrough in cosmological research. Given the present status of cosmological observations such a confirmation is one of the most probable directions from which new physics may emerge.

Given the preliminary evidence for anisotropy discussed above, it is important to extend and intensify efforts for the possible confirmation of this evidence. Such confirmation may be achieved by extending the SnIa compilations towards larger datasets and deeper redshifts, such as the Pantheon sample (1048 spectroscopically confirmed SnIa) that span as uniformly as possible all directions in the sky. This is important in view of the fact that the Union2 compilation is less uniform and detailed in the south galactic hemisphere. In addition it is important to extend other cosmological data related to CMB low multipole moments, bulk velocity flows and quasar polarization to confirm the present existing evidence for preferred

axes in these datasets. Finally, alternative probes of cosmological anisotropies may be considered like higher CMB multipole moments, non-Gaussian features and polarization in the CMB maps, alignments of geometric features of various structures on large scales (there is already some preliminary evidence for alignment of handedness of spiral galaxies [170] along an axis not far from the directions of the other preferred axes of Table 2.2), alignment of optical polarization from various cosmological sources or studies based on cosmic parallax [171]. It is also important to derive observational signatures that can clearly distinguish between the various different origins of the preferred axes discussed in the introduction.

Chapter 3

Dilatonic Monopoles in 3+1 Dimensions and their Embeddings

According to ΛCDM model, the accelerating expansion of the universe can be explained by the presence of dark energy which fills the universe. Although the nature of dark energy is unknown, it is possible that consists of a scalar field. Generally, scalar fields can describe the variation of some cosmological constants, such as the fine structure constant or inhomogeneities in dark energy. Due to non-trivial configurations of the scalar fields, emerging topological defects, such as monopoles, are formed in a symmetry breaking phase transition during the evolution and expansion of the Universe. In this Chapter we investigate some properties of a dilatonic 't Hooft-Polyakov monopole, such as the stability in the presence of an external gauge field, through the minimization of its self energy. This is a special type of monopole where the scalar field couples directly to the gauge field tensors and thus fine structures constant is allowed to vary in space. The variation of the fine structure constant is a deviation of the standard model. Thus, this Chapter mentions to another direction of deviation from the Standard ΛCDM model as discussed in section 1.15.

We consider the 't Hooft-Polyakov monopole ansatz which contains a couple of radial functions $X(r)$ and $W(r)$. The function $X(r)$ is a part of the dilatonic function $B(\Phi^a)$ which couples with the electromagnetic term in Lagrangian and the function $W(r)$ is a part of the electromagnetic field. At small distances the scalar field $X(r)$ increases rapidly with distance, but the electromagnetic field $W(r)$ dominates, since it is much bigger. At bigger distances (far away from the monopole) the scalar field dominates and the gauge field tends to zero. Also, we consider the case where the monopole is embedded in a model with $O(4)$ symmetry. In order to determine the scalar and the gauge field, we minimize the perturbative energy of the monopole in a presence of a Gaussian external magnetic field. In this case, the monopole is unstable in every case. The existence of a dilatonic coupling in field theories, which predicts the existence of topological defects implies the presence of new properties for the defects.

3.1 Variation of fundamental constants through scalar fields

The spacetime variation of fundamental constants [172–174] like the gravitational constant [175] or the charges of gauge field interactions [176] is usually implemented at the Lagrangian level by promoting these constants to scalar fields [175–177]. Their dynamics are determined by potential and kinetic terms properly chosen to make the allowed variations consistent with current experiments and cosmological observations. For example in order to allow spacetime variation of the gravitational constant G and the fine structure constant $\alpha = e^2/\hbar c$ we may consider the replacement of the Einstein-Maxwell action

$$S = \int d^4x\sqrt{-g}\left(\frac{c^4}{16\pi G_0}R - \frac{1}{4\alpha_0}F_{\mu\nu}F^{\mu\nu} + \mathcal{L}_m\right) \tag{3.1}$$

by a generalization

$$S = \int d^4x\sqrt{-g}\left(\phi R - \omega_\phi \frac{\phi_{,\mu}\phi^{,\mu}}{\phi} - V_\phi(\phi) - e^{-2\psi}\frac{1}{4\alpha_0}F_{\mu\nu}F^{\mu\nu} - \frac{\omega_\psi}{2}\psi_{,\mu}\psi^{,\mu} - V_\psi(\psi)\right) \tag{3.2}$$

inspired from the Brans-Dicke (BD) theory [175] (gravitational part) and the Bekenstein, Sandvik, Barrow and Magueijo [177, 178] BSBM (electromagnetic part) actions. For free fields, the potentials take the forms

$$V(\phi) = \frac{1}{2}m_\phi^2\phi^2, \quad V(\psi) = \frac{1}{2}m_\psi^2\psi^2$$

In this action the gravitational constant G_0 is replaced by the dynamical BD field ϕ as $\phi = \frac{16\pi G}{c^4}$ and the fine structure constant is replaced by the dynamical BSBM field ψ as

$$\alpha = \alpha_0 e^{2\psi}$$

Laboratory experiments and astrophysical/cosmological observations impose limits on the allowed spacetime variations of G [179] and α [180]. These limits can be translated into constraints on the parameters ω_ϕ, ω_ψ and on the masses of the corresponding scalar fields. In the limit of infinite values of these parameters, the dynamics of the scalar fields freeze and the dynamics of the action (3.2) reduces to the Einstein-Maxwell action dynamics. The scalar fields ϕ and ψ emerge naturally in the context of string theory as *dilatons* [181, 182].

The BD parameter ω_ϕ is dimensionless while the BSBM parameter ω_ψ has dimensions of energy squared $m^2 \sim l^{-2}$ (in units where $\hbar = c = 1$). If the potentials are ignored ($m_\phi = m_\psi = 0$) then the experimental/observational constraints on ω_ϕ, ω_ψ are [179, 180, 183]

$$\omega_\phi > 4 \times 10^4 \tag{3.3}$$

$$(100MeV)^2 < \omega_\psi < M_{Pl}^2 \tag{3.4}$$

These constraints are based mainly on tests of the equivalence principle and fifth force search experiments as well as on solar system tests (for ω_ϕ). When the field masses are non-equal to zero, the above constraints are significantly relaxed [184].

In a cosmological setup both fields ϕ and ψ have been considered as possible dark energy candidates [24, 183, 185–190]. In the context of the recent possible detection of temporal [191–193] and spatial [194] variation of the fine structure constant α on cosmological scales (the α dipole [194, 195]), the field ψ has the potential to play a dual role: the role of inhomogeneous dark energy and the cause of α variation [24, 183, 185–189]. Cosmological models based on inhomogeneous dark energy are motivated by CMB and other cosmic anomalies [196] which may hint towards deviations from the cosmological principle on large cosmic scales [196–198].

Negative pressure and large sound velocity would tend to wipe out any inhomogeneities of this scalar field on all scales. Topologically non-trivial field configurations however have the potential to sustain such field inhomogeneities on cosmological scales. Such configurations have been considered as a possible mechanism to sustain inhomogeneous dark energy (topological quintessence [197–199]) possibly combined with correlated spatial variation of fine structure constant (extended topological quintessence [196, 200]). The later possibility is amplified by the observational fact that a dipole fit of the dark energy distribution using Type Ia supernovae leads to a dipole whose direction is only about 10° away from the α dipole direction [195]. Therefore, topological defects emerging due to topologically non-trivial configurations of the field ψ (dilatonic defects) have the potential to play an interesting role in cosmology [196, 201–205]. It is therefore interesting to investigate their field configuration properties which emerge as generalizations of the corresponding ordinary defects where there is no coupling between the scalar field and the gauge field kinetic term. These properties can be summarized as follows:

- The dilatonic coupling induces spatial variation of the gauge charge and a spatial variation of the effective mass of the scalar field. This can lead to modification of the scale of the gauged topological defect core.

- The stability of the gauged embedded defects [206–211] is significantly affected by the dilatonic coupling due to the spatial variation of the effective mass of the scalar field [204].
- The dilatonic coupling can lead to the formation of a scalar field condensate in the core of embedded defects because it can induce a local instability which is confined in the core region where the gauge fields are excited.
- Global embedded defects are unstable without the dilatonic coupling. However, in the presence of a dilatonic coupling and an external gauge field they can be locally stabilized in their core region.

The aim of the analysis in this Chapter is to demonstrate the existence of dilatonic defect solutions and investigate in some detail the above properties in the case of dilatonic monopoles.

3.2 Monopoles

3.2.1 Dilatonic 't Hooft-Polyakov Monopole

Monopoles are formed in field theories involving symmetry breaking phase transitions where the vacuum manifold is $M \cong S^2$ [212]. This is the case for example, when an $SO(3)$ symmetry gets spontaneously broken to $U(1)$. Consider for example the Lagrangian density

$$\boxed{\mathcal{L} = \frac{1}{2}\,(D_\mu\,\Phi^a)\,(D^\mu\,\Phi^a) - V(\Phi^a) - \frac{B(\Phi^a)}{4e_0^2}\,F^a_{\mu\nu}\,F^{a\mu\nu},} \tag{3.5}$$

describing an $O(3) \to O(2)$ symmetry breaking which accepts magnetic 't Hooft-Polyakov monopole solutions [213] with a dilatonic coupling $B(\Phi^a)$ to the gauge kinetic term of the Lagrangian. The dilatonic function $B(\Phi^a)$ describes a possible variation of the gauge charge and thus for the effective charge we have

$$e^2 = e_0^2/B(\Phi^a)$$

where $a = 1, 2, 3$ are internal indices. As usual, we define the non-Abelian gauge field strength by

$$F^a_{\mu\nu} = \partial_\mu A^a_\nu - \partial_\nu A^a_\mu + e_0 \epsilon^{a\,b\,c}\,A^b_\mu A^c_\nu, \tag{3.6}$$

The covariant derivatives are written in the usual form

$$D_\mu \Phi^a = \partial_\mu \Phi^a + e_0\,\epsilon^{a\,b\,c} a^b_\mu\,\Phi^c, \tag{3.7}$$

where $\epsilon^{a\,b\,c}$ is the Levi-Civita tensor. The symmetry breaking potential $V(\Phi^a)$ is of the usual form

$$V(\Phi^a) = \frac{\lambda}{4}\,\left(\Phi^a\,\Phi^a - \eta^2\right)^2 \tag{3.8}$$

The 't Hooft-Polyakov monopole ansatz [213] is of the form

$$\Phi^a(r) = X(r)\,\frac{x^a}{r}, \tag{3.9}$$

$$a^a_0(r) = 0, \tag{3.10}$$

$$a^a_i(r) = \epsilon_{iak}\,\frac{x_k}{e_0\,r^2}\,\Big(W(r) - 1\Big), \tag{3.11}$$

where x^a are the Cartesian coordinates and $r^2 = x^k\,x_k$. The radial functions $X(r)$ and $W(r)$ are obtained by minimization of the self-energy, i.e. the mass of the monopole which is defined as

$$\boxed{E = 4\,\pi \int_0^\infty dr\; r^2\;\rho} \tag{3.12}$$

or by solving the field equations. The energy density is obtained from the Lagrangian (3.5) as

$$\rho = T_{00} = -g_{00}\mathcal{L} \tag{3.13}$$

After a rescaling of the form

$$X \to \bar{X} = \eta X \tag{3.14}$$

$$r \to \bar{r} = \frac{r}{\eta e_0} \tag{3.15}$$

the energy density becomes (we omit the bar)

$$\rho = \frac{\eta}{e_0}\left[B(X)\left[\left(\frac{W'}{r}\right)^2 + \frac{1}{2}\left(\frac{1-W^2}{r^2}\right)^2\right] + \frac{(X')^2}{2} + \left(\frac{WX}{r}\right)^2 + \frac{\beta}{2}(1-X^2)^2\right] \tag{3.16}$$

where the prime denotes a derivative with respect to the dimensionless coordinate r. Using (3.12) we obtain the self energy

$$E = \frac{4\pi\eta}{e_0}\int_0^\infty dr\{\frac{r^2}{2}\left(\frac{dX}{dr}\right)^2 + X^2W^2 + \frac{\beta r^2}{2}(1-X^2)^2 + B(X)\left[\left(\frac{dW}{dr}\right)^2 + \frac{(1-W^2)^2}{2r^2}\right]\} \tag{3.17}$$

The dimensionless parameter β is defined as

$$\boxed{\beta \equiv \left(\frac{m_\Phi}{m_A}\right)^2} \tag{3.18}$$

where $m_\Phi = \frac{\sqrt{\lambda}\eta}{\sqrt{2}}$ and $m_A = e_0\,\eta$ are the masses of the scalar and gauge fields respectively. It is straightforward to find that

$$\beta = \frac{\lambda}{2e_0^2}$$

.

In order to find the solution of the field equations we minimize the energy (3.17) using the boundary conditions $X(r\to\infty) = 1$, $X(r\to 0) = 0$, $W(r\to\infty) = 0$ and $W(r\to 0) = 1$. Without loss of generality we normalize the effective charge e so that $B(r\to 0) = 1$.

In this section we parameterize the dilatonic coupling as

$$B(X) = e^{qX^2} \tag{3.19}$$

In order to obtain the dilatonic 't Hooft-Polyakov monopole solution, we minimize the energy (3.17) using the above boundary conditions, for several values for the parameters β and q. In Fig. 3.1 we show the resulting fields $X(r)$ and $W(r)$ when $(q=0,\beta=0.1)$, $(q=0,\beta=1)$, $(q=1,\beta=0.1)$, $(q=1,\beta=1)$. For each pair of the fields $X(r)$ and $W(r)$ we use the same color for the plot in order to be easily visible. As we observe, decreased value of β and increased value of q leads to a dilatonic monopole with larger core scale.

We have verified that a polynomial form of $B(X)$, such as

$$B(X) = 1 + qX^2$$

leads to similar results, which we present in Fig. 3.2.

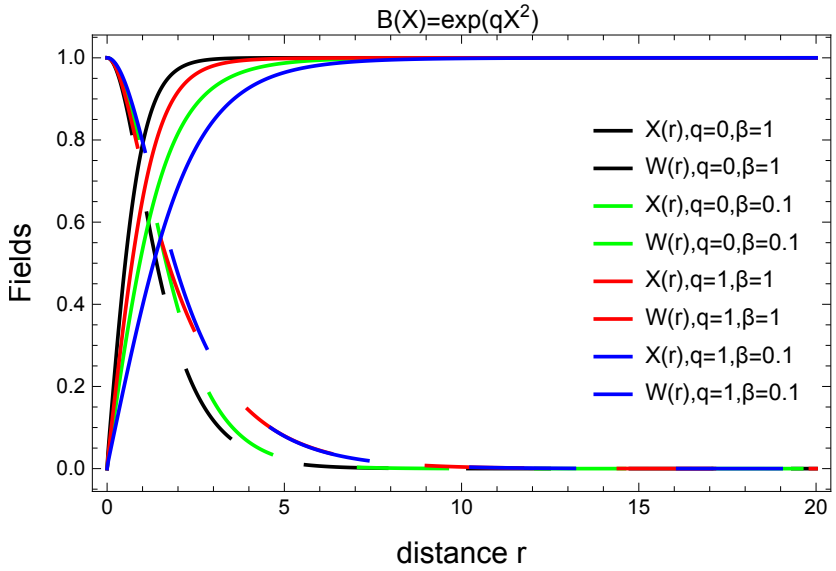

Figure 3.1: Solutions for the radial fields $X(r)$ (continuous lines) and $W(r)$ (dotted lines) for the dilatonic magnetic monopole when the dilatonic function is $B(X) = e^{qX^2}$, for several values of the parameters β and q. The same color in the fields corresponds to the same values of β and q. At small distances the scalar field increases rapidly, while the gauge field decreases rapidly. At big enough distances the fields are stabilized, the scalar field $X(r)$ dominates, while the gauge field $W(r)$ is negligible. Notice that, when q is constant, as β increases the slope of the curves increases and the fields acquire their vacuum expectation values at smaller distance r.

3.2.2 Embedded Dilatonic Monopole

We now consider the embedding of the gauge monopole [213] in a model with $O(4)$ symmetry [210, 214]. This is achieved by adding in the scalar Φ one more component (becomes a four-vector) as

$$\boxed{\Phi^4(r) = g(r)} \tag{3.20}$$

The embedded monopole potential (semilocal monopole) takes the form

$$\boxed{V(\Phi^a) = \frac{\lambda}{4}\left(X(r)^2 + g(r)^2 - \eta^2\right)^2} \tag{3.21}$$

Using the methods and arguments of Ref. [210] it is straightforward to show that the embedded dilatonic monopole solution in this model is unstable for all values of parameters. The instability persists because the embedded gauge group $O(3)$ acts trivially on the additional field component $\Phi^4(r) = g(r)$. In this case it may be shown that there is a smooth sequence of field configurations parametrized by a parameter ξ with energy monotonically decreasing with ξ that starts from the embedded monopole configuration for $\xi = 0$ and ends at the vacuum for $\xi = \pi/2$. In view of this simple and powerful result we omit presenting the perturbative energy minimization analysis of the embedded dilatonic monopole which involves minimization of the embedded gauged monopole energy corresponding to the energy density

$$\boxed{\rho = \frac{\eta}{e_0}\left[B(X)\left[\left(\frac{W'}{r}\right)^2 + \frac{1}{2}\left(\frac{1-W^2}{r^2}\right)^2\right] + \frac{(X')^2}{2} + \left(\frac{WX}{r}\right)^2 + \frac{(g')^2}{2} + \frac{\beta}{2}(1-X^2-g^2)^2\right]} \tag{3.22}$$

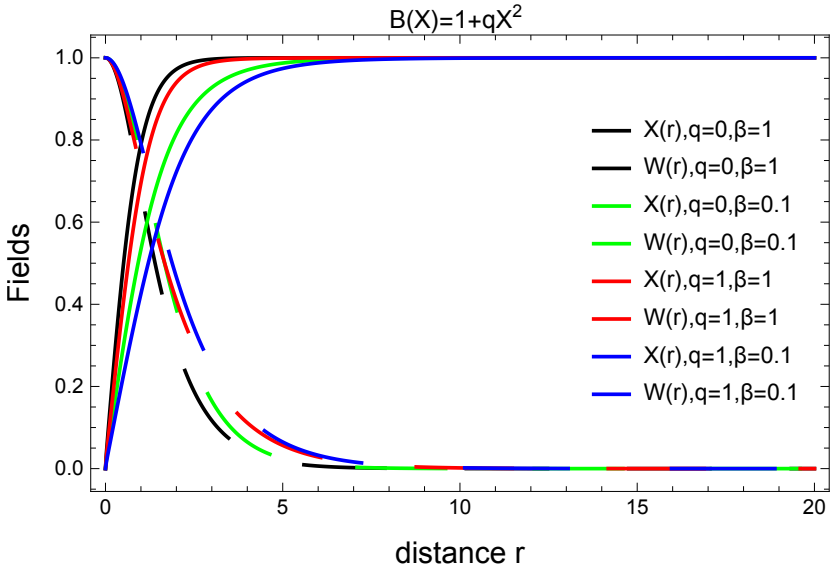

Figure 3.2: Solutions for $X(r)$ (continuous lines) and $W(r)$ (dotted lines) for the dilatonic embedded monopole when the dilatonic function is $B(X) = 1 + qX^2$, for the same values of the parameters β and q as in Fig. 3.1. The same color in the fields corresponds to the same parameter values of β and q. Qualitatively, the fields have the same behaviour, as in Fig. 3.1. The fields stabilized to their vacuum expectation values and as β increases the fields acquire their vacuum expectation values for smaller r.

Such an analysis simply verifies the anticipated instability for all values of the parameters β and q. The corresponding analysis for the embedded dilatonic monopole also leads to instability either using the approach of Ref. [210], or through direct energy minimization of the density

$$\boxed{\rho = \frac{\eta}{e_0}\left[B(X)(e^{-\frac{r^2}{r_0^2}})^2 + \frac{(X')^2}{2} + \left(\frac{X}{r}\right)^2 + \frac{(g')^2}{2} + \frac{\beta}{2}(1 - X^2 - g^2)^2\right]} \tag{3.23}$$

where we have assumed a similar external gauge field as in the previous section. The field configurations that minimize the above energy using boundary conditions at $r = 10$ ($X(r = 10) = 1$) are shown in Fig. 3.3.

Notice that as expected the instability tends to expand outwards leading to the vacuum in regions away from the external field region. However, for $r < r_0$ where the external field is significant, the field remains out of the vacuum due to the effects of the external field which stabilizes locally the embedded global monopole.

3.3 Physical Effects

In the presence of a large enough dilatonic coupling the corresponding stability region increases arbitrarily as discussed in section 3.2. We anticipate that this stability improvement will persist even for the experimentally measured parameter value of β. It is therefore important to identify the required value of the dilatonic coupling q for stability of the dilatonic monopole for the measured values of β. We point out that if the required value of q for stability is consistent with current experiments, then the possibility of formation of metastable topological defects in accelerators and/or in the early universe arises. In this case, we anticipate the existence of interesting signatures and effects in both accelerator and cosmological setups. In particular, such effects include:

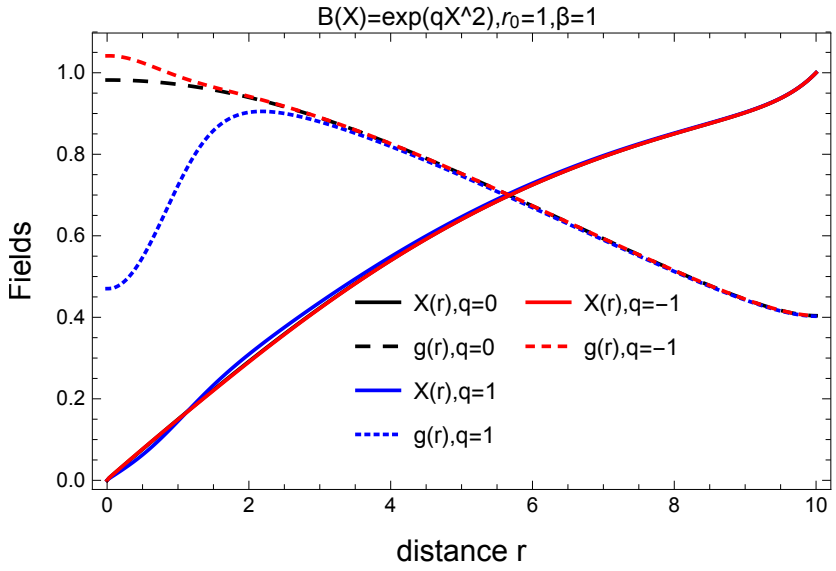

Figure 3.3: The energy minimizing fields $g(r)$ and $X(r)$ as a function of distance r for embedded dilatonic monopole, in the presence of a Gaussian external "magnetic" field $e^{-\frac{r^2}{r_0^2}}$ for several values of the parameter q, when $\beta = 1$ and $r_0 = 2$. We assume an exponential dilatonic coupling $B(X) = e^{qX^2}$. It is clear that the fields always change, which means that the fields are not stabilized and the embedded dilatonic monopole is always unstable. Only in small distances, near the core, where the external field is significant, the embedded dilatonic monopole is locally stable.

- **Primordial Magnetic Fields:** A gas of metastable electroweak segments formed during the electroweak phase transition is necessarily accompanied by a gas of electroweak monopoles. The eventual collapse and disappearance of electroweak strings removes all the electroweak monopoles but the long range magnetic field emanating from the monopoles is expected to remain trapped in the cosmological plasma. This will then lead to a residual primordial magnetic field in the present universe. An estimate of the average flux of this primordial magnetic field was obtained in [215, 216].

- **Generation of Baryon Number-Cosmic Rays:** A gas of metastable electroweak string segments and loops would in general, contain some helicity density of the Z-field. So when the electroweak strings eventually annihilate, it is possible that the helicity gets converted into baryon number [216]. In more exotic models (such as this), strings at the electroweak scale that were stable and had superconducting properties, could also be responsible for baryogenesis [217] and the presence of primary antiprotons in cosmic rays [218].

- **Variation of Fine Structure Constant:** A dilatonic coupling in models involving electromagnetism like the electroweak model, leads naturally to the possibility of variation of the fine structure constant α. In the presence of a metastable dilatonic electroweak string this variation is anticipated to be spatial on the scale of the core of the dilatonic defect. Such microscopic localized variation of α could be detectable in accelerators where either metastable dilatonic electroweak strings or dilaton-Higgs particles are produced and decay. This effect becomes more interesting in view of the recent claim for a 4σ detection of spatial variation of α on cosmological scales obtained from careful analysis of quasar absorption spectra [194].

- **Signatures in accelerators: Dilatonic Dumbells** The production of solitonic states in particle accelerators as well as their experimental signatures constitute open issues that become particularly important in the context of the existence of metastable electroweak strings. A rotating electroweak

monopole-antimonopole pair connected by a Z-string and stabilized by a centrifugal barrier is known as a dumbbell. The decay signature of such a metastable system was first studied by Nambu [219] who estimated the energy and angular momentum of such a system as well as its lifetime and decay products. In the context of a dilatonic coupling such a system may get stabilized not only due to its angular momentum but also at the field theoretic level. Thus, we anticipate an increased lifetime and a cleaner signature in accelerators.

The role of topological defects such as electroweak strings in Cosmology depends on their abundance during and after the electroweak phase transition. If this abundance is negligible, electroweak strings may at best only be relevant in future accelerator experiments. Such relevance is expected to increase significantly in the presence of a dilatonic coupling which is anticipated to improve their stability.

3.4 Conclusions-Discussion

Topological defects are formed in theories where the scalar field couples to the gauge field strength tensor (dilatonic defects) and have significant novel properties. In particular, some of them are

- Their core scales can be significantly larger than the corresponding ordinary defects with minimal coupling.
- The corresponding embedded defects have modified stability properties.
- The instability of dilatonic defects in the presence of an external gauge field does not proceed towards the vacuum. Instead it proceeds towards a field configuration which deviates from the vacuum in the region where the external gauge field is excited. This configuration may be interpreted as a local stabilization of the global embedded defects.
- The instability of the gauged embedded vortex may proceed (for certain parameter values) towards a scalar field condensate where the instability is excited but is confined to the region of the embedded defect core.

In conclusion, the existence of a dilatonic coupling in field theories predicting the existence of topological defects implies the presence of interesting new properties for the predicted defects which makes these models worth of further investigation.

Chapter 4

Bounds from scalar coupling to electromagnetism

In the course of this Chapter we review a possible non-minimal coupling (dilatonic) of a scalar field (axion like particle) to electromagnetism, through experimental and observational constraints. Such a coupling is motivated from recent quasar spectrum observations that indicate a possible spatial and/or temporal variation of the fine-structure constant. We consider a dilatonic coupling of the form $B_F(\phi) = 1 + g\phi$. The strongest bound on the coupling parameter g is derived from weak equivalence principle tests, which impose $g < 1.6 \times 10^{-17} GeV^{-1}$. This constraint is strong enough to rule out this class of models as a cause for an observable cosmological variation of the fine structure constant unless a chameleon mechanism is implemented. We argue that a similar coupling occurs in chameleon cosmology, a candidate dark energy particle and we estimate the cosmological consequences of both effects. It should be clarified that this class of models is not necessarily ruled out in the presence of a chameleon mechanism which can freeze the dynamics of the scalar field in high density laboratory regions.

Since the cosmological constant problem remains unsolved, scalar field models have been proposed in the past either to adjust dynamically the value of the vacuum energy in different versions or to endow the dark energy of a convenient dynamics with the notion of quintessence [220]. Quintessence models make use of a homogeneous, time dependent minimally coupled scalar field ϕ whose dynamics is determined by a specially designed potential $V(\phi)$ inducing the appropriate time dependence of the field equation of state $w(z) = \frac{P(\phi)}{\rho(\phi)}$ [20]. Recent analyses reveals that scalar field models fit better the cosmological data than the ΛCDM model at a confidence level of around 4σ [221]. In particular, in Section 4.4 of this Chapter we consider a quintessence dark energy model with scalar field. We find that, in the presence of a scalar field which is coupled with the electromagnetism, when electrostatic energy dominates against magnetostatic energy, the Big Crunch singularity occurs later. Finally, we connect theoretically these models with the variation of the fine structure constant and we compare them with the current observational status.

The contexts of this chapter consist a deviation from the Standard ΛCDM model as we have pointed in section 1.15, since it assumes variation of the fine structure constant and its constraints. Deviation from the ΛCDM model is any research on the quintessence model, since the parameter of equation of state is different than $w = -1$. We have discussed these aspects of Standard model in section 1.15.

4.1 Variation of fine structure constant through scalar fields

There are recent observational indications that the fine structure constant may be varying spatially and/or temporally [180, 222–227] on cosmological scales. Such a variation could be due to a scalar field ϕ non-minimally coupled to electromagnetism. This field could also play the role of quintessence inducing the observed accelerating expansion of the universe [228–231]. The possible spatial variation of the fine

structure constant α would require a corresponding spatial variation of the scalar field which could be supported by non-trivial topological properties of the field configuration [2, 196, 200, 232]. The variation of the fine structure constant is given by the relation

$$\frac{\Delta\alpha}{\alpha} = \frac{\alpha - \alpha_0}{\alpha_0}$$

where α_0 is the present value. For a spatial variation, the value of $\frac{\Delta\alpha}{\alpha}$ is of order $O(10^{-5})$ [194].

We focus on cases where scalar particles or chameleons are subject to coupling with the electromagnetic tensor [233]. We consider a Lagrangian interaction term of the form

$$\boxed{L_{coupling} = -\frac{1}{4}B_F(\phi)F_{\mu\nu}F^{\mu\nu}} \tag{4.1}$$

where the coupling function $B_F(\phi)$ is known as the gauge kinetic function. We consider that $B_F(\phi)$ evolves linearly with the scalar field as

$$\boxed{B_F(\phi) = 1 + g\phi} \tag{4.2}$$

The scalar field can be a axion-like particle (ALP), chameleon or quintessence, while g (which has units of inverse energy) is the coupling constant, which must be constrained experimentally.

Axions are particles, whose existence helps to solve the strong CP (Charge+Parity) problem [1]. Also, they are dark matter candidate particles [234, 235] because they interact at most gravitationally and can induce the required dark matter density of the universe. Their mass and their coupling to electromagnetism is constrained by laboratory, cosmological and astrophysical bounds [236]. For consistency with the observed accelerating expansion rate, the required magnitude of the coupling g of the scalar field is described for example in Ref. [190, 237]. It is therefore interesting to inquire if such values of the coupling are consistent with local experiments and astrophysical observations.

4.2 Electromagnetism and optical properties of light

We focus on the class of experiments which have been designed to constrain or detect the interaction between scalar ALPs and photons. Generally, a positive signal from these experiments can determine mass, parity and coupling strength to electromagnetism of the hypothetical scalar particle. If ALPs are scalar, this coupling is described by the Lagrangian term [238]

$$L_{scalar} = -\frac{g}{4}\phi F_{\mu\nu}F^{\mu\nu} \tag{4.3}$$

where the product $F_{\mu\nu}F^{\mu\nu}$ is equal to

$$F_{\mu\nu}F^{\mu\nu} = 2\left(\mathbf{B}^2 - \mathbf{E}^2\right) \tag{4.4}$$

If we compare the relations (4.1), (4.2) and (4.3), it is easy to derive that

$$L_{coupling} = L_{scalar} - \frac{1}{4}F_{\mu\nu}F^{\mu\nu} \tag{4.5}$$

If ALPs are pseudoscalar, the corresponding Lagrangian term is

$$L_{pseudoscalar} = -\frac{g}{4}\phi F_{\mu\nu}\widetilde{F}^{\mu\nu} \tag{4.6}$$

[1] According to quantum chromodynamics there could be a violation of CP symmetry in the strong interactions. However, no violation of the CP-symmetry is known to have occurred in experiments.The strong CP problem is sometimes regarded as an unsolved problem in physics. The most acceptable solution for this problem is the Peccei–Quinn theory, which includes the existence of axions.

where the product $F_{\mu\nu}\widetilde{F}^{\mu\nu}$ is

$$F_{\mu\nu}\widetilde{F}^{\mu\nu} = -2\mathbf{E}\cdot\mathbf{B} \tag{4.7}$$

The tensor $\widetilde{F}^{\mu\nu}$ is the dual electromagnetic tensor which violates parity and time reversal invariance. It conserves charge conjugation invariance, so it violates CP symmetry and solves the CP problem. In both cases (scalar and pseudoscalar), the expression for the coupling between ALPs and photons is given by the formula [239]

$$\boxed{g \equiv \frac{1}{M} \approx \frac{\alpha}{2\pi}\frac{m}{f_\alpha}} \tag{4.8}$$

where $\alpha \simeq 1/137$ is the fine structure constant, m the mass of the scalar or pseudoscalar particle and f_α the symmetry breaking scale (or decay constant). As the decay constant increases, the coupling parameter g decreases. However, it must be less than $f_\alpha \sim 10^{-16}GeV$ [240], because this would lead to closed universe, which disagrees with recent cosmological observations.

ALPs can have *odd parity* (for pseudoscalar particles), which have their sign flipped by spatial inversion or *even parity* (for scalar particles), which do not change upon spatial inversion and can couple to photons. There are four classes of experiments attempting to detect such particles. The first class is based on the so-called haloscope [241]. In this experiment, ALPs from galactic halo are converted to photons in a cavity with a powerful magnetic field. The second category comes from the so-called helioscope [242], which corresponds to weakly interacting slim particles (WISPs) which are emitted by the Sun. The third class involves searches for ALPs which couple to photos and induce in a laser beam, which propagates in a magnetic field, optical dichroism and birefringence [243]. The fourth class includes photon regeneration experiments [244], such as GammeV [238], BFRT [245], OSCAR [246] and others which are described bellow. A possible signal currently exists from the third class of experiments (PVLAS). For a brief but not complete review, the reader can see Ref. [247].

Most of these experiments are based on fundamental optical properties of the materials affecting their interaction with polarized light, such as [248, 249]

- **optical rotation (activity)**, which is the turning of the plane of linearly polarized light about the direction of motion as the light travels through materials. It is due to a selective attenuation of one polarization component [243].
- **birefringence**, which is the optical property of a material having a refractive index that depends on the polarization and direction of light propagation [250]. The birefringence is often quantified as the maximum difference between refractive indices exhibited by the material.
- **dichroism**, where someone can distinguish two related but distinct meanings [251]. Dichroism is the phenomenon where light rays, having different polarizations are absorbed by different amounts, or where a visible light can be split up into distinct beams of different wavelengths [252, 253].
- **ellipticity**, which is the phenomenon where the polarization of electromagnetic radiation, such that the tip of the electric field vector, describes an ellipse in any fixed plane intersecting the direction of propagation [254]. It is due to selective retardation of one polarization component. In that case the direction of the rotation and the specified polarization, may be either clockwise or counterclockwise.

4.3 Constrains on scalar coupling from experiments

4.3.1 PVLAS experiment

The PVLAS experiment takes place at the INFN Legnaro National Laboratory, near Padua in Italy. In the year 2006, the scientific team reported a positive signal for a zero-spin particle [243]. This experiment is based on the fact that vacuum in the presence of the scalar field becomes birefringent and dichroic [255], when applying an external magnetic field [256]. So, when a linear polarized beam is propagated in a Fabry-Perot cavity with strong magnetic field, the plane of polarization is rotated by an angle α.

The polarized laser beam has wavelength $\lambda = 1064\ nm$ or $\lambda = 532\ nm$ and enters in a high transverse magnetic field of order $5T$, in a cavity. It passed 44000 times through a 1 m long magnet. The components of the laser polarization had a slight weakening. This effect is observed at varying levels if the polarization is transverse or parallel to the external magnetic field. The rotation angle was found to be

$$\alpha = (3.9 \pm 0.5) \times 10^{-12}\ rad/pass$$

The signal was associated to a neutral, light boson which is produced by a two-photon vertex. The amplitude of the dichroism, which depends on the coupling constant g, was estimated as [238]

$$g \sim 2.5 \times 10^{-6}\ GeV^{-1}$$

The mass of the particle was estimated as $m_\phi \sim 1.2meV$ but its parity was undetermined, although the sign of the phase shift hints towards even parity, which is evidence for the existence of a scalar particle.

Also, this signal could be explained by assuming the existence of millicharged particles [257]. They are light particles with electric charge $q \ll e$, where e is the elementary (electron/proton) charge and appear in field theories, but they aren't part of the Standard Model [258]. The PVLAS experiment was repeated without detection of any signal [259]. Thus, its results are currently under question.

4.3.2 GammeV experiment

The GammeV experiment [238] takes place at Fermilab and is divided into two similar experiments. They are 'light shining through a wall' experiments which are based on the Primakoff effect [2], where a couple of photons with high energy interact and produce ALP. One photon is real from the laser field and the other one is virtual from an external magnetic field.

The GammeV experiment is a gamma (γ) to milli-eV ALP search. The mass of this particle is expected to be of order meV. A scalar particle couples to photons with a polarization orthogonal to the magnetic field [244, 260]. The photon beam is blocked by the wall, but the ALP hardly interact with the wall and passes through the wall. The particles are converted again to photons in the magnetic field and the regenerated photons are counted with an appropriate detector. The primary and the regenerated photons have the same properties. The photon regeneration experiment is based on different effects of light, compared to the optical rotation experiment. In the first, the appearance of light beyond the wall is detected, while in the second, perturbations of the initial beam are detected.

The photon to scalar particle conversion probability (and the reverse process) is given by the relation

$$\boxed{P_{\gamma \leftrightarrow s} = \frac{1}{4u}\left(gBL\sin\theta\right)^2\left(\frac{2}{qL}\sin\frac{qL}{2}\right)^2} \tag{4.9}$$

where the transverse magnetic field B has length L, while θ is the angle between the laser polarization and the magnetic field. It is obvious from Eq. (4.9) that the direction of polarization must be perpendicular to magnetic field for optimum conversion. For pseudoscalar particles it must be parallel to magnetic field, because the probability (4.9) includes the term $\cos\theta$ instead of $\sin\theta$. In Eq. (4.9) the coupling constant is denoted with g, while u is the velocity of the scalar particle and q the momentum transfer. The probability becomes maximum when $q \cdot L \to 0$, i.e. when the particle has very little mass compared to its energy ($m \ll \omega$). In order to increase the convention probability we must use strong, long range magnetic fields. The momentum transfer is proportional to the square mass of the particle

$$q = \mid \omega - \sqrt{\omega^2 - m^2} \mid \simeq \frac{1}{2}\frac{m^2}{\omega} \tag{4.10}$$

[2] The Primakoff effect is the production of bosons, when high energy photons interact with an atomic nucleus. Also, include the rotation of the plane of polarization when a linearly polarized beam passes through a magnetic field. The beam has many directions of polarization. The Primakoff effect reduces the parallel component of polarised light to the magnetic field and leaves the perpendicular component to the magnetic field unchanged. This phenomenon can occur in a reverse manner (a particle can decay to a couple of photons).

We can split the above probability (4.9) in two phases. The first one is the probability in the production region

$$P_{\gamma\to s} = \frac{(2gB\omega sin\theta)^2}{m_\alpha^4}\left(\sin\frac{L_1 m_\alpha^2}{4\omega}\right)^2 \tag{4.11}$$

where the photons are converted to scalar particles [261]. The probability increases with the number of passes through the wall. The second is the probability in the regeneration region

$$P_{s\to\gamma} = \frac{(2gB\omega sin\theta)^2}{m_\alpha^4}\left(\sin\frac{L_2 m_\alpha^2}{4\omega}\right)^2 \tag{4.12}$$

where the scalars are reconverted to photons. This probability increases by using a resonant cavity in the regeneration region. The expected counting rate of photons in the detector is of the form

$$\boxed{\frac{dN_\gamma}{dt} = \frac{P}{\omega}\eta\left(P_{\gamma\leftrightarrow s}\right)^2} \tag{4.13}$$

where η is the detector efficiency and P is the optical power.

Short laser pulses of wavelength $\lambda = 532\ nm$ were used in the experiment and the external magnetic field was $5T$ [238]. The weakly-interacting ALP interpretation of the PVLAS data was excluded at more than 5σ by the GammeV data for scalar particles. No events were found above the background and thus a bound is defined for the coupling [238] which is

$$g \leq 3.1 \times 10^{-7} GeV^{-1}$$

This limit is the mean value of two configurations for the magnetic field and it is valid for small values of the mass m_ϕ (bellow meV). Generally, the coupling depends on the mass of the scalar particle, but when the mass is small (bellow few meV), the coupling is almost unchanged.

4.3.3 Fifth force experiments

The coupling between a scalar particle and a couple of photons $\phi\gamma\gamma$ [262], which can be described with the Lagrangian term (4.3) leads to the existence of long-range non-Newtonian forces (fifth force). These forces are bounded by Eötvös type experiments and they don't violate the Equivalence Principle [3]. The relative difference between inertial and gravitational mass is less than 10^{-12} [263] and drives to constrains on the coupling constant. The Lagrangian contains a interaction term of the form

$$L_{interaction} = -\frac{g\phi}{4}F_{\mu\nu}F^{\mu\nu} - L_2 \tag{4.14}$$

The above term of the Lagrangian density induces radiatively a coupling to charged particles, such as electrons or protons. The additional term in Lagrangian density is $L_2 = y\phi\overline{\Psi}\Psi$ where y is the Yukawa coupling and Ψ is the field of the charged particle. The authors of Ref. [262] used existing experimental limits to constrain the coupling constant g as a function of the mass of the scalar field m_ϕ. These limits emerge from a micromechanical resonator which measures the Casimir force between parallel plates [264, 265] (two mirrors in a vacuum will be attracted to each other) placed a few nanometers apart from experiments with torsion pendulum and a rotating attractor [266] and from experiments which use torsion-balance [267]. Using the last class of experiments, the authors of Ref. [262] reached very stringent results when the field satisfies the condition $\Lambda \gg m_p$ (Λ is the cosmological constant and m_p the proton-mass). When $m_\phi \sim meV$, they found that [267]

$$g < 1.6 \times 10^{-17} GeV^{-1}$$

[3] The equivalence principle is any of several related concepts dealing with the equivalence of gravitational and inertial mass. Albert Einstein observed that the gravitational "force" as experienced locally while standing on a massive body (such as the Earth) is the same as the pseudo-force experienced by an observer in a non-inertial (accelerated) frame of reference.

This is a stringent limit and the terrestrial experiments don't have until now, the sensitivity to detect some event of this order.

Scalar particles with almost zero mass can lead not only to long-range forces (in the same manner as quintessence), but also to variation of fundamental constants [189]. Bekenstein type models with a scalar field ϕ that affects the electromagnetic permeability, lead to variations of the effective fine structure constant up to very high red-shifts. The coupling between scalar field and electromagnetic tensor of the form

$$\beta_{F^2}(\phi/M)F_{\mu\nu}F^{\mu\nu} \equiv \frac{g}{4}\phi F_{\mu\nu}F^{\mu\nu} \tag{4.15}$$

can lead to a time variation [268] of the fine structure constant due to the time variation of the scalar field. The scalar field ϕ is expected to have a variation at the present time (in cosmological timescales) of order M_{Pl} and there are several observations to bound such variation. From the Oklo natural reactor in Gabon [269], the researchers analyzed the isotope ratios of $^{149}Sm/^{147}Sm$ in the natural uranium fission reactor (mine) that operated 1.8 billion years ago. The isotopic abundances lead to $|\dot{\alpha}/\alpha| < 10^{-15}\ yr^{-1}$ over the last 1.8 billion years and constrains the coupling as

$$g \leq 4 \times 10^{-6}\left(\frac{H_0}{\langle\dot{\phi}\rangle}\right) \tag{4.16}$$

where $H_0 \sim 10^{-33}eV$ and $\langle\dot{\phi}\rangle$ is the mean rate of change of ϕ in the above range of time.

4.3.4 BFRT experiment

One of the first photon regeneration experiments took place in Brookhaven National Laboratory [245]. In this experiment the beam had wavelength $\lambda = 514\ nm$ and the magnetic field was $3.7T$. The search for scalar particles requires the laser polarization to be perpendicular to the magnetic field. The photons are produced during the regeneration and detected by sensitive photocathode of a photomultiplier tube (PMT) [270]. For 220 minutes the laser was on and subsequently for 220 minutes the laser was off. They didn't observe significant difference between laser on and laser off states. Thus, the authors of Ref. [245, 271] in the absence of any signal estimated an upper bound for the coupling constant g, which is

$$g < 6.7 \times 10^{-7}GeV^{-1}$$

at 90% confidence level. This limit is applicable when the scalar particle is very light with mass $m < 10^{-3}\ eV$. If we assume the mass of the scalar particle in the range $1\ meV \leq m_\phi \leq 1.5\ meV$ we can combine the PVLAS signal and the BFRT constraint as [271]

$$1.7 \times 10^{-6}GeV^{-1} \leq g \leq 5 \times 10^{-6}GeV^{-1}$$

4.3.5 OSCAR experiment

The OSCAR experiment takes place at LHC and it is a photon regeneration experiment which uses two LHC dipole magnets. The laser beam has wavelength $\lambda = 514\ nm$ and the dipole superconducting magnets are cooled down to $1.9K$ [246]. The innovation in this experiment is that they use a buffer of neutral gas as a resonant amplifier medium. The conversion probability, is divided by the refractive index $n = \sqrt{\varepsilon}$ as

$$P_{\gamma\leftrightarrow s} = \frac{1}{4u\sqrt{\varepsilon}}(gBL)^2\left(\frac{2}{qL}\sin\frac{qL}{2}\right)^2 \tag{4.17}$$

while the expected counting rate is given by Eq. (4.13). The device of the OSCAR experiment has not recorded any signal and the upper limit of the coupling constant is estimated as [272]

$$g < 1.15 \times 10^{-7}GeV^{-1}$$

experiment	g($\times GeV^{-1}$)	m_ϕ	effect
PVLAS [238]	$\sim 2.5 \times 10^{-6}$	$\sim 1.2meV$	birefrigence
GammeV [238]	$\leq 3.1 \times 10^{-7}$	$\leq 1meV$	LSW
Fifth force [267]	$< 1.6 \times 10^{-17}$	$\sim meV$	Casimir force
BFRT [271]	$< 6.7 \times 10^{-7}$	$\leq 1meV$	LSW
OSCAR [273]	$< 5.76 \times 10^{-8}$	massless	LSW
ALPS [276]	$< 7 \times 10^{-8}$	massless	LSW
LIPSS [277]	$< 1 \times 10^{-6}$	$\sim meV$	LSW

Table 4.1: Bounds from coupling between photons and scalar particles from all known experiments. Each limit is valid for the corresponding range of the mass of the scalar particle, which is shown in the third column. In the fourth column we present the basic physical effect on which each experiment is based (LSW means light shinning through a wall experiment).

An updated result [273] is currently the lowest limit from such experiments. In the case of massless scalar particle the coupling parameter is constrained as

$$g < 5.76 \times 10^{-8} GeV^{-1}$$

at 95% confidence limit.

4.3.6 ALPS experiment

The ALPS (Any Light Particle Search) is another experiment of the same class, which is based on the effect "light shining through the wall". The experiment takes place in Deutsches Electronen Synchrotron (DESY), in Germany [274, 275]. The researchers use a HERA superconducting dipole magnet where the magnetic field is $5T$. The photons have wavelength $\lambda = 1024\ nm$, or $\lambda = 512\ nm$. The data are collected in vacuum and in low pressure gas inside a tube, but in the absence of any positive signal for photon regeneration, they estimated [276] the coupling constant at the range

$$g < 7 \times 10^{-8} GeV^{-1}$$

in the case of massless scalar particle in vacuum.

4.3.7 LIPSS experiment

The Light Pseudoscalar and Scalar Particle Search (LIPSS) collaboration [277] was another similar experiment, which searches for photons who coupled to light neutral particles. It took place in Jefferson Lab in the Spring of 2007 and was based on the light shining through the wall effect. The magnetic field was $1.77T$ for both generation and regeneration regions. The wall was a mirror and the wavelength of the photons was $\lambda = 935\ nm$. The innovation of this approach was that data were taken for longer time (almost 1 hour), than previous similar experiments. No signal was recorded above background and the constraint [277] on the corresponding coupling strength is

$$g < 10^{-6} GeV^{-1}$$

assuming a mass of the scalar particle of order meV.

In Table 4.1 we present the bounds for the coupling between scalar particles and photons from all known experiments in order to compare them and identify the most stringent. For small masses of the scalar particle (bellow meV), the coupling g is mass independent, because the oscillation length between ALPs and photons far exceeds the length of the magnet. As we see, the controversial result of PVLAS leads to a weak constraint. The other experiments give more stringent bounds, which in fact are not consistent with the PVLAS result.

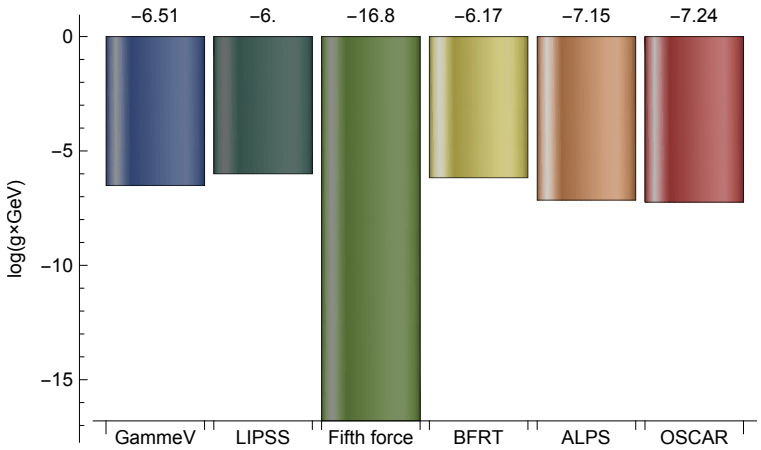

Figure 4.1: Constrains on scalar coupling to electromagnetism from all known experiments, except PVLAS experiment. The vertical axis shows the common logarithm of the coupling g, in dimensionless form.

Also, the data of Table 4.1 are presented through a histogram in Fig. 4.1, where the vertical axis corresponds to the coupling constant g in common logarithmic scale. In order the values of vertical axis to be dimensionless, we have multiplied the values of g with energy units (GeV). We have neglected the PVLAS experiment, because the Italian collaboration does not defend it. Thus, the most stringent bound is obtained from the fifth force experiments.

4.4 Bounds from Chameleon experiments

Chameleon theories are intriguing and lead to new physics. Hints of such theories have been observed in active galactic nuclei's (AGNs), which exist in the center of quasars and in the structure of starlight polarization. As we have underline in Chapter 1, chameleon mechanism make this class of models cosmologically interesting despite of the strong laboratory constrains imposed by the fifth force experiments.

There are two classes of laboratory experiments which aim to detect chameleons

- experiments in empty, closed **container or jar**, such as GammeV and CHASE.
- experiments in **microwave cavity**, such as ADMX.

They are based on the coupling between photons and chameleons, where the coupling to electromagnetism is dominant. These experiments are not photon regeneration experiments [278] because the mass of the chameleons depends on the local density and thus they can't pass through the wall. Inside the wall the density is high compared to the vacuum and the chameleons get reflected by the wall. These experiments are based on the afterglow effect [279], which we describe below. In both cases the coupling to electromagnetism may be described by a dilatonic function

$$B_F(\phi) = e^{g\phi} \simeq 1 + g\phi \tag{4.18}$$

because g is very small ($g \ll 1$). This coupling allows photon-chameleon oscillations in the presence of an external strong magnetic field. The scalar field ϕ with mass m_ϕ is expected of order meV. Such a mass could explain the dark energy density, which is of order $\sim (meV)^4$.

4.4.1 GammeV experiment

As we have seen in section 4.3.2 of this Chapter, the GammeV collaboration includes experiments searching for ALPs but also experiments for chameleons [278, 280], which coupled to photons. The GammeV

experiment constitutes the first test of dark energy models in laboratory. Chameleons are produced inside a optical transparent jar from photon oscillations (Primakoff effect [281]) and are trapped there, if its total energy is less than its effective mass. Then, the chameleons get reflected by the walls and they are detected via their afterglow as they are slowly converted to photons. The afterglow is possible if the mixing time between scalars and photons is larger than the travelling time of photons into the chamber. An afterglow photon can be observed by a photomultiplier tube (PMT) at the exit window, when the original photon source (laser) is tuned off. The pressure in the chamber is $P \approx 10^{-7} Torr$ and the probability per photon to chameleon production is

$$P_{pr} = \frac{4g^2 B^2 \omega^2}{m_{eff}^4} sin^2\left(\frac{m_{eff}^2 L}{4\omega}\right) \widehat{k} \times (\widehat{x} \times \widehat{k}) \tag{4.19}$$

proportional to the square of coupling parameter g.

The magnetic field lies in the $\widehat{x}$ direction, while $\widehat{k}$ is the direction of motion of the particle. If we want to have the maximum probability, the photons must propagate in a direction perpendicular to magnetic field. The photons have energy 2.33 eV, production rate $\sim 10^{19}$ photons per second and the magnetic field is $5T$. In this case, the action which describes the coupling between photons and chameleons is

$$S = \int d^4x \left(-\frac{1}{2}\partial_\mu \phi \partial^\mu \phi - V(\phi) - \frac{e^{\phi/M_\gamma}}{4} F_{\mu\nu} F^{\mu\nu} + \mathcal{L}_m(e^{2\phi/M_m} g_{\mu\nu}, \psi_m^\imath) \right) \tag{4.20}$$

where $V(\phi)$ is the chameleon potential and $\mathcal{L}_m$ the Lagrangian density for the matter. The coupling to matter is defined as

$$\beta_m = M_{Pl}/M_m$$

while the coupling to electromagnetism is the dimensionless parameter

$$\beta_\gamma = M_{Pl}/M_\gamma \equiv g M_{Pl}$$

Data were taken for one hour after the laser turned off, but there wasn't detection of any significant signal in the highly sensitive PMT. The upper and lower bound of the parameter g are estimated as [278]

$$2.1 \times 10^{-7} GeV^{-1} < g < 2.7 \times 10^{-6} GeV^{-1}$$

This limit is valid for coherent oscillations and therefore the effective mass must be quite small ($m_{eff} \ll 0.98\ meV$).

4.4.2 ADMX experiment

The Axion Dark Matter experiment has two parts, just as the GammeV experiment. The first part is the search for ALPs, while the second part is the detection of chameleons. In both cases the particles interact with photons inside a cavity and the range of the coupling is estimated. The advantage of the microwave cavity is that, the resonance is stronger than the case where laser is used. This effect increases the conversion probability and the expected counting rate of photons in the detector. A microwave receiver amplifies the excitation of the resonance. The mixing is maximum when photons and chameleons have the same energy ($\omega_{cham.} = \omega_\gamma$). It is crucial to emphasize that if the coupling is very weak, the chameleons don't have enough energy to be detected, while if the coupling is very strong the chameleons immediately decay. Thus, a fine tunning of the coupling parameter is necessary.

As discussed in Ref. [282], this experiment used a magnetic field $7T$, while the cavity had volume $220\ell t$. It was hold under vacuum at 2 Kelvin. No significant signal was observed and the excluded region for the coupling constant was estimated as [282]

$$3.75 \times 10^{-9} GeV^{-1} < g < 2.1 \times 10^{-4} GeV^{-1}$$

at 90% confidence level. This bound is valid for a very small range of the effective mass, between 1.9510 μeV and 1.9525 μeV. It is clear that, the above limit overlaps with the corresponding limit of the GammeV experiment.

4.4.3 CHASE experiment

The Chameleon Afterglow Search Experiment (CHASE) is a continuation of the GammeV experiment in the same laboratory [283]. The excluded region for the chameleon-photon coupling in this case, is significantly improved. Also, the results smooth out the differences between the two previous experiments [284].

The novelty of this experiment is twofold. First, it uses a couple of glasses into the cavity. Thus, the magnetic field is divided in three parts with different ranges. The shorter part has sensitivity to chameleons with high mass. Second, in order to improve the sensitivity for large g, they used several magnetic fields, with values lower than $5T$. Finally, in order to improve the sensitivity for small g, a shutter (chopper) is used to modulate any possible signal from afterglow. The data didn't show any signal of a photon-chameleon coupling and the excluded region for the coupling parameter (when $m_{eff} \leq 1\ meV$) was estimated as [283]

$$4 \times 10^{-6} GeV^{-1} < g < 1.3 \times 10^{-3} GeV^{-1}$$

at 90% confidence level.

experiment	excluded $g(\times GeV^{-1})$	m_{eff}
GammeV [278]	$(2.1 \times 10^{-7}, 2.7 \times 10^{-6})$	$\ll 0.98meV$
ADMX [282]	$(3.75 \times 10^{-9}, 2.1 \times 10^{-4})$	$[1.9510\mu eV, 1.9525\mu eV]$
CHASE [283]	$(4 \times 10^{-6}, 1.3 \times 10^{-3})$	$\leq 1meV$

Table 4.2: Bounds of excluded regions for the coupling parameter g between photons and chameleons from all known afterglow experiments. In third column, we record the corresponding effective mass for the chameleons.

4.5 Quintessence Dark Energy model with scalar field

We can extend the Bekenstein theory if we introduce the dilatonic function

$$\boxed{B_F(\phi) = e^{-2\phi}} \tag{4.21}$$

in Eq. (4.1). This function induces effects on the cosmological evolution of a quintessence scalar field [186] and effects of multidimensional gravity [285]. We discuss these effects in some detail.

We aim to investigate the cosmological evolution and the effects of the new coupling on the Big Crunch singularity [286–288], that is present in linear potentials. In Ref. [186] the authors introduced the Lagrangian density

$$\boxed{L = \frac{R}{2} - \frac{\omega(\phi)}{2}\partial_a\phi\partial^a\phi - V(\phi) - \frac{1}{4}e^{-2\phi}F_{\mu\nu}F^{\mu\nu} + L_m} \tag{4.22}$$

where L_m denotes the Lagrangian for the other matter fields in the theory and the fine structure constant varies through the relation (due to variable electric charge)

$$\alpha = \alpha_0 e^{2\phi}$$

The coupling function $\omega(\phi)$ and the potential $V(\phi)$ are both arbitrary functions of the scalar field, which is assumed massless. In order to stabilize the theory, we must demand the above functions of ϕ to be not negative. We consider FRW flat spacetime with $\omega(\phi) = 1$ and $V(\phi) = -s\phi$, where the parameter s is a constant. We introduce new dimensionless variables as $H = \bar{H}H_0$, $t = \frac{\bar{t}}{H_0}$, $V = \bar{V}H_0^2$, $\rho_m = \bar{\rho_m}H_0^2$ and $\rho_r = \bar{\rho_r}H_0^2$, ($H_0$ is the present value of the Hubble constant) in the dynamic equations of Ref. [186] and

from now on we omit the bar. The scalar field equation of motion takes the form

$$\boxed{\ddot{\phi} + 3H\dot{\phi} + V'(\phi) = \frac{-6\zeta_m \Omega_{0m} e^{-2\phi}}{a^3\left(1 + |\zeta_m| e^{-2\phi_0}\right)}} \tag{4.23}$$

where ϕ_0 is the present value of the scalar field and the dimensionless electromagnetic parameter ζ_m, which occurs in Eq. (4.23) is defined as

$$\boxed{\zeta_m = L_{em}/\rho_m} \tag{4.24}$$

and describes the ratio between the electromagnetic energy density L_{em} and the non relativistic energy density ρ_m. The cosmological value ζ_m should be approximately constant, but it is not easy to be appreciated for several reasons (for details see Ref. [186]). One of the interesting consequences of theories like (4.22) is that they generically predict violations of the weak equivalence principle, since the force on a particle falling in a gravitational potential will have an additional contribution term which is proportional to $|\zeta_m|$. Thus, for different ζ_m the particles falls with different way, since the force is not the same.

The usual electromagnetic Lagrangian term L_{em}, which is defined as

$$L_{em} = -\frac{1}{4} F_{\mu\nu} F^{\mu\nu} \tag{4.25}$$

is equal to

$$L_{em} = \frac{1}{2}\left(E^2 - B^2\right)$$

When the configuration is dominated by electrostatic energy, the electromagnetic parameter ζ_m is positive, while ζ_m is negative when the system is dominated by its magnetostatic energy. The matter density is always dominant, since $\rho_m \gg L_{em}$. In this work we consider the case where $\zeta_m > 0$. In a radiation epoch, variations of fine structure constant are driven only by the electromagnetic energy of non-relativistic matter, since $L_{em} = 0$.

In our consideration, the acceleration equation for the scale factor respectively becomes [186]

$$\boxed{\frac{\ddot{a}}{a} = -\frac{\Omega_{0m}\left(1 + |\zeta_m| e^{-2\phi}\right)}{2a^3\left(1 + |\zeta_m| e^{-2\phi_0}\right)} - \frac{\Omega_{0r} e^{-2(\phi - \phi_0)}}{a^4} - \frac{1}{3}\left(\dot{\phi}^2 - V(\phi)\right)} \tag{4.26}$$

We have solved the system of the cosmological dynamical equations for the scalar field and for the scale factor (4.23) and (4.26). We assume $\Omega_{0r} = 10^{-4}$, $\Omega_{0m} = 0.3$ and initial conditions deep in the radiation era where the scalar field ϕ_i was almost constant ($\dot{\phi}(t_i) = 0$). Due to rescaling, the acceptable solutions must satisfy the conditions $a(t_0) = 1$, $H(t_0) = 1$ and $\Omega_{0\phi} = 0.7$, where t_0 is the present time. In Fig. 4.2 we present the scalar field as a function of time when $V(\phi) = -0.1\phi$, while in Fig. 4.3 we have plot the logarithm of the scale factor $ln(a(t))$ as a function of time, for several values of the parameter ζ_m.

It is clear from Fig. 4.3 that, when the scalar field increases rapidly, the effective force becomes attractive, the scale factor decreases rapidly and the universe is driven to the Big Crunch singularity. When the rate of the electrostatic energy density increases and consequently ζ_m increases, the effect occurs later. This is an expected result, if we carefully observe the equation (4.23). The right hand side is a function of ζ_m and as ζ_m increases, the r.h.s decreases (bellow zero). Thus, the scalar field needs more time to begin increasing rapidly. In other words, the increasing rate of electromagnetic energy as a fraction of non relativistic matter in the system can stabilize the system for longer time (before Big Crunch).

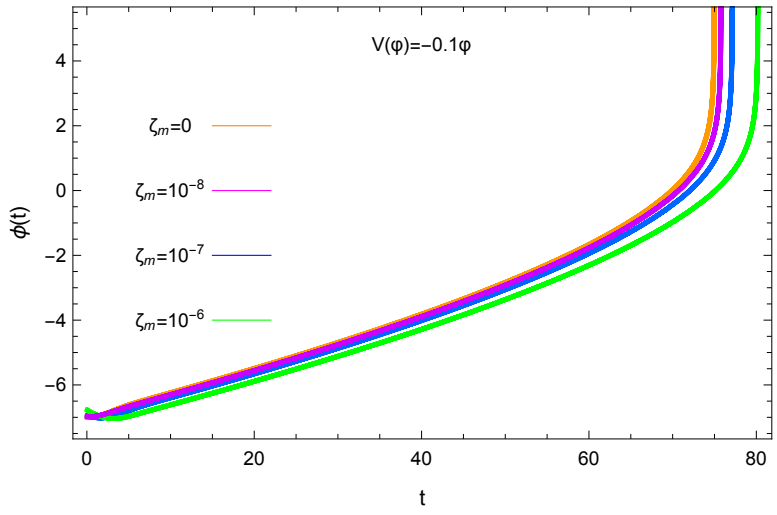

Figure 4.2: The scalar field $\phi(t)$ as a function of time t when $\zeta_m = 0$, $\zeta_m = 10^{-8}$, $\zeta_m = 10^{-7}$ and $\zeta_m = 10^{-6}$ where the linear potential is of the form $V(\phi) = -0.1\phi$. The present time t_0 is derived from the solution of Eqs. (4.23) and (4.26) and must be almost equal to 1. As we see, the field $\phi(t)$ after some time increases rapidly and the effective force becomes attractive. The rate of electromagnetic energy as a fraction of non-relativistic matter density ζ_m in the configuration can stabilize the system for longer time.

Subsequently, using the solution of the system, we calculated the scalar field dark energy (DE) equation of state parameter

$$w_{DE} = \frac{P_{DE}}{\rho_{DE}}$$

as a function of redshift z through the relation

$$\boxed{w(z) = \frac{0.5\dot{\phi}^2 + V(\phi)}{0.5\dot{\phi}^2 - V(\phi)}} \tag{4.27}$$

and we have plot the results in Fig. 4.4. The model corresponds to quintessence cosmology, since $w > -1$ but negative and as we see (magenta or green line), the dilatonic function induces small fluctuations in the equation of state parameter $w(z)$, if we compare with the case where $\zeta_m = 0$ (red line, absence of electrostatic energy). Specifically, when the parameter ζ_m increases, the equation of state parameter $w(z)$ also increases in the context of quintessence cosmology. In order to distinguish the small differences between the $\zeta_m = 0$ curve and the $\zeta_m = 10^{-8}$, we have plot these functions in Fig. 4.5 using more precise values in vertical axis. It is clear that the dilatonic coupling induces fluctuations in the equation of state parameter above the value $w = -1$ and describes quintessence model. Also, in Fig. 4.6, we have plot the parameter w, as a function of time. Initially, the parameter w varies oscillating with time when $\zeta_m = 10^{-8}$, but as the time evolves the equation of state parameter increases, in the context of quintessence cosmology.

The dilatonic function $B_F(\phi) = e^{-2\phi}$ can also describe spatial variations of the fine structure constant in *nonlinear multidimensional theories of gravity* [285, 289, 290]. This term arises naturally from the metric determinant, by taking into account spatial perturbations (of order of the cosmological horizon scale) of the scalar field and the metric, when the system is reduced to four dimensions. The observational data of variations of α depend on the size of the extra factor space and define the model parameters. In this cosmological model, the values of the fine structure constant changes slightly or remain almost constant in all cosmological epochs (radiation epoch, matter epoch or accelerating expansion epoch due to

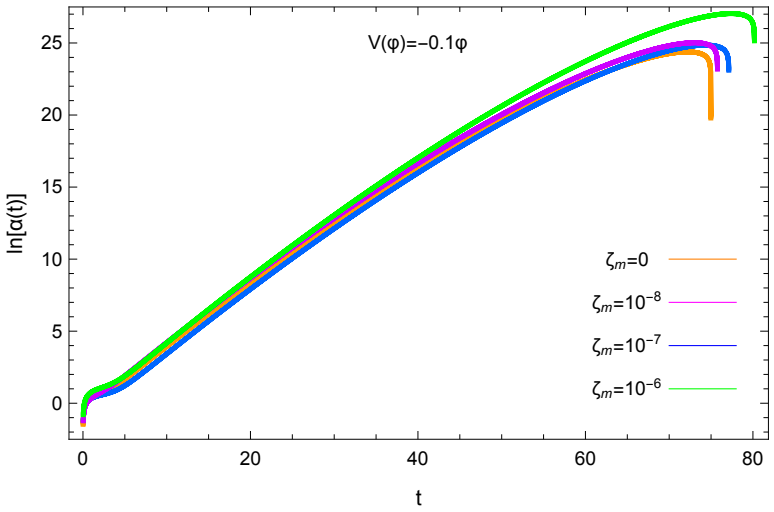

Figure 4.3: The common logarithm of the scale factor $ln(a(t))$ as a function of time t, for several values of the dimensionless parameter ζ_m, when the linear potential is of the form $V(\phi) = -0.1\phi$ and the present time is $t_0 \simeq 1$. After some time interval, the system begins to shrink due to attractive force caught by the scalar field. As ζ_m (the rate of electromagnetic energy in the configuration as a fraction of non-relativistic matter density) increases, the system is stable for longer time and the Big Crunch singularity occurs later.

a cosmological constant). This process can be used for the research of variations and other fundamental constants, such as the gravitational constant G [291].

Large scale inhomogeneity of the scalar field ϕ of multidimensional origin can induce spatial variations of α. The variations of α are very small (of order 10^{-6}), as we have mentioned in the introduction [222] and have been observed from Very Large Telescope (VLT) in Chile [292] and Keck telescope in Hawaii [293, 294]. The results are obtained from spectra of distant quasars and shows a smaller value for fine structure constant when $z < 1.8$ from both telescopes. When $z > 1.8$, the Keck data shows that $\frac{\Delta\alpha}{\alpha} < 0$, but the VLT data drives to $\frac{\Delta\alpha}{\alpha} > 0$. The combined dataset fits a spatial dipole for the variation of α, which is unlikely to be caused by systematic effects.

4.6 Cosmological and Astrophysical Effects

There are many cosmological and astrophysical observations, which could be explained by the existence of scalar ALPs or chameleons and their coupling with photons. One of them is the dark energy density of the universe [295–297], which is of order $\rho_\Lambda \sim (meV)^4$. If the scalar ALPs or chameleons exist and have masses of order of meV, the vacuum energy density has the cosmologically required value.

Scalar dark radiation with a sector ϕ of spin-0, can be tightly coupled to thermal plasma of hydrogen, α particles, baryons, photons and electrons. Such a particle can be scattered from the plasma. The full Lagrangian [298] in this case has the form

$$L_{total} = L_{vissible} + L_{dark\ matter} + L_{interaction} \tag{4.28}$$

where $L_{interaction}$ contains the coupling between ALPs and plasma. This term includes Yukawa-type and dilaton-like operators and obeys the relation [298]

$$L_{interaction} = -\frac{g\phi}{4} F_{\mu\nu}F^{\mu\nu} - \sum_i \frac{m_i}{\Lambda_{4i}} \phi\overline{\psi}_i\psi_i \tag{4.29}$$

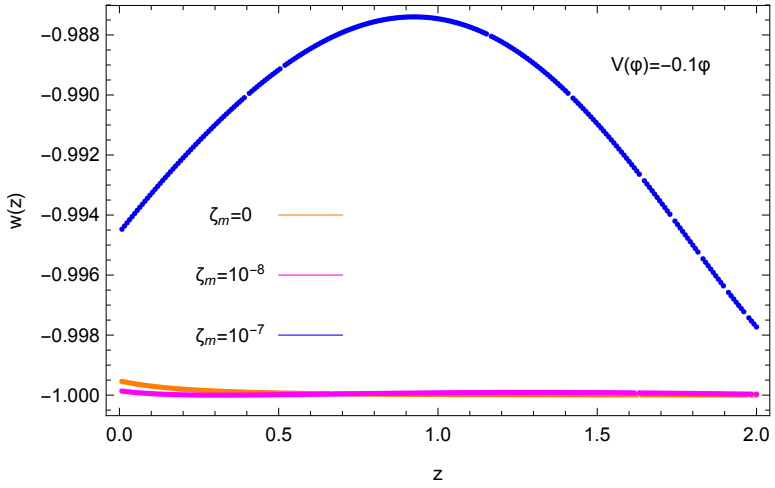

Figure 4.4: The equation of state parameter $w(z)$ as a function of redshift z when the electromagnetic parameter ζ_m takes the values $\zeta_m = 0$, $\zeta_m = 10^{-8}$ and $\zeta_m = 10^{-7}$ in the case where the linear potential is of the form $V(\phi) = -0.1\phi$ and the present time is $t_0 \simeq 1$. It is obvious that the model describes quintessence cosmology since $w > -1$, but it is close to a cosmological constant model where $w = -1$, with negligible deviations.

Astronomical observations [271, 299] from the duration of the red giant phase and the population of Helium Burning stars [4] in globular clusters [300], require

$$g < 6.25 \times 10^{-11} GeV^{-1}$$

This constraint isn't as stringent as experimental constraints due a couple of uncertainty effects. First, the ALPs may be emitted with less energy than they are produced, due to stellar medium diffusion and second, there may be much less ALPs which are produced due to a possible stellar suppression mechanism. Scattering rate of scalar dark radiation near the above bound of g, will be too small to significantly distort the CMB blackbody spectrum. Stronger limits on g can be extracted by considering the cosmological evolution of the vacuum expectation value of ϕ.

There are many cosmological sources, such as quasars [301], X-rays from the Sun [302], cosmic rays with ultra high energy (of order $10^{18} eV$) [303] which produce photons. These photons can be converted to scalar particles due to magnetic fields around their sources. They travel to Earth and are reconverted back to photons due to magnetic fields from our galaxy, or due to intergalactic or intracluster magnetic fields ('cosmic photon regeneration'). The photons can be detected through experiments on Earth. The required mass [304] for the ALPs is situated in the range $m_a \ll (1\ peV - 1\ neV)$ and the required coupling is in the range

$$g \sim (10^{-12} - 10^{-11})\ GeV^{-1}$$

The existence of such particles could explain the alignment of the polarization from distant quasars [305], the variations in luminosity of active galactic nuclei [304], the Sun activity in X-rays [306], the unexpected existence of ultra high energy cosmic rays [307] and the detection of TeV gamma rays [308] from very distant cosmological sources on Earth (usually they are absorbed high).

Scalar particles can also be produced inside the stars [309] and their properties depend on the density of the environment [271]. They can be produced in stellar plasma, only if their mass is tuned to be resonant with the frequency of the plasma [310].

[4] A helium flash is a very brief thermal runaway nuclear fusion of large quantities of helium into carbon through the triple-alpha process in the core of low mass stars (between 0.8 $M_\odot$ and 2.0$M_\odot$) during their red giant phase (the Sun is predicted to experience a flash 1.2 billion years after it leaves the main sequence). Helium burning generates enough energy to prevent further contraction of the star core.

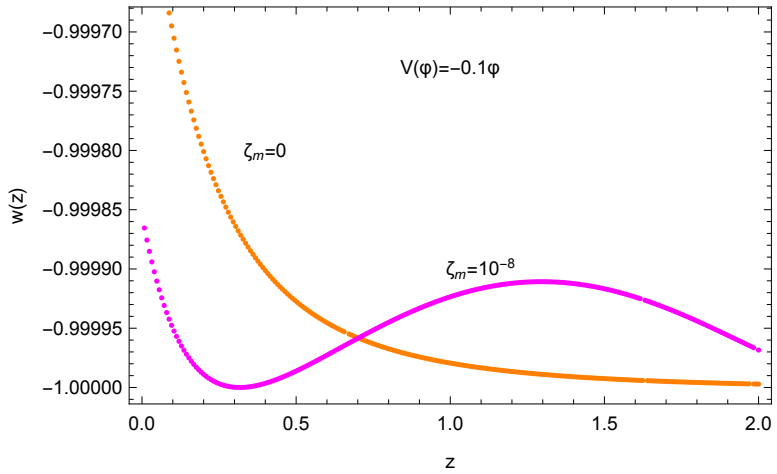

Figure 4.5: The equation of state parameter $w(z)$ as a function of redshift z when $\zeta_m = 0$ (absence of electromagnetic energy density) and $\zeta_m = 10^{-8}$ (presence of electromagnetic energy, mainly electrostatic) when the linear potential is of the form $V(\phi) = -0.1\phi$ and $t_0 \simeq 1$. The model describes quintessence cosmology since $w > -1$, even if it is very close to a cosmological constant model ($w = -1$). This figure focus on the left side of Fig. 4.4, but we have use more accurate scale in the vertical axis, in order to distinguish the slight differences of these curves.

Also, scalar fields can change the energy of the bound states in atoms [309]. The nuclear electric field, in and around the atom, induces a perturbation to scalar field and the corresponding energy levels of hydrogenic atoms are shifted. Thus, the gap between the energy levels increases. These shifts (for example Lamb shift), can be used to constrain the parameter g. The energy gap between the levels $2S_{1/2}$-$2P_{1/2}$ requires

$$g \leq 10^{-3} GeV^{-1}$$

so, it is easier to detect scalar couplings in laboratory experiments from photon regeneration experiments than from atomic measurements [271].

ALPs maybe emitted by explosion of Supernovae. They could be produced by the Primakoff effect with energy $E \sim 100 MeV$ and finally are converted into high energy photos in the magnetic field of our Galaxy. For example, at a distance 50 kpc of Milky Way lies the remnant of $SN1987A$, in Large Magellanic Cloud. The authors of Ref. [311] used the current models for the Supernova magnetic field and the Milky Way magnetic field and they obtained a bound for the coupling between photons and ALPs. In the future, any supernova core-collapse could be used to detect this process.

The coupling between photons and chameleons can be observed through effects in light from astrophysical sources [312]. This coupling can induce linear and circular polarization which can be detected on Earth. The intergalactic region has very low density [313], where the chameleons behave as ALPs. They must have mass $m_\phi \lesssim 10^{-11} eV$, the range of the chameleon force is $\lambda_\phi \gtrsim 20\ Km$ and the required coupling is

$$g \gtrsim 10^{-11} GeV^{-1}$$

The dilatonic function

$$B_F(\phi) = 1 + g(\phi - \phi_0)$$

can describe variations of the fine structure constant [313]. The evolution of α is given by the relation [203]

$$\boxed{\frac{\Delta\alpha}{\alpha} = \Big(B_F(\phi)\Big)^{-1} - 1} \tag{4.30}$$

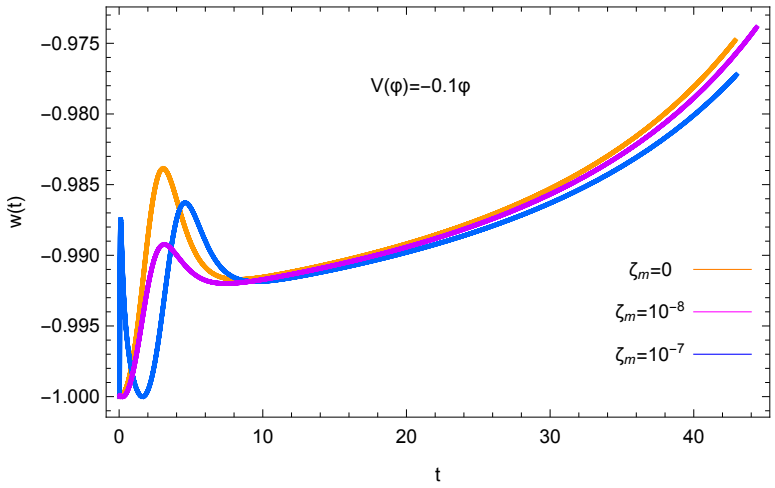

Figure 4.6: The equation of state parameter $w(t)$ as a function of time t for several values of the electromagnetic parameter ζ_m, when the linear potential is of the form $V(\phi) = -0.1\phi$ and $t_0 \simeq 1$. Note that, in the quintessence model only small deviations from $w = -1$ occur and when the time is big enough ($t > 10$), the rate of the electrostatic energy affects negligible the evolution of the parameter w, since the curves are almost the same.

Assuming that $\phi_0 = 0$, scalar particles or chameleons would change the value of this constant, when they interact with photons. If we determine the order of coupling g, then we would check if this value could support the observed variation of the fine structure constant.

4.7 Conclusions

The existence of scalar (or pseudoscalar) ALPs and chameleons can play the role of dark matter or can induce the accelerating expansion of the universe, respectively. The detection of these light particles (with masses in the sub-eV range) is a challenge for modern cosmology [314]. In this direction, many experiments until today have been designed and executed. They are laboratory experiments and astrophysical or cosmological observations based on light shining through the wall effect or optical effects in laser polarization [315], which have the purpose to detect the coupling between scalar particles and photons through effects, that are induced in light. Until now, these experiments haven't recorded any positive signal, because the coupling, as it seems from the results, is very weak, beyond the present detection sensitivity of observational instruments on Earth.

In this Chapter, we examined the case where the coupling is described by a dilatonic function and varies linearly with the scalar field ϕ (4.2). Due to the shift symmetry of scalar field, quadratic terms of ϕ are excluded. Experiments are being conducted, which try to detect optical effects from these particles in polarized laser beam, or photon regeneration inside a strong magnetic field. The detection sensitivity of these experiments is restricted by the technical features of each apparatus. In these experiments there isn't currently any positive signal for the existence of ALPs, so we currently have an upper bound. The most stringent bound comes from the fifth force experiments where long range forces are induced by the scalar field (Casimir force).

An alternative way to explain the accelerating expansion of the universe is the chameleon scalar particles, a kind of particles whose mass depends on the local density. In dense environment, the chameleon becomes massive (mediate a short range force), but in sparse environment becomes very light (mediate a long range force) [316]. This feature makes chameleons consistent with local experiments but still effective on the cosmological dynamics beyond the cosmological constant. They coupled to photons and this coupling can approximately be described with the same dilatonic function, as scalar

ALPs. The experiments are based on different effects because the chameleons get reflected by the wall due to their mass, so they cannot induce photon regeneration. Chameleons are consistent with cosmological constraints on the existence of non-minimally coupled scalars.

In quintessence models, if we consider linear potential of a scalar field ϕ, the Big Crunch singularity occurs in the future. The universe stops to expand and begins rapidly to compressed. The rate of the electromagnetic energy density in the configuration can stabilize the system for longer time, since we shown that the Big Rip singularity occurs later. The equation of state parameter w varies negligible, with values bigger than -1, but very close to the rate $w = -1$.

In many astrophysical, astronomical and cosmological effects, light travel from one distant cosmological source, such as a galaxy, to our planet. It passes through several magnetic fields and it is possible to detect changes in light, when we observe it in laboratory. This is the purpose of a wide range of laboratory experiments on the Earth.

Many extensions of the standard model of particle physics predict the existence of new light bosons, such as ALPs. Astrophysical environments offer the possibility of strong magnetic fields on long baselines and thus consist promising targets in the search for ALPs. In contrast with laboratory experiments, magnetic fields in astrophysical environments are usually not coherent.

Axion-like particles (ALPs) belong to a class of new scalar or pseudoscalar particles that generically couple to photons, opening the possibility of oscillations from photons into ALPs in an external magnetic field. Having witnessed the turbulence of their magnetic fields, these oscillations are expected to imprint irregularities in a limited energy range of the spectrum of astrophysical sources. Thus, it is more possible to detect these particles from astrophysical observations, such as direct light or spectra.

Chapter 5

Theoretical Models for Spatially Oscillating Sub-mm Forces

Recently have appeared in literature analyses, which indicate the presence of a 2σ signal of spatially oscillating new force residuals, such as in the torsion balance data of the Washington experiment [317]. At the theoretical level such deviations from the Newtonian potential are generic predictions in a wide range of extensions of General Relativity including f(R) theories [318, 319], massive Brans-Dicke scalar tensor theories [184, 320], compactified extra dimension models [321, 322] and non-local extensions of GR [323, 324]. In the latter, oscillating deviations occur naturally on sub-millimeter scales without any instabilities. In this Chapter, we extend previous studies and analyze the data of the Stanford Optically Levitated Microsphere Experiment (SOLME) [325] searching for sub-mm spatially oscillating new force signals.

We find a statistically significant oscillating signal for a force residual of the form $F(z) = \alpha\ \cos(\frac{2\pi}{\lambda}\ z + c)$ where z is the distance between the macroscopic interacting masses (levitated microsphere and cantilever). The best fit parameter values are $\alpha = (1.1 \pm 0.4) \times 10^{-17} N$ and $\lambda = (35.2 \pm 0.6)\mu m$. Monte Carlo simulation of the SOLME data under the assumption of zero force residuals has indicated that the statistical significance of this signal is at about 2σ level. The improvement of the χ^2 fit compared to the null hypothesis (zero residual force) corresponds to $\Delta\chi^2 = 13.1$. Therefore, this Chapter contents is a deviation from the Standard ΛCDM model since it investigates the effects of deviations from Newton's constant and thus from General Relativity at sub-mm scales in short range gravity experiments. We have emphasized this point in the section 1.15.

Private communication with the authors of Ref. [325] has indicated that this previously unnoticed signal is indeed in the data but is most probably induced by a systematic effect caused by diffraction of non-Gaussian tails of the laser beam. Thus, the amplitude of this detected signal can only be useful as an upper bound to the amplitude of new spatially oscillating forces on sub-mm scales. In the context of gravitational origin of the signal emerging from a fundamental modification of the Newtonian potential of the form $V_{eff}(r) = -G\frac{M}{r}\big(1 + \alpha_O \cos(\frac{2\pi}{\lambda}\ r + \theta)\big) \equiv V_N(r) + V_{osc}(r)$, we evaluate the source integral of the oscillating macroscopically induced force. If the origin of the SOLME oscillating signal is systematic, the parameter α_O is bounded as $\alpha_O < 10^7$ for $\lambda \simeq 35\mu m$. Thus, the SOLME data can not provide useful constraints on the modified gravity parameter α_O. However, the constraints on the general phenomenological parameter α ($\alpha < 0.3 \times 10^{-17} N$ at 2σ) can be useful in constraining other fifth force models related to dark energy (for example, chameleon oscillating potentials).

The physical scale associated with the accelerating expansion of the universe is the dark energy scale which is obtained from the dark energy density $\rho_{de} \simeq 10^{-29} g/cm^3 \simeq (2.4meV)^4$. This scale corresponds to an energy scale of $\Lambda = 2.4meV$ and a length scale of about

$$\lambda_{de} = \frac{\hbar c}{\Lambda} \simeq 80\mu m$$

It is therefore plausible that the physical cause of the cosmological expansion on cosmological scales may also produce experimental signatures in the form of new forces that manifest themselves on sub-mm scales. Chameleon scalar field screened interactions [3, 11, 95, 106, 326–329], modified gravity Yukawa forces [330, 331] and vacuum energy Casimir forces [332–334] are some examples of new sub-mm forces that could also be connected with the observed cosmological accelerating expansion.

A wide range of experiments have been performed searching for signatures of new forces on sub-mm scales. They include torsion balance experiments [335–348], Casimir force experiments [349, 350] or levitating microsphere experiments [325, 351–353]. These experiments fit particular parametrizations to datasets that usually involve force or torque residuals as function of distance between interacting bodies.

Parametrizations that are commonly used to model the spatial dependence of new forces on sub-mm scales are monotonic and include Yukawa and power law parametrizations [267]. Yukawa parametrizations generalize the gravitational potential generated by a mass M to the form

$$\boxed{V_{eff} = -G\frac{M}{r}\left(1 + \alpha_Y e^{-r/\lambda}\right)} \tag{5.1}$$

where α_Y, λ are parameters to be constrained by the data. The effective potential (5.1) includes the Newtonian term and the Yukawa term. Power law parametrizations generalize the gravitational potential generated by a mass M to the form

$$\boxed{V_{eff} = -G\frac{M}{r}\left(1 + \beta^k\left(\frac{\lambda}{r}\right)^{k-1}\right)} \tag{5.2}$$

where β and k are parameters. These parametrizations are motivated by viable extensions of GR such as Brans-Dicke and scalar-tensor theories [184, 320, 354], brane world modes [355–360], $f(R)$ theories [318, 319, 361] and compactified extra dimension models [321, 322, 362–365]. Alternative more complicated parametrizations which may not appear in closed analytic form are obtained in the context of non-relativistic, steady-state chameleon fields, that couple directly to matter density and can mediate screened new forces between macroscopic objects [104, 325, 366, 367] which may even be significantly larger than gravity [366].

Recent studies [317, 368–370] have pointed out that a new class of parametrizations describing *spatially oscillating new forces* on sub-mm scales is well motivated theoretically and viable experimentally. Such oscillating parametrizations may describe deviations of the gravitational force from the Newtonian force or may drive to extensions of theory of GR

- in a wide range of modified gravity theories [317], such as $f(R)$ theories,
- in theories involving small scale granularity of dark energy [371, 372]
- in massive scalar tensor theories Brans-Dicke [184] and most importantly
- in non-local (infinite derivative) gravity theories [317, 331, 368–370, 373–378]

The main advantages of these theories are the following

1. they are free from singularities [375, 376, 379, 380] (such as black holes)
2. they are free from instabilities [377, 378, 381]
3. they can naturally emerge from quantum effects [374] (such as light particle loops)
4. they do not need the existence of the cosmological constant Λ to interpret the cosmological observations [382]

They constitute a viable physical mechanism for the observed accelerating expansion of the universe [383–386] while they predict specific signatures in the gravitationally light bending angle [387] testable by the Chandra X-ray Observatory[1].

Oscillating force residuals are experimentally viable and mildly favored [317] according to current torsion balance experiments searching for new forces on sub-mm scales [335]. These parametrizations also emerge as analytic continuations of the Yukawa parametrization (5.1) and generalize the Newtonian gravitational potential as

$$\boxed{V_{eff} = -G\frac{M}{r}\left(1 + \alpha_O \cos\left(\frac{2\pi}{\lambda}r + \theta\right)\right) \equiv V_N(r) + V_{osc}(r)} \tag{5.3}$$

where α_O, λ, θ are free parameters and the spatial wavelength λ is assumed to be of sub-mm scale for consistency with current experimental constraints. This type of parametrization leads to oscillating new forces of sub-mm wavelength of the form

$$\boxed{\vec{F} = -\hat{r}\frac{GMm}{r^2}\left[1 + \alpha_O \cos\left(\frac{2\pi}{\lambda}r + \theta\right) + \alpha_O \frac{2\pi}{\lambda} r \sin\left(\frac{2\pi}{\lambda}r + \theta\right)\right]} \tag{5.4}$$

In the case of interacting macroscopic bodies the gravitational potential energy (and therefore the gravitational force) can be obtained by integration of the oscillating potential energy correction term (source integral obtained from the potential V_{osc} of Eq. (5.3)) over the volumes of the interacting bodies. Assuming macroscopic interacting masses M and m with a common density ρ, the corresponding potential energy source integral may be written as

$$V_{osc}(r) = -G\alpha_O \int_{V_m} d^3 r_m \rho(\vec{r}_m) \int_{V_M} d^3 r_M \rho(\vec{r}_M) \frac{\cos\left(\frac{2\pi}{\lambda}|\vec{r}_m - \vec{r}_M| + \theta\right)}{|\vec{r}_m - \vec{r}_M|} \tag{5.5}$$

The effective force obtained from the potential source integral (5.5) macroscopic cylinder of mass M interacting with a small mass m located at a distance z from one of its bases along its symmetry axis is well approximated for intermediate to large z as

$$\boxed{\vec{F}(z) = A\cos(\frac{2\pi}{\lambda}z + c)\hat{z}} \tag{5.6}$$

where c is a phase parameter. Oscillating sub-mm force residuals like (5.6) were shown in Ref. [317] to be consistent with current torsion balance experiments [335] and in fact to provide a somewhat better fit than the null hypothesis of zero force residuals.

In this Chapter we fit the spatially oscillating force residual (5.6) to the dataset of Stanford Optically Levitated Microsphere Experiment (SOLME) [325] involving force measurements on optically levitated microspheres as a function of its distance z from a gold coated silicon cantilever. The residual force obtained after the subtraction of a best fit electrostatic background from the total measured force in units of fN for $z \in [25, 235]\mu m$ is fit to the oscillating force residual parametrization of Eq. (5.6) and the quality of fit is compared to the null hypothesis of zero force residual. The analytic expression of the source integral (5.5) is also investigated and its quality of fit to the SOLME data is compared to the corresponding quality of fit of the simpler approximate form (5.6) and other monotonic parametrizations.

5.1 Bounds for a Phenomenological Oscillating Parametrization from SOLME

The SOLME [325] uses optically levitated dielectric microspheres supported by the radiation pressure from a single upward pointing laser beam. The laser traps the microsphere in a high vacuum thus

[1] http://chandra.harvard.edu/

counterbalancing Earth gravity. Any additional force is assumed to be due to a gold-coated silicon cantilever, located in the same height with the microsphera. In order to minimize electrostatic background forces the trap and cantilever are shielded in a cubic container consisting of six gold-plated electrodes which are set to approximately equal potential as the cantilever. Despite of this shielding, the main background force remains of electrostatic origin. It emerges due to the interaction of the small but non-zero permanent electric dipole moment of the micro-spheres which couples to the electric field due to the small but non-zero potential difference fluctuations ($< 30mV$) between the cantilever and shielding electrodes. Thus, the best fit electrostatic background may be used to obtain the residual force data as the difference between the measured total force and the best fit electrostatic background force at a given microsphere-cantilever distance z. The magnitude of the residual force dF defined as

$$\boxed{dF \equiv F_{measured} - F_{background}} \tag{5.7}$$

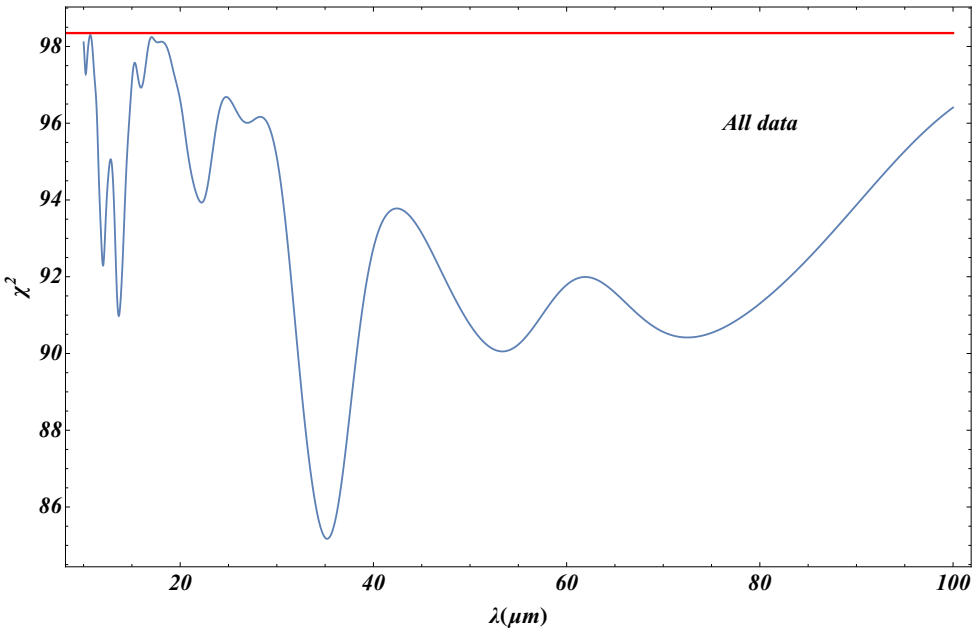

Figure 5.1: The value of the minimized χ^2 as a function of the wavelength λ for the full dataset (96 points). The red straight line corresponds zero residual force $dF = 0$. The depth of the minimum is $\delta\chi^2 = 13.1$.

The dataset analyzed in this Chapter corresponds to the data shown in Fig. 3 of Ref. [325]. The data and the best fit electrostatic background were kindly provided by the members of the SOLME [325] after our request. This dataset was obtained using three silica microspheres with the same radius $r = 2.5\mu m$ and mass $m = 0.13ng$, but different polarizabilities. Each microsphera was trapped in a high vacuum with pressure $P < 10^{-6}mbar$ and its position was measured by a position-sensitive photodiode using a laser beam.

The small unshielded electrostatic background forces are monotonic with the distance z between cantilever and microsphera and have been modelled and fit by the members of the SOLME as functions of the distance z between the cantilever and the microsphere. We have found that this background is very well fit by a parametrization of the form

$$F_B = a + \frac{b}{r^{3/2}}$$

where a, b are appropriate parameters that depend on the polarizabity of the interacting micropshere.

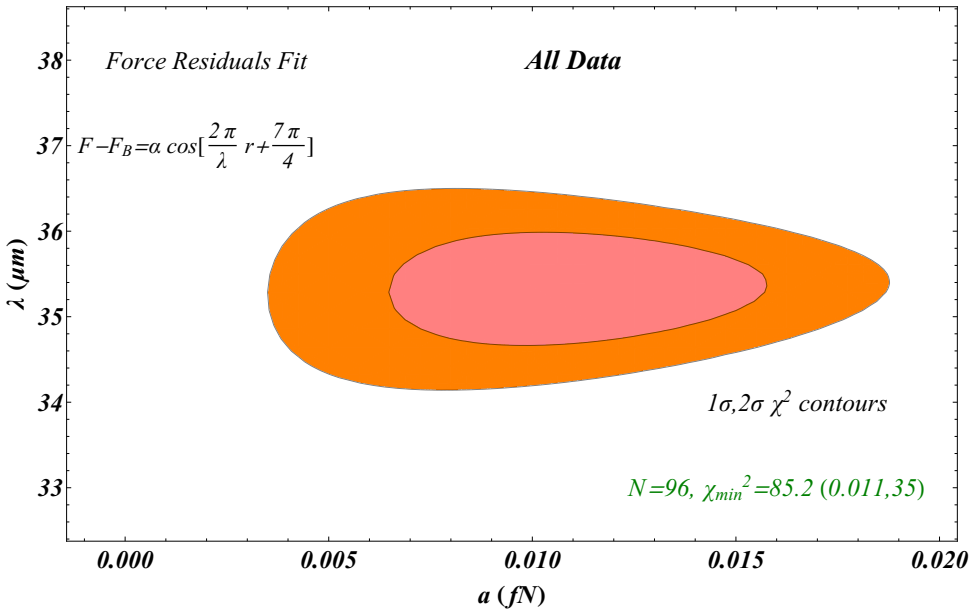

Figure 5.2: The 1σ and 2σ contours in the parameter space (α, λ) for the oscillating parametrization with $c = 7\pi/4$. For the combined dataset (96 datapoints) there is a well defined high quality fit at $(\alpha, \lambda) = (0.011, 35.2\mu m)$ corresponding to a wavelength $\lambda = 35.2\mu m$. This best fit is about 3σ away from the zero force residual value $\alpha = 0$.

Any new type of force would manifest itself as a statistically significant nonzero residual force beyond the modelled electrostatic background.

For each one of the three silica microsphere the residual force of Eq. (5.7) was obtained for 32 distances z between cantilever and microsphere in the distance range z from $25\mu m$ up to $235\mu m$. The total of 96 values of these residual forces along with the corresponding distances z and their 1σ error is shown in Table B.1 in the Appendix B (32 values for each one of the three microsphere).

We fit the residual forces of the SOLME data derived from equation (5.7) using the oscillating parametrization of the form

$$\boxed{dF(\alpha, \lambda, c, z) = \alpha \; cos\left(\frac{2\pi}{\lambda}\, z + c\right)} \tag{5.8}$$

where α, λ and c are parameters to be fit. We have used the parametrization (5.8) to minimize $\chi^2(\alpha, \lambda, c)$ defined as

$$\boxed{\chi^2(\alpha, \lambda, c) = \sum_{j=1}^{N} \frac{\Big(dF(j) - dF(\alpha, \lambda, c, z_j)\Big)^2}{\sigma_j^2}} \tag{5.9}$$

where j refers to the j^{th} datapoint as resulted from Eq. (5.7) and $dF(\alpha, \lambda, c, z_j)$ is the residual force parametrized by Eq. (5.8) for the same distance z_j between cantilever and microsphera, that corresponds to measured residual force $dF(j)$. Also N is the number of datapoints which is 96 for the full dataset.

We found that, for the full dataset, $\chi^2(\alpha, \lambda, c)$ is minimized for

$$\alpha = (0.011 \pm 0.004) fN \tag{5.10}$$

$$\lambda = (35.2 \pm 0.6)\mu m \tag{5.11}$$

$$c = (5.47 \pm 0.06) rad \simeq 7\pi/4 \tag{5.12}$$

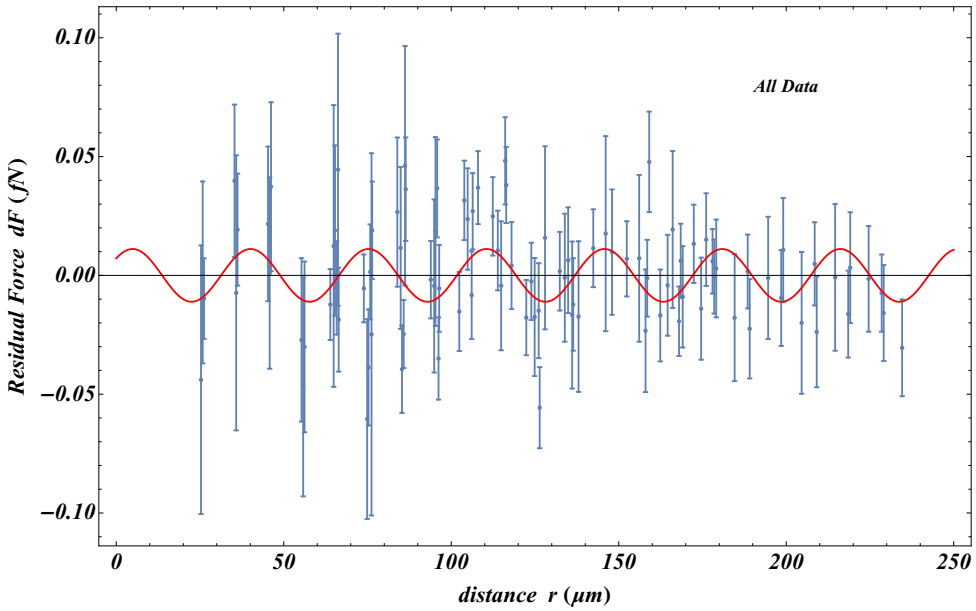

Figure 5.3: The residual force SOLME data with error bars along with the best fit oscillating parametrization (thin red line) for the full dataset. The best fit harmonic parametrization has spatial wavelength $\lambda = 35.2\mu m$.

This value of the best fit phase c differs by about π from the corresponding best fit phase obtained in Ref. [317] when fitting the Washington experiment data to the same parametrization. The minimum value of χ^2 is $\chi^2(\alpha, \lambda, c) = 85.2$ compared to $\chi^2(0, \lambda, c) = 98.3$ corresponding to zero residual force ($dF = 0$). In Fig. 5.1 we show the (minimized with respect to α, c) $\chi^2(\alpha, \lambda, c)$ for the full dataset as a function of the spatial wavelength λ. Clearly, there is a well pronounced minimum at the spatial wavelength $\lambda = 35.2\mu m$.

The red horizontal line corresponds to the value of χ^2 of zero residual force $dF(\alpha = 0, \lambda, c, r_j) = 0$. The difference between zero force residual and best fit oscillating parametrization is $\delta\chi^2 = 13.1$. The 1σ and 2σ contours for the two parameters α, λ (fixing $c = 7\pi/4$) are shown in Fig. 5.2. These contours indicate that the zero residual $\alpha = 0$ line is about 3σ away from the best fit $\alpha = 0.01$. In Fig. 5.3 we show the full dataset (residual force in fN vs distance in μm) along with the best fit oscillating model (5.8). The oscillating signal in the data is clearly visible.

5.2 Testing the Signal with Monte Carlo Simulations

In view of the presence of other less deep χ^2 minima at different spatial wavelengths, this 3σ estimate is an overestimate of the true significance of the oscillating signal. In order to estimate the correct statistical significance of the signal we have performed a Monte Carlo simulation. The goal of such a Monte Carlo simulation is to estimate how often would such a deep χ^2 minimum occur in SOLME simulated data derived under the assumption of an underlying zero residual force.

In order to verify the level of significance of the identified oscillating signal we have generated Gaussian Monte Carlo datasets under the assumption of zero residual force. In particular, we used the Normal Distribution to take random values for the residual forces (with mean value equal to zero) for each datapoint distance z with the same standard deviation as the experimental data. We processed multiple datasets of random datapoints with the same method as the measured data. A typical form of

$$\delta\chi^2(\lambda) \equiv \chi^2_{oscillating} - \chi^2_{\alpha=0}$$

after minimization with respect to α, c at each value of λ, is shown in Fig. 5.4. Clearly, the depth of the

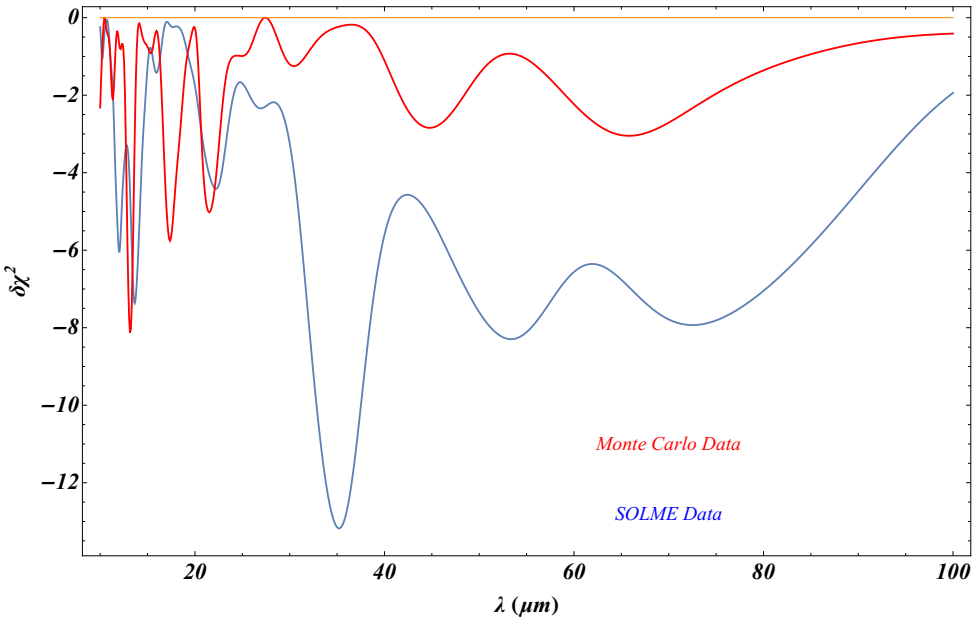

Figure 5.4: The value of the minimized difference $\delta\chi^2 = \chi^2_{oscillating} - \chi^2_{\alpha=0}$ as a function of the spatial wavelength λ for the experimental data and a random Monte-Carlo dataset simulating the SOLME data under the assumption of zero residual force and Gaussian errors. The depth of the $\delta\chi^2$ deepest minimum is significantly larger when the real data are fit to the oscillating parametrization.

deepest minimum of the Monte Carlo dataset (red line) is significantly smaller than the maximum depth obtained with the real dataset (blue line).

We considered a hundred (100) Monte Carlo zero residual force datasets and we calculated for each Monte-Carlo dataset the deepest χ^2 minimum in the range $\lambda \in [10-100]\mu m$ and subtracted this minimum χ^2 from the corresponding of zero residual force χ^2 obtained from the Monte-Carlo data. Thus we calculated the difference

$$\delta\chi^2 = \chi^2_{zero\ residual} - \chi^2_{min-oscillating\ residual} \tag{5.13}$$

For the real data this corresponds to the difference $\delta\chi^2$ between the $\alpha = 0$ red line of Fig. 5.1 and the deepest minimum of the blue line. This is the horizontal line in Fig. 5.5 at $\delta\chi^2 = 13.1$. For the Monte Carlo datasets this difference corresponds to the difference between the deepest minimum of the red line and the horizontal red line of Fig. 5.4. Each one of the red dots of Fig. 5.5 corresponds to such Monte Carlo difference. Clearly if all the 100 red dots were found below the horizontal line of Fig. 5.5 ($\delta\chi^2 < 13.1$) then there would be less than 1% probability that the deep χ^2 minimum of Fig. 5.1 is due to a statistical fluctuation. Instead we find that about 5% of the zero residual simulated data lead to deeper χ^2 minima (five red dots in Fig. 5.5 are above the horizontal line). Thus, the true level of significance of the oscillating signal is at about 2σ. A similar effect leading to reduced level of significance compared to the one indicated by the χ^2 contour plot was observed and discussed in Ref. [317].

We conclude that there is evidence for an oscillating signal at the 2σ level in the SOLME data. Since there is only about 5% probability that this signal is due to a statistical fluctuation, most likely it is due either to a systematic effect that was not discussed in Ref. [325] or it is due to new physics. Private communication with the authors of Ref. [325] has indicated that the signal is most probably due to a systematic effect caused by a background due to non-Gaussian tails of the laser beam whose pressure levitates the microsphere. Due to diffraction, the intensity of these non-Gaussian tails has a periodic oscillation, which can mimic a spatially oscillating force signal. Thus, the amplitude of this detected signal can only be useful as an upper bound to the amplitude of new spatially oscillating forces on sub-mm scales. In addition to the oscillating parametrization (5.8) we have tried to fit the data using various

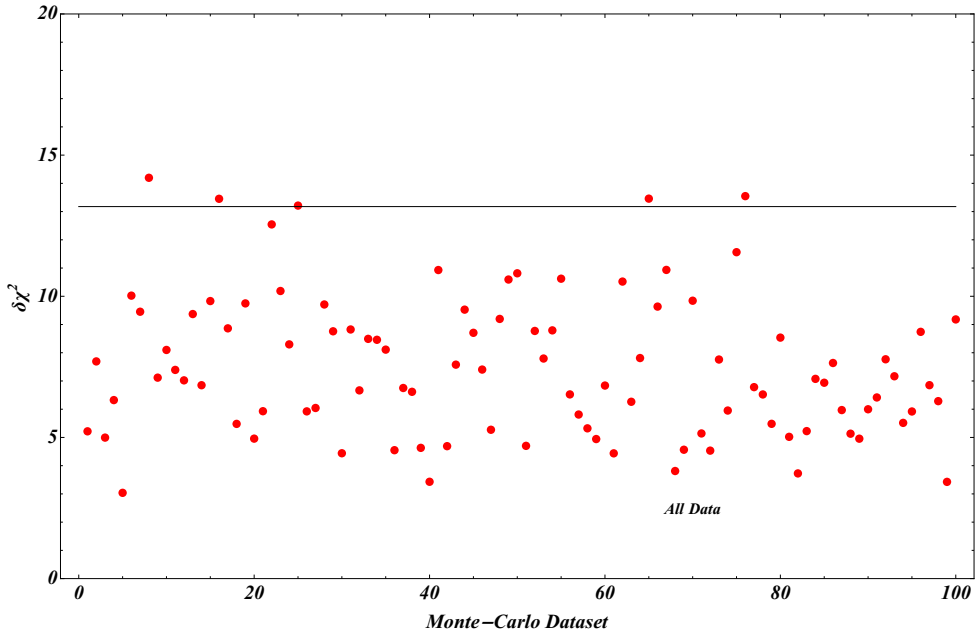

Figure 5.5: The maximum $\delta\chi^2$ depth in the range $\lambda \in [10, 100]$ for 100 Monte Carlo datasets assuming zero residual force (red dots). The horizontal line corresponds to the maximum $\delta\chi^2$ depth for the actual SOLME dataset.

monotonic parametrizations like a Yukawa parametrization of the form

$$dF(\alpha, \lambda, z) = \alpha\, e^{z/\lambda} \tag{5.14}$$

However, in all cases the improvement of the quality of fit was minor with $\delta\chi^2 < 1$ and thus we will not discuss these cases further.

The oscillating parametrization (5.8) is a phenomenological parametrization which can not be used as to impose constraints on fundamental parameters. In order to impose such constraints the macroscopic residual force parametrization must be derived starting from a fundamental theory. For example we may assume a gravitational origin of the signal and derive the macroscopically induced residual force starting from a modified Newtonian potential of the form (5.3). Thus, we may derive the predicted macroscopic residual force between cantilever and microsphere in terms of the fundamental parameters α_O and λ of Eq. (5.3) by evaluating the source integral (5.5) over the cantilever. This derived effective residual force may then be fit to the SOLME data leading to constraints on the fundamental parameters α_O and λ rather than the corresponding phenomenological parameters of Eq. (5.8). This task is undertaken in the next section.

5.3 Constraints on Fundamental Parameters: Source Integral

We approximate the orthogonal cantilever of the SOLME by a cylindrical one of the same base area and height as the one used in the experiment. This approximation allows for analytical evaluation of the source integral and of the macroscopic gravitational forces of the cantilever on the small microsphere located at a distance z along the symmetry axis from the center of the base of the cylindrical cantilever. Such a cantilever would have a radius $R \simeq 40\mu m$, height $D = 2000\mu m$ (see Fig. 5.6) and density $\rho = 2.3 gr/cm^3$. As stated above, the mass of the microsphere was $m = 0.13 ng$ and its radius $r = 2.5\mu m$.

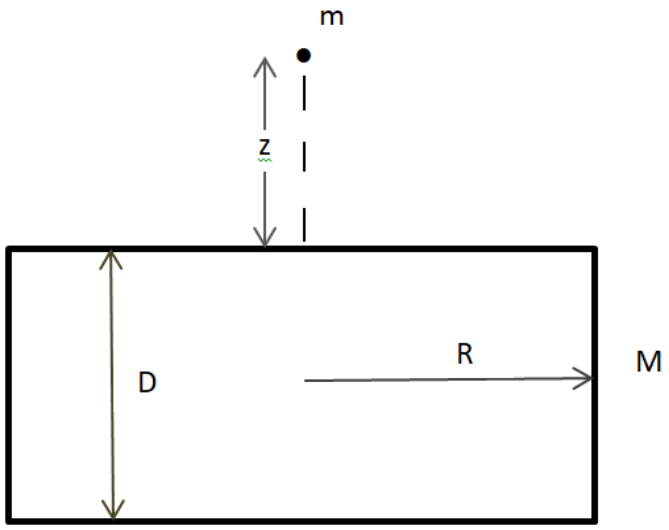

Figure 5.6: The cantilever approximated as a cylinder and a point mass m at distance z from its surface.

5.3.1 Newtonian Force between a Cylindrical Cantilever and a Microsphere

First, we calculate the Newtonian gravitational force between the cantilever and the microsphere. The gravitational potential energy between the cantilever and a point mass m at distance z from its surface is of the form

$$V_N(z) = -2\pi\rho G m \int_0^R r dr \int_z^{z+D} \frac{dz'}{\sqrt{r^2 + z'^2}} \tag{5.15}$$

We now introduce a rescaling to dimensionless length dividing all lengths by the cantilever radius R and denote with a 'bar' the new dimensionless quantities. Under this rescaling the potential (5.15) takes the form

$$V_N(\bar{z}) = -\underbrace{2\pi\rho G m R^2}_{V_1} \underbrace{\int_0^1 r' dr' \int_{\bar{z}}^{\bar{z}+\bar{D}} \frac{dz''}{\sqrt{r'^2 + z''^2}}}_{\bar{V}_N(\bar{z})} \tag{5.16}$$

where the definitions of the potential unit V_1 and of the dimensionless gravitational potential $\bar{V}_N$ are shown in Eq. (5.16). The corresponding z component of the interaction force is

$$F_{zN}(\bar{z}) = -\underbrace{2\pi G m \rho R}_{F_1} \underbrace{\frac{\partial \bar{V}_N(\bar{z})}{\partial \bar{z}}}_{\bar{F}_{zN}(\bar{z})} \tag{5.17}$$

It is straightforward to calculate the dimensionless part of the force $\bar{F}_{zN}(\bar{z}) \equiv \frac{\partial \bar{V}_N(\bar{z})}{\partial \bar{z}}$ as

$$\bar{F}_{zN}(\bar{z}, \bar{D}) = -\bar{D} - \sqrt{1 + \bar{z}^2} + \sqrt{1 + (\bar{D} + \bar{z})^2} \tag{5.18}$$

For small $\bar{z}$ ($\bar{z} \ll 1$) the dimensionless part of the force F_{zN} is constant as expected

$$\bar{F}_{zN}(\bar{z}, \bar{D}) \simeq \sqrt{1 + \bar{D}} - (1 + \bar{D}) \tag{5.19}$$

while, for $\bar{z} \gg 1$ it also has the anticipated asymptotic behavior as an inverse square of the distance

$$\bar{F}_{zN}(\bar{z}, \bar{D}) \simeq -\frac{\bar{D}}{2\bar{z}^2} \tag{5.20}$$

The dimensions corresponding to the SOLME are $R = 40\mu m$, $\bar{D} = 50$, $\bar{r}_1 = 0.0625$, $\bar{z}_{min} = 0.5$, $\bar{z}_{max} = 6.25$ where $\bar{r}_1 \equiv \frac{r_1}{R}$ is the dimensionless form of the radius of the microsphere which is clearly much smaller than all the other dimensions of the experiment. In view of this fact we may approximate the microsphere as a point mass and assume that the predicted Newtonian force on it, is provided to a good approximation by Eqs. (5.17) and (5.18).

An improved approximation for the calculation of the Newtonian force on the microsphere is the averaging of the force through the evaluation of the integral

$$\bar{F}_{zN,total}(\bar{z}, \bar{D}, \bar{r}_1) = \frac{1}{2\bar{r}_1} \int_{\bar{z}_0 - \bar{r}_1}^{\bar{z}_0 + \bar{r}_1} dz' \bar{F}_{zN}(z', \bar{D}) \tag{5.21}$$

We have found that this improved approximation has a minor effect (less than 1%) on the estimated force on the micropshere. Thus, in what follows we approximate the micropshere as a point mass that is subject to a Newtonian force from the cantilever provided by Eqs. (5.17) and (5.18) as

$$F_{zN}(\bar{z}, \bar{D}) = \alpha_N \times \underbrace{2\pi G m \rho R}_{F_1} \times \bar{F}_{zN}(\frac{z}{40}, 50) \tag{5.22}$$

where z is measured in μm and $F_1 = 2\pi G m \rho R \simeq 5 \times 10^{-9} fN$ for the geometry and the objects used in the SOLME. We have allowed for a short range amplification factor α_N to the Newtonian force. Since

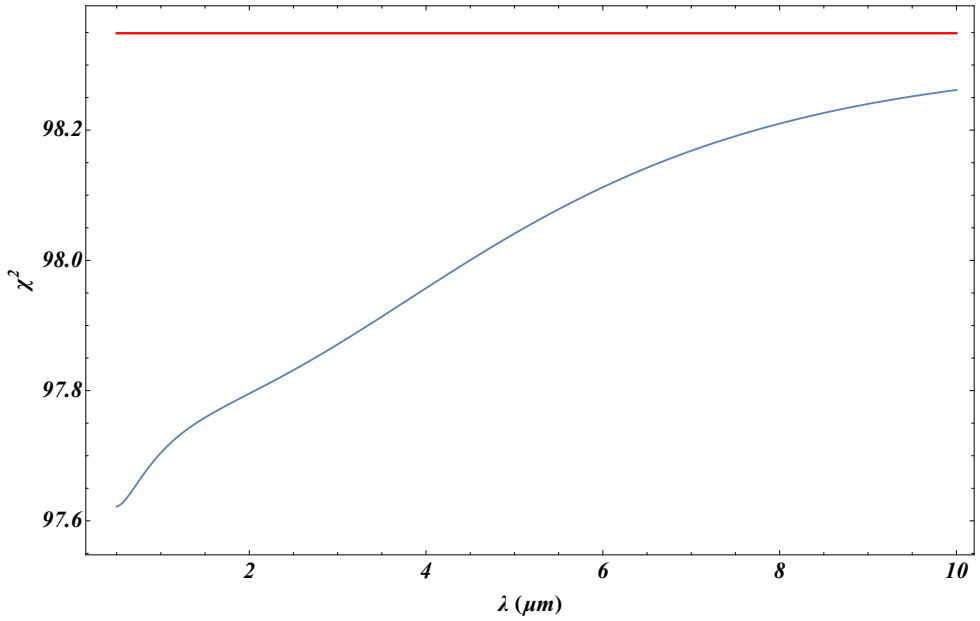

Figure 5.7: The minimized χ^2 using the SOLME data as a function of the parameter λ of the Yukawa force ansatz including the effects of the source integral. The improvement of the fit is marginal despite the additional two parameters α_Y, λ.

$\bar{F}_{zN}(\frac{z}{40}, 50) < 1$ for the distances considered in the SOLME ($z > 20\mu m$) it is clear that the Newtonian force is much smaller than the residual forces measured in the SOLME which are of $O(10^{-2}) fN$ and an amplification by a factor $\alpha_N \simeq 10^7$ on these scales would be required for such a force to be observable by the SOLME.

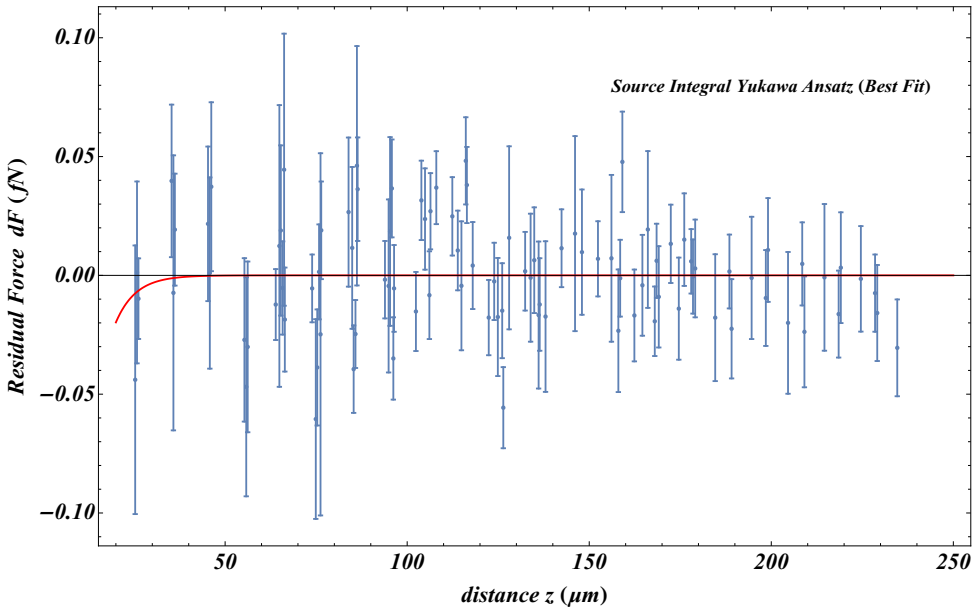

Figure 5.8: The best fit form of the the source integral for the Yukawa residual force is practically indistinguishable from the zero force residual.

5.3.2 Yukawa Residual Force between a Cylindrical Cantilever and a Microsphere

Deviations from the Newtonian potential on sub-millimeter scales can be parameterized through a Yukawa interaction, an oscillating model or a power law parametrization. In the case of the Yukawa deviation, the potential energy of a point mass M interacting with a point mass m at a distance r gets generalized as $V(r) = V_N(r) + V_Y(r)$ with

$$V_Y(r) = -\frac{GMm}{r}\alpha_Y e^{-\frac{r}{\lambda}} \tag{5.23}$$

where α_Y and λ are appropriate parameters to be constrained. In this case, the Yukawa rescaled dimensionless interaction potential energy, as defined in Eq. (5.15), between a cylinder of dimensionless height $\bar{D}$ (the cantilever) and a point mass m (the microsphere) located at a distance $\bar{z}$ from the center of one of the cylinder bases is

$$\bar{V}_Y(\bar{z}) = -\alpha_Y \int_0^1 r'dr' \int_{\bar{z}}^{\bar{z}+\bar{D}} dz' \frac{e^{-\frac{\sqrt{r'^2+z'^2}}{\bar{\lambda}}}}{\sqrt{r'^2+z'^2}} \tag{5.24}$$

The corresponding z component of the force $\bar{F}_{zY}(\bar{z}) \equiv \frac{\partial \bar{V}_Y(\bar{z})}{\partial \bar{z}}$ induced on the mass m can be analytically evaluated by first obtaining the source integral (5.24). The result is

$$\bar{F}_{zY}\left(\bar{z}, \bar{D}, \bar{\lambda}\right) = \alpha_Y \lambda \left(e^{-\frac{\bar{D}+\bar{z}}{\bar{\lambda}}} + e^{-\frac{\sqrt{1+\bar{z}^2}}{\bar{\lambda}}} - e^{-\frac{\bar{z}}{\bar{\lambda}}} - e^{-\frac{\sqrt{1+(\bar{D}+\bar{z})^2}}{\bar{\lambda}}} \right) \tag{5.25}$$

with $\bar{\lambda} = \frac{\lambda}{R}$. The asymptotic behaviour of the macroscopic Yukawa force is expected, namely it is exponentially suppressed for $\bar{z} >> 1$, while for small $\bar{z}$ it is constant approximated as

$$\bar{F}_{zY}(\bar{z}, \bar{D}, \bar{\lambda}) = \alpha_Y \bar{\lambda} \left(-1 + e^{-\frac{1}{\bar{\lambda}}} + e^{-\frac{\bar{D}}{\bar{\lambda}}} - e^{-\frac{\sqrt{1+\bar{D}^2}}{\bar{\lambda}}} \right) \tag{5.26}$$

For the SOLME the full residual Yukawa force may be expressed as

$$F_{zY,tot} = \bar{F}_{zY,tot}(\frac{z}{40}, 50, \frac{\lambda}{40}) \times 5 \times \underbrace{10^{-9} \times \alpha_Y}_{\alpha_{Y9}} \tag{5.27}$$

where z, λ must be substituted in μm and the force is calculated in fN. We have found that as in the case of the simple phenomenological Yukawa parametrization discussed in the previous section, the source integral Yukawa force (5.27) is unable to improve the fit of the SOLME residual force data by more than 1 ($\delta\chi^2 < 1$) compared to the zero residual force parametrization. This is demonstrated in Fig. 5.7 where we show the minimum value of χ^2 as a function of λ for the macroscopic Yukawa force residual (5.27) and for the zero force residual (red line). Clearly we have $\delta\chi^2 < 1$ for all values of λ considered. The Yukawa potential does not provide a more efficient macroscopic residual force parametrization for fitting the force residuals of the SOLME data compared to null hypothesis of the zero force residual. This is also demonstrated in Fig. 5.8 where we show the best fit Yukawa residual force for $\alpha_Y = 1$ which is achieved for $\lambda = 5.6\mu m$ and is practically indistinguishable from the zero residual force for most of the range of the force residual SOLME data.

5.3.3 Power Law Residual Force between a Cylindrical Cantilever and a Microsphere

A similar conclusion is obtained for other monotonic residual force parametrizations like power law deviations from the Newtonian potential. In this case, the generalized gravitational potential would be of the form $V(r) = V_N(r) + V_P(r)$ with

$$V_P(r) = -\frac{\alpha_P GMm}{r^n} \tag{5.28}$$

The rescaled dimensionless source integral may be written as

$$\bar{V}_P(\bar{z}) = -\alpha_P \int_0^1 r'dr' \int_{\bar{z}}^{\bar{z}+\bar{D}} \frac{dz'}{\left(r'^2 + z'^2\right)^{n/2}} \tag{5.29}$$

leading to the z component of the rescaled dimensionless force $\bar{F}_{zP}(\bar{z}) \equiv \frac{\partial \bar{V}_P(\bar{z})}{\partial \bar{z}}$ in the analytic form

$$\bar{F}_{zP}(\bar{z}, \bar{D}, n) = \alpha_P \frac{\bar{z}^{-n}(\bar{D}+\bar{z})^{-n}}{n-2} \left[(1+\bar{z}^2)\left[1+(\bar{D}+\bar{z})^2\right]\right]^{\frac{-n}{2}} \left\{ -\bar{z}^n(\bar{D}+\bar{z})^n(1+\bar{z}^2)^{\frac{n}{2}}\left[1+(\bar{D}+\bar{z})^2\right] \right.$$
$$\left. + \left[1+(\bar{D}+\bar{z})^2\right]^{\frac{n}{2}} \left[\bar{z}^n(\bar{D}+\bar{z})^n(1+\bar{z}^2) + (1+\bar{z}^2)^{\frac{n}{2}}\left[\bar{z}^n(\bar{D}+\bar{z})^2 - \bar{z}^2(\bar{D}+\bar{z})^n\right]\right] \right\} \tag{5.30}$$

Introducing the parameters of the SOLME, the dimensionfull force in fN takes the form

$$F_{zP,tot} = \bar{F}_{zP,tot}(\frac{z}{40}, 50, n) \times 5 \times \underbrace{10^{-9} \times \alpha_P}_{\alpha_{Pg}} \tag{5.31}$$

It is straightforward to show that the quality of fit of this power law source integral force residual is similar to that of the corresponding Yukawa residual and thus it is not of particular interest since it is not favoured over the zero residual hypothesis. Thus, we will not pursue this case further.

5.3.4 Oscillating Force Residual between a Cylindrical Cantilever and a Microsphere

We now consider an oscillating gravitational residual potential of the form $V(r) = V_N(r) + V_O(r)$ with

$$V_O(r) = -\frac{GMm}{r}\alpha_O \cos\left(\frac{2\pi}{\lambda}r + \theta\right) \tag{5.32}$$

The macroscopic dimensionless form of the potential energy between a cylindrical cantilever and a microsphere on the cantilever's axis of symmetry is expressed in terms of the dimensionless source integral as

$$\bar{V}_O(\bar{z}) = -\alpha_O \int_0^1 r'dr' \int_{\bar{z}}^{\bar{z}+\bar{D}} dz' \frac{\cos\left(\frac{2\pi\sqrt{r'^2+z'^2}}{\bar{\lambda}} + \theta\right)}{\sqrt{r'^2+z'^2}} \tag{5.33}$$

The corresponding z component of the rescaled dimensionless force $\bar{F}_{zO}(\bar{z}) \equiv \frac{\partial \bar{V}_O(\bar{z})}{\partial \bar{z}}$ can be obtained

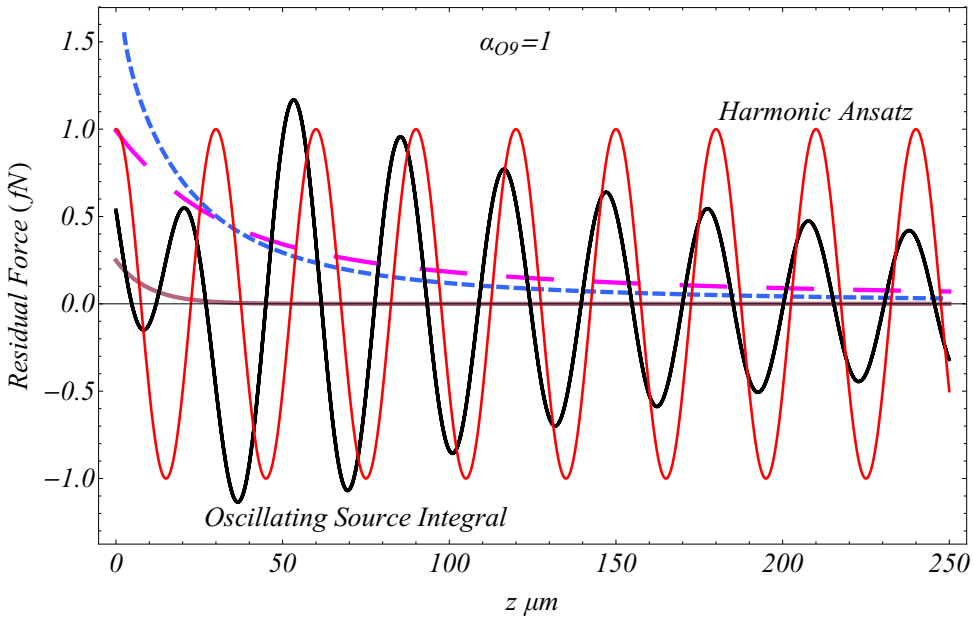

Figure 5.9: Comparison between the source integral signal for oscillating force with the naive constant amplitude cosine oscillator. On scales z larger than the disk radius ($R = 40\mu m$) they both behave like harmonic functions with very similar wavelength,while on small scales the signal is not periodic. Also, we have plot the Newtonian ansatz (blue line), the Yukawa ansatz (gray line) and a power law force with $n = 1.5$ (magenta line). For the oscillating source integrals we have set $\alpha_{O9} = 1$ which implies $\alpha_O = 10^9$.

analytically as

$$\bar{F}_{zO}(\bar{z},\bar{D},\bar{\lambda},\theta) = \frac{\alpha_O\bar{\lambda}}{2\pi}\left[\sin\left(\frac{2\pi\bar{z}}{\bar{\lambda}}+\theta\right) - \sin\left(\frac{2\pi(\bar{D}+\bar{z})}{\bar{\lambda}}+\theta\right) + \right.$$
$$\left. + \sin\left(\frac{2\pi\sqrt{1+(\bar{D}+\bar{z})^2}}{\bar{\lambda}}+\theta\right) - \sin\left(\frac{2\pi\sqrt{1+\bar{z}^2}}{\bar{\lambda}}+\theta\right)\right] \tag{5.34}$$

For large z, the residual force (5.34) is oscillating with an amplitude that decreases as $1/\bar{z}$ and is of the

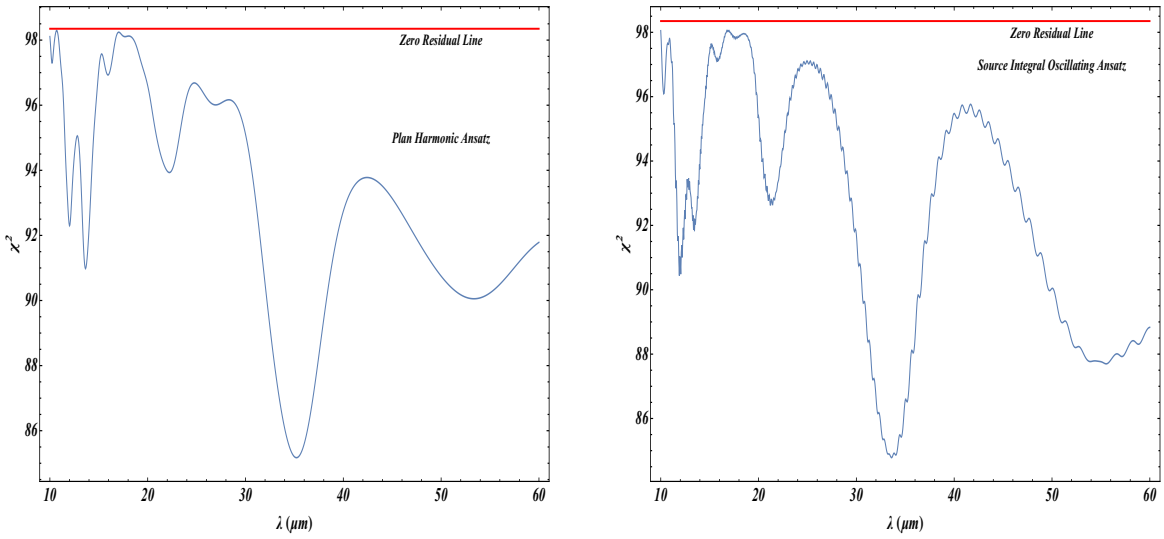

(a) (b)

Figure 5.10: Left panel: The χ^2 value as a function of the wavelength λ for plain harmonic ansatz. Right panel: The χ^2 value for the source integral oscillating ansatz. In both cases the fit improvement to the data is significant compared to a null residual fit. The difference in χ^2 is more than 13 units and the minimum appears in almost the same wavelength (about $35\mu m$).

form

$$\bar{F}_{zO}\left(\bar{z},\bar{D},\bar{\lambda},\theta\right)=\cos\left(\frac{2\pi\bar{z}}{\bar{\lambda}}\right)\frac{\cos\left(\frac{2\pi\bar{D}}{\bar{\lambda}}+\theta\right)-\cos\theta}{2\bar{z}}-\sin\left(\frac{2\pi\bar{z}}{\bar{\lambda}}\right)\frac{\sin\left(\frac{2\pi\bar{D}}{\bar{\lambda}}+\theta\right)-\sin\theta}{2\bar{z}} \tag{5.35}$$

For small $\bar{z}$ we find

$$\bar{F}_{zO}\left(\bar{z},\bar{D},\bar{\lambda},\theta\right)=\frac{\bar{\lambda}}{2\pi}\left[\sin\theta-\sin\left(\frac{2\pi}{\bar{\lambda}}+\theta\right)-\sin\left(\frac{2\pi\bar{D}}{\bar{\lambda}}+\theta\right)+\sin\left(\frac{2\pi\sqrt{1+\bar{D}^2}}{\bar{\lambda}}+\theta\right)\right] \tag{5.36}$$

For the case of the SOLME the oscillating residual force on the microsphere located at a distance z μm from the cantilever it would be of the form

$$F_{zO,tot}=\bar{F}_{zO,tot}(\frac{z}{40},50,\frac{\lambda}{40},\theta)\times 5\times\underbrace{10^{-9}\times\alpha_O}_{\alpha_{O9}} \tag{5.37}$$

where z, λ in μm and the force is measured in fN. In Fig. 5.9 the force source integral (5.37) with $\lambda=30\mu m$ and $\alpha_{O9}=1$ (thick black dotted line) is compared with the plain harmonic residual force (5.8) with the same λ and $\alpha=1$ (continuous red line), with the Newtonian source integral force (5.18) (long dashed line), with a power law source integral ($n=1.5$, Eq. (5.30), blue dashed line) and with a Yukawa source integral force with $\lambda=10\mu m$ (gray line). Notice that the oscillating force source integral for the particular parameters is an oscillating non-periodic function with initially increasing amplitude which reaches a maximum and subsequently decreases at large distances in accordance with the predicted asymptotic behaviour (5.35).

It is straightforward to fit the SOLME data using the macroscopic oscillating residual force (5.37) obtained from the source integral. In this case, as in the case of the plain harmonic residual force (5.8) we have a significant improvement of the quality of fit compared to the zero residual hypothesis by $\delta\chi^2>13$. This is demonstrated in Fig. 5.10 (right panel) where we show the minimized χ^2 as a function of the

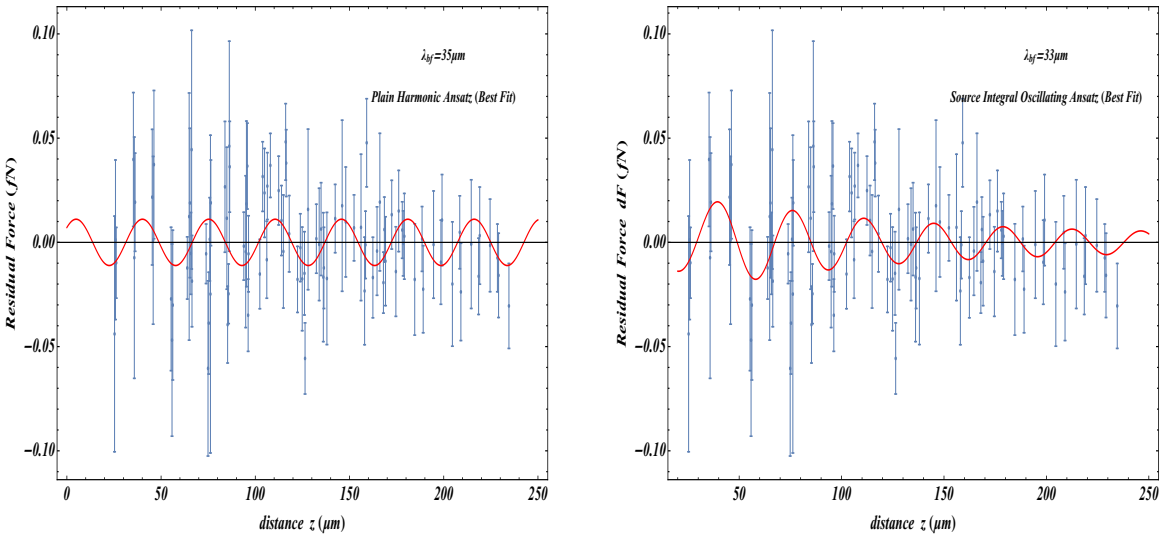

(a) (b)

Figure 5.11: Left panel: The best fit plain harmonic ansatz with $\lambda = 35\mu m$. Right panel: The best fit source integral oscillating ansatz with $\lambda = 33\mu m$. As we see, in both cases the waveform is practically the same even though the amplitude for the best fit source integral decreases slowly with distance.

spatial wavelength λ of the macroscopic oscillating force (5.37). The depth of the best fit χ^2 minimum is $\delta\chi^2 > 13$ and is obtained for $\lambda \simeq 33\mu m$ which is almost the same value $\lambda \simeq 35\mu m$ of the plain harmonic force parametrization (5.8) shown on the left panel[2].

In Fig. 5.11 (right panel) we show the best fit macroscopic oscillating force parametrization (5.37) superposed with the SOLME residual force data. For comparison we also show the corresponding best fit of the plain harmonic parametrization (5.8). The quality of fit (value of χ^2) is almost identical despite the fact that the right panel shows the full source integral best fit parametrization where the oscillation amplitude decreases slowly with z.

5.3.5 Oscillating Source Integral in Cartesian Coordinates

In order to make the evaluation of the source integral analytically tractable we have approximated the orthogonal cantilever used in the SOLME by a cylindrical one of the same base area. The orthogonal cantilever used in the SOLME had dimensions $a \times b \times D = 10\mu m \times 500\mu m \times 2000\mu m$. Had we kept the orthogonal geometry in the evaluation of the oscillating force source integral and rescaled with the dimension $a = 10\mu m$ of the cantilever we would have to calculate the following source integral

$$F_{Oz}\left(\bar{z_0}, \bar{\lambda}, \theta\right) = Gm\rho a \times \alpha_O \times \frac{\partial}{\partial \bar{z}_0} \int_{-1}^{1} d\bar{x} \int_{-\bar{b}}^{\bar{b}} d\bar{y} \int_{\bar{z}_0}^{\bar{z}_0+\bar{D}} \frac{\cos\left(\frac{\sqrt{\bar{x}^2+\bar{y}^2+\bar{z}^2}}{\bar{\lambda}} + \theta\right)}{\sqrt{\bar{x}^2+\bar{y}^2+\bar{z}^2}} d\bar{z} \tag{5.38}$$

which in contrast to the cylindrical geometry is not analytically tractable. Using a numerical approach we have evaluated the source integral (5.38) at the distances of the datapoints and confirmed that a similar quality of fit can be obtained using the orthogonal source integral (5.38) as with the cylindrical analytic source integral (5.37) for the same spatial wavelength. Thus, our result for the existence of the oscillating signal is robust and insensitive to the particular geometry used for the evaluation of the source integral. This is demonstrated in Fig. 5.12 where we show the best fit source integrals for cylindrical

[2]The left panel of Fig. 5.10 is identical with Fig. 5.1 but we show it here again for easier comparison with the corresponding figure obtained using the full source integral (5.37) rather than the simple parametrization (5.8).

(5.37) and orthogonal (5.38) cantilever along with the best fit plain harmonic force residual ansatz (5.8). Clearly the three best fit parametrizations are very similar leading to practically the same quality of fit ($\chi^2 \simeq 85$) compared to the much lower quality of fit for the zero residual hypothesis and the Yukawa or power law residuals ($\chi^2 \simeq 98$).

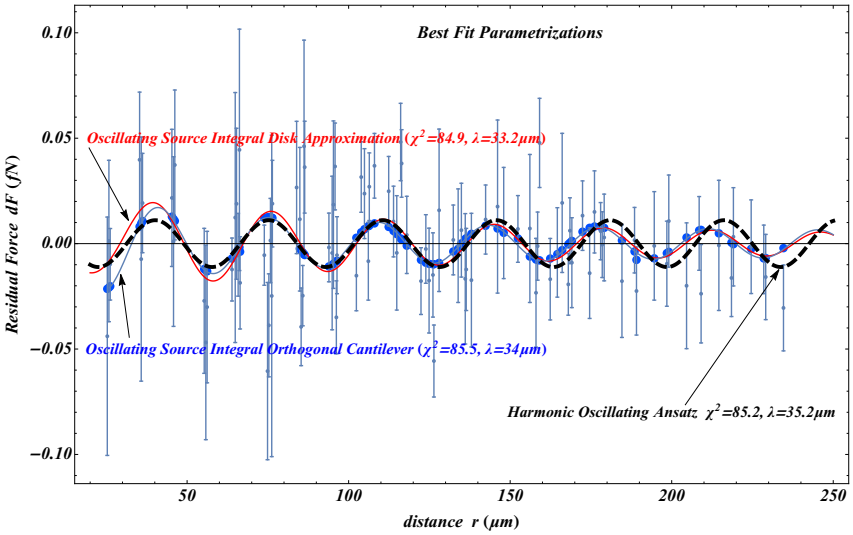

Figure 5.12: The best fit source integrals for cylindrical (5.37) and orthogonal (5.38) cantilever along with the best fit plain harmonic force residual ansatz (5.8).The three best fit parametrizations are very similar leading to practically the same quality of fit.

5.4 Oscillating Chameleon Model

If the origin of the oscillating signal (5.11) is assumed to be gravitational through a modified Newtonian potential of the form of Eq. (5.3) the bounds obtained on the parameter α_O are particularly weak ($\alpha_O < 10^7$) due to the partially shielded electrostatic backgrounds that limit the sensitivity of the experiment in measuring gravitational forces between the cantilever and the microsphere.

More interesting bounds on fundamental fifth force parameters could be obtained if the origin of the signal is assumed to be non-gravitational. In particular, it is plausible that a chameleon potential with multiple extrema can lead to a spatially oscillating fifth force which is screened in regions of high density via the chameleon mechanism. Consider for example [11] the chameleon field profile around a large spherical object (e.g., the Earth) of radius R_c and density $\rho(r)$. The profile of the chameleon field which acts also as a potential for the chameleon fifth force is determined by the equation

$$\boxed{\frac{d^2\phi}{dr^2} + \frac{2}{r}\frac{d\phi}{dr} = V_{,\phi} + \frac{\beta}{M_{Pl}}\rho(r)e^{\beta\phi/M_{Pl}}} \,, \tag{5.39}$$

where β is a coupling parameter, M_{Pl} is the Planck mass scale, $V(\phi)$ is the chameleon field self-interaction potential and $V_{,\phi} \equiv \frac{dV}{d\phi}$ the first derivative of the potential with respect to ϕ. The density profile may be approximated as

$$\rho(r) = \begin{cases} \rho_c & \text{for} \quad r < R_c \\ \rho_\infty & \text{for} \quad r > R_c \end{cases} . \tag{5.40}$$

Let ϕ_c and ϕ_∞ be the chameleon field values that minimizes the effective potential V_{eff} defined as

$$\boxed{V_{eff}(\phi) \equiv V(\phi) + \rho(r)e^{\beta_i\phi/M_{Pl}}} \tag{5.41}$$

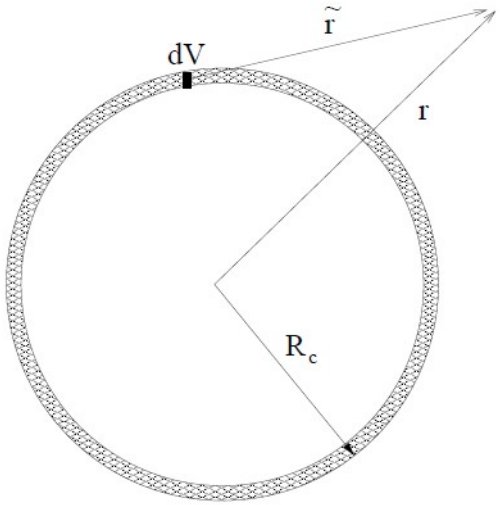

Figure 5.13: The thin shell effect suppresses the chameleon force, because only a thin shell (shaded region) of a dense object with radius R_c contributes to the ϕ field outside the object. All the other infinitesimal volumes within the object have not significant contribution, due to exponential reduction. Thus, the magnitude of the force is significantly reduced. Adopted from [11].

for $r < R_c$ and $r > R_c$, respectively. Well within the object, one finds that the chameleon nearly minimizes the effective potential at the value $\phi \simeq \phi_c$ and the mass of the chameleon is large [3]. The contribution from a volume element dV within the core is exponentially suppressed and it contributes negligibly to the ϕ field outside. This result valid for all infinitesimal volume elements within the object, except for those lying within a thin shell near the surface, as we present in Fig. 5.13 (*thin-shell effect*). For these field values we have [11]

$$\begin{aligned} V_{,\phi}(\phi_c) + \frac{\beta}{M_{Pl}}\rho_c e^{\beta\phi_c/M_{Pl}} &= 0 \\ V_{,\phi}(\phi_\infty) + \frac{\beta}{M_{Pl}}\rho_\infty e^{\beta\phi_\infty/M_{Pl}} &= 0 \end{aligned} \tag{5.42}$$

The screened chameleon fifth force is obtained from the profile solution of Eq. (5.39) with boundary conditions

$$\begin{aligned} \frac{d\phi}{dr} &= 0 \qquad \text{at} \quad r = 0 \\ \phi &\to \phi_\infty \qquad \text{as} \quad r \to \infty \end{aligned} \tag{5.43}$$

It can be shown from the chameleon field action that the chameleon fifth force on a test particle of mass M is of the form

$$\boxed{\vec{F}_\phi = -\frac{\beta}{M_{Pl}} M\vec{\nabla}\phi} \tag{5.44}$$

It is obvious that the field ϕ plays the role of a potential for the chameleon induced fifth force.

[3] The mass of the chameleon field inside or outside the large object is the mass of small fluctuations about ϕ_c and ϕ_∞, respectively. It is obvious from Fig. 1.9 in Chapter 1 that, as density decreases, the minimum of the potential shifts to larger values of ϕ and the mass of small fluctuations decreases.

If the chameleon self interaction potential is monotonic between the central value ϕ_c and the asymptotic field value ϕ_∞ then $\phi(r)$ varies monotonically between its value ϕ_c in the center of the massive object and its asymptotic value ϕ_∞ which is approached exponentially fast in the exterior of the massive body. We obtain the usual screened fifth force obtained from the gradient of $\phi(r)$ which is maximized around a thin shell at the borderline of the massive object and goes rapidly to zero in the interior and in the exterior of the object with significantly larger mass in the interior (screened region).

If on the other hand, there are multiple extrema of the potential $V(\phi)$ in the range between the central value ϕ_c and the asymptotic field value ϕ_∞, then Eq. (5.39) implies that these extrema may be inherited to the chameleon field profile around the massive object. Thus, from Eq. (5.44) these multiple extrema may induce localized sub-mm spatial oscillations of the chameleon induced screened fifth force. A similar behavior may be obtained if the exponential conformal coupling to the density $e^{\beta\phi/M_{Pl}}$ is replaced by an oscillating function.

5.5 Conclusions

We have analyzed and fit the Stanford Optically Levitated Microsphere Experiment (SOLME) [325] force residual data using a wide range of parametrizations including plain phenomenological ones and parametrizations obtained by evaluating source integrals based on simple functional forms. We have shown that monotonic parametrizations, such as Yukawa and power laws are unable to improve the quality of fit of the null hypothesis (zero force residuals) at any significant level despite the introduction of a number of parameters ($\delta\chi^2 < 1$). However, oscillating parametrizations at the plain phenomenological level and at the level of source integral can improve significantly the quality of fit compared to the null hypothesis ($\delta\chi^2 > 13$). The statistical significance of this oscillating signal is at about 2σ level.

The most probable cause of this signal is a systematic effect caused by the non-Gaussian tails of the laser beam whose pressure levitates the microsphere. Due to diffraction, the intensity of these non-Gaussian tails has a periodic oscillation, which can mimic a spatially oscillating force signal. Thus the detected signal can only be used as an upper bound to physically interesting new forces of sub-mm oscillating nature. The amplitude α of such an oscillating force background with spatial wavelength $\lambda \simeq 35\mu m$ is bounded at the 2σ level as

$$\alpha < 0.3 \times 10^{-17} N$$

This bound is phenomenological and applicable to the conditions and geometry of the SOLME.

Chapter 6

Effects on gravitational waves in an expanding Universe

In the course of this Chapter we solve the Laplace equation $\Box h_{ij} = 0$ describing the propagation of gravitational waves in an expanding background metric with a power law scale factor in the presence of a point mass in the weak field approximation (Newtonian limit of McVittie background). We can use gravitational waves to investigate and check some deviations of the Standard model, such as the isotropy of the universe [388], the expansion rate H_0 [389] and thus the Hubble tension and the General Relativity in strong gravitational fields [390]. However, I point out that this Chapter is an exception compared to the other chapters as it assumes validity of General Relativity and the Standard ΛCDM model.

We use boundary conditions at large distance from the mass corresponding to a standing spherical gravitational wave in an expanding background which is equivalent to a linear combination of an incoming and an outgoing propagating gravitational wave. We compare the solution with the corresponding solution in the absence of the point mass and show that the point mass increases the amplitude of the wave and also decreases its frequency (as observed by an observer at infinity) in accordance with gravitational time delay. Also, the power spectrum of the spherical wave contains the low frequencies in bigger degree than the corresponding frequencies of the wave spectrum in the absence of mass.

The direct discovery of the GWs has been achieved by the LIGO/Virgo collaboration associating the GW150914 event [116, 117, 391] to the coalescence of a Binary Black Hole (BBH). This binary detection suggests that BBH masses and merging rates may be higher than estimated previously. The rates however, are in agreement with more recent estimates obtained with a population synthesis approach predicting the early formation of detectable BBH [392, 393]. Thus, the stochastic gravitational waves background (SGWB) produced by merging cosmological BBH sources could be larger than previously assumed [391] (and references therein) and may be detectable by advanced detectors [394]. Recent direct searches for continuous gravitational waves (CGW) from 15 well localized candidate neutron stars assuming none of the stars has a binary companion and an extrasolar planet candidate which has been suggested to be a nearby old neutron star failed to find any astrophysical signal [395].

A stochastic background of relic gravitational waves (RGWs) is predicted by inflationary models [396, 397] and has been well studied [398, 399]. The power spectrum of relic gravitational wave background reflects the physical conditions in the early Universe thus providing valuable information for cosmology [400]. This spectrum is determined by the early stage of inflation as well as by the expansion properties of the subsequent epochs, including the current one. The calculation of the spectrum [401, 402] was initially performed for a currently decelerating universe. However, it is now well known that the universe expansion is currently accelerating [16, 403] and since the evolution of RGWs depends on the expanding background space time, the spectrum of RGWs should be modified accordingly. This modification was confirmed and studied in Refs [404, 405] using the well-known formulation of GWs in an expanding Universe [406] and an approximation of the scale factor $a(\tau)$ in the context of a sequence of successive

expansion epochs, including the current stage of accelerating expansion. It was found that the current accelerating expansion induces modifications in both the shape and the amplitude of the RGW spectrum.

Since existence of RGWs is a key prediction of the inflationary models, their detection could provide evidence that inflation actually took place. Thus, it is important to accurately calculate the expected detailed form of the RGW spectrum. Calculations related to RGWs in an accelerating Universe have been performed [407] and a numerical method has been developed to calculate the power spectrum of the RGWs. Late evolution of RGWs in coupled dark energy models has been examined extensively in Ref. [408].

Even though the effects of cosmological expansion on GWs have been investigated mainly in the context of RGWs, these effects are relevant in all cases when the source is located at cosmologically large distances from the observer (redshift $z \geq 0.1$). The GW150914 ($z = 0.09$) event is in the limit of such distances and therefore, the effects of cosmic expansion may be relevant. Thus, a wide range of studies have investigated the effects of cosmological expansion of GWs from a variety of viewpoints such as

- the effects of expansion on the GW group and phase velocities [409, 410]
- mathematical aspects and exact solutions [411–415]
- quantum and thermodynamic properties of GWs [124, 416]
- general properties [414, 417, 418]
- nonlinear effects [419]
- properties of the GW energy momentum tensor [420]
- collision of GWs with electromagnetic waves [421]
- evolution of GWs in gravitational plasma [422]

Even though these studies have properly taken into account the expansion of the background metric, they have not taken into account the effects of the gravitational field of mass distributions on the evolution of the GWs. Such a gravitational field combined with the expanding background may induce new observable effects on the spectrum of propagating gravitational waves affecting the amplitude and the frequency of such waves, due to gravitational time delay [423].

Assuming spherical symmetry, the background metric around a point mass embedded in an expanding Friedmann-Lemaitre-Robertson-Walker (FLRW) cosmological background is well approximated by the McVittie [424, 425] spacetime. Such a metric is further simplified in the Newtonian limit and has been used as the background metric for the investigation of bound system geodesics in phantom and quintessence cosmologies [4, 229, 426, 427]. This metric can also be used as a background for the propagation of GWs in order to investigate the influence of a mass distribution of a GW propagating in an expanding cosmological background.

In the present Chapter we address the following question: 'What are the weak field effects of a point mass on a multipole component of a GW evolving in an expanding background in the vicinity of the mass?'. In particular we numerically solve the dynamical equation for the evolution of GWs in the background of the Newtonian McVittie metric and identify the effects induced by the point mass on the amplitude and frequency of the evolving GW as a function of the parameters, determining the mass and the background expansion rate. As a test of our analysis in the zero mass limit, our numerical solution reduces to the well known analytic solution of a GW evolving in an expanding background.

6.1 Wave equation as a result from Tensor Perturbations

We first briefly review the propagation evolution of a plane GW in the $\hat{z}$ direction (the direction of the wavevector $\vec{k}$) with tensor perturbations in the $x-y$ plane. The perturbations to the metric are described

by two functions, h_+ and $h_\times$, assumed small. We use the FRW metric in cartesian coordinates with the components $g_{00} = 1$, zero space-time components $g_{0i} = 0$, spatial elements and set $c = 1$. Thus, the spatial part of the metric is of the form

$$g_{ij} = -a^2(t) \begin{pmatrix} 1 + h_+ & h_\times & 0 \\ h_\times & 1 - h_+ & 0 \\ 0 & 0 & 1 \end{pmatrix} \tag{6.1}$$

The perturbation tensor H_{ij} is symmetric, divergenceless, traceless and has the form

$$H_{ij} = \begin{pmatrix} h_+ & h_\times & 0 \\ h_\times & -h_+ & 0 \\ 0 & 0 & 0 \end{pmatrix} \tag{6.2}$$

From the Einstein equations for tensor perturbations, it is easy to derive a set of equations governing the evolution of the tensor functions h_+ and $h_\times$. We write the FRW metric in Cartesian coordinates and in conformal time τ, which is defined by the relation

$$d\tau = dt/a$$

as follows

$$ds^2 = a^2(\tau)\Big(d\tau^2 - (\delta_{ij} + h_{ij})dx^i dx^j\Big) \tag{6.3}$$

The dynamical equation determining the evolution of the GWs is of the form

$$\boxed{\Box H_{ij} = \partial_\mu\Big(\sqrt{-g}\partial^\mu H_{ij}(\vec{r}, \tau)\Big) = 0} \tag{6.4}$$

Since all components of the tensor perturbations evolve in accordance with the same wave equation (6.4) we may set $H_k \equiv H_{ij}$. Without loss of generality we assume propagation in the z direction and thus we use the ansatz

$$\boxed{H_k(\tau, z) = h_k(\tau)e^{\pm ikz}} \tag{6.5}$$

Substituting Eq. (6.5) in (6.4) it is straightforward to derive the dynamical equation for the evolution of gravitational waves in conformal time in an FRW background as [428]

$$\boxed{h_k'' + 2\frac{a'}{a}h_k' + k^2 h_k = 0} \tag{6.6}$$

where the prime ($'$) denotes the derivative with respect to conformal time τ. Notice that both the perturbation tensor components h_+ and $h_\times$ obey the same equation. Further, we introduce a rescaling of conformal time as $\bar{\tau} = k\tau$ and thus it becomes clear that

$$h_k(\tau) = h(k\tau) \tag{6.7}$$

The rescaling expressed by Eq. (6.7) can only be made in conformal time provided that the scale factor is a power law $a(\tau) \sim \tau^\alpha$. In the radiation dominated epoch we have $\alpha = 1$ and during the matter dominated era $\alpha = 2$. We try to explore how the gravitational wave responds to all these modifications of the spacetime dynamics. The wave solution (6.5) can be converted in spherical coordinates as

$$\boxed{H_{ij}(\tau, \rho, \theta) = h(k\tau)e^{\pm ik\rho\cos\theta}} \tag{6.8}$$

The spectrum of the GWs may be obtained as [429]

$$\boxed{P(k, \tau) = \frac{4l_{Pl}}{\sqrt{\pi}}k \mid h_k(\tau) \mid} \tag{6.9}$$

The plane wave of equation (6.8) can be expanded in spherical waves, since

$$e^{ik\rho\cos\theta} = \sum_{l=0}^{\infty} i^l (2l+1) j_l(k\rho) P_l(\cos\theta) \tag{6.10}$$

where $j_l(x)$ are the spherical Bessel functions and $P_l(\cos\theta)$ are the Legendre's polynomials. Thus, the partial spherical GW is (at order l)

$$H_{ij}(\tau,\rho,\theta) \sim h(k\tau) j_l(k\rho) P_l(\cos\theta) \tag{6.11}$$

After rescaling, the dynamical equation (6.6) is written as

$$\boxed{h''(k\tau) + 2\frac{a'}{a}h'(k\tau) + h(k\tau) = 0} \tag{6.12}$$

where the prime ($'$) now denotes differentiation with respect to the rescaled conformal time $k\tau$.

Assuming a power law for the background scale factor as $a(\tau) \sim \tau^\alpha$, the solution of the wave equation (6.12) is of the form

$$h(k\tau) = \frac{1}{a(\tau)}\left(\tilde{A}_k\sqrt{k\tau}H^{(1)}_{\alpha-1/2}(k\tau) + \tilde{B}_k\sqrt{k\tau}H^{(2)}_{\alpha-1/2}(k\tau)\right) \tag{6.13}$$

where $H^{(1)}$, $H^{(2)}$ are the Hankel functions, while $\tilde{A}_k$ and $\tilde{B}_k$ are arbitrary constants which may depend on k and are determined by the initial conditions. The above solution (6.13) may also be written as

$$h(k\tau) = (k\tau)^{\frac{1}{2}-\alpha}\left(A_k J_{\alpha-1/2}(k\tau) + B_k Y_{\alpha-1/2}(k\tau)\right) \tag{6.14}$$

where J and Y are the Bessel functions of first and second kind respectively and $A_k = \tilde{A}_k k^\alpha$, $B_k = \tilde{B}_k k^\alpha$. For a power law scale factor the spherical GW is

$$\boxed{H_{ij}(\tau,\rho,\theta) = (k\tau)^{\frac{1}{2}-\alpha}\left(A_k J_{\alpha-1/2}(k\tau) + B_k Y_{\alpha-1/2}(k\tau)\right) j_l(k\rho) P_l(cos\theta)} \tag{6.15}$$

As a warm up exercise before the introduction of a point mass in the metric, we now rederive the solution (6.14), (6.15) starting from the FRW metric in spherical coordinates

$$ds^2 = a(\tau)^2\left(d\tau^2 - \left(d\rho^2 + \rho^2(d\theta^2 + \sin^2\theta d\phi^2)\right)\right) \tag{6.16}$$

Because of the azimuthal symmetry, the solution does not depend on the variable ϕ and we will seek solutions of the Eq. (6.4) of the form

$$H_{ij}(\tau,\rho,\theta,\phi) = f(\tau)R(\rho)P_l(cos\theta) \tag{6.17}$$

From the Eqs. (6.4), (6.17), after separation of variables we find

$$\frac{1}{R}\left(\frac{d^2R}{d\rho^2} + \frac{2}{\rho}\frac{dR}{d\rho} - \frac{l(l+1)}{\rho^2}\right) = -k^2 \tag{6.18}$$

and

$$\frac{1}{f}\left(\frac{d^2f}{d\tau^2} + \frac{2a'}{a}\frac{df}{d\tau}\right) = -k^2 \tag{6.19}$$

where k^2 is arbitrary constant. As expected Eq. (6.19) is identical to Eq. (6.6) while Eq. (6.18) is the spherical Bessel equation with acceptable solution

$$R_l(\rho) = A_l j_l(k\rho) \tag{6.20}$$

We thus reobtain the general solution in spherical coordinates (6.15).

6.2 Gravitational waves in the vicinity of a point mass

We can now generalize the above analysis to investigate the behavior of GWs when they interact with a point mass M. In the presence of a point mass and cosmological expansion, the appropriate background metric is the McVittie metric. In the Newtonian limit, using comoving coordinates the McVittie metric is [4, 430]

$$ds^2 = \left(1 - \frac{R_s}{\rho a(t)}\right)dt^2 - a(t)^2\left(d\rho^2 + \rho^2(d\theta^2 + \sin^2\theta d\phi^2)\right) \tag{6.21}$$

where

$$R_s = 2GM$$

is the Schwarzschild radius. The angular variable θ separates and thus we use the perturbation ansatz

$$H_{ij}(t, \rho, \theta, \phi) = Q(t, \rho)P_l(cos\theta) \tag{6.22}$$

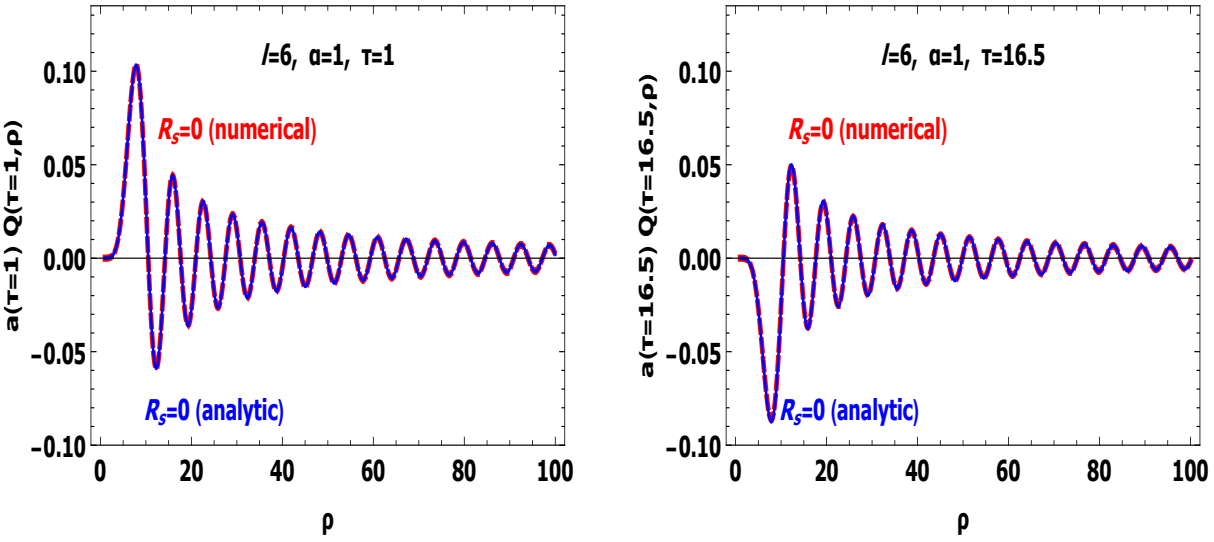

(a) A superposition of the analytic solution with the numerical simulation initial condition taken at $\tau = 1$. The spherical wave with $l = 6$ and scale factor $a(\tau) = \tau$ is shown.

(b) The numerically evolved solution for the gravitational wave $Q(\tau, \rho)$ at $\tau = 16.5$ with $R_s = 0$, is in excellent agreement with the corresponding analytic evolved solution.

Figure 6.1: Comparison between the analytic solution of Eq. (6.17) with the numerical simulation of (6.25), where the initial conditions taken at $\tau = 1$ (the time which appeared the point mass). The spherical wave with $l = 6$ and scale factor $a(\tau) = \tau$ is shown. We have plot the solutions for a couple of randomly chosen times, namely $\tau = 1$ and $\tau = 16.5$ and the results are identical. This is a test of the quality of the numerical solution.

Using the background metric (6.21) and the ansatz (6.22) in the gravitational wave equation (6.4) we obtain the dynamical equation for $Q(t, \rho)$ as

$$\frac{\partial^2 Q}{\partial\rho^2} + \frac{2}{\rho}(1 - \frac{3R_s}{4a\rho})(1 - \frac{R_s}{a\rho})^{-1}\frac{\partial Q}{\partial\rho} - \frac{l(l+1)Q}{\rho^2} = \frac{a^2}{1 - \frac{R_s}{a\rho}}\left(\frac{\partial^2 Q}{\partial t^2} + \frac{3\dot{a}}{a}(1 - \frac{7R_s}{6a\rho})(1 - \frac{R_s}{a\rho})^{-1}\frac{\partial Q}{\partial t}\right) \tag{6.23}$$

Assuming that

$$\frac{R_s}{a\rho} \ll 1 \tag{6.24}$$

and keeping terms $R_s/a\rho$ only in first order we can write Eq. (6.23) in conformal time as

$$\boxed{(1+\frac{R_s}{a\rho})\frac{\partial^2 Q}{\partial\tau^2}+\frac{2a'}{a}(1+\frac{3R_s}{4a\rho})\frac{\partial Q}{\partial\tau}=\frac{\partial^2 Q}{\partial\rho^2}+\frac{2}{\rho}(1+\frac{R_s}{4a\rho})\frac{\partial Q}{\partial\rho}-\frac{l(l+1)Q}{\rho^2}} \tag{6.25}$$

The above Eq. (6.25) is not separable and it is not tractable analytically in a simple manner. As expected, in the limit of zero mass ($R_s = 0$) it separates and reduces to Eqs. (6.18) and (6.19).

In the next section we integrate Eq. (6.25) numerically and investigate the dependence of the solution on the values of the parameter R_s. It will be seen that as the wave approaches the point mass it experiences two types of distortion

- gravitational time delay and increase of its period in conformal cosmological time.
- increase its amplitude in comparison with the amplitude it would have in the absence of the point mass.

According to general relativity the expected period of the wave at a comoving distance ρ from the point mass, as measured by an observer at infinity, is

$$\boxed{T=\frac{T_0}{\sqrt{1-\frac{R_s}{a\rho}}}} \tag{6.26}$$

where T_0 is the corresponding period at infinity (or in the absence of the mass). For small mass or large distance from the source the increase of the period as a fraction of T_0 is

$$\boxed{\frac{\Delta T}{T_0}=\frac{1}{2a\rho}R_s} \tag{6.27}$$

where $\Delta T = T - T_0$ is the difference of the wave periods with and without the presence of the mass. The validity of Eq. (6.27) for the GW in the vicinity of a point mass will be demonstrated numerically in the next section.

6.3 Numerical Analysis and Results

In order to keep the analogy with the massless case $R_s = 0$ we rescale the dynamical equation (6.25) to dimensionless form, using the wavenumber k defining $k\rho = \bar{\rho}$ and $k\tau = \bar{\tau}$. In this case we have an additional physical dimensionless parameter

$$\bar{R_s} = kR_s \tag{6.28}$$

In the numerical analysis which we present immediately we use only dimensionless quantities, even though we will omit the bar in what follows.

We solve numerically Eq. (6.25) with initial conditions corresponding to a standing gravitational wave evolving in a homogeneous FRW spacetime ($R_s = 0$) using Eq. (6.14) with $B_k = 0$ starting the evolution at $\tau = 1$. This is equivalent to assuming that the point mass appears at $\tau = 1$. For definiteness we set $\alpha = 1$ or $a(\tau) \sim \tau$ corresponding to an expanding background in the radiation era. The boundary conditions are imposed for Q and for its first derivative at large ρ where the effects of the point mass are negligible and also correspond to a standing GW evolving in a homogeneous FRW spacetime ($R_s = 0$) using Eq. (6.14) with $B_k = 0$.

We have used for the wave equation at large distance from the source the Bessel function boundary conditions (6.14) and (6.15), which describe a standing GW and however can be expressed as a superposition of two propagating modes (Hankel functions). The asymptotic behaviour of Hankel functions,

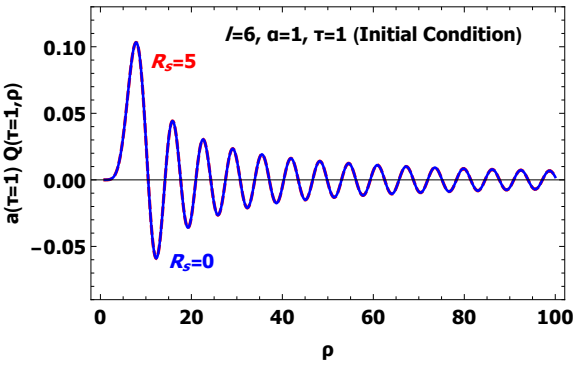

(a) Initially ($\tau = 1$), both waves in the presence or the absence of a point mass M have the same behaviour, since the waveforms are identical.

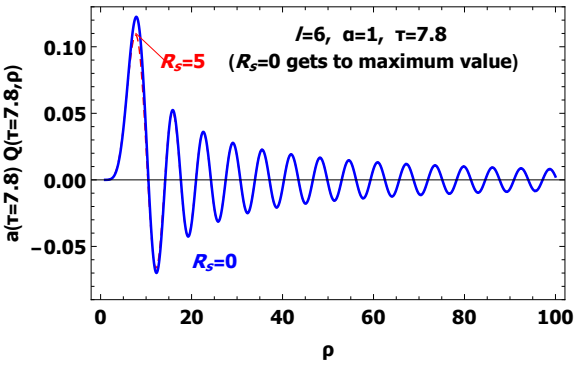

(b) The free wave reaches its maximum first, while the wave in the presence of the point mass shows a delay in reaching its maximum due to gravitational redshift.

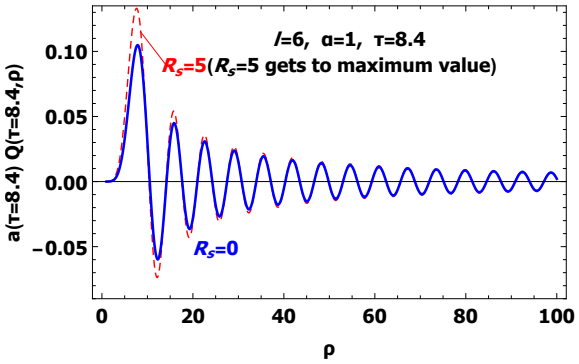

(c) The wave in the presence of the point mass shows a delay in reaching its maximum due to gravitational time delay.

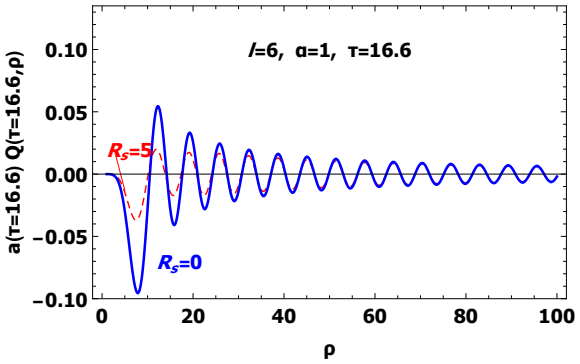

(d) The phase difference increases with time in the vicinity of the mass. This a obvious if we compare the red and blue line.

Figure 6.2: The evolution of the profile of a partial spherical gravitational wave with $l = 6$, $R_s = 5$ (red dashed line) in comparison with the corresponding free solution ($R_s = 0$, blue continuous line), which actually is a wave propagating in empty space. The wave in the presence of the mass has a higher amplitude (compare Fig. 6.2b with Fig. 6.2c) in the vicinity of the mass.

which is proportional to $e^{ik\tau}$, corresponds to a propagating GW, while the asymptotic behavior of Bessel functions is proportional to $\cos(k\tau)$ and corresponds to a standing GW.

We stress that, since we have made the Newtonian approximation (weak gravity, low velocities) our results are reliable in regions where the weak field condition (6.24) is satisfied. We thus construct numerically the solution $Q(\rho, \tau, R_s, l, \alpha)$ and compare with the corresponding analytical solution $Q(\rho, \tau, R_s = 0, l, \alpha)$. We have tested our numerical evolution by verifying that the numerical solution for $R_s = 0$ agrees with the corresponding analytical solution at a level better that 1% (Fig. 6.1).

Following the above comments about the boundary condition we fix Q (and its derivative with respect to conformal time) at the boundary $r_{end} > 500$ (far away from the point mass) as

$$Q(\tau, \rho_{bound}) = \frac{-ie^{-2i\sqrt{\tau}}(-1 + e^{4i\sqrt{\tau}})}{4\sqrt{\tau}} j_l(\rho_{bound}) \tag{6.29}$$

Similarly, the initial conditions set at $\tau_i = 1$ are

$$Q(\tau_i, \rho) = \frac{-ie^{-2i\sqrt{\tau_i}}(-1 + e^{4i\sqrt{\tau_i}})}{4\sqrt{\tau_i}} j_l(\rho) \tag{6.30}$$

and

$$\frac{\partial Q(\tau_i,\rho)}{\partial \tau} = \frac{\partial}{\partial \tau}\Big(\frac{-ie^{-2i\sqrt{\tau}}(-1+e^{4i\sqrt{\tau}})}{4\sqrt{\tau}} j_l(\rho)\Big)\Big|_{\tau=\tau_i} \tag{6.31}$$

In addition to the test of the validity of numerical solution presented in Fig. 6.1 we have performed other tests including the verification of the independence of the numerical solution from the location of the boundary for $r_{bound} > 200$.

We have solved the partial differential equation (6.25) for various values of l with results that are qualitatively similar. For definiteness we present in Fig. 6.2 the solution corresponding to $l = 6$ for $R_s = 5$ superposed with the corresponding solution for $R_s = 0$ in order to identify the new features introduced in the evolution of the GW by the presence of the point mass. There are three main features to observe in Fig. 6.2.

1. the waves are practically identical far away from the point mass as expected.
2. there is a time delay for the wave in the presence and in the vicinity of the point mass (Fig. 6.2b).
3. the amplitude of the wave in the presence and in the vicinity of the mass increases (compare Fig. 6.2b with Fig. 6.2c).

The main effect of the expansion is to reduce the amplitude of the gravitational wave by a factor proportional to the scale factor in the absence of the mass. This is shown in Fig. 6.3 which shows that the amplitude multiplied by the scale factor remains constant in the absence of the mass (blue oscillating line has constant amplitude) for the particular time dependence of the scale factor considered ($a(\tau) \sim \tau$). In the presence of the mass however, the increase of the amplitude due to the expansion is less efficient (red line) and the product of the amplitude times the scale factor increases slowly with time.

In Fig. 6.3 we show the conformal time evolution of the metric perturbation multiplied by the scale factor at $\rho = 7.9$ (closest maximum amplitude to the mass for $l = 6$) for $R_s = 5$ (red dashed line) superposed with the corresponding evolution for $R_s = 0$ (blue continuous line). We multiply the wave $Q(\tau,\rho)$ by the scale factor to eliminate the effects of the expansion that tend to decrease the gravitational wave amplitude. This plot shows more clearly the relative (linear) increase of the amplitude with time, as well as the increased period of the wave in the presence of the mass. It also demonstrates the well known fact that the wave amplitude in the absence of the mass ($R_s = 0$) is inversely proportional with the scale factor (the blue wave has a constant amplitude).

The effects of the gravitational time delay on the evolution of the wave may also be demonstrated by plotting the power spectrum obtained by a Fourier series expansion of the evolving in conformal time numerical solution at $\rho = 7.9$ in harmonic waves.

6.3.1 Effects on Power spectrum of wavefunction

The finite time interval power spectrum may be defined through the expansion of the numerical solution

$$\boxed{Q(\tau,\rho) = \frac{a_0}{2} + \sum_{i=1}^{n}(a_n \cos(n\tau) + b_n \sin(n\tau))} \tag{6.32}$$

as

$$\boxed{P(n) \equiv \log\sqrt{a_n^2 + b_n^2}} \tag{6.33}$$

where the coefficients a_n and b_n are determined by the Fourier expansion of the wavefunction $Q(\tau,\rho)$. We used a time interval of approximately two complete oscillations which corresponds to a time interval $[1, 20]$ ($t_i = 1, t_{max} = 20$ as shown in Fig. 6.4. The exact form of the spectrum clearly depends on the time interval considered, however the qualitative feature of higher amplitudes for lower frequencies persists for all time intervals. This feature is more prominent for lower values of ρ.

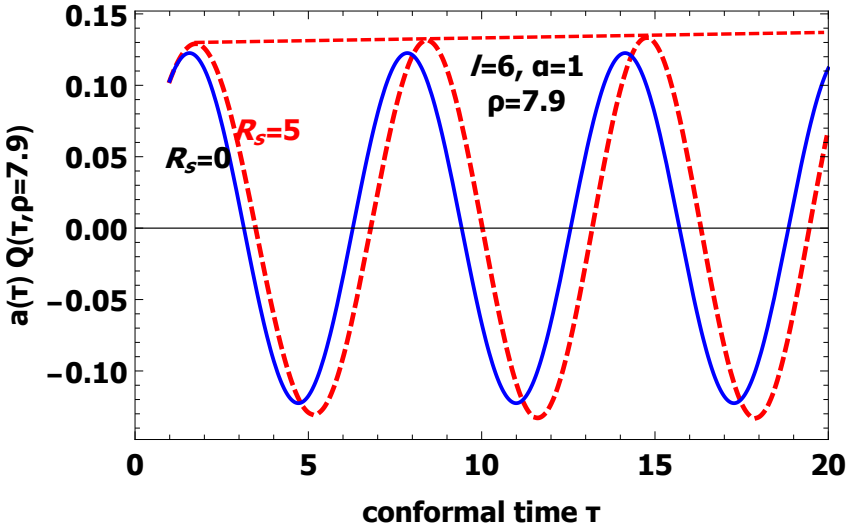

Figure 6.3: The time evolution of the first spatial maximum (at $\rho = 7.9$) of the partial spherical wave with $l = 6$, $R_s = 5$ (red line) in comparison with the corresponding free solution ($R_s = 0$, blue continuous line) at the same spatial point. The free wave reaches its maximum first (Fig. 6.2b) while the wave in the presence of the point mass shows a delay in reaching its maximum (Fig. 6.2c) due to gravitational redshift. The wave in the presence of the mass has an amplitude that increases with time as indicated with the dashed red line that in tangent to the gravitational wave maxima. As expected, the product $a(\tau)Q(\tau)$ is constant for the free wave in an expanding background.

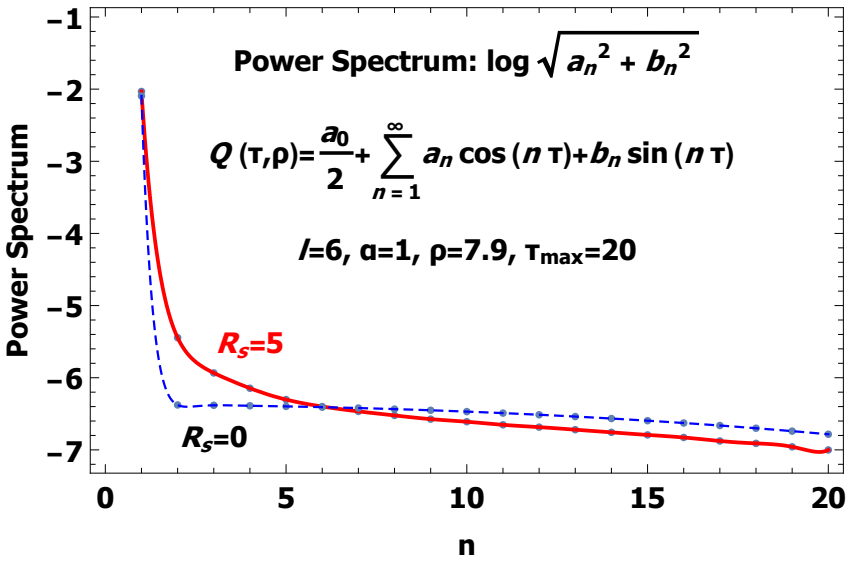

Figure 6.4: The time power spectra of the gravitational wave in the presence (red line) and in the absence (blue line) of the mass. Notice that lower frequencies have a higher amplitude for the wave in the presence of the mass as expected due to the gravitational time delay.

6.3.2 Effects on Period and Amplitude

As shown in Fig. 6.4, the presence of the mass (red continuous line) leads to an increase of the amplitude of low harmonics and to decrease of the amplitude of higher harmonics which is consistent with the effects

of gravitational time delay.

In accordance with Eq. (6.27) the increase of the period of the wave at a given distance from the mass is proportional to the mass in the weak field approximation. This is consistent with our numerical solution as shown in Fig. 6.5 where we show the relative increase of the period of the wave $\Delta T/T_0$ at given distances ρ ($\rho = 7.9$ and $\rho = 15.89$) from the mass for various values the parameter R_s (points in plot). In order to evaluate the relative change of the period $\Delta T/T_0$ we consider the time evolution of the wave perturbation as shown in Fig. 6.3 to obtain the period of the wave in the presence of the mass and the corresponding period in the absence of the mass. Superposed in Fig. 6.5 is the best fit straight line in each case. As is theoretically expected there is a linear relationship in accordance with Eq. (6.27). The correlation coefficients of the points with the corresponding best fit straight line are equal to 0.99 indicating an excellent quality of fit.

The theoretically predicted slope is $\frac{1}{2a\rho}$ where the scale factor can be taken as approximately constant and equal to its average value during a wave period.

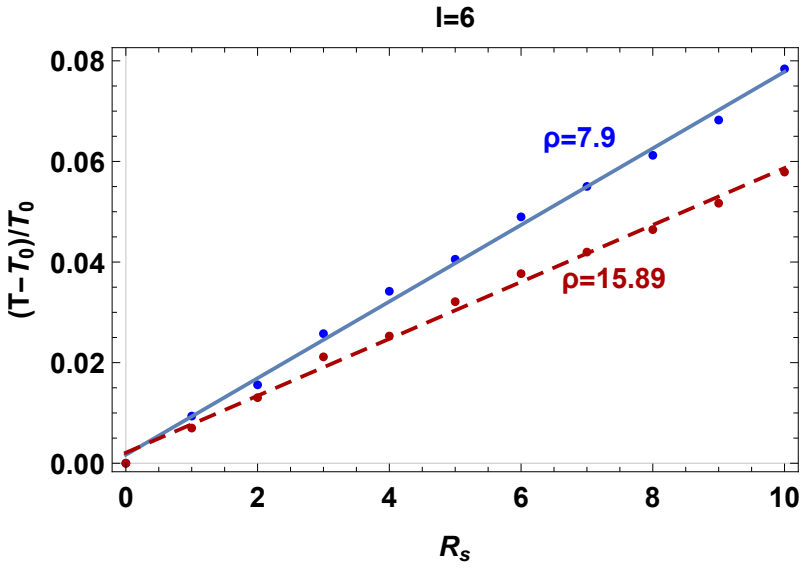

Figure 6.5: The relative difference of the wave periods $\Delta T/T_0$, where T is the period in the presence of mass and T_0 is the period in the absence of mass, as a function of R_s. It is clear that as the value of the variable ρ increases, the statistical slope of the curve decreases. This is an anticipated result due to theoretical slope of the curve, which is $\frac{1}{2a\rho}$.

In order to estimate the theoretical value of the scale factor, we calculate the mean value $\bar{a}(\tau)$, in the time interval $\tau_1 - \tau_2$ of a single period, through the formula

$$\bar{a}(\tau) = \frac{1}{\tau_2 - \tau_1} \int_{\tau_1}^{\tau_2} a(\tau) d\tau = \frac{\tau_2 + \tau_1}{2} \tag{6.34}$$

For $\rho = 7.9$ we considered the wave period starting from $\tau_1 = 3.15$ and ending at $\tau_2 = 10.55$. For this range of conformal time, the mean value of scale factor is $\bar{a} = 6.85$. Thus, the theoretical slope is 9.2×10^{-3} and the best fit slope from the plot, obtained through the least squares method, is 7.6×10^{-3}. Similarly, when $\rho = 15.89$ we considered the wave period starting from $\tau_1 = 3.15$ and ending at $\tau_2 = 10.15$. For this range of conformal time, the mean value of scale factor is $\bar{a} = 6.65$, the theoretical slope is 4.7×10^{-3} and the best fit slope from Fig. 6.5, through the least squares method, is 5.6×10^{-3}.

The observed deviations by about 20% between theoretically expected slope and numerically obtained can be attributed to the approximations we have made which include, the weak field assumption ($R_s \ll a\rho$ while in the cases considered $\frac{R_s}{a\rho} \leq 0.1$), the assumed constant scale factor for the evaluation of the slope

etc. As shown in Figs. 6.2 and 6.3 the amplitude of the wave also increases as the point mass is approached. A quantitative estimate of this effect is shown in Fig. 6.6 where we show the ratio of the amplitudes of the waves A/A_0 in the presence of a mass (A) and in the absence of the mass (A_0) for various values of the parameter R_s, when $\rho = 7.9$ and $\rho = 15.89$. The best fit straight line is also superposed on the points showing that a linear relationship between A/A_0 and R_s is a good approximation (the correlation coefficients of the points with the best fir straight lines are equal to 0.99) .

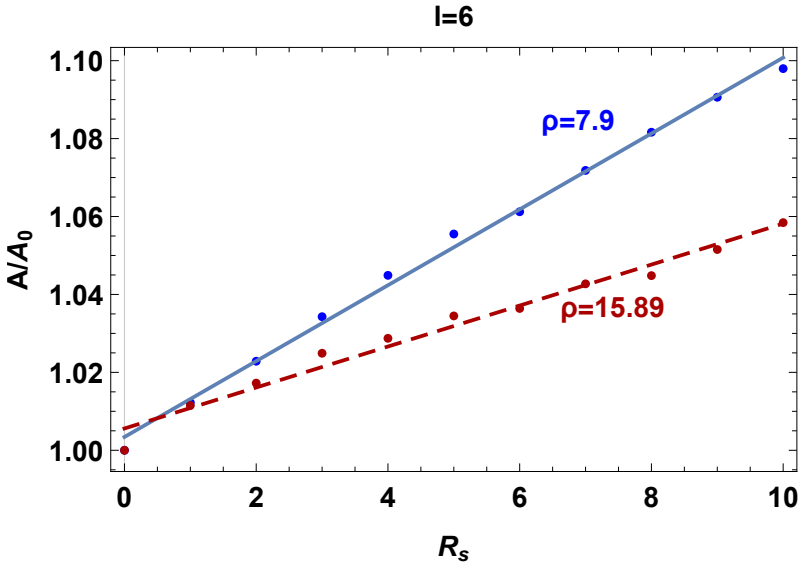

Figure 6.6: The ratio of the amplitudes of the waves A/A_0 in the presence of a mass (A) and in the absence of the mass (A_0) as a function of the parameter R_s, when $\rho = 7.9$ and $\rho = 15.89$. It is obvious that as the mass M increases and/or the distance ρ is decreased, the amplitude grows.

The amplitude increases up to 10% when $\rho = 7.9$ and $R_s = 10$, while for $\rho = 15.89$ the increase is about 5%. Thus the amplitude increase appears to vary inversely proportional with ρ which is consistent with the fact that the GW gains energy as it enters regions of space with higher curvature.

6.4 Cosmological Consequences and Conclusions

The effects of a point mass on a GW evolving in an expanding universe are determined by the mass M and the physical distance $r = a\rho$ of the wave from the mass through the expression $\frac{R_s}{a\rho} \equiv \frac{2GM}{a\rho}$ ($c = 1$). In the context of a perturbative weak field analysis we have demonstrated that a point mass tends to increase the amplitude and the period of the GW linearly with respect to $\frac{R_s}{a\rho}$. This result is consistent with expectations based on gravitational time delay and energy considerations.

Even though our numerical results were presented for the special case of a radiation dominated cosmological background ($a(\tau) \sim \tau$) and a specific multipole component of the wave ($l = 6$) we have checked that their qualitative features persist for all multipole components and cosmological backgrounds provided that the weak field condition (6.24) is respected. Thus, even though we have considered specific spherical waves in this analysis, we anticipate that our results can also describe a plane wave when expressed as a superposition of spherical waves.

The time slicing we considered corresponds to the coordinate time of the particular metric we used. This coordinate time is particularly interesting and generic as it corresponds to the proper time of a static observer located far away from the point mass or in the absence of the point mass. This is the standard cosmic observer whose observations are consistent with the cosmological principle. Clearly a different

choice of time slicing would correspond to a different observer and would lead to a different metric and thus different results.

We know that the energy density of GWs is proportional to $\omega^2 A^2$. From the results shown in Fig. 6.5 and Fig. 6.6, we conclude that $T = T_0(1+\mu R_s)$ and $A = A_0(1+\nu R_s)$ where μ and ν are the slopes of the curves which are approximately equal. Thus we have demonstrated that the energy density of GWs which is proportional to $\omega^2 A^2$ has a weak dependence on R_s in the context of our weak field approximation as long as the slopes μ and ν are approximately equal.

Our result has interesting implications for the calculation of the RGW spectrum which currently assumes [431–436] a smooth homogeneous cosmological background and ignores the presence of mass concentrations which as shown in this Chapter would tend to modify both the magnitude and the shape of this spectrum. A proper stochastic analysis including the effects of mass concentrations on the relic GW spectrum is therefore an interesting extension of this work.

A distortion of the RGW spectrum is expected due to the presence of point masses on various scales due to the increase of each mode amplitude and decrease of each mode frequency. The effect will be stronger in regions of higher mass concentrations. On scales larger than the galactic scales the role of the point mass could be played by a galaxy while on scales of the solar system the role of the point mass could be played by a planet. In the solar system the effect is expected to be rather weak of the order

$$\Delta T/T_0 \simeq 10^{-6}$$

Even though our numerical analysis has been well tested and provides detailed quantitative information on the GW evolution in the presence of expansion and a point mass, an analytical perturbative solution describing this evolution would provide further physical insight.

Chapter 7

Dissociation of Bound Systems in a Phantom Cosmological Background

In the course of this Chapter we investigate the geodesics in a Schwarzschild spacetime embedded in an isotropic expanding cosmological background (McVittie metric). We focus on bound particle geodesics in a background including matter and phantom dark energy with constant dark energy equation of state parameter $w < -1$, involving a future Big Rip singularity at a time t_*. Such geodesics have been previously studied in the Newtonian approximation and found to lead to dissociation of bound systems at a time $t_{rip} < t_*$ which for fixed background w, depends on a single dimensionless parameter $\bar{\omega}_0$ related to the angular momentum and depending on the mass and the size of the bound system. The contents of this chapter are a deviation from the standard model since it investigates the effects of deviations from the Standard ΛCDM expansion rate on bound systems and especially of their future evolution in the case when the acceleration of the Universe increases rapidly in the future (phantom cosmologies) compared to the Standard ΛCDM cosmic acceleration.

We extend this analysis to large massive bound systems where the Newtonian approximation is not appropriate and we compare the derived dissociation time with the corresponding time in the context of the Newtonian approximation. By identifying the time when the effective potential minimum disappears due to the repulsive force of dark energy we find that the dissociation time of bound systems occurs earlier than the prediction of the Newtonian approximation. Also, the systems become stable for longer time when the mass of the system decreases and/or the angular velocity increases. However, the effect is negligible for all existing cosmological bound systems and it would become important only in hypothetical bound extremely massive ($10^{20} M_{\odot}$) and large ($100 Mpc$) bound systems. We verify this result by explicit solution of the geodesic equations. This result is due to an interplay between the repulsive phantom dark energy effects and the existence of the well known innermost stable orbits of Schwarzschild spacetimes.

A generalization of ΛCDM model where the cosmic acceleration is induced by a dark energy fluid with constant equation of state introduces a new parameter w in the models which is constrained by cosmological observations at the 1σ level to be in the range [437–440]

$$-1.5 < w < -0.7. \tag{7.1}$$

Based on these constraints and in the context of the above minimal generalization of ΛCDM there is a significant probability that $w < -1$, which corresponds to *Phantom Cosmology*. For such a range of w, this class of models predicts the existence of a future singularity, which is known as the *Big Rip singularity*, where the scale factor diverges at a finite future time.

This behavior emerges by solving the Friedmann equations in the presence of matter density ρ_m and dark energy density ρ_{de} (negligible radiation density) which may be written as [229, 441]

$$\frac{\dot{a}^2}{a^2} = \frac{8\pi G}{3}\left(\rho_m + \rho_{de}\right) = H_0^2\left(\Omega_m^0 (\frac{a_0}{a})^3 + \Omega_{de}^0 (\frac{a_0}{a})^{3(1+w)}\right) \tag{7.2}$$

and

$$\begin{aligned}\frac{\ddot{a}}{a} &= -\frac{4\pi G}{3}\Big(\rho_m + \rho_{de}(1+3w)\Big) = -\frac{4\pi G}{3}\rho_{de}\big(\Omega_{de}^{-1}+3w\big) \\ &= -\frac{4\pi G}{3}\rho_{de}\left(\frac{\Omega_m^0}{\Omega_{de}^0}(\frac{a_0}{a})^{-3w}+1+3w\right) \end{aligned} \tag{7.3}$$

Solving the system of these equations (7.2) and (7.3), we derive the scale factor as

$$a(t) = \frac{a(t_m)}{\Big(-w+(1+w)\frac{t}{t_m}\Big)^{-\frac{2}{3(1+w)}}}, \qquad t > t_m \tag{7.4}$$

where t_m is the time when the dark energy density becomes larger than the matter density. For $w < -1$ the scale factor and its derivatives diverge, when the denominator vanishes at a finite time (the Big Rip time) [442–445]. It is clear that the time t_* of Big Rip singularity is

$$t_* = \frac{w}{1+w}t_m > 0 \tag{7.5}$$

This divergence results in a diverging repulsive gravitational force which rips apart all bound systems at times $t_{rip} < t_*$ that depend on their binding energies and forms of effective potentials.

An important question to address is: *What is the physical mechanism that induces this dissociation of bound systems and what is the time when the dissociation occurs as a function of w?* In order to address this question, a gravitationally bound system may be represented as a single test particle bound in a circular orbit of radius r_0 by the gravitational force of a central spherical massive object of mass m. The features of the trajectory of the test particle may be obtained in any of the following ways

1. Using a rough comparison of the attractive gravitational force with the repulsive force induced by the expansion [442].

2. By using a derivation of the particle trajectory using equations of motion in the Newtonian approximation (weak gravity, low velocities) which take into account the attractive gravitational force, the repulsive force due to the expansion as well as the centrifugal effects due to angular momentum [229, 446–448].

3. Using the full relativistic geodesic equations obtained from a metric that is a solution of the Einstein equations and interpolates between a Schwarzschild metric and an FRW metric. Such a metric is the McVittie metric [424]. Other approaches to such an interpolation may be found in Refs. [449–451].

Previous studies have pursued the first two approaches with results that are in qualitative agreement within a factor of 3. According to the approach of Ref. [229], the dissociation of the bound system is associated with the disappearance of the minimum of the effective potential that determines the radial motion of the test particle. This minimum disappears when the dynamics become dominated by the effects of the accelerating expansion of the phantom cosmological background. Thus, the dissociation of a bound system occurs at a time t_{rip} given by

$$t_* - t_{rip} = \frac{16\sqrt{3}}{9}\frac{T\sqrt{2|1+3w|}}{6\pi|1+w|} \tag{7.6}$$

where T is the period of the gravitationally bound system with mass m, radius r_0 and angular velocity ω_0 of the form

$$\omega_0^2 \equiv (\frac{2\pi}{T})^2 = \frac{Gm}{r_0^3} \tag{7.7}$$

This result improves over the corresponding result of Ref. [442] by the factor $16\sqrt{3}/9 \simeq 3$ because it takes into account the effects of the centrifugal term and provides a clear definition of the dissociation time as the time when the minimum of the effective potential disappears due to the domination of the repulsive gravitational effects of the expansion. On the other hand, the analysis of Ref. [229] is limited by the fact that it uses the Newtonian approximation for the dynamical equations of the particle orbits and therefore it may not be applicable for the analysis of the dissociation of strongly bound systems like accretion disks [452, 453].

In this Chapter we extend the analysis of Ref. [229] by going beyond the Newtonian approximation and taking into account relativistic effects. In particular, we consider the full geodesics corresponding to the McVittie metric in a phantom cosmological background. Using these geodesic equations we construct the relativistic effective potential corresponding to bound particle orbits and derive the time of dissociation (t_{rip}) when the minimum of the potential disappears due to expansion effects. These results are confirmed by comparing with numerical solutions of the geodesic equations corresponding to initial circular bounded orbits. We compare these results with the corresponding results of previous studies [229] obtained in the Newtonian limit.

7.1 Geodesic equations in McVittie spacetime

An acceptable way to describe a bound system embedded in an expanding cosmological background is provided by the McVittie metric [424]. For a flat cosmological background this metric is of the form

$$ds^2 = -(f - \frac{r^2H^2}{c^2})d(ct)^2 - 2rHf^{-1/2}dtdr + f^{-1}dr^2 + r^2d\Omega^2 \tag{7.8}$$

where $m > 0$ is a constant,

$$f = f(r) = 1 - 2Gm/(c^2r) > 0$$

and $H = H(t) = \frac{\dot{a}}{a}$ is the Hubble parameter of the cosmological background. In what follows we do not set $c = G = 1$ in order to clearly show the Newtonian limit ($c \to \infty$).

In Eq. (7.8) the physical spatial coordinate r connected with the comoving spatial coordinate ρ with the relation $\rho = \frac{r}{a(t)}$. Setting $m = 0$ and using the comoving coordinate we obtain the flat background FRW metric

$$\begin{aligned} ds^2 &= -(1 - r^2H^2)d(ct)^2 - 2rHdtdr + dr^2 + r^2d\Omega^2 \\ &= -dt^2 + a^2(d\rho^2 + \rho^2d\Omega^2) \end{aligned} \tag{7.9}$$

Similarly, setting $H = 0$ the metric (7.8) reduces to the Schwarzschild metric.

The Schwarzschild-de Sitter metric may also be obtained as a special case of the McVittie metric by fixing the Hubble parameter to a constant $H^2 = H_0^2 = \frac{\Lambda}{3}$ and performing a coordinate transformation [427]

$$T = t + u(r) \tag{7.10}$$

with

$$u'(r) = \frac{H_0 r}{c}\left(\sqrt{f}(f - \frac{r^2H^2}{c^2})\right) \tag{7.11}$$

leading to the Schwarzschild de Sitter (or Köttler) metric

$$ds^2 = -(1 - \frac{2Gm}{c^2r} - \frac{\Lambda}{3}r^2)d(cT)^2 - (1 - \frac{2Gm}{c^2r} - \frac{\Lambda}{3}r^2)^{-1}dr^2 + r^2d\Omega^2 \tag{7.12}$$

In the Newtonian limit, using comoving coordinates, the McVittie metric may be written as [229, 426]

$$ds^2 = \left(1 - \frac{2Gm}{c^2a(t)\rho}\right)d(ct)^2 - a(t)^2\left(d\rho^2 + \rho^2(d\theta^2 + \sin^2\theta d\varphi^2)\right) \tag{7.13}$$

The Newtonian geodesics corresponding to the metric (7.13) are of the form [451, 454]

$$\ddot{r} - \frac{\ddot{a}}{a} r + \frac{Gm}{r^2} - r\dot{\varphi}^2 = 0 \tag{7.14}$$

and

$$r^2 \dot{\varphi} = L \tag{7.15}$$

where r is the physical coordinate ($r = a\rho$) and L is the angular momentum per unit mass ($L = \omega r^2$), which is a constant of motion. Combining Eqs. (7.14) and (7.15) we find the radial dynamical equation in the Newtonian limit

$$\ddot{r} = \frac{\ddot{a}}{a} r + \frac{L^2}{r^3} - \frac{Gm}{r^2} \tag{7.16}$$

Notice that c does not appear in this equation since it is non-relativistic. If we ignore the term due to the expansion (the first term in the R.H.S. of Eq. (7.16)), then the angular velocity of a test particle in a bound circular orbit with radius r_0 at an initial time t_0 is obtained from Eq. (7.16) as

$$\dot{\varphi}(t_0)^2 = \omega_0^2 = \frac{Gm}{r_0^3} \tag{7.17}$$

The radius of the circular orbit will be perturbed once the expansion is turned on but the above Eq. (7.17) remains a good approximation close to the end of the era of matter domination (Eq. (7.16)) $t_m = t_0$, when the expansion repulsive force is subdominant. It is convenient to rescale Eq. (7.16) to a dimensionless form by defining the dimensionless quantities $\bar{r} \equiv \frac{r}{r_0}$, $\bar{\omega}_0 \equiv \omega_0 t_0$ and $\bar{t} \equiv \frac{t}{t_0}$. The choice of this rescaling is made so that the effect of the expansion is initially small (at time $\bar{t} = 1$) and the initial minimum of the effective potential is approximately at $\bar{r} = 1$. Typical values of $\bar{\omega}_0$ are obtained using the scale and the mass of bound systems. Thus $\bar{\omega}_0$ is of order $O(1)$ for a cluster of galaxies, about 200 for a galaxy and 10^6 for the solar system.

Assuming a constant w and using the form of the scale factor in Eq. (7.4), the radial dynamical equation (7.16) takes the form

$$\ddot{\bar{r}} + \frac{\bar{\omega}_0^2}{\bar{r}^2}(1 - \frac{1}{\bar{r}}) + \frac{2}{9}\frac{(1+3w)\bar{r}}{\Big(-w + (1+w)\bar{t}\Big)^2} = 0 \tag{7.18}$$

From Eq. (7.18) we derive the effective radial force

$$F_{eff} = -\frac{\bar{\omega}_0^2}{\bar{r}^2}\left(1 - \frac{1}{\bar{r}}\right) - \frac{2}{9}\frac{(1+3w)\bar{r}}{\Big(-w + (1+w)\bar{t}\Big)^2} \tag{7.19}$$

and the corresponding effective potential

$$V_{eff} = -\frac{\bar{\omega}_0^2}{\bar{r}} + \frac{\bar{\omega}_0^2}{2\bar{r}^2} - \frac{1}{2}\lambda(\bar{t})^2\bar{r}^2 \tag{7.20}$$

where (for $w < -1$)

$$\lambda^2(\bar{t}) = \frac{2}{9}\frac{(1+3w)}{\Big(-w + (1+w)\bar{t}\Big)^2} \tag{7.21}$$

The repulsive term $\frac{1}{2}\lambda(\bar{t})^2\bar{r}^2$, which occurs in the effective force or potential describes the expansion of the spacetime, is proportional to λ^2, increases with time and at a time $\bar{t}_{rip}$ given by Eq. (7.6), it destroys the effective potential minimum induced by the interplay between the attractive gravity and centrifugal terms. Thus a bound system gets dissociated by the expansion at time $\bar{t} = \bar{t}_{rip}$ [229].

This analysis, which made in the context of the Newtonian approximation, is inappropriate for some massive large strongly bound systems where relativistic effects need to be taken into account. A proper relativistic analysis requires the use of the geodesic equations obtained from the McVittie metric Eq. (7.8). These dynamical equations are of the form [427]

$$\ddot{r} = rf^{1/2}H'\dot{t}^2 + (1 - \frac{3Gm}{c^2 r})\frac{L^2}{r^3} - \frac{Gm}{r^2} + rH^2 \tag{7.22}$$

and

$$\ddot{t} = -(1 - \frac{3Gm}{rc^2})f^{-1/2}H\dot{t}^2 - \frac{2Gm}{r^2}f^{-1}\dot{t}\dot{r} + f^{-1/2}H \tag{7.23}$$

The overdot represents the derivative with respect to the proper time τ and the prime represents derivative with respect to the coordinate time t. A first integral of these equations may also be obtained as

$$\chi\dot{t}^2 + 2\frac{\alpha\dot{t}\dot{r}}{c} - \frac{f^{-1}\dot{r}^2}{c^2} - \frac{L^2}{c^2 r^2} = 1 \tag{7.24}$$

where

$$\chi(t,r) = f - \frac{r^2H^2}{c^2} \qquad \text{and} \qquad \alpha(t,r) = \frac{rf^{-1/2}H}{c} \tag{7.25}$$

We may choose $\dot{t} > 0$ along causal geodesics and focus on the system of the radial geodesic Eq. (7.22) coupled with the first integral (7.24).

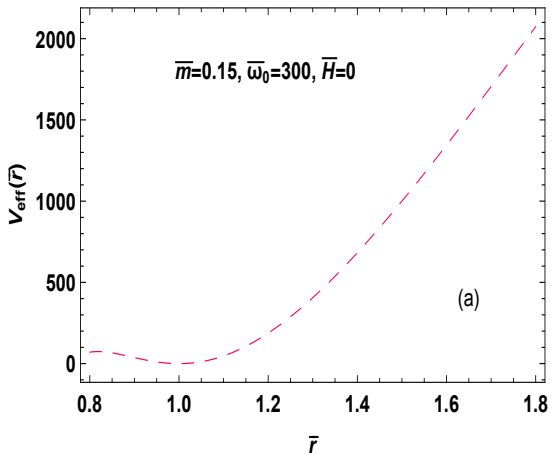

(a) Variation of the effective potential as a function of $\bar{r}$ when $\bar{m} = 0.15 < \frac{1}{6}$. The bound system is stable, since the potential has a minimum.

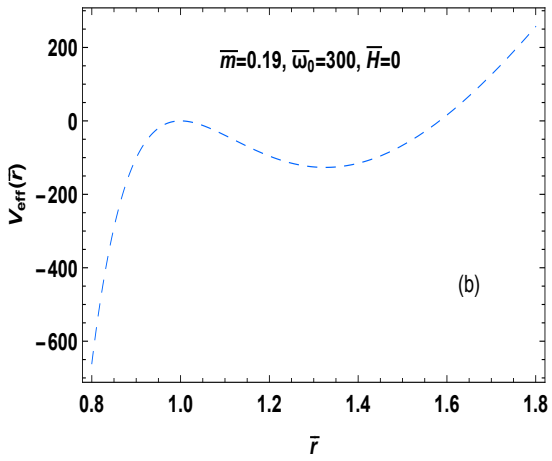

(b) Variation of the effective potential as a function of $\bar{r}$ when $\bar{m} = 0.19 > \frac{1}{6}$. The minimum is less than $\bar{m} = 0.15$, but the system is stable.

Figure 7.1: The effective potential as a function of $\bar{r}$ in a static universe when $\bar{\omega}_0 = 300$ for $\bar{m} = 0.15 < \frac{1}{6}$ and $\bar{m} = 0.19 > \frac{1}{6}$ (below and above the critical value $\bar{m} = 1/6$ respectively). The bound systems are stable, since the minimum remains. The mass of the system affects the position and the value of the minimum.

As a first step towards the investigation of this system we use a proper rescaling. In particular we assume a background expansion model corresponding to constant $w < -1$ (Eq. (7.4)) and rescale the system using the scales r_0 (circular orbit radius in the absence of expansion) and $t_0 = t_m$. We then define the dimensionless quantities: $\bar{t} \equiv t/t_0$, $\bar{\tau} \equiv \tau/t_0$ (τ is the proper time), $\bar{r} \equiv r/r_0$, $\bar{m} \equiv Gm/r_0c^2$, $\bar{H} \equiv Ht_0$, $\bar{\omega}_0 \equiv \omega_0 t_0$. Using the dimensionless coordinates, the radial geodesic (7.22) and the first integral (7.24) take the form

$$\ddot{\bar{r}} = \bar{r}f^{1/2}\bar{H}'\dot{\bar{t}}^2 + (1 - \frac{3\bar{m}}{\bar{r}})\frac{\bar{\omega}_0^2}{\bar{r}^3} - \frac{\bar{m}}{\bar{r}^2}(\frac{ct_0}{r_0})^2 + \bar{r}\bar{H}^2, \tag{7.26}$$

and

$$\left(f-(\frac{r_0}{ct_0})^2\bar{r}^2\bar{H}^2\right)\dot{\bar{t}}^2+2(\frac{r_0}{ct_0})^2\bar{r}\bar{H}f^{-1/2}\dot{\bar{t}}\dot{\bar{r}}-\frac{\dot{\bar{r}}^2}{f}(\frac{r_0}{ct_0})^2-\frac{\bar{\omega}_0^2}{\bar{r}^2}(\frac{r_0}{ct_0})^2=1 \tag{7.27}$$

where f is expressed in terms of $\bar{m}$ as

$$f=1-\frac{2\bar{m}}{\bar{r}} \tag{7.28}$$

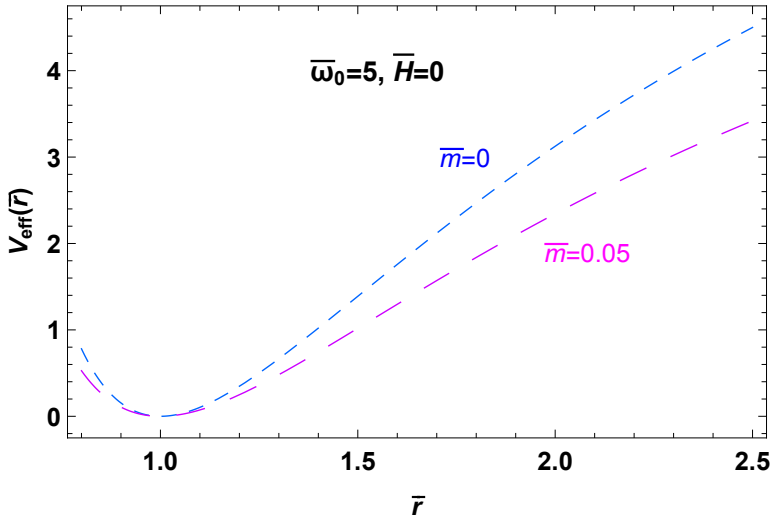

Figure 7.2: The effective potential as a function of distance $\bar{r}$, when $\bar{\omega}_0=5$, $\bar{m}=0$ and $\bar{m}=0.05$ with the effects of expansion turned off. The relativistic effects tend to make the bound state weaker and more susceptible to dissociation due to the effects of the expansion, while the minimum of the potential changes slightly. The stronger effects of gravity in the relativistic case tend to destabilize rather than stabilize bound systems.

We now determine the scale distance r_0 for the relativistic case considered here and compare with the corresponding Newtonian scale. The effective radial force in the absence of cosmological expansion ($H=0$) takes the form

$$F_{eff}=(1-\frac{3\bar{m}}{\bar{r}})\frac{\bar{\omega}_0^2}{\bar{r}^3}-\frac{\bar{m}}{\bar{r}^2}(\frac{ct_0}{r_0})^2 \tag{7.29}$$

which vanishes for ($\bar{r}=1$)

$$\bar{\omega}_0=\frac{ct_0}{r_0}\sqrt{\frac{\bar{m}}{1-3\bar{m}}} \tag{7.30}$$

Equation (7.30) constitutes also the definition of the scale r_0 used for the rescaling of the geodesic equations. From Eqs. (7.22) and (7.30) we obtain the dimensionless form of the radial geodesic equation

$$\ddot{\bar{r}}=\bar{r}f^{1/2}\bar{H}'\dot{\bar{t}}^2+(1-\frac{3\bar{m}}{\bar{r}})\frac{\bar{\omega}_0^2}{\bar{r}^3}-\frac{(1-3\bar{m})\bar{\omega}_0^2}{\bar{r}^2}+\bar{r}\bar{H}^2 \tag{7.31}$$

Similarly, the dimensionless form of the first integral Eq. (7.24) is

$$\left(\frac{\bar{r}^2\bar{m}\bar{H}^2}{\bar{\omega}_0^2(1-3\bar{m})}-f\right)\dot{\bar{t}}^2+\frac{2\bar{m}}{\bar{\omega}_0^2(1-3\bar{m})}\bar{r}\bar{H}f^{-1/2}\dot{\bar{t}}\dot{\bar{r}}-\frac{\dot{\bar{r}}^2}{f\bar{\omega}_0^2}\frac{\bar{m}}{1-3\bar{m}}-\frac{\bar{m}}{\bar{r}^2(1-3\bar{m})}=1 \tag{7.32}$$

The Newtonian limit is obtained for $c\to\infty$ which corresponds to

$$\bar{m}\equiv\frac{Gm}{c^2r_0}\to 0 \tag{7.33}$$

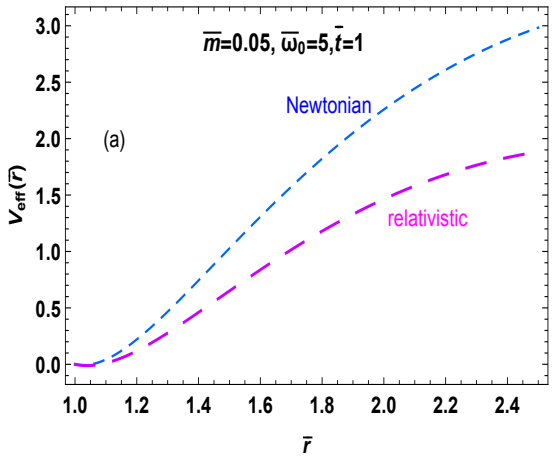

(a) The effective potential with the effects of the expansion have been turned on ($H \neq 0$, $w = -1.2$) but the time shown is before the bound system dissociation time $\bar{t}_{rip}$.

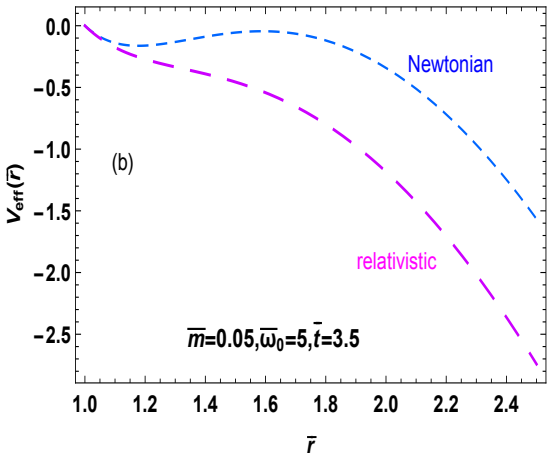

(b) The form of the effective potential for $t = 3.5t_m$, where the system has been dissociated according to the full relativistic analysis but it remains bound according to the Newtonian approximation.

Figure 7.3: The relativistic effective potential before (left) and after (right) the dissociation when $\bar{\omega}_0 = 5$ and $\bar{m} = 0.05$. Both cases, the Newtonian potential describes a bound system, since the minimum exists (no dissociation). Clearly, the relativistic effects tend to dissociate the bound systems earlier.

As expected, in this limit we obtain $\dot{\bar{t}} = 1$ from the integral equation (7.32) while the radial equation reduces to the corresponding Newtonian equation (7.16). Similarly, in this limit the scale r_0 (defined through (7.30)) reduces to the corresponding Newtonian scale (Eq. (7.17)) since $c^2\bar{m} = \frac{Gm}{r_0}$.

Therefore, assuming a fixed expanding cosmological background, the geodesics in the McVittie metric are fully determined by two dimensionless parameters $\bar{m}$ and $\bar{\omega}_0$ while the corresponding Newtonian orbits are determined by a single parameter ($\bar{\omega}_0$) and are obtained as the limit $\bar{m} \to 0$ of the relativistic orbits. The dimensionless parameters $\bar{m}$ and $\bar{\omega}_0$ are obtained from the mass m (measured in solar masses $M_\odot$) and the scale r_0 (measured in Mpc) of the physical system by the relations

$$\boxed{\bar{m} \simeq \frac{5 \times 10^{-20} m}{r_0}} \tag{7.34}$$

and

$$\boxed{\bar{\omega}_0 \simeq \frac{1780}{r_0}\sqrt{\frac{\bar{m}}{1-3\bar{m}}}} \tag{7.35}$$

while the reverse relations (expressions for m and r_0) are

$$\boxed{m \simeq \frac{3.5 \times 10^{22}\bar{m}}{\bar{\omega}_0}\sqrt{\frac{\bar{m}}{1-3\bar{m}}}} \tag{7.36}$$

and

$$\boxed{r_0 \simeq \frac{1780}{\bar{\omega}_0}\sqrt{\frac{\bar{m}}{1-3\bar{m}}}} \tag{7.37}$$

In the Schwarzschild limit ($H = 0$) the radial geodesic equation becomes

$$\boxed{\ddot{\bar{r}} = (1 - \frac{3\bar{m}}{\bar{r}})\frac{\bar{\omega}_0^2}{\bar{r}^3} - \frac{(1-3\bar{m})\bar{\omega}_0^2}{\bar{r}^2}} \tag{7.38}$$

The effective radial force (r.h.s. of Eq. (7.38)) has two roots given by the values

$$\bar{r} = 1, \qquad \bar{r} = \frac{3\bar{m}}{1-3\bar{m}} \tag{7.39}$$

The root $\bar{r} = 1$ is easily shown (by considering the derivative of the effective force) to correspond to a stable circular orbit for $\bar{m} < \frac{1}{6}$ while for $\frac{1}{6} < \bar{m} < \frac{1}{3}$ the root $\bar{r} = \frac{3\bar{m}}{1-3\bar{m}} > 1$ corresponds to a weakly stable circular orbit. We therefore recover the well known fact that the innermost stable circular orbit of the Schwarzschild metric is obtained for $\bar{m} = \frac{1}{6}$ which corresponds to a radius $r_0 = \frac{6Gm}{c^2} = 3R_s$.

In Fig. 7.1 we show the effective potential obtained by integration of the effective force of Eq. (7.29) for $\bar{m} = 0.15 < \frac{1}{6}$ and for $\bar{m} = 0.19 > \frac{1}{6}$. The plot shows the development of the local maximum of the effective potential at $\bar{r} = 1$ when $\bar{m} > \frac{1}{6}$ and the development of a new minimum at $\bar{r} > 1$. Interestingly, the new minimum is weaker and there is less restoring force for perturbations towards larger $\bar{r}$. Thus, as $\bar{m}$ increases towards the limiting value of $\frac{1}{3}$ (beyond this value there is no circular orbit) the circular orbit becomes less stable and susceptible to destabilization by the repulsive effects of the accelerating expansion.

We now turn on the expansion to investigate how affects the effective radial force and the potential of the radial geodesics. For definiteness we set $w = -1.2$ (where $\bar{t}_* = 6$) which corresponds to a phantom background expansion consistent with current observational constraints [437]. The effective force may be obtained in the general relativistic geodesics when expansion is present by solving the first integral Eq. (7.32) for $\dot{\bar{t}}^2$ and substituting in the radial geodesic Eq. (7.31). Assuming a slow shift of the location of the potential minimum with time, we ignore the terms proportional to $\dot{\bar{r}}$ in constructing the effective force and the effective potential. This approximation is justified in the next section where we obtain the numerical solution of the full system of the coupled geodesic equations (7.32) and (7.31). The effective force thus obtained is of the form

$$\boxed{F_{eff} = \bar{r} f^{1/2} \bar{H}' \left(\frac{1 + \frac{\bar{m}}{\bar{r}^2(1-3\bar{m})}}{f - \frac{\bar{r}^2 \bar{H}^2 \bar{m}}{\bar{\omega}_0^2(1-3\bar{m})}} \right) + \left(1 - \frac{3\bar{m}}{\bar{r}}\right) \frac{\bar{\omega}_0^2}{\bar{r}^3} - \left(1 - 3\bar{m}\right) \frac{\bar{\omega}_0^2}{\bar{r}^2} + \bar{r}\bar{H}^2} \tag{7.40}$$

The corresponding effective potential may be obtained by integrating numerically the effective force F_{eff} through the relation

$$V_{eff}(\bar{r}) = -\int_1^r F_{eff}(\bar{r}')d\bar{r}' \tag{7.41}$$

In Fig. 7.2 we present a plot of the effective potential for $\bar{m} = 0$ and $\bar{m} = 0.05$ with the effects of expansion turned off. The plot shows that the relativistic effects tend to make the bound state weaker and more susceptible to dissociation due to the effects of the expansion. This effect is related to the development of the local maximum (Fig. 7.1) of the relativistic potential for a radius smaller than the radius of the stable orbit (potential minimum) which is also the reason for the existence of an innermost stable circular orbit. Thus in contrast to naive intuition, the stronger effects of gravity in the relativistic case tend to destabilize rather than stabilize bound systems.

This is also demonstrated in Fig. 7.3a where the effects of the expansion have been turned on ($H \neq 0$, $w = -1.2$) but the time shown is before the bound system dissociation time $\bar{t}_{rip}$. Clearly, the binding power of the potential has been weakened on large scales in both the relativistic (lower curve) and the Newtonian case (upper curve). At $t = 3.5t_m$ the bound system relativisticaly has dissociated, while classically the system is stable. Fig. 7.3b shows the form of the effective potential for $t = 3.5t_m$.

At that time the system has been dissociated according to the full relativistic analysis but it remains bound according to the Newtonian approximation.

It is therefore clear that relativistic effects tend to destabilize bound systems leading to an earlier dissociation (smaller value of $\bar{t}_{rip}$) compared to the predictions in the context of the Newtonian approximation. In the next section we verify this result by a full numerical solution of the geodesic equations (7.31) and (7.32) and we present a quantitative analysis of the magnitude of the relativistic correction required for various bound systems defined by the dimensionless parameters $\bar{\omega}_0$ and $\bar{m}$.

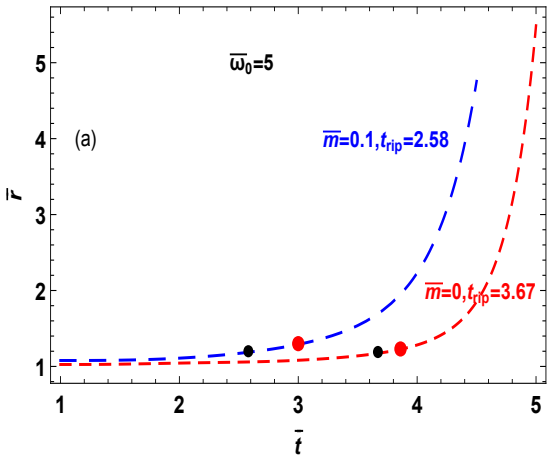

(a) The radius $\bar{r}$ as a function of $\bar{t}$ when $\bar{\omega}_0 = 5$ for several values of $\bar{m}$. If we take into account relativistic effects, the system become less stable, since the Big Rip occurs earlier.

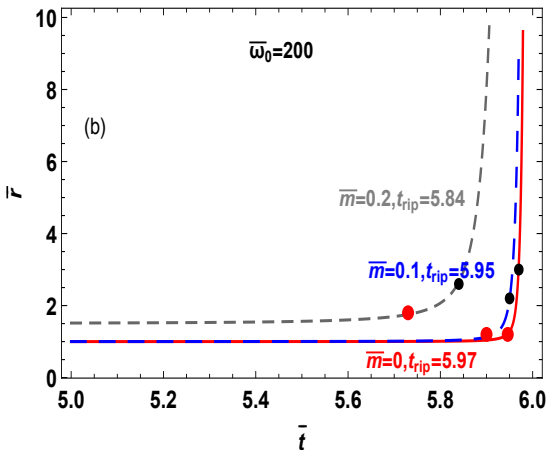

(b) The radius $\bar{r}$ as a function of $\bar{t}$ when $\bar{\omega}_0 = 200$ for several values of $\bar{m}$. Again, the relativistic effects are significant and they reduce the needed time to dissocate the system.

Figure 7.4: The dissociation time $\bar{t}_{rip}$ of a bound system is well represented by the time when the size $\bar{r}(t)$ of the system has increased by about 20% compared to its equilibrium value. The black points correspond to the time when the minimum of the effective potential disappears. Notice that, the scale of the horizontal axis in Fig. 7.4b is different and therefore the agreement between red and black points is much better. The trend for earlier dissociation in the relativistic treatment compared to the Newtonian approach is clear. However, the difference of dissociation times decreases as $\bar{\omega}_0$increases.

7.2 Time of Dissociation for a typical bound system

In the previous section we defined the time of dissociation of a bound system, as the time when the minimum of the effective potential disappears due to the effects of the expansion. In the context of a numerical solution of the system of geodesic equations, this definition is not as useful because the effective force and potential are only probed at the location of the solution $\bar{r}(\bar{t})$ with no information about neighboring values of $\bar{r}$ which could determine the binding status and stability of the system.

System	**Mass**($M_\odot$)	**Size**(Mpc)	$\bar{\omega}_0$	$\bar{m}$	$\Delta\bar{t}_{rip}$
Solar System	1.0	2.3×10^{-9}	3.5×10^{6}	2.1×10^{-11}	$< 10^{-8}$
Milky Way Galaxy	1.0×10^{12}	1.7×10^{-2}	1.8×10^{2}	2.9×10^{-6}	2.4×10^{-7}
Typical Cluster	1.0×10^{15}	1.0	12	4.9×10^{-5}	5.9×10^{-5}
Accretion Disk (neutron star)	1.5	3.3×10^{-19}	4.3×10^{21}	0.22	$< 10^{-8}$
Hypothetical Large Massive	3.0×10^{20}	1.0×10^{2}	9.1	0.15	0.93

Table 7.1: The parameter values and the corresponding level of relativistic corrections to the dissociation time for some typical bound systems. The last column shows the difference in $\bar{t}_{rip}$ between the Newtonian approximation and the relativistic value $\bar{t}_{nr_{rip}} - \bar{t}_{gr_{rip}}$ where $\bar{t}_{nr_{rip}}$ is the value of $\bar{t}_{rip}$ in the Newtonian approximation and $\bar{t}_{gr_{rip}}$ the relativistic value.

By comparing the dissociation times predicted by the effective potential with the form of the trajectories $\bar{r}(\bar{t})$ we conclude that to within a good approximation the minimum of the effective potential disappears when the solution $\bar{r}(\bar{t})$ diverges by about 20% from its initial equilibrium value. We thus use this as a *criterion of dissociation* when solving the system of geodesic equations numerically. Due to the different nature of this criterion we expect only qualitative agreement between the values of $\bar{t}_{rip}$ obtained

from the potential minimum and those obtained from the numerical trajectories $\bar{r}(\bar{t})$. However, as will be discussed below in most cases the agreement is good even in the quantitative level.

We solved the system of geodesic equations (7.31)-(7.32) with initial conditions corresponding to $\bar{t}_i = 1$ and $\bar{r}_i$ corresponding to the minimum of the effective potential at $\bar{t} = \bar{t}_i = 1$, including the expansion of the background. This value was in all cases considered, close to $\bar{r} = 1$ corresponding to the minimum of the effective potential without the effects of the expansion. In Fig. 7.4 we show the solution $\bar{r}(t)$ for $\bar{\omega}_0 = 5$, $\bar{\omega}_0 = 200$ when $\bar{m} = 0.1$ superposed with the corresponding radial function obtained in the Newtonian approximation ($\bar{m} = 0$). The trend for earlier dissociation in the relativistic treatment compared to the Newtonian approach is clear. However, the difference of dissociation times decreases as $\bar{\omega}_0$ increases.

As shown in Fig. 7.4 the bound system dissociation time $\bar{t}_{rip}$ is well represented by the time when the size $\bar{r}(t)$ of the system has increased by about 20% compared to its equilibrium value. Given the rapid increase of the physical size of the system after dissociation, the assumed relative size increase for dissociation does affect significantly the obtained value for $\bar{t}_{rip}$. This is less accurate for larger systems (smaller $\bar{\omega}_0$ shown in Fig. 7.4a) when the dissociation proceeds more smoothly. Notice also that in all cases $\dot{\bar{r}}$ is small before the dissociation which justifies the fact that we ignored it in the construction of the effective potential.

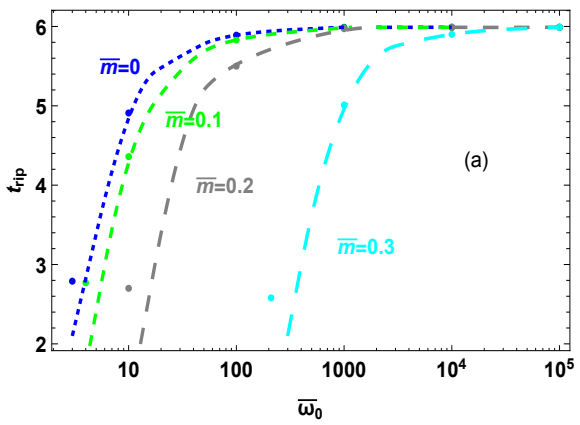

(a) The value of $\bar{t}_{rip}$ as a function of $\bar{\omega}_0$ for various values of $\bar{m}$. The curve for $\bar{m} = 0$ corresponds to the Newtonian limit.

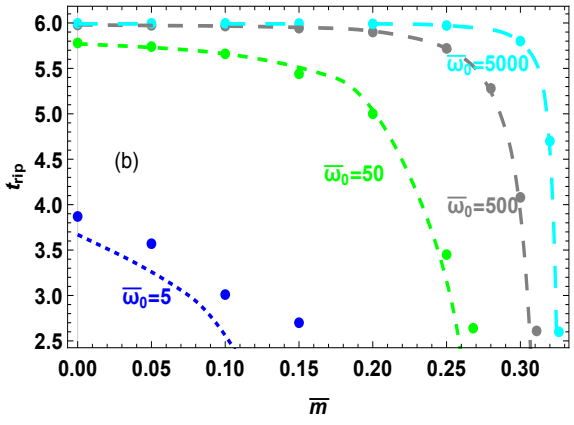

(b) The value of $\bar{t}_{rip}$ as a function of $\bar{m}$ for various values of $\bar{\omega}_0$. The Newtonian limit corresponds to the point each curve crosses the vertical axis of $\bar{t}_{rip}$.

Figure 7.5: The value of $\bar{t}_{rip}$ as a function of $\bar{\omega}_0$ in Fig. 7.5a and as a function of $\bar{m}$ in Fig. 7.5b. The thick dots correspond to dissociation times obtained using the numerical solution of the geodesic equations $r(t)$ while the lines were obtained using the effective potential of Eq. (7.41) by finding the time when the potential minimum disappears.

Figure 7.5a shows the value of $\bar{t}_{rip}$ as a function of $\bar{\omega}_0$ for various values of $\bar{m}$. The curve for $\bar{m} = 0$ corresponds to the Newtonian limit. As $\bar{m}$ increases, the relativistic correction to the value of $\bar{t}_{rip}$ increases dramatically for low values of $\bar{\omega}_0$ (large massive systems). Therefore, the dissociation of some large and strongly bound systems due to the expansion, proceeds significantly earlier than anticipated in the context of the Newtonian approach. This is also demonstrated in Fig. 7.5b where we have plot the $\bar{t}_{rip}$ as a function of $\bar{m}$ for various values of $\bar{\omega}_0$. The Newtonian limit corresponds to the point each curve crosses the vertical axis of $\bar{t}_{rip}$. Both figures 7.5a and 7.5b, the thick dots correspond to dissociation times obtained using the numerical solution of the geodesic equations $\bar{r}(t)$ while the lines were obtained using the effective potential of Eq. (7.41) by finding the time when the potential minimum disappears.

System	**Mass**($M_\odot$)	**Size**(Mpc)	$\bar{\omega}_0$	$\bar{m}(\times 10^{-5})$	$\Delta \bar{t}_{rip} \times (10^{-5})$
Typical Cluster	10^{15}	1.0	12.4	4.9	5.9
	10^{15}	0.8	17.4	6.1	5.6
	10^{15}	0.6	26.8	8.1	4.6
	10^{15}	0.4	49.2	12	3.8
	10^{15}	0.2	139	24	2.7

Table 7.2: The parameter values and the corresponding level of relativistic corrections to the dissociation time for a typical cluster, when we introduce a rescale in the size of the system. In the last column we have the difference of the Newtonian $\bar{t}_{nr-rip}$ minus the corresponding relativistic value. Notice that the relativistic rip occurs slightly earlier as expected but the difference from the Newtonian value decreases slowly with the rescaling to smaller sizes as the cosmological effects become less important.

Notice however that systems with $\bar{\omega}_0$ larger than about 10^4 (relatively small systems) have dissociation times $\bar{t}_{rip}$ that are practically indistinguishable from the Newtonian approximation independent of the value of $\bar{m}$. An appreciable deviation of the value of $\bar{t}_{rip}$ from the Newtonian approximation occurs for low values of $\bar{\omega}_0$ $(5-100)$ and large values of $\bar{m}$ $(O(10^{-1}))$. This range of parameters corresponds to large and massive systems (eg size of about 10-100Mpc and mass 10^6 times larger than a typical cluster of galaxies). Such systems where relativistic corrections are important need to fulfill two conditions

1. They need to be large so that the cosmological acceleration repulsive force to be important even at early times. Thus $\bar{t}_{rip}$ is relatively small (early dissociation) even at the Newtonian level allowing for significant change in the context of the relativistic correction.

2. They also need to be massive so that their Schwarzschild radius R_s and the innermost stable orbit to be comparable (a few times smaller) to their initial stable orbit radius.

We stress that in most cosmological bound systems correspond the parameter $\bar{m}$ which is much smaller than $\frac{1}{3}$. In particular some representative values are, for a cluster of galaxies $\bar{m} \simeq 10^{-5}$, for a galaxy $\bar{m} \simeq 10^{-6}$ and for the solar system $\bar{m} \simeq 10^{-11}$. For such systems the Newtonian approach provides an accurate approach for the dissociation time $\bar{t}_{rip}$, while the relativistic effects are negligible.

Even some systems that are considered strongly bound ($\bar{m} \simeq 0.1$) such as an accretion disk around a neutron star are not large enough to have appreciable difference of $\bar{t}_{rip}$ due to relativistic effects (they have a very large $\bar{\omega}_0$). A system with appreciable relativistic corrections of the dissociation time would be a hypothetical bound system with mass 10^{20} $M_\odot$ and size about $100Mpc$ (about 10^6 times more massive than a cluster of galaxies).

In Table 7.1 we show the parameter values and the corresponding level of relativistic corrections to the dissociation time for some typical bound systems.

Figure 7.6a shows the mass of physical systems as a function of the dimensionless parameter $\bar{\omega}_0$ for various values of $\bar{m}$. Some physical bound systems are also indicated on the plot. Similarly Fig. 7.6b shows the size of physical systems as a function of the dimensionless parameter $\bar{\omega}_0$ for various values of $\bar{m}$. An accretion disk around a neutron star ($r \simeq 50km$, $M \simeq 1.4M_\odot$) is out of the range of these plots as it has $\bar{m} \simeq 0.1$ but $\bar{\omega}_0 \simeq 10^{20}$ (see also Eqs. (7.34) and (7.35)). As shown in Table 7.1, despite the relative large value of $\bar{m}$ of such a strongly bound system, its dissociation time would practically be identical to the one derived in the context of the Newtonian approximation due to its relatively small size and large value of $\bar{\omega}_0$.

Relativistic corrections tend to change slowly when the size of a given bound decreases. Such a decrease implies an increase of both $\bar{m}$ and $\bar{\omega}_0$. The parameter values and the corresponding relativistic corrections as the scale of a typical cluster shrinks by a factor of 5 are shown in Table 7.2. Notice that the increase of $\bar{\omega}_0$ appears to be more important during shrinking a system than the increase of $\bar{m}$ and therefore the relativistic corrections to $\bar{t}_{rip}$ decrease slowly as the size of the bound system is reduced.

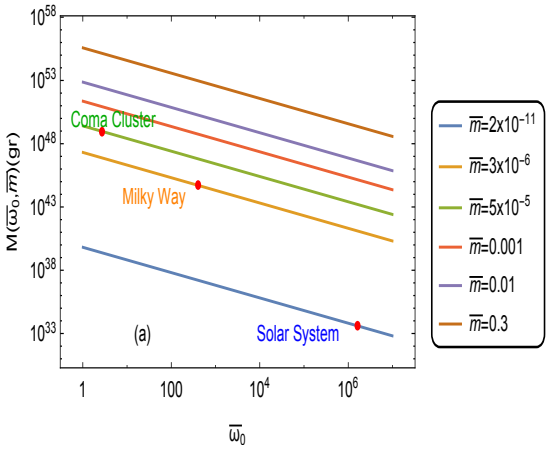

(a) The mass of some physical systems as a function of the dimensionless parameter $\bar{\omega}_0$ for several values of $\bar{m}$.

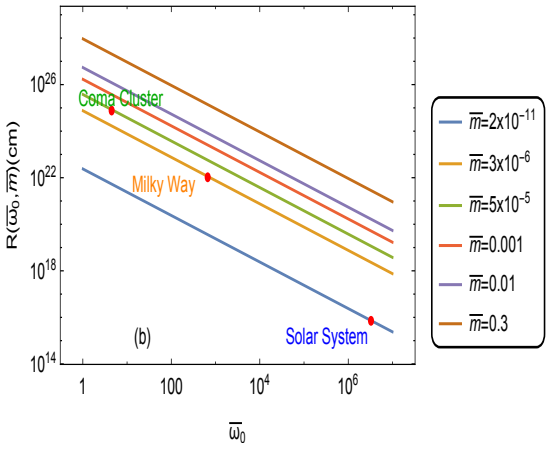

(b) The size of some physical systems in as a function of the dimensionless parameter $\bar{\omega}_0$ for several values of $\bar{m}$.

Figure 7.6: In Fig. 7.6a we have plot the mass of some physical systems as a function of the dimensionless parameter $\bar{\omega}_0$ for a few values of $\bar{m}$, while the size of such physical systems as a function of the dimensionless parameter $\bar{\omega}_0$ is presented in Fig. 7.6b.

7.3 Conclusion-Discussion

In this Chapter we investigated the dissociation of bound system in a phantom cosmological background taking into account relativistic effects. We defined that the time momentum of dissociation occurs when the size of a typical system increases up to 20% from its initial value. In Newtonian consideration the definition is different, since the dissociation occurs when the minimum of the potential disappears.

We have demonstrated that when relativistic effects are taken into account, the dissociation of bound systems in phantom cosmologies occurs earlier than it would have been predicted in the Newtonian approximation used by previous studies. The correction in all known bound systems is small. However, there are hypothetical cosmologically large and massive bound systems where the correction is significant.

It is interesting to analyze more general classes of geodesics like infalling radial geodesics with no angular momentum which at the time of the Big Rip are close or even beyond the black hole horizon. Also, it is worthwhile to use the McVittie geodesics to derive the relativistic corrections on the turnaround radius which is the non-expanding shell furthest away from the center of a bound structure. In the context of the Newtonian approximation the maximum possible value of the turnaround radius for $w = -1$ (ΛCDM) is equal to $(3GM/\Lambda c^2)$ [455].

Chapter 8

Spinning particle orbits around a black hole in an expanding background

In this Chapter we investigate analytically and numerically the orbits of spinning particles around a black hole in the post Newtonian limit of McVittie spacetime and in the presence of cosmic expansion. This chapter is also an exception as it assumes no deviation from the Standard model and GR, but it focuses on a non-standard property of trajectories (its modification due to spin and due to cosmic expansion). We show that orbits that are circular in the absence of spin and expansion, get deformed when the orbiting particle has spin. We prove that the origin of this deformation is twofold:

(a). the background expansion rate which induces an attractive (repulsive) interaction due to the cosmic background fluid when the expansion is decelerating (accelerating) and

(b). a spin-orbit interaction which can be attractive or repulsive depending on the relative orientation between spin and orbital angular momentum and on the expansion rate.

We consider several rates of expansion, accelerating and decelerating, beyond the Standard ΛCDM expansion. Also, in this chapter we discuss concepts beyond the standard model since we investigate the effects of various different expansion rates beyond the Standard ΛCDM accelerating expansion. Finally, this chapter is associated with the effects of nonstandard expansion. We estimate for some cosmological structures, the time interval after which the cosmological expansion effects become apparent on the orbits.

Even though most astrophysical bodies have spin and evolve in an expanding cosmological background, their motion is described well by ignoring the cosmic expansion and under the nonspinning test particle approximation for large distances from a central massive body and for relatively low spin values [456]. These approximations however become less accurate for large values of the spin and/or when the mass of the cosmic fluid inside the particle orbit becomes comparable to the mass of the central massive object. For such systems, new types of interactions appear which are proportional to the time derivatives of the cosmic scale factor and the spin of the orbiting particle. For example, phantom dark energy models can lead to dissociation of all bound systems in the context of a Big-Rip future singularity [4, 229, 427, 442]. Also, the spin-curvature interaction [457] can modify the motion of the test particles in black hole spacetimes [458–462] due to spin-spin or spin-orbit couplings [463–465], or can make the motion chaotic [466–468] thus modifying significantly the orbit of the test body leading to the emission of characteristic forms of gravitational waves [469–472].

Such interactions have been investigated previously for nonspinning test particles in an expanding background around a massive body (McVittie background [473]) and it was shown that accelerating cosmic expansion can lead to dissociation of bound systems in the presence of phantom dark energy with

equation of state parameter $w < -1$ [4, 229, 442]. In the absence of expansion but in the presence of spin for the test particles, it has been shown that spin-orbit and spin-spin interactions in a Kerr spacetime can lead to deformations of circular orbits for large spin values [465]. In view of these facts, the following interesting questions emerge

1. Are there circular orbit deformations for spinning test particles embedded in the post Newtonian limit of McVittie background (Schwarzschild metric embedded in an expanding background)? Such deformations could be anticipated due to the coupling of the particle spin with its orbital angular momentum.

2. What is the nature of such deformation and how do the corresponding deformations depend on the orientation of the spin with respect to the angular momentum?

3. How do these deformations depend on the nature of the background expansion?

These questions are addressed in this chapter of the present dissertation.

8.1 The Equations of Motion of a Spinning Particle. The MP Equations.

Consider a massive spinning test particle, in Mathisson-Papapetrou (MP) model [474, 475]. The equations of motion of a spinning particle originally derived from Papapetrou (1951) and later on reformulated by Dixon [476, 477] can be extracted through the corresponding Hamiltonian [478, 479] or through the extremization of the corresponding action [480], whose variation is [481]

$$\delta L = -p^{\mu}\delta v_{\mu} - \frac{1}{2}S^{\mu\nu}\delta\Omega_{\mu\nu} \tag{8.1}$$

where $v^{\mu} = \frac{dx^{\mu}}{d\tau}$ is the four-velocity of the test particle tangent to the orbit $x^{\mu} = x^{\mu}(\tau)$, τ is the proper time across the worldline $x^{\mu}(\tau)$, p^{μ} is its four-momentum and $S^{\mu\nu}$ are the components of the antisymmetric spin tensor. Also, $\Omega_{\mu\nu} = \eta^{IJ}e_{\mu I}\frac{De_{\nu J}}{d\tau}$ is an antisymmetric tensor, $\eta^{IJ} = e^{\mu}_{I}e^{\nu}_{J}g_{\mu\nu}$ and e^{μ}_{I} is a tetrad attached to each point of the worldline.

The MP equations are of the form [481–484]:

$$\frac{Dp^{\mu}}{d\tau} \equiv \frac{dp^{\mu}}{d\tau} + \Gamma^{\mu}_{\lambda\nu}v^{\lambda}p^{\nu} = -\frac{1}{2}R^{\mu}_{\nu\lambda\rho}S^{\lambda\rho}v^{\nu} \tag{8.2}$$

$$\frac{DS^{\mu\nu}}{d\tau} \equiv \frac{dS^{\mu\nu}}{d\tau} + \Gamma^{\mu}_{\lambda\rho}v^{\lambda}S^{\rho\nu} + \Gamma^{\nu}_{\lambda\rho}v^{\lambda}S^{\mu\rho} = p^{\mu}v^{\nu} - p^{\nu}v^{\mu} \tag{8.3}$$

The dynamical equations imply spin-orbit coupling, i.e., spin couples to the velocity of the orbiting spinning particle, thus deforming the geodesic. Therefore, the spin force deforms the geodesic.

The spin tensor keeps track of the intrinsic angular momentum associated with a spinning particle. The term in the r.h.s. of Eq. (8.2) shows an interaction between the curvature of the spacetime and the spin of the particle. Due to the coupling between curvature and spin, the four-momentum is not always parallel to the v^{μ}. This may be seen by multiplying Eq. (8.3) with v_{ν}. Then, leads to

$$p^{\mu} = mv^{\mu} - v_{\nu}\frac{DS^{\mu\nu}}{d\tau} \tag{8.4}$$

where $m = -p^{\mu}v_{\mu}$ is the rest mass of the particle with respect to v_{μ}.

Since τ is the proper time, the condition $v_{\mu}v^{\mu} = -1$ applies. The measure of the four-momentum $p_{\mu}p^{\mu} = -\mu^2$ provides the 'total' or 'effective' [459] rest mass μ ($p^{\mu} = \mu u^{\mu}$) with respect to p^{μ} where u^{μ} is the 'dynamical four-velocity' and is equal to m, only if v^{μ} coincides with the four-velocity u^{μ} ($u^{\mu} = v^{\mu}$). In the linear approximation of the spin, p^{μ} and v^{μ} are parallel. Generally, since $u^{\mu} \neq v^{\mu}$ which means

that $\frac{DS^{\mu\nu}}{d\tau} \neq 0$ (see Eq. (8.4)) a spinning particle does not follow the geodesics of the spacetime (the r.h.s. of Eq. (8.2) is non zero, since $S^{\mu\nu} \neq 0$). Therefore its motion is generalized on a worldline rather than geodesics.

In the context of the MP equations the multipole moments of the particle higher than a spin dipole are ignored [485]. This is the spin-dipole approximation, because the particle is described as a mass monopole and spin dipole [486]. The equations in quadratic order of spin have also been derived [487]. The MP equations can also get generalized in order to describe a test spinning particle in Modified theories of Gravity [488].

The MP equations (8.2) and (8.3) have been discussed by many authors and solutions have been presented. These solutions refer mainly to Schwarzschild background spacetime [472, 489–495], to Kerr spacetime [472, 496–503], to de Sitter spacetime [504–507] and to FRW spacetime [508] for chargeless or charged test spinning particles [509, 510]. The evolution of spinning particles in spacetimes with torsion has also been investigated [511, 512].

Eqs (8.2) and (8.3) are the equations of motion for a spinning body which reduce to the familiar geodesic equations when the spin tensor $S^{\mu\nu}$ vanishes identically. However, they do not form a complete set of equations and we need further equations to close the system [513]. The problem of the unclosed set of equations in (8.2) and (8.3) can be physically understood by the requirement that the particle must have a finite size which does not make the choice of the reference worldline uniquely defined [1]. The additional conditions which are used, are the spin supplementary conditions (SSC) [514]. When we choose a SSC, we define the evolution of the test body in a unique worldline $x^{\mu}(\tau)$ and we fix the center of mass (corresponds to the centre where the mass dipole vanishes), which is usually called centroid. The centroid is a single reference point inside the body, with respect to which the spin is measured [515].

There are several SSC, but two of them are more commonly used

- The P condition (Mathisson-Pirani) [516]

$$v_{\mu} S^{\mu\nu} = 0 \tag{8.5}$$

  so that the spin four-vector is perpendicular to the four-velocity and implies that $\frac{d\mu}{d\tau} = 0$ [517]. It does not provides a unique choice of representative worldline, as it is dependent on the observer's velocity and therewith on the initial conditions. It is often referred to as the proper centre of mass [514].

- The T condition (Tulczyjew-Dixon) [518]

$$p_{\mu} S^{\mu\nu} = 0 \tag{8.6}$$

  so that the spin four-vector is perpendicular to the four-momentum and implies that $\frac{dm}{d\tau} = 0$ [513]. This condition is physically correct, since the trajectory of the extended body is determined by the position of the center of mass of the body itself [519]. This constraint is a consequence of the theory, i.e., the Tulczyjew constraint can derived from the Lagrangian theory [520] and restricts the spin tensor to generate rotations only.

Analytic discussions and thorough reviews on different choices about the SSCs may be found in Refs [521–523]. Generally, different SSC are not equivalent since every SSC defines a different centroid for the system. The author of Ref. [456] point out that the difference between the two conditions (8.5) and (8.6) is third order in the spin, so results for physically realistic spin values, are unaffected. In what follows we use the T condition, which defines the centre of mass of the particle in the rest frame of the central gravitating body.

The McVittie metric describes an expanding cosmological background with strong gravity, such as a spacetime near a black hole or a neutron star. In a (t, r, θ, ϕ) coordinate system, McVittie [424] found a solution given by the equation (see Eq. (29) of Ref. [424] with $G = c = 1$)

$$ds^2 = -\left(1 - \frac{m(t)}{2r}\right)^2 \left(1 + \frac{m(t)}{2r}\right)^{-2} dt^2 + \left(1 + \frac{m(t)}{2r}\right)^4 a^2(t)\left(dr^2 + r^2 d\Omega^2\right) \tag{8.7}$$

[1] https://d-nb.info/1098374932/34

where $d\Omega^2 = d\theta^2 + \sin^2\theta d\phi^2$. The component G^t_r of the Einstein tensor is

$$G^t_r = \frac{8(2r+m)}{a(2r-m)^3}(\dot{a}m + a\dot{m}) \tag{8.8}$$

Imposing the "no-accretion" condition $G^t_r = 0$ (there is no flux of relativistic mass across the equatorial surface [424]) we find that $\frac{\dot{a}}{a} = -\frac{\dot{m}}{m}$ or $m = \frac{m_0}{a(t)}$, where m_0 is a constant of integration and is identified with the mass of the central body at the origin [524]. Here, the curvature of space is assumed to be asymptotically zero.

At any instant of time t_1 the observer's coordinate for measuring distance from the origin is $\tilde{r} = ra(t_1)$. If we write $M = m(t_1)a(t_1)$, the metric (8.7) becomes

$$ds^2 = -\Big(\frac{1-\frac{M}{2\tilde{r}}}{1+\frac{M}{2\tilde{r}}}\Big)^2 dt^2 + \Big(1+\frac{M}{2\tilde{r}}\Big)^4\Big(d\tilde{r}^2 + \tilde{r}^2 d\Omega^2\Big) \tag{8.9}$$

In the weak field limit we have $\frac{M}{2r} \ll 1$, ie

$$ds^2 = -\Big(1-\frac{2GM}{r}\Big)dt^2 + \Big(1+\frac{2GM}{r}\Big)\Big(dr^2 + r^2 d\Omega^2\Big) \tag{8.10}$$

which is the *Newtonian limit* of Schwarzschild's spacetime. Setting $r = a(t)\rho$ and $R_s = 2M$ the metric (8.10) reads

$$ds^2 = -\Big(1-\frac{R_s}{a\rho}\Big)dt^2 + a^2\Big(1+\frac{R_s}{a\rho}\Big)\Big(d\rho^2 + \rho^2 d\Omega^2\Big) \tag{8.11}$$

For a static background ($a = 1$) the metric (8.11) becomes the Schwarzschild metric in isotropic coordinates (the spacelike slices are as close as possible to Euclidean) as expected [525], while for $R_s = 0$ becomes the FRW metric in spherical coordinates.

The 'areal' radius [526] of the metric (8.11) is equal to the square root of the modulus of the coefficient of the angular part $d\Omega^2$ of the metric, namely

$$R(t,\rho) = \Big(1+\frac{R_s}{a\rho}\Big)^{1/2} a\rho \tag{8.12}$$

and the corresponding modulus of angular momentum, which is a constant of motion for a spinless particle, is defined as

$$\mathcal{L} = R^2(t,\rho)\dot{\phi} \tag{8.13}$$

8.2 Spinning particle in McVittie spacetime-Post Newtonian Limit

8.2.1 The MP equations in an expanding Universe

We consider the case where the spinning particle orbits on the equatorial plane, which means that $\theta = \pi/2$. Also, on the equatorial plane valid $v^2 \equiv v^\theta = 0$ and $p^\theta = 0$ since $p^\mu = \frac{\mu^2}{m}v^\mu$. The metric (8.11) is independent of the ϕ coordinate, therefore admits a ϕ-Killing vector e.g. $\xi^\mu = (0,0,0,1)$ which gives

$$J_z = p_\mu \xi^\mu - \frac{1}{2}\xi_{\mu,\nu}S^{\mu\nu} \tag{8.14}$$

or

$$J_z = p_\phi - \frac{1}{2}g_{\phi\mu,\nu}S^{\mu\nu} \tag{8.15}$$

where J_z is the z component of the angular momentum, which is a conserved quantity of the motion of a spinning particle. This constant of motion exists independently of the choice of the supplementary condition and reflects the symmetry of the background spacetime.

The spin tensor has six independent components but since we demand equatorial planar motion, the particle must have angular momentum only in z axis ($J_z \neq 0$). The conditions $J_x = 0$, $J_y = 0$ and $p^\theta = 0$ (necessary conditions for motion in the equatorial plane) require that $S^{r\theta} = 0$ and $S^{\theta\phi} = 0$. Also, the absence of acceleration perpendicular to the equatorial plane implies that $S^{t\theta} = 0$ [508]. Thus, planar motion requires alignment of the spin with the orbital angular momentum and the motion characterized only by three independent spin components. With these assumptions, the spin tensor becomes a vector and the formulation will be simpler. From the T condition (8.6) we derive the spin components S^{03} and S^{13} in terms of S^{01} as

$$\begin{aligned} S^{03} &= -\frac{p_1}{p_3} S^{01}, \\ S^{13} &= \frac{p_0}{p_3} S^{01} \end{aligned} \tag{8.16}$$

In order to complete the system of Eqs. (8.2) and (8.3) we have to add two more equations, corresponding to conserved quantities in the context of the T condition. The first is the dynamical mass μ [527] with respect to the four-momentum p^μ which defined as $-\mu^2 = p_\mu p^\mu$ and leads to

$$-\mu^2 = g_{00}(p^0)^2 + g_{11}(p^1)^2 + g_{33}(p^3)^2 \tag{8.17}$$

and the second is the particle's total spin s which is defined as the positive root of $s^2 = \frac{1}{2} S_{\mu\nu} S^{\mu\nu}$. The first derivative of s^2 with respect to τ is $\dot{s^2} = 2 p_\mu S^{\mu\nu} v_\nu$ [513] which is zero in the context of T condition.

With the use of expressions (8.16) for the spin components we find

$$\begin{aligned} s^2 &= S_{01}S^{01} + S_{03}S^{03} + S_{13}S^{13} \\ &= g_{00}g_{11}(S^{01})^2 + g_{00}g_{33}(S^{03})^2 + g_{11}g_{33}(S^{13})^2 \\ &= g_{00}g_{11}(S^{01})^2 + g_{00}g_{33}(-\frac{p_1}{p_3})^2(S^{01})^2 + g_{11}g_{33}(\frac{p_0}{p_3})^2(S^{01})^2 \end{aligned} \tag{8.18}$$

Let us define the useful parameters μ_0 and ξ as

$$\mu_0^2 = (p^0)^2 - a^2(p^1)^2 - a^2\rho^2(p^3)^2 \tag{8.19}$$

and

$$\xi \equiv \frac{R_s}{a\rho} \ll 1 \tag{8.20}$$

respectively. If we combine the Eqs (8.17) and (8.19) we find

$$\mu^2 = \mu_0^2 + \xi\Big(\mu_0^2 - 2(p^0)^2\Big) \tag{8.21}$$

while, from (8.18) we have

$$s^2 = \frac{(1-\xi)(S^{01})^2}{\rho^2(p^3)^2}\mu^2 \tag{8.22}$$

Using the Eqs (8.21) and (8.22) we define the parameter Ω^2 as the ratio

$$\Omega^2 \equiv \frac{s^2}{\mu^2} = \frac{(S^{01})^2}{\rho^2(p^3)^2}(1-\xi) \tag{8.23}$$

which is a constant of motion, since μ and s are conserved quantities. Then, from Eq. (8.23) it is easy to calculate the spin component S^{01}

$$\frac{S^{01}}{p^3} = \frac{\rho\Omega}{\sqrt{1-\xi}} \tag{8.24}$$

Summarizing, from Eqs. (8.16) and (8.24) the non zero spin components in our consideration are

$$\begin{aligned} S^{01} &= \frac{\rho\Omega p^3}{\sqrt{1-\xi}} \\ S^{03} &= -\frac{p^1}{\rho^2 p^3} S^{01} \\ S^{13} &= -\frac{(1-2\xi)p^0}{a^2\rho^2 p^3} S^{01} \end{aligned} \tag{8.25}$$

Using now the post Newtonian limit of McVittie metric (8.11), starting from the MP equation (8.2) and setting the index $\mu = 1 =$ it is straightforward to derive the radial geodesic equation for the spinning particle. We replace the distance ρ as $\rho = r/a$ and the corresponding derivatives with respect to t, $\dot{\rho} = d\rho/dt$ and $\ddot{\rho} = d^2\rho/dt^2$. Also, we ignore terms of order $(R_s)^2$ (post Newtonian limit) and the final result is

$$\ddot{r} - \frac{\ddot{a}}{a} r - r\dot{\phi}^2 = -r\Omega\dot{\phi}\left(\frac{\ddot{a}}{a} - \frac{\dot{a}^2}{a^2}\right) + \frac{R_s}{2}\left(-\frac{1}{r^2} - \dot{\phi}^2 - \frac{\dot{a}^2}{a^2} + \frac{\dot{r}^2}{r^2} - \frac{3\Omega\dot{\phi}}{r^2}\right) \tag{8.26}$$

Similarly, from the MP equation (8.2) and setting $\mu = 3 = \phi$ the geodesic equation for the azimuthal angle ϕ is

$$\frac{d\left(r^2\dot{\phi}\right)}{dt} = \dot{r}\dot{\phi}R_s + \Omega r^2\left(\frac{\dot{r}}{r} - \frac{\dot{a}}{a}\right)\left(\frac{\ddot{a}}{a} - \frac{\dot{a}^2}{a^2}\right) \tag{8.27}$$

which would lead to orbital angular momentum conservation in the absence of spin ($\Omega = 0$). Indeed, the first derivative of Eq. (8.13) with respect to time must be zero and gives the Eq. (8.27) for a spinless particle [526].

Now, we introduce the rescalling through the variables $\bar{t} \equiv \frac{t}{R_s}$, $\bar{r} \equiv \frac{r}{R_s}$ and $\Omega_s \equiv \frac{\Omega}{R_s} = \frac{s}{\mu R_s}$ and from now on we omit the bar. The radial equation (8.26) leads to

$$\boxed{\ddot{r} - \frac{\ddot{a}}{a} r - r\dot{\phi}^2 = -r\Omega_s\dot{\phi}\left(\frac{\ddot{a}}{a} - \frac{\dot{a}^2}{a^2} + \frac{3}{2r^3}\right) + \frac{1}{2}\left(-\frac{1}{r^2} - \dot{\phi}^2 - \frac{\dot{a}^2}{a^2} + \frac{\dot{r}^2}{r^2}\right)} \tag{8.28}$$

In the same way, the azimuthal equation (8.27) leads to

$$\boxed{\frac{d\left(r^2\dot{\phi}\right)}{dt} = \dot{r}\dot{\phi} + \Omega_s r^2\left(\frac{\dot{r}}{r} - \frac{\dot{a}}{a}\right)\left(\frac{\ddot{a}}{a} - \frac{\dot{a}^2}{a^2}\right)} \tag{8.29}$$

Equations (8.28) and (8.29) are the main results of the present analysis. They generalize the geodesic equation of non-spinning particles in the post-Newtonian limit of McVittie metric and they reduce to those equations for $\Omega_s = 0$. It is straightforward to solve numerically the system (8.28)-(8.29) and we implement such solutions in what follows. The following comments can be made on Eqs. (8.28)-(8.29):

- It is clear from Eq. (8.29) that the orbital angular momentum is not conserved due to the presence of the spin angular momentum. What is actually conserved is the z component of the total angular momentum J_z which is expressed through Eq. (8.15) in terms of the angular and the spin angular momenta.
- The driving force term proportional to Ω_s and $\dot{\phi}$ in the radial geodesic equation (8.28) has the form of a spin-orbit coupling and changes sign when the spin angular momentum reverses its direction with respect to the orbital angular momentum which is proportional to $\dot{\phi}$. This term is responsible for the deformation of the circular orbits and induces the well known chaotic behavior [528] of the spinning particle orbits in the absence of background expansion.

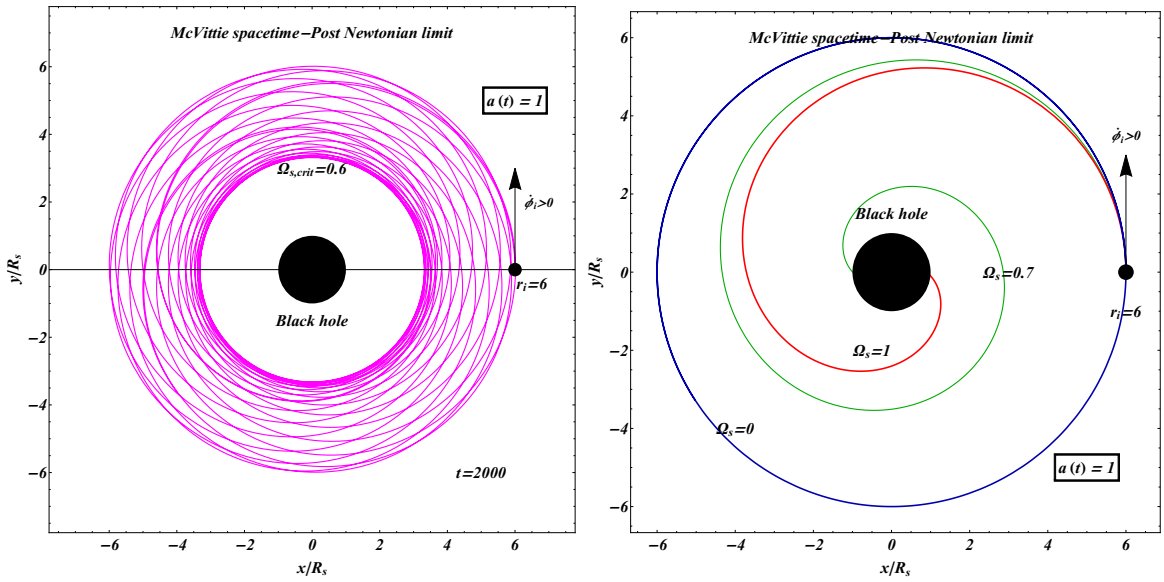

Figure 8.1: Spinning particle orbits in a static universe. The circular orbits that would be present for a non-spinning particle get disrupted due to the spin-orbit coupling in the presence of spin. For $\Omega_s\dot{\phi} > 0$ the spin-orbit coupling force is attractive and the circular orbits are deformed inward. The left panel corresponds to maximum (critical) value of Ω_s, for which the particle remains bounded. When $\Omega_s > 0.6$, at some time the radius of the orbit becomes less than $3R_s$ (innermost stable orbit) and the particle is captured by the black hole (right panel). For non-spinning particle ($\Omega_s = 0$) the circular orbit is shown in right panel with blue color.

In what follows we solve the geodesic equations (8.28)-(8.29) for different forms of the expansion (static, accelerating and decelerating and) of the cosmological background and various values of the magnitude of the spin s and consequently of the dimensionless parameter Ω_s. In the present analysis we have focused on the distortion of orbits that would be circular in the absence of expansion and spin. In order to solve the system of equations (8.28) and (8.29) we have assumed that initially the test particle has zero radial velocity ($\dot{r}(t_i = 1) = 0$) and zero radial acceleration ($\ddot{r}(t_i = 1) = 0$). The initial value of the derivative $\dot{\phi}(1)$ can derived through the geodesic equation (8.28), if we choose the suitable values for all the other functions and parameters. We set $a(t_i = 1) = 1$ and initial position for the particle $r_i = 6$ in units of R_s. Assuming a static Universe with $a(t) = 1$ we compute the initial angular momentum from Eq. (8.28). We set all the time derivatives of the scale factor equal to zero and thus we arrive at the following quadratic equation

$$r_i^2(2r_i - 1)(\dot{\phi}(1))^2 - 3\Omega_s\dot{\phi}(1) - 1 = 0 \tag{8.30}$$

Setting $\Omega_s = 0$, it is straightforward to derive the roots of the equation (8.30), which correspond to circular motion for a spinless particle

$$\dot{\phi}(1) = \pm\frac{\sqrt{11}}{66} \simeq \pm 5 \times 10^{-2} \tag{8.31}$$

Since, the above equation (8.30) has two roots for $\dot{\phi}(1)$ which corresponds to initially opposite rotation, it is clear that we must distinguish two cases. The positive value of $\dot{\phi}(1)$ corresponds to counterclockwise rotation, while the value $\dot{\phi}(1) < 0$ corresponds to clockwise rotation of the test particle. We set the same positive root ($\frac{\sqrt{11}}{66}$) of Eq. (8.31) for counterclockwise rotation in all cases considered in this analysis and the same negative root ($-\frac{\sqrt{11}}{66}$) for clockwise rotation. Finally, we assume that the initial azimuthal

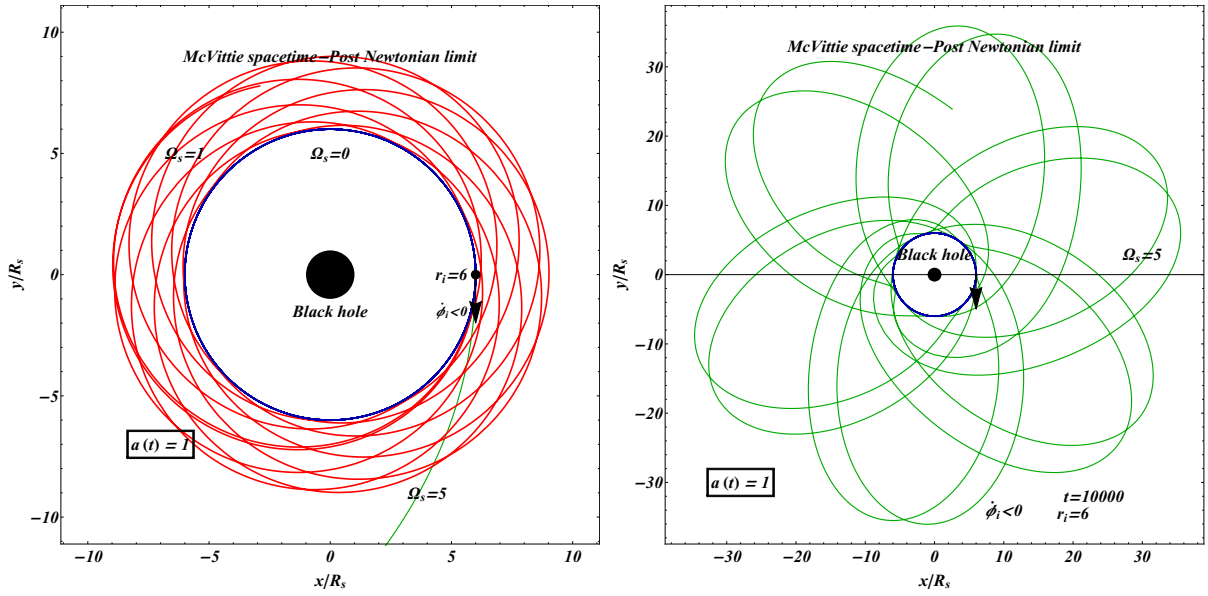

Figure 8.2: Same as Fig. 8.1 but the spinning particle orbits in the opposite direction. The circular orbits that would be present for a non-spinning particle get disrupted due to the spin-orbit coupling in the presence of spin. For $\Omega_s\dot{\phi} < 0$ the spin-orbit coupling force is repulsive and the circular orbits are deformed outward. For non-spinning particle ($\Omega_s = 0$) the circular orbits shown in both panels remain undisrupted. Notice that the $\Omega_s = 0$ circular orbit, which corresponds to the absence of spin, is an inner bound for clockwise rotation. In any case the particle remains bound.

angle is equal to zero, namely $\phi(1) = 0$. Using these initial conditions we have estimate the influence of the spin in the trajectories in an expanding background and the deviation these effects cause from the otherwise circular orbit in a static universe.

8.2.2 Numerical Solutions

For a static universe ($a(t) = 1$) Eq. (8.28) reduces to

$$\ddot{r} = r\dot{\phi}^2 + \frac{1}{2}\Big(- \frac{1}{r^2} - \dot{\phi}^2 + \frac{\dot{r}^2}{r^2} - \frac{3\Omega_s\dot{\phi}}{r^2}\Big) \tag{8.32}$$

while the Eq. (8.29) becomes

$$\frac{d(r^2\dot{\phi})}{dt} = \dot{r}\dot{\phi} \Rightarrow r^2\ddot{\phi} + (2r-1)\dot{r}\dot{\phi} = 0 \tag{8.33}$$

The effect of the spin-orbit coupling force is demonstrated in Figures 8.1 and 8.2 where we show the circular orbits disrupted due to the spin-orbit coupling. For $\Omega_s\dot{\phi} > 0$ (see Fig. 8.1) the spin-orbit coupling force is attractive, since the term $-\frac{3\Omega_s\dot{\phi}}{2r^2}$ in Eq. (8.28) is negative and the circular orbits (for a spinless particle) are deformed inward. The orbit of the motion of the particle remains bounded if the radius of the orbit is larger than $3R_s$. This is the well known effect of the '*innermost stable circular orbit*' (ISCO) [501, 529, 530]. It is defined as the smallest circular orbit in which a test particle can stably orbit a massive object [531]. Since $r_{ISCO} = 3R_s$ for a spinless central body in Schwarzschild spacetime, it is obvious that only black holes have innermost radius outside their surface.

This minimum allowed radius for bounded motion corresponds to a critical value of the dimensionless parameter $\Omega_s = 0.6$ (left panel). Generally, in the presence of spin the orbits are bounded between

a minimum and a maximum radius ($R_s = 6$). As the spin increases ($\Omega_s > 0.6$), at some time the orbit's radius becomes less than $3R_s$ and the particle gets captured by the black hole (right panel). For non-spinning particle ($\Omega_s = 0$) the circular orbits shown in right panel remain undisrupted.

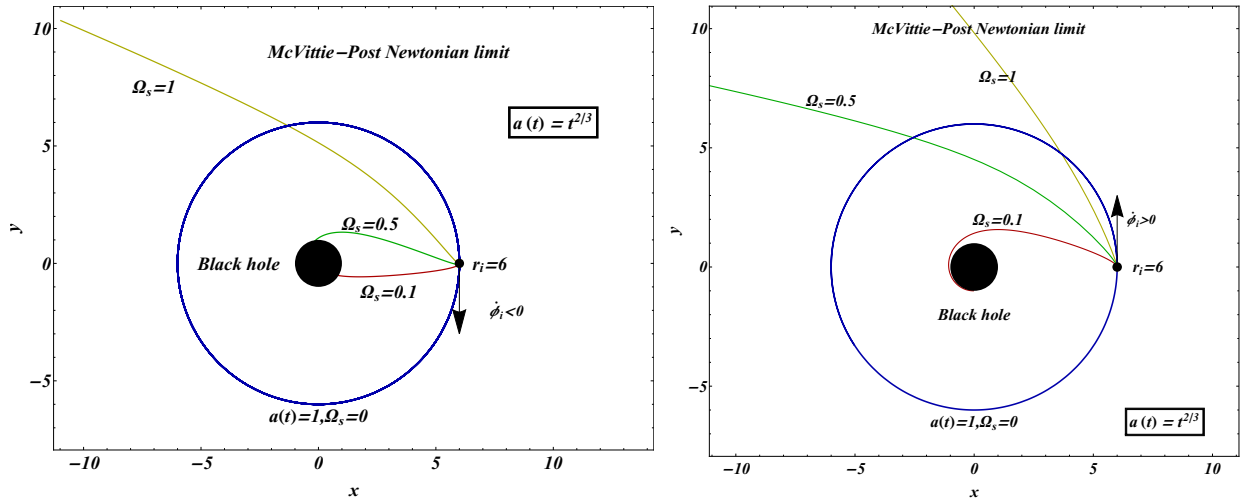

Figure 8.3: The spinning particle orbits in the presence of decelerating universe expansion $a(t) \sim t^{2/3}$ for several values of the spin and initial clockwise (left panel with $\dot{\phi}(1) < 0$) and counterclockwise (right panel with $\dot{\phi}(1) > 0$) rotation. For small values of Ω_s the particle gets captured by the black hole, but as the parameter Ω_s increases the particle rapidly gets deflected to an unbounded orbit.

For $\Omega_s \dot{\phi} < 0$ (see Fig. 8.2) the spin-orbit coupling force is repulsive, since the term $-\frac{3\Omega_s \dot{\phi}}{2r^2}$ in Eq. (8.28) is positive and the circular orbits (for $s = 0$) are deformed outward. The orbits of the motion of the spinning particle in all cases are bounded between a minimum ($R_s = 6$) and a maximum radius.

In the presence of a decelerating expansion with $a(t) \sim t^{2/3}$ the orbits (solutions of Eqs. (8.28)-(8.29)) are shown in Fig. 8.3 for clockwise and counterclockwise rotation and initial conditions that would lead to a circular orbit in the absence of spin and expansion. In this case the effects of the expansion combined with the effects of the spin lead to rapid dissociation of the system or capture by the black hole. The result depends on the magnitude of the attractive and repulsive terms in Eq. (8.28). Some orbits of the spinning particles for this case are shown in Fig. 8.3.

In left panel of Fig. 8.3 the initial rotation is clockwise, since $\dot{\phi}(1) < 0$. In this case, the term $-\frac{3\Omega_s \dot{\phi}}{2r^2}$ in Eq. (8.28) is repulsive and even if the cosmological background is decelerating, for large enough values of spin, such as $\Omega_s = 1$ the particle rapidly gets deflected to an unbounded orbit. However, for small values of spin, such as $\Omega_s = 0.1$ or $\Omega_s = 0.5$ the decelerating background dominates and at some time the particle gets captured by the black hole.

Similar results are shown in the right panel of Fig. 8.3, where the initial rotation of the particle is counterclockwise. In this case, the term $-\frac{3\Omega_s \dot{\phi}}{2r^2}$ in Eq. (8.28) which describes the spin-orbit interaction is attractive. For small values of the dimensionless parameter Ω_s, such as $\Omega_s = 0.1$ the spinning particle approaches the black hole and when the radius of the orbit becomes less than $3R_s$, the particle gets captured by the strong gravity of the central body. However, when the spin takes larger values such as $\Omega_s = 0.5$ or $\Omega_s = 1$ the particle gets deflected to an unbounded orbit, despite of the initially attractive effective force induced on the spinning particle. The expansion effects lead to dissociation of the initially bound system.

Now, we consider the effects of a de Sitter background expansion of the form

$$a(t) = e^{Ht} \tag{8.34}$$

where $H = \sqrt{\frac{\bar{\Lambda}}{3}}$ and $\bar{\Lambda}$ is the cosmological constant in dimensionless form . We solve the system of Eqs. (8.28) and (8.29) with the same initial conditions (circular orbit in the absence of spin and expansion). We set the cosmological constant equal to $\bar{\Lambda} = \Lambda R_s^2 = 3 \times 10^{-2}$ [532] and we present the trajectories of the particle in Fig. 8.4. We also show the corresponding orbit of a spinless particle in a static universe, in order to observe the deviation of each orbit from the circular.

Setting a mass value of a typical black hole as $M = 10 M_{\odot} = 2 \times 10^{31} Kg$, we conclude that the dimensionless value $\Lambda R_s^2 = 0.03$ corresponds to $\Lambda \simeq 3 \times 10^{6} sec^{-2}$ or $\Lambda \simeq 1.3 \times 10^{-42} GeV^2$ much larger than the cosmological constant leading to the cosmic acceleration $\Lambda \simeq 10^{-82} GeV^2$. Due to this normalization, orbit disturbances are much larger than the realistic form corresponding to a realistic cosmological setup.

In left panel of Fig. 8.4 the initial rotation is clockwise, since $\dot{\phi}(1) < 0$. In this case, the term $(-\frac{3\Omega_s \dot{\phi}}{2r^2})$ in Eq. (8.28) is positive and induces repulsion. In this case the repulsive effects of the accelerating cosmic expansion are amplified by the effects of the spin.

For initial counterclockwise rotation (right panel in Fig. 8.4) the term $-\frac{3\Omega_s \dot{\phi}}{2r^2}$ in radial equation is negative and induces attraction. However, for spinless particle or small values of spin and consequently of the parameter Ω_s, such as $\Omega_s = 10$, the accelerating cosmological background dominates and the particles get deflected to unbounded orbit. On the contrary, when the spin of the particle is large, such as $\Omega_s = 100$, the attractive term $-\frac{3\Omega_s \dot{\phi}}{2r^2}$ in radial equation dominates the expansion and the spinning particle gets captured by the black hole.

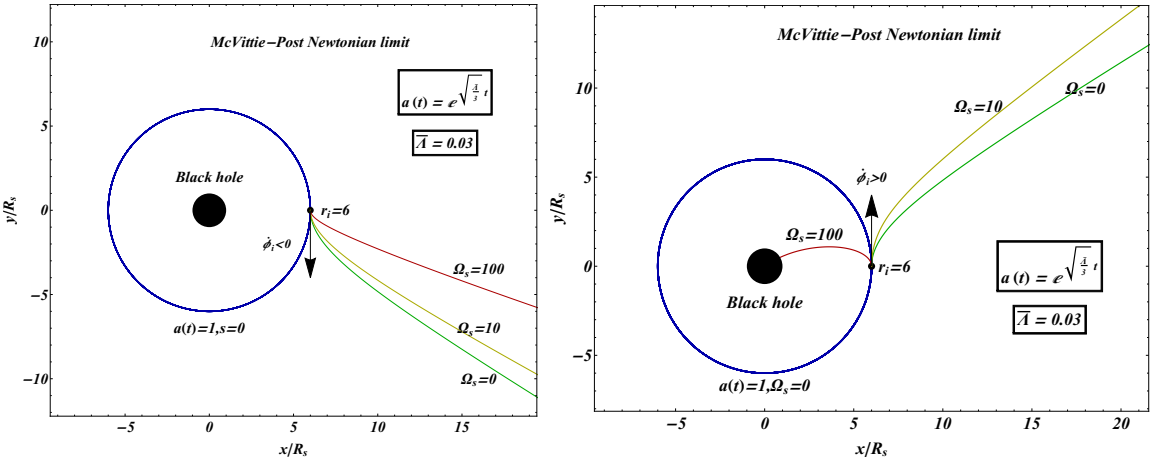

Figure 8.4: Same as Fig. 8.3, but the scale factor obeys an accelerating expansion of the form $a(t) = e^{\sqrt{\frac{\bar{\Lambda}}{3}} t}$ (de Sitter universe) with $\bar{\Lambda} = \Lambda R_s^2$. Notice the strong repulsive effects on the trajectories of the spinning/spinless particle for initial clockwise rotation (left panel) due to accelerating background expansion. The term $-\frac{3\Omega_s \dot{\phi}}{2r^2}$ in radial equation (8.28) induces repulsion (left panel). However, for initial counterclockwise rotation (right panel) and extremely large spin, the particle captured by the black hole since the term $-\frac{3\Omega_s \dot{\phi}}{2r^2}$ in radial equation induces attraction and dominates.

A crucial question of our analysis is which are the cosmological time intervals after which the effects of the expansion would become apparent. The answer can be easily obtained on dimensional grounds by equating the dimensionless parameters relevant for gravitational attraction (M/r) and background expansion $H_0 \Delta t$ where H_0 is the Hubble parameter $\dot{a}/a$ at the present time and Δt is the required time interval for the expansion effects to be observable. By equating these two parameters we find that the required time interval after which the cosmological expansion effects would become apparent on the

trajectories is

$$\boxed{\Delta t \simeq \frac{M}{H_0 r}} \tag{8.35}$$

where we have set $G = 1$. The time interval Δt can be easily derived in S.I. as

$$\Delta t \simeq \frac{GM}{H_0 r c^2}$$

and in Table 8.1 we give some estimates of the cosmological time intervals for a typical black hole, the solar system, a typical galaxy and a typical cluster of galaxies. The time intervals are in years, since we have consider that $1/H_0 \simeq 1.4 \times 10^{10}$ years (the approximate age of the Universe).

structure	distance r (m)	mass M (Kg)	Δt (years)
solar system	5×10^{12}	2×10^{30}	$\sim 4 \times 10^{0}$
typical galaxy	9×10^{20}	2×10^{41}	$\sim 3 \times 10^{3}$
cluster of galaxies	3×10^{22}	2×10^{45}	$\sim 7 \times 10^{7}$
black hole	2×10^{5}	2×10^{31}	$\sim 1 \times 10^{9}$

Table 8.1: In this table we present estimations for some cosmological structures for the required time interval $\Delta t \simeq \frac{1}{H_0}\frac{GM}{rc^2}$ after which the cosmological expansion effects would become apparent on the trajectories. For the Hubble rate we have set $H_0^{-1} \simeq 1.4 \times 10^{10}$years. In the case of black hole the have consider the distance $r = 6R_s$, as in the present work.

The MP equations have also been generalized to the case of modified theories of gravity, in which the matter energy-momentum tensor is not conserved. In modified gravity theories the Schwarzschild metric gets modified and so does the weak field limit, as we can see e.g. from eq. (32) of ref. [533], which state to $f(R)$ theories ($G = 1$)

$$\chi(r) = 1 - \frac{2M}{r} + \frac{(1 + f'(R_0))Q^2}{r^2} - \frac{R_0}{12} r^2 \tag{8.36}$$

Here, $Q = rV(r)$ is the charge of a black hole, $V(r)$ the potential and R_0 the curvature of the spacetime which we consider constant. An analysis along the line of the derivation of the McVittie metric for General Relativity (as discussed in [427]) could generalize this metric to the case of $f(R)$ theories and also lead to the derivation of its Newtonian limit (the generalization of eq. (8.11)). Alternatively, one could directly include the scale factor $a(t)$ as a new factor along with the radial coordinate in Eq. (32) of [533] and then take the Newtonian limit showing that it is a good approximation of the dynamical field equations for $f(R)$ gravity. This task is beyond the scope of the present analysis but it should be straightforward to implement in a future extension of our analysis.

8.3 Conclusions

We have constructed and solved numerically the MP equations in the post Newtonian limit of McVittie background thus obtaining the orbits of spinning particles close to a massive object in an expanding cosmological background. We have identified the effects of a spin-orbit coupling which can be repulsive or attractive depending on the relative orientation between spin and orbital angular momentum. A static universe (no expansion) was shown to lead to disrupted spinning particle orbits which are not closed and are confined between a maximum and a minimum radius. This range increases with the value of the spin. As expected for the spin values, for which the radius of the motion of the particle becomes less that $3R_s$, the particle is captured by the black hole. This result is in agreement with previous studies that have indicated the presence of such behavior of the orbits [482]. If we consider an expanding background and

the spin of the particle, the trajectories diverse or converse from the central mass. The result depends on the rate of expansion and on the direction and magnitude of the spin.

Interesting extensions of our analysis include the construction and solution of the MP equations for the strong field regime of the McVittie metric, or the consideration of different SSC like the P condition. Also, it is interesting to consider the motion of the spinning particle in non equatorial plane, or to study the case where both bodies (central and rotating) have spin.

Chapter 9

Summary of Thesis and Outlook

9.1 Summary and Conclusions

In this chapter, we present the conclusions of the study performed in this dissertation and the potential extensions. The present Thesis addresses interesting open questions of the current cosmological Physics, which we discuss in detail below.

In Chapter 1, we review the basic principles of modern Cosmology. We discuss about the components of the Universe, the basic cosmological models and many of their observational predictions. We describe in detail the concordance model and some extensions, modifications and deviations of this model. In section 1.15 we state the connecting principle of the Chapters of this Thesis: *Deviation directions from the Physics of the Standard ΛCDM model*. Such deviations refer to Hubble tension, to cosmological principle, to cosmological models for which applies $w \neq -1$ (quintessence and phantom models), to existence of topological defects, to the validity of law of gravity or to the variation of the fine structure constant and the gravitational constant.

In Chapter 2, we tested the cosmological principle through the analysis of the Union2 Supernova Ia data. That principle is also known as the Copernican principle and assumes that the universe is homogeneous and isotropic in large scales (larger than $100Mpc$). The Union2 compilation had the larger number of data when we worked with this project. Today, the largest compilation of Supernova Ia is the PANTHEON, which contains 1048 data. To process the data we used the hemisphere comparison method, which initially generates a random direction in the celestial concave. Then, we divided the data in two hemispheres and found the best fit values on the parameter Ω_{0m} in each hemisphere, through the minimization of the quantity $\chi^2(\Omega_{0m}, \mu_0)$ of equation (2.6). Afterward, we obtained the anisotropy level and we repeated the procedure 400 times in order to find the direction of maximum anisotropy. Simultaneously, we derived the 1σ error of the estimated direction. We obtained the best fit value as $\Omega_{0m} = 0.19$ and the direction of maximum acceleration as $\left(l = 129^{\circ}{}^{+3^{\circ}}_{-23^{\circ}}, b = -18^{\circ}{}^{+10^{\circ}}_{-11^{\circ}}\right)$, while the opposite direction corresponds to minimum acceleration. Finally, we obtained the maximum anisotropy level of the data which is $\left(\frac{\Delta\Omega_{0m,max}}{\Omega_{0m}}\right)^{U2} = 0.43 \pm 0.06$

As a next step, we divided the data in subsets of redshift and we repeated the procedure in order to identify possible redshift dependence. The tomography showed that there is no redshift dependence, since the most of the subsets had maximum anisotropy direction near the maximum anisotropy of the full dataset (in a region of about 40°).

Naturally, the question if the maximum anisotropy level of Union2 data is consistent with statistical isotropy arises. To answer this question, we used the Monte Carlo method with simulated isotropic data which followed a Gaussian distribution. We chose only 10 random directions, since our purpose was to compare the anisotropy level between Union2 data and random data and we ran the data 40 times. We found that the level of anisotropy for the Union2 data is about 1σ, since only 1/3 of the

experiments had anisotropy level larger than the isotropic simulated data. It is obvious that the level of anisotropy is negligible. Thus, the Union2 data are consistent with statistical isotropy, which means that the cosmological principle is valid and not violated by the distribution of Supernova Ia compilation.

An important result of our work is that the distribution of Supernova Ia in celestial concave has a preferred direction. Also, from the bibliography, we observed that there are other cosmological effects which have a preferred direction. These structures are the quasars alignment polarization, the bulk velocity flows and the dipole, quadrupole and octopole moments of the CMB. Since all coordinates are located in a small part of the North galactic hemisphere, it is straightforward to estimate the probability that six random points would lie in such a small region. Using again the Monte Carlo simulation, we found that the probability is less than 1%. Thus, the coincidence of these independent preferred axes in such a small angular region is a highly unlikely event, even if we don't take into account the CMB multipole moments (the probability in this case is about 7%). We conclude that, there is a preferred cosmological axis for these uncorrelated cosmological probes, but the reasons of this coincidence are not obvious. It constitutes an open field in Cosmological Physics.

The confirmation of the cosmological preferred axis would constitute a breakthrough in Cosmology and a region which new Physics may emerge. In order to check this direction, we need more Supernova Ia data, especially in South hemisphere, in bigger redshifts and other cosmological probes with preferred axis.

In Chapter 3, we dealt with some scalar fields and their role in Cosmology. Scalar fields occur naturally in Lagrangian in order to describe variations of cosmological constants such as the gravitational and the fine structure constant or inhomogeneities in dark energy. Due to non-trivial configurations of the scalar fields, emerging topological defects are formed in a symmetry breaking phase transition during the evolution and expansion of the Universe. Generally, topological defects can be used to describe the large scale structures of the Universe. Even if, in a four dimensional spacetime there are four kinds of topological defects (monopoles, strings, domain walls and textures), we dealt with monopoles which are formed when a $SO(3)$ symmetry gets spontaneously broken to $U(1)$, during the evolution of the Universe.

We considered the 't Hooft-Polyakov monopole ansatz which contains two radial functions $X(r)$ and $W(r)$. The function $X(r)$ is a part of the dilatonic coupling $B(\Phi^a)$ which couples to electromagnetic term in Lagrangian and the function $W(r)$ is a part of the electromagnetic field. The potential energy density of the scalar field has some minima, each of them corresponds to a vacuum and determines the mass of the scalar field. The lowest vacuum is the 'true' vacuum, while the others are 'false' vacuum. Any higher energy vacuum is necessarily unstable, so a false vacuum has to decay by converting into true vacuum. Symmetry can generally be broken in several different ways, and thus we expect to have a number of vacuum states with different properties. Particle physicists refer to these states as different vacua.

The radial functions determined through the minimization of the self energy of the monopole, since physical systems tend to minimize their energy. We investigated the cases where the potential is $V(\Phi^a) = \frac{\lambda}{4}(\Phi^a\Phi^a - \eta^2)$ and the dilatonic function has polynomial $\Phi^a(r) = 1 + qX^2$ and exponential form $\Phi^a(r) = e^{qX^2}$. Since, the mass which develops the gauge field is m_A and the mass of the Higgs field is m_Φ, we defined the ratio $\beta = \frac{m_\Phi}{m_A}$. We derived the radial functions for a few values of the parameters β and q. The results shown that these functions have almost the same form for both dilatonic functions. At small distances the scalar field increases fast with distance, but the electromagnetic field dominates since it is much bigger. At bigger distances (far away from the monopole) the scalar field dominates and the gauge field tends to zero.

As a next step, we considered that the monopole is embedded in a model with $O(4)$ symmetry. For this reason, we added one more component $g(r)$ in the scalar field Φ^a. In order to detect the scalar field and the gauge field, we minimized the perturbative energy of the monopole in a presence of a Gaussian external magnetic field. The dilatonic function obeys exponential form. We found that the fields always vary (except the region very close to the core, inside and outside) and they are not stabilized. Thus, we conclude that in this case the monopole is always unstable, for any value of the parameters β and q.

More precisely, the scalar field increases almost proportional with distance, while the field $g(r)$ decreases. However, at small distances, where the external field is significant, the field remains out of the vacuum (minimum) due to the effects of the external field which stabilizes locally the embedded mono-

pole. As the dimensionless parameter β increases, the slope of the curves increases and the fields acquire their vacuum expectation value at smaller distances. Concluding, the existence of a dilatonic coupling in field theories, which predicts the existence of topological defects, implies the presence of new properties for the defects.

ALPs belong to a new class of scalar particles that generically couple to photons, opening the possibility of oscillations from photons into ALPs in an external magnetic field. They can constitute a possible component of the dark matter. The coupling between photons and ALPs, as we emphasize in Chapter 4, described by the Lagrangian term $-\frac{1}{4}B_F(\phi)F_{\mu\nu}F^{\mu\nu}$, where $B_F(\phi) = 1+g\phi$ is the coupling function and g the coupling constant. The coupling constant connected with the mass of the ALP through the Eq. (4.8) and the estimation of the coupling constant drives to estimation of the particle mass. Many experiments around the world aim to estimate this coupling constant. They are photon regeneration experiments, since the photons convert to ALPs and then the ALPs convert to photons. All the experiments failed to detect any positive signal for this interaction and an upper bound for the coupling constant is estimated. We found that the most stringent bound estimated from fifth force experiments and is so stringent, that it is beyond the sensitivity of the current experimental apparatuses.

A similar coupling to electromagnetism occurs in chameleon Cosmology, when the coupling constant is enough below unity ($g << 1$). The experiments which aim to detect chameleons based on the afterglow effect because the chameleon mass depends on the density of the environment. Due to chameleon mechanism, these dark energy candidate particles avoid the experimental detection. The experiments which have been executed, failed to detect chameleon interactions and estimated energy bounds where excluded the evidence of chameleons. Finally, in Chapter 4 we extended the Bekenstein theory introducing in Lagrangian a similar dilatonic function of the form $B_F(\phi) = e^{-2\phi}$, in order to investigate the cosmological evolution and the effects of this coupling in Quintessence Cosmology. It is known that in quintessence models, when the potential is linear, the Big Crunch singularity occurs which corresponds to a phase of rapidly decreasing of the scale factor, since the effective force is strongly attractive, due to increasing of the scalar field. This effect destabilize the cosmological systems. We solved the equation of motion for the scalar field and the acceleration equation for the scale factor in FRW spacetime during a pure radiation epoch. We defined the electromagnetic parameter $\zeta_m = \frac{L_{em}}{\rho_m}$ and we considered the cases where this parameter is positive which corresponds to electrostatic energy domination against magnetostatic energy. The non-relativistic energy density is big enough and dominates the system, since $\zeta_m \ll 1$. We found that as the parameter ζ_m increases the Big Crunch occurs later, since the scalar field increases rapidly later. It is obvious that, as the rate of the electromagnetic energy increases as a fraction of non-relativistic matter, the cosmological systems remain stable for longer time.

In Quintessence models the equation of state parameter w is negative, but bigger than the rate $w = -1$. We investigated the evolution of the state parameter as a function of redshift, when $\zeta_m > 0$. We found that the dilatonic function $B_F(\phi) = e^{-2\phi}$ induces very small fluctuations in the equation of state parameter w, very close and above the value $w = -1$. As the electromagnetic parameter ζ_m increases, the degree of fluctuations is bigger. We found similar results, when we investigated the evolution of the equation of state parameter as a function of time. When the time is big enough, the rate of electromagnetic parameter ζ_m, negligibly affects the evolution of the parameter w, since the curves are almost the same.

The dilatonic function $B_F(\phi)$ can describe variation of the fine structure constant α. Scalar fields and chameleons would induce these variations, when they interact with photons and the order of the coupling g can estimate the order of variation of α. Thus, the experimental estimation of the order of g is of great importance, since we can test if the experimental value of g can support the observed variation of the fine structure constant.

It is widely acceptable that the universal law of Newtonian gravity applies in every distance scale. The gravitational force is proportional to the product of the two masses, and inversely proportional to the square of the distance between them. However, there are indications from recent experiments that in sub-mm distances, the interactions do not follow the inverse square law of gravity. In the work of Chapter 5 we used the data from the Stanford Optically Levitated Experiment (SOLME) in order to detect deviations from Newtonian gravity or indications for new forces in sub-mm scale. In this experiment a silica microsphera is trapped in a region with high vacuum, very close (the distance was from $25\mu m$ to

$234\mu m$) to a horizontal cantilever. A laser beam balances the gravity of the microsphera for a short time and the force between microsphera and cantilever measured. The sensitivity of the apparatus is of order of $10^{-18}N$ and the experiment is repeated with 3 identical microspheres.

In our consideration, we calculated the residual force between the measured force and the electrostatic background force and we found the best fit values for several interaction parameterisations minimizing the quantity χ^2 of eq. (5.9). We fit the residual force using oscillating parameterization and we found that the data have a strong minimum when the wavelength is $\lambda \simeq 35\mu m$. This wavelength is of order of Dark energy density, since we expect that $\lambda_{de} \simeq 80\mu m$. In order to check the result statistically, we found that if there is not residual force in data, the difference in χ^2 is more than 13 units. Then, we used a Monte Carlo simulation with random residual force data which follows Gaussian distribution with zero mean value and we found that the quantity χ^2 in most cases was bigger. As a last step, we repeated the Monte Carlo simulation 100 times and we found that only at 5% of the probes, the quantity χ^2 was smaller. Thus, we estimated that the oscillating signal is at 2σ confidence level, which is strong enough.

The existence and verification of this signal through more experiments is of great importance, since we can connect the signal with new interactions (fifth force), or modified theories of gravity, or extensions of the theories of General Relativity and with Dark energy candidate particles. A wide range of extensions of GR include $f(R)$ theories, massive Brans-Dicke (BD) and scalar tensor theories, compactified extra dimension models. A theoretical model where stable spatial oscillations naturally occur for the gravitational potential are non-local theories of gravity, where the action contains infinite derivatives. These theories have many advantages since they are free from singularities and instabilities. Also, they arise naturally from the quantum level and they are consistent with the cosmological observations with no need of cosmological constant.

In order to find if another parametrization for the residual force induces a better best fit than oscillating parametrization, we fit for the residual force Yukawa exponential and power law parametrization. These parametrizations gave $\delta\chi^2 < 1$, which means that these fits are not good for the data.

After a communication with SOLMEs team, we mentioned to them our observation. They told us that possibly the signal is a systematic effect caused by the non-Gaussian tails of the laser beam whose pressure levitates the microsphere. The intensity of these tails has a periodic oscillation, which can mimic oscillating force signal. In this case we can use the signal to estimate an upper bound for the amplitude of the oscillating residual force. We estimated that the amplitude must be $\alpha < 0.3 \times 10^{-17}N$ at 2σ confidence level, when the wavelength is $\lambda \simeq 35\mu m$.

An alternative to ΛCDM model is the Phantom Cosmology, where the equation of state parameter is less that -1 ($w < -1$). For such a range of w, this class of models predicts the existence of a future singularity, where the scale factor increases rapidly, diverges and the bound systems get dissociated. It is known as the Big Rip singularity and the time of Big Rip occurs according to previous studies with Newtonian consideration, when the minimum of the effective potential disappears.

The recent direct discovery of gravitational waves from the LIGO/Virgo collaboration is a triumph of the theory of GR. Many researchers have begun to study the effects of cosmological expansion on the gravitational waves. In Chapter 6, we studied the effects on the wavefunction of a gravitational wave as it approaches in a region with strong gravity, such as the neighborhood of a big mass, for example a black hole. We consider that the spacetime expands and it is described by the McVittie metric in Newtonian limit. We solved the wave equation numerically introducing boundary conditions far away from the big mass.

As a test of our derivation, we found that in the absence of the mass ($R_s = 0$), which corresponds to evolution of the wave in an empty space, the wavefunction describes a harmonic wave with constant wavelength and amplitude. Also, in our investigation we found that both waves (that which corresponds to evolution in the absence of the mass and that which corresponds to the presence of the mass) are practically identical far away from the point mass.

Also, we found that the period of the wave increases (the frequency decreases) as it approaches the central mass with strong gravity. This effect is known as gravitational time delay and this observation is a goal of our work. The difference in time period $T - T_0$, where T_0 corresponds in the period of the wave when propagated in empty space, is proportional to the mass of the central body (R_s) when the distance

is stable. As the wave approaches the central body, the difference in period increases, which means that the gravitational time delay depends on the radial distance and the gravity of the central body.

The amplitude of the gravitational wave increases as the wave approaches the central mass. As it seems, the increasing curvature and gravity of spacetime increases the amplitude since the energy of the wave becomes bigger. The ratio A/A_0, where A_0 is the constant amplitude of the wave in vacuum, depends on the central mass R_s and on the distance from the origin. As the wave approaches the origin and the gravity gets more stronger, the amplitude increases and this effect is proportional to the mass. Due to interaction between wave and strong gravity in the vicinity of the mass, the wave gains energy from the spacetime.

The time power spectrum of a wave is the Fourier expansion of the wave. It contains information about the harmonic frequencies, their amplitude and their degree of participation in the wavefunction. We expended the wave for a time interval of approximately two complete periods. We found that in the presence of a point mass with strong gravity, the lower frequencies have a higher amplitude than the higher frequencies. Even if, this observation depends on the time interval, qualitatively is one more evidence for the time delay gravitational effect. The above results are held for every multipole component of a spherical or planar wave in the weak field condition. Thus, from a power spectrum of a gravitational wave, we can find information for the gravity in the vicinity of the wave.

The point mass could be any celestial body such as a planet, a star, a neutron star or a galaxy. In the case of the solar system we estimated that the difference in period is expected to be of the order of 1 part in 10^6 parts. It is negligible, but today this magnitude is measurable since the precision of the measurement of the time is many orders bigger.

In Chapter 7 we take into account relativistic effects, since the Newtonian approximation is inappropriate for some massive large strongly bound systems, in order to estimate the time of Big Rip for a bound system. We consider the full McVittie metric for the cosmological background and we solve the geodesic equations in order to find if the time of Big Rip occurs earlier or latter than the Newtonian consideration and which parameters of the system affect the time of Big Rip. For the gravitational bound systems we define the parameters $\bar{m}$ and $\bar{\omega}_0$ from the equations (7.34) and (7.35) respectively. We found that in Schwarzschild limit which corresponds to $H = 0$, when $\bar{m} < 1/6$ the system is stable and the orbits are circular. When $1/6 < \bar{m} < 1/3$ the orbits are also circular but weakly stable, while when $\bar{m} > 1/3$ there is no circular orbit. Thus, in contrast to naive intuition, the stronger effects of gravity in the relativistic case tend to destabilize rather than stabilize bound systems.

Then, we analyze the case when the effects of the expansion have been turned on ($H \neq 0$). The system of geodesic equations can be solved only numerically. We define the time of dissociation (criterion of dissociation) of a bound system as the time when the size of the system has increased by about 20% compared to its equilibrium value. We found that relativistic effects tend to destabilize bound systems leading to an earlier dissociation compared to the predictions in the context of the Newtonian approximation. In particular, when the parameter $\bar{\omega}_0$ is stable, as the parameter $\bar{m}$ increases, the dissociation occurs earlier. Also, the time momentum of dissociation increases as the parameter $\bar{\omega}_0$ increases.

For completeness, we calculated for several cosmological bound systems the time difference of Big Rip between the Newtonian approximation and relativistic consideration. We found that for the most cosmological systems, the difference is negligible and the Newtonian approximation is sufficient to describe the effect. Only for hypothetical very large massive systems, one must approach the effect relativically, since the time difference is not negligible. Generally, systems with $\bar{\omega}_0$ bigger than 10^4, which are relatively small have almost the same dissociation time, while systems with big values of the parameter $\bar{m}$ and small values of $\bar{\omega}_0$ have appreciated difference of t_{rip} due to relativistic effects. These hypothetical systems must have mass $10^{20}\ M_\odot$ and size about $100Mpc$ (about 10^6 times more massive than a typical cluster of galaxies).

A most commonly project in General Relativity is the investigation of the orbits of a particle in a given cosmological background. If we consider that the motion evolves only with the influence of gravity and ignore the spin of the particle, then the orbits are the geodesics in such a spacetime. In Chapter 8, we considered the motion of a spinning particle in a background which is the post Newtonian limit of the McVittie metric. The problem described from the MP equations which indicate that the coupling

between spin and velocity induces additional force and the motion of the particle is a worldline, different than geodesic. This force can be attractive or repulsive depending on the orientation of the spin.

The system of MP equations is under-defined, even if we consider the motion of the particle in the equatorial plane. There are only 10 independent equations of motion for the 13 variables. Thus, in order to define a unique worldline, we supplement the system with the SSC, which defines the centroid of the system. We adopted the T condition where the magnitude of the spin s and the dynamical mass μ are constants of motion. In a static universe, the orbit of a spinless particle is circular. The presence of spin deforms the orbits and the particle orbits between a minimum and a maximum radius. The radial range of the motion depends on the magnitude of the spin, the dynamic mass μ of the particle and the Schwarzschild radius R_s of the black hole. In the case where the spin-orbit interaction is attractive, the innermost stable circular orbit (ISCO) has radius $r = 3R_s$. The particle gets captured and merged with the black hole when $\frac{s}{\mu R_s} > 0.6$, since the radial distance becomes less than the ISCO.

The behaviour of a spinless particle depends on the expansion rate of the cosmological background and it is crucial in order to understand the deformation of the orbits of a spinning particle. In a decelerating universe with $a(t) = t^{2/3}$ the spinless particle gets captured by the black hole. In an accelerating universe with a de Sitter type expansion $a(t) = e^{Ht}$, where $H = \sqrt{\frac{\Lambda}{3}}$, the system gets dissolved, since the repulsive background dominates against gravity.

Further, we investigate the influence of spin in the orbits. In a decelerating cosmological background, where the scale factor is $a(t) = t^{2/3}$, when the magnitude of spin is less the particle gets captured by the black hole, for attractive or repulsive coupling between spin and orbital angular momentum. The result seems to be unexpected in the case of repulsive interaction. After a more careful observation of the orbits we found that even if initially the particle rotates clockwise, after short time reserves his orientation of rotation, approaches the central body, the interaction becomes attractive and with the aid of gravity the particle gets captured by the black hole. For large enough values of spin, even if the initial rotation is clockwise or counterclockwise, the orbit gets dissociated, mainly due to the domination of the expanding cosmological background. The spin-orbit coupling is subdominant.

In an accelerating cosmological background such as a de Sitter spacetime with $a(t) = e^{Ht}$, the expansion rate dominates almost in all cases. The expansion effects lead to dissociation of the initially bound system. An exception is the case of attractive coupling between spin and orbital angular momentum and extremely large values of spin, where the particle gets captured by the black hole, since the attractive coupling is strong and dominates the repulsive expansion rate. The time interval which is necessary to observe expansion effects when we consider spinning particles in a cosmological structure, ranges between a few years for our solar systems and a few decades of billion years for a cluster of galaxies.

9.2 Future perspectives

The present Thesis addresses interesting open questions of the current cosmological theories and observations, which we discuss below.

The validity of the cosmological principle is fundamental in General Relativity. Even if, all the experiments until now indicate the validity of this principle, it is always necessary to check that the Universe is homogeneous and isotropic. Thus, as the number and the accuracy of cosmological data increases through more observations, the accuracy of the tests will become better. In Chapter 2 we test the validity of the cosmological principle with the data from the Union2 compilation, which contains 557 supernova type Ia. Nowadays, the PANTHEON compilation consists of almost a double number of supernova type Ia (1048) and we can use this compilation to test more accurately the cosmological principle or to calculate the expansion rate H_0 in order to estimate the statistical significance of the Hubble tension. Also, we can check if the preferred axis, which we found in our work in Chapter 2, is in the same direction, or how far from this direction it is.

The topological defects have formed in the early Universe and contain information about the first moments of the Universe. In Chapter 3 we study the stability of the embedded monopoles. We can

extend our research in the other kinds of topological defects, especially the cosmic stings since it seems that they are more stable than monopoles. Thus, interesting extensions are the following:

- Investigation of the stability properties of more realistic embeddings like the electroweak vortex [209, 211, 219, 534]. The possible formation of new electroweak vortices with core condensates representing confinement of the instability is a particularly interesting prospect. In addition, the possible stabilization of the electroweak vortex for realistic parameter values can be described by a dilatonic coupling.

- Investigation of the core properties of other dilatonic defects like textures, skyrmions and domain walls in the presence of external gauge fields.

- The presence of dilatonic defects with Hubble scale cores could naturally induce spatial variation of the corresponding gauge charges and in particular of the fine structure constant. This prospect is interesting in view of the claims of the existence of a fine structure constant dipole on cosmological scales obtained from the absorption spectra of quasars on cosmological scales [194, 195]. This class of models naturally predicts an alignment of the fine structure constant and dark energy dipoles. Indications for such an alignment have been observed in a combination of type Ia data and quasar absorption spectra data [195]. Thus, the detailed study of the cosmological properties of this class of models (extended topological quintessence) constitutes an exciting extension.

In a quintessence model such as that we study in Chapter 4, we can change the potential of the scalar field setting quadratic form $V(\phi) = \gamma\phi^2$, where γ is a negative constant. For several values of the fraction ζ_m of the electromagnetic density to matter density, we can observe the consequences at the time of Big Crunch and the parameter w_{DE} of the equation of state.

Most previous studies analyzing sub-mm force data have consistently used Yukawa parameterizations of the new forces. Such parameterizations are well motivated theoretically but they are not uniquely favored especially in view of the fact that their analytic continuation is an oscillating parameterization. The use of new and in particular oscillating parameterizations of sub-mm new forces to fit the data of experiments searching for new forces on sub-mm scales is a novel quite promising approach, such as our consideration in Chapter 5. If these oscillating improved fits are not statistical or systematic artifacts of the data, they could be early hints of modified gravity with major impact on the scientific community. It is therefore important to purse this line of research further using additional datasets, improved data analysis methods and search for further theoretical support of the best fit parameterizations.

The detection of GWs by the Laser Interferometer Gravitational Wave Observatory (LIGO) Collaboration and the Virgo Collaboration opens a new window for the investigation of strong gravitational fields and exotic physics. New windows also open for testing extensions of GR. Of particular interest is the recent detection of the GW170817 originating from the merger of a binary neutron star and the almost simultaneous detection of its γ-ray counterpart which laid the foundation of a new era of multi-messenger GW astronomy and demonstrated the equality between the speed of GWs and the speed of light ruling out a range of scalar-tensor extensions of GR. Until now they have announced 11 cosmological events which accompanied by detection of GW.

The proposed investigation of field theoretical effects on the generation of GW bursts from cosmic string cusps is original and novel since the field theoretical origin of GW bursts due to colliding scalar-field configurations (e.g. cosmic strings) have not been considered in literature. All relevant previous analyses have focused on a simplified version of the action or have considered field theoretical effects on macroscopic stochastic GW background using preexisting software. Therefore the impact of the proposed project on the scientific community will be significant as it may lead to non-trivial modifications in the current bounds on cosmic string parameters as well as to predictions of very specific signatures in GW detectors which may identify such possible future events.

In Chapter 8, of this Thesis we dealt with the dynamics of spinning particles in the pole-dipole approximation as described by the Mathisson-Papapetrou equations. Since, the majority of the celestial bodies has less or large spin angular momentum, it is necessary to investigate the influence of the spin in the

orbits of each body, which rotates around a much bigger mass. The spin orbit coupling must be investigated with more details in a relativistic consideration (McVittie background), since many cosmological systems evolve with almost relativistic speed.

Also, interesting extensions of the work of Chapter 8 will be the behaviour of the systems in the case where the spin of the particle is not parallel to the orbital angular momentum, the consideration of another supplementary condition (such as the P condition), where the magnitude of the spin is also a constant of motion, or the investigation of the motion in the non-equatorial plane.

Appendix A

Riemann Tensor-McVittie spacetime-Newtonian approximation

A.1 Christoffel symbols

The non-vanishing Christoffel symbols for the line element (6.21), which we have used in the present dissertation (approximate McVittie spacetime for a moving test body) are the following

$$
\begin{aligned}
\Gamma^0_{00} &= \frac{\dot{a}M}{a(a\rho-2M)} \\
\Gamma^0_{01} &= \frac{M}{\rho(a\rho-2M)} \\
\Gamma^0_{11} &= \frac{a^2\dot{a}\rho}{a\rho-2M} \\
\Gamma^0_{22} &= \frac{a^2\dot{a}\rho^3}{ar-2M} \\
\Gamma^0_{33} &= \frac{a^2\dot{a}\rho^3\sin^2\theta}{a\rho-2M} \\
\Gamma^1_{00} &= \frac{M}{a^3\rho^2} \\
\Gamma^1_{01} &= \frac{\dot{a}}{a} \\
\Gamma^1_{22} &= -\rho \\
\Gamma^1_{33} &= -\rho\sin^2\theta \\
\Gamma^2_{12} &= \frac{1}{\rho} \\
\Gamma^2_{02} &= \frac{\dot{a}}{a} \\
\Gamma^2_{33} &= -\sin\theta\cos\theta \\
\Gamma^3_{03} &= \frac{\dot{a}}{a} \\
\Gamma^3_{13} &= \frac{1}{\rho} \\
\Gamma^3_{23} &= \frac{\cos\theta}{\sin\theta}
\end{aligned}
\tag{A.1}
$$

where the dot represents derivative with respect to coordinate time.

A.2 Riemann tensor

The corresponding non-vanishing components of the Riemann (curvature) tensor are:

$$
\begin{aligned}
R_{0101} &= \frac{a\rho\Big(2M + \rho^2\big(-\dot{a}^2 M + a\ddot{a}(a\rho - 2M)\big)\Big) - 3M^2}{a\rho^3(a\rho - 2M)} \\
R_{0202} &= \frac{2M^2 + a\rho\Big(-M + \rho^2\big(-\dot{a}^2 M + a\ddot{a}(a\rho - 2M)\big)\Big)}{a\rho(a\rho - 2M)} \\
R_{0212} &= -\frac{a\dot{a}\rho M}{a\rho - 2M} \\
R_{0303} &= \sin^2\theta \frac{2M^2 + a\rho\Big(-M + \rho^2\big(-\dot{a}^2 M + a\ddot{a}(a\rho - 2M)\big)\Big)}{a\rho(a\rho - 2M)} \\
R_{0313} &= -\frac{a\dot{a}\rho M \sin^2\theta}{a\rho - 2M} \\
R_{1212} &= -\frac{a^3\dot{a}^2\rho^3}{a\rho - 2M} \\
R_{1313} &= -\frac{a^3\dot{a}^2\rho^3 \sin^2\theta}{a\rho - 2M} \\
R_{2323} &= -\frac{a^3\dot{a}^2\rho^5 \sin^2\theta}{a\rho - 2M}
\end{aligned}
\tag{A.2}
$$

When $\theta = \pi/2$ and $r = a(t)\rho$ the above components of the Riemann tensor are simplified as

$$
\begin{aligned}
R_{0101} &= \frac{r\Big(2M - \frac{\dot{a}^2}{a^2} r^2 M + \frac{\ddot{a}}{a} r^2 (r - 2M)\Big) - 3M^2}{\frac{r^3}{a^2}(r - 2M)} \\
R_{0202} &= \frac{r\Big(-M + r^2 \frac{\ddot{a}}{a}(r - 2M) - r^2 \frac{\dot{a}^2}{a^2} M\Big) + 2M^2}{r(r - 2M)} \\
R_{0212} &= -\frac{\dot{a} r M}{r - 2M} \\
R_{0303} &= \frac{r\Big(-M + r^2 \frac{\ddot{a}}{a}(r - 2M) - r^2 \frac{\dot{a}^2}{a^2} M\Big) + 2M^2}{r(r - 2M)} \\
R_{0313} &= -\frac{\dot{a} r M}{r - 2M} \\
R_{1212} &= -\frac{r^3 \dot{a}^2}{r - 2M} \\
R_{1313} &= -\frac{r^3 \dot{a}^2}{r - 2M} \\
R_{2323} &= -\frac{r^5 \dot{a}^2}{a^2(r - 2M)}
\end{aligned}
\tag{A.3}
$$

Appendix B

Data from SOLME

In Table B.1 we present the datapoints which we used to find the best fit for the oscillating parameterization of the residual force dF in Chapter 5. The data contains the distance r between the center of the microsphera and the origin of a cartesian coordinate system which located in the center of the front size of the cantilever (see Fig. 1 of [325]), the residual force $F - F_N$ (the difference between the measured force F and the electrostatic background F_N), the corresponding error and the number of the experiment (number of microsphera). These datapoints, kindly was provided by the authors of Ref. [325] after request.

Table B.1: The 96 residual force datapoints from the Stanford Optical Levitated Experiment, which were used for the χ^2 analysis. The data contains the distance r between the center of the microsphera and the origin of a cartesian coordinate system which located in the center of the front size of the cantilever, the residual force $F - F_N$ (the difference between the measured force F and the electrostatic background F_N), the corresponding error and the number of the experiment

$r\ (mm)$	$F - F_N\ (fN)$	$1\sigma\ (F - F_N)$	Microsphera
0.228	-0.007	0.015	I
0.218	-0.015	0.017	I
0.208	0.006	0.018	I
0.198	-0.008	0.019	I
0.188	0.002	0.015	I
0.178	-0.001	0.015	I
0.173	0.013	0.015	I
0.168	0.005	0.015	I
0.162	-0.016	0.020	I
0.158	-0.002	0.017	I
0.152	0.007	0.015	I
0.142	0.013	0.016	I
0.136	-0.012	0.020	I
0.132	0.002	0.016	I
0.126	-0.055	0.017	I
0.122	-0.017	0.016	I
0.117	0.040	0.015	I
0.112	0.027	0.015	I
0.106	0.030	0.016	I
0.102	-0.012	0.014	I
0.097	-0.003	0.018	I
0.096	-0.034	0.017	I

0.087	0.048	0.049	I
0.086	0.036	0.022	I
0.077	0.020	0.027	I
0.076	-0.022	0.068	I
0.066	-0.017	0.021	I
0.066	0.045	0.056	I
0.056	-0.026	0.035	I
0.047	0.041	0.034	I
0.037	0.027	0.023	I
0.027	-0.005	0.016	I
0.229	-0.014	0.020	II
0.219	0.005	0.023	II
0.209	-0.022	0.023	II
0.199	0.012	0.021	II
0.189	-0.021	0.020	II
0.179	0.003	0.020	II
0.176	0.016	0.018	II
0.169	-0.010	0.020	II
0.166	0.021	0.033	II
0.159	-0.048	0.021	II
0.156	0.007	0.033	II
0.146	0.018	0.041	II
0.136	-0.018	0.032	II
0.134	0.006	0.022	II
0.125	-0.015	0.020	II
0.125	-0.018	0.024	II
0.116	0.049	0.018	II
0.114	-0.003	0.025	II
0.106	-0.007	0.018	II
0.105	0.024	0.021	II
0.095	0.022	0.040	II
0.095	-0.004	0.036	II
0.085	-0.039	0.018	II
0.084	0.012	0.032	II
0.075	-0.040	0.024	II
0.075	-0.061	0.042	II
0.065	0.020	0.037	II
0.064	0.012	0.058	II
0.055	-0.025	0.033	II
0.045	0.023	0.032	II
0.035	0.040	0.030	II
0.025	-0.045	0.055	II
0.234	-0.030	0.020	III
0.224	-0.002	0.022	III
0.214	-0.003	0.029	III
0.204	-0.021	0.029	III
0.194	-0.003	0.024	III
0.184	-0.019	0.026	III
0.178	0.006	0.013	III
0.174	-0.014	0.020	III
0.168	-0.018	0.015	III
0.164	-0.004	0.020	III

0.158	-0.023	0.024	III
0.148	0.008	0.026	III
0.137	-0.017	0.030	III
0.134	-0.001	0.027	III
0.128	0.014	0.038	III
0.123	-0.004	0.014	III
0.117	0.004	0.017	III
0.114	0.008	0.017	III
0.108	0.035	0.014	III
0.103	0.030	0.016	III
0.095	0.036	0.020	III
0.094	-0.002	0.016	III
0.086	-0.024	0.014	III
0.084	0.025	0.030	III
0.076	0.002	0.020	III
0.074	-0.005	0.014	III
0.066	-0.004	0.019	III
0.064	-0.013	0.016	III
0.055	-0.047	0.045	III
0.045	0.002	0.040	III
0.036	-0.010	0.057	III
0.025	-0.005	0.037	III

Appendix C

Numerical Code for the Dissociation of Bound Systems in a Phantom Cosmological Background

C.1 Mathematica code

In this Appendix, we present the numerical code which we have developed in the context of Ref. [4] and we used to derive the figures of Chapter 7 of this dissertation. In particular, we plot the effective potential $V_{eff}(\bar{r})$ of a bound system in phantom cosmological background as a function of the rescalled distance $\bar{r}$, for several values of the parameters of the analysis $\bar{m}$, $\bar{\omega}_0$ and $\bar{H}$.

```
SetDirectory["D:\\"];
Clear[om, w, m]
am = 1;
a[t_]:=am/(-w + (1 + w)t)^(-2/(3(1 + w)));
d2a = D[a[t], {t, 2}];
ff = d2a/a[t]//FullSimplify;
f[r[t]] = 1 - 2m/r[t];
H[t_]:=0;
dH[t_]:=D[H[t], t];
eq1 = r''[t] == dH[tt[t]]Sqrt[1 - 2m/r[t]]r[t]tt'[t]^2 + (1 - 3m/r[t])om^2/r[t]^3-
((1 - 3m)om^2/r[t]^2 - r[t]H[tt[t]]^2);
alpha[tt[t], r[t]] = r[t]f[r[t]]^(-1/2)H[tt[t]];
eq2 = -(f[r[t]] - mr[t]^2H[tt[t]]^2/(om^2(1 - 3m)))tt'[t]^2 - 2alpha[tt[t], r[t]]m/(om^2(1 - 3m))
tt'[t]r'[t] + f[r[t]]^(-1)r'[t]^2m/(om^2(1 - 3m)) + m/((1 - 3m)r[t]^2) + 1 == 0; (*first integral*)
ttp = Part[Solve[eq2, tt'[t]], 1, 1, 2]//FullSimplify; (*first derivative of coordinate time*)
lam2 = -2(1 + 3w)/(3(-w + (1 + w)t))^2;
potpap = -om^2/r[t] + om^2/(2r[t]^2) - 0.5lam2r[t]^2;
forcepap = -D[potpap, r[t]]/.{r[t] → ar, t → ti} //FullSimplify; (*Newtonian force*)
forcemm = Part[eq1, 2]/.{tt'[t] → ttp}; (*relativistic force*)
forcemm1 = forcemm/.{r[t] → ar, tt[t] → ti, r'[t] → rp};
Off[FindMinimum::lstol, FindRoot::lstol, FindMinimum::cvmit, FindMinimum::sdprec];
forcemm1; Clear[forcet]
forcet[rr_, tit_, omt_, mt_]:=forcemm1/.{w-> - 1.2, rp → 0, ar → rr, ti → tit, om → omt, m → mt}
pott[rt_, tit_, omt_, mt_]:=NIntegrate[-forcet[rr, tit, omt, mt], {rr, 1, rt}]
```

```
omt = 300;
mbart = 0.15;
tit = 1;
rfin = 1.8;
plv1 = Plot[pott[rr, tit, omt, mbart], {rr, 0.8, rfin},
PlotStyle → {Hue[0.95], Dashing[0.025], Thickness[0.002]},
Frame → True, PlotRange → All, FrameLabel → {"r̄", "V_eff(r̄)"},
LabelStyle → {Bold, 12, FontFamily → "Helvetica"},
Axes → {False, False}];
grv1 = Graphics[{Text[Style["m̄=0.15, ω̄0=300, H̄=0", Bold, 12, Black], {1.6, 1900}, {2, 1}],
Text[Style["(a)", 12, Black], {1.7, 500}, {2, 1}]}];
plotvs = Show[plv1, grv1]
Export["plotvs.pdf", plotvs] Clear[forcet]
```

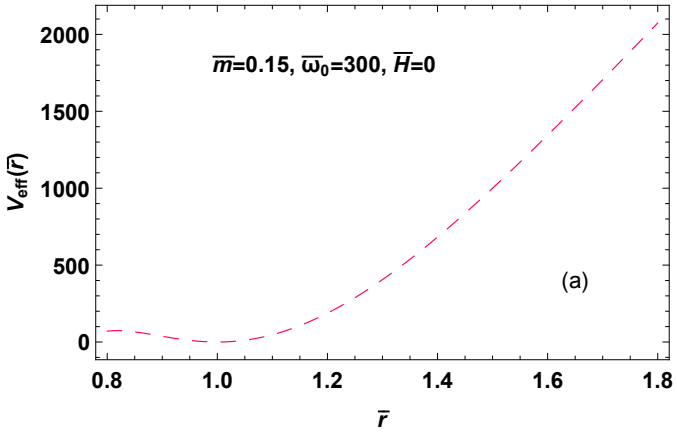


```
forcet[rr_, tit_, omt_, mt_]:=forcemm1/.{w-> − 1.2, rp → 0, ar → rr, ti → tit, om → omt, m → mt}
pott[rt_, tit_, omt_, mt_]:=NIntegrate[−forcet[rr, tit, omt, mt], {rr, 1, rt}]
omt = 300;
mbart = 0.19;
tit = 3.6;
rfin = 1.8;
plv2 = Plot[pott[rr, tit, omt, mbart], {rr, 0.8, rfin}, PlotStyle → {Hue[0.6], Dashing[0.02],
Thickness[0.002]}, Frame → True, PlotRange → All, FrameLabel → {"r̄", "V_eff(r̄)"},
LabelStyle → {Bold, 12, FontFamily → "Helvetica"},
Axes → {False, False}];
grv2 = Graphics[{Text[Style["m̄=0.19, ω̄0=300, H̄=0", Bold, 12, Black], {1.7, 210}, {2, 1}],
Text[Style["(b)", 12, Black], {1.7, −400}, {2, 1}]}];
plotvsch = Show[plv2, grv2]
Export["plotvsch.pdf", plotvsch] Clear[forcet]
forcet[rr_, tit_, omt_, mt_]:=forcemm1/.{w-> − 1.2, rp → 0, ar → rr, ti → tit, om → omt, m → mt}
pott[rt_, tit_, omt_, mt_]:=NIntegrate[−forcet[rr, tit, omt, mt], {rr, 1, rt}]
omt = 5;
mbart = 0;
tit = 3.6;
rfin = 2.5;
plv3 = Plot[pott[rr, tit, omt, mbart], {rr, 0.8, rfin}, PlotStyle → {Hue[0.6], Dashing[0.02], Thickness
[0.002], }Frame → True, PlotRange → All, FrameLabel → {"r̄", "V_eff(r̄)"}, LabelStyle → {Bold,
12, FontFamily → "Helvetica"}, Axes → {False, False}] Clear[forcet]
forcet[rr_, tit_, omt_, mt_]:=forcemm1/.{w-> − 1.2, rp → 0, ar → rr, ti → tit, om → omt, m → mt}
```

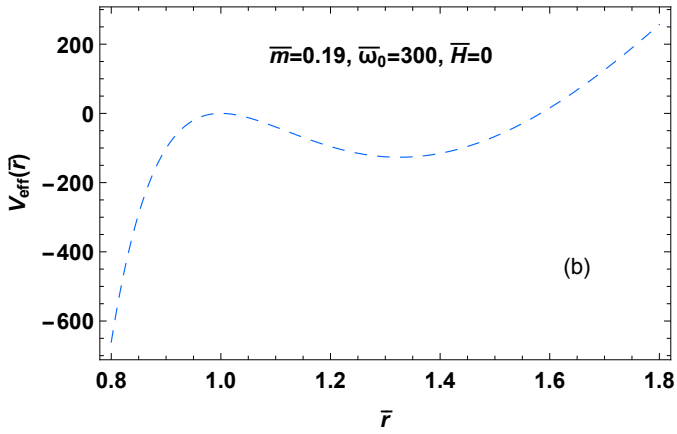


```
pott[rt_, tit_, omt_, mt_]:=NIntegrate[−forcet[rr, tit, omt, mt], {rr, 1, rt}]
omt = 5;
mbart = 0.05;
tit = 3.6;
rfin = 2.5;
plv4 = Plot[pott[rr, tit, omt, mbart], {rr, 0.8, rfin}, PlotStyle → {Hue[0.8], Dashing[0.04], Thickness
[0.002]}, Frame → True, PlotRange → All, FrameLabel → {"r̄", "V_eff(r̄)", LabelStyle → {Bold, 12,
FontFamily → "Helvetica"}, Axes → {False, False}];
grvm = Graphics[{Text[Style[" ω̄0=5, H̄=0", Bold, 13, Black], {1.9, 4.2}, {2, 1}], Text[Style["m̄=0", 12,
Blue], {1.9, 3}, {2, 0}], Text[Style["m̄=0.05", 12, Magenta], {2.3, 1.9}, {2, 0}]}];
plotvm = Show[plv3, plv4, grvm]
Export["plotvm.pdf", plotvm]
```

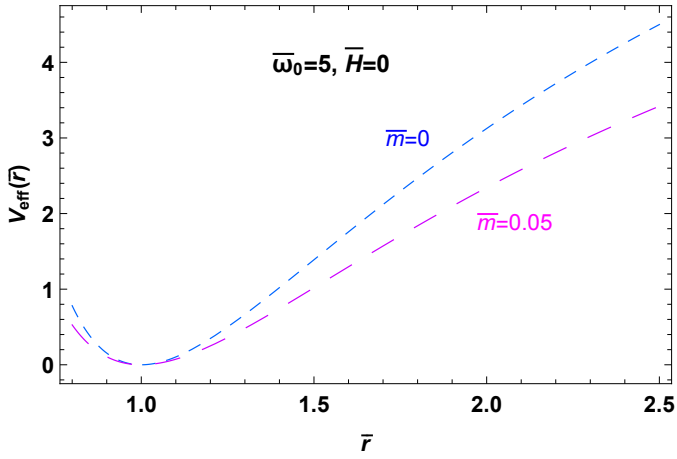

Appendix D

Numerical Code for the Quintessence Model with a Dilatonic coupling

In this appendix we present the Mathematica code, which we have used in Ref. [3] in order to describe the dilatonic coupling $B_F(\phi) = e^{-2\phi}$ in quintessence models with linear potential and its influence in the cosmological parameters and the time appearance of the Big Rip singularity. This analysis is presented analytically in Chapter 4.

```
SetDirectory["D:\\"];
Clear[aa, fi, aad, aadd, tas, hht, hha];
fii = -7; fi0 = -2.11;
ti = 0.02; t0 = 74.973359824888284; (* fii = φi, ti = initial time deep in the radiation era,
t0 = time of Big Crunch*)
aa = a[t]; fi = f[t]; (* φ function*)
aad = D[aa, t];
aadd = D[aa, {t, 2}];
fid = D[fi, t];
fidd = D[fi, {t, 2}];
ss = 0.1; (*V(φ) = -sφ, s = 0.1*)
zem = 0;
om0m = 0.3;
om0r = 0.0001;
ω[fi] = 1;
eq1 = aadd/aa == -om0m/(2aa^3) (1+Abs[zem]E^(-2fi))/(1+Abs[zem]E^(-2fi0)) - om0r/aa^4 E^(-2(fi - fi0)) - 1/3 (ω[fi]fid^2 + ssfi);
eq2 = fidd + 3 fid(aad/aa) - ss/ω[fi] + D[ω,fi]fid^2/(2ω[fi]) == -6zemom0mE^(-2fi)/(ω[fi]aa^3(1+Abs[zem]E^(-2fi0))) ;
eqb1 = f[ti]==fii;
eqb2 = f'[ti] == 0;
eqb3 = a[ti] == (4om0rE^(-2(fii - fi0)))^(1/4) ti^(1/2);
eqb4 = a'[ti] == (om0r/4 E^(-2(fii - fi0)))^(1/4) ti^(-1/2);
sol2 = NDSolve[{eq1, eq2, eqb1, eqb2, eqb3, eqb4}, {aa, fi}, {t, ti, t0}, MaxSteps → 1000000];
asol = Part[Evaluate[a[t]/.sol2], 1];
fsol = Part[Evaluate[f[t]/.sol2], 1];
as[t1_]:=asol/.t->t1;
tt = Part[FindRoot[as[t]==1, {t, 1}], 1, 2];
fis[t1_]:=fsol/.t → t1;
fis[tt];
```

```
tas[a_]:=Part[FindRoot[as[t] == a, {t, 1}], 1, 2];
hht[t1_]:=D[asol, t]/asol/.t->t1;
hha[a_]:=hht[tas[a]];
hhz[z_]:=hha[1/(z + 1)];
"=H(z=0)"hhz[0];
fi0n = fsol/.t → tt;
"=φ(z=0)"fi0n;
dfsol = D[fsol, t];
enf0 = (ω[fi]dfsol^2/2 - ssfsol) /.t → tt;
"=Ω_0Φ"enf0; "=t_0"tt;
dfsol/.t → tt;
asol/.t → tt;
om0r/asol^4 E^(-2(fsol - fi0))/.t → ti;
om0m/2asol^3 /.t → ti;
asol/.t → t0;
dasol = D[asol, t];
Ht = dasol/asol;
dHt = D[Ht, t];
dfsol = D[fsol, t];
ddfsol = D[dfsol, t];
enf = (0.5dfsol^2 - ssfsol); (* (1/2 dφ/dt - sφ) *)
ppf = (0.5dfsol^2 + ssfsol); (* (1/2 dφ/dt + sφ) *);
wt = ppf/enf;
wt/.t → t0;
wft[t1_]:=ppf/enf/.t → t1;
wfa[a_]:=wft[tas[a]];
wfz[z_]:=wfa[1/(z + 1)];
w0 = Plot[wfz[z], {z, 0, 2}, Frame → True, PlotRange → All, PlotStyle → Blue,
FrameLabel → {z, "w(z)"}];
ddz = 0.00001;
imax = 250; zmax = 2; dz = zmax/imax;
ttable = Table[{0, 0}, {i, 1, imax}];
Do[
ttable[[i]] = {idz, wfz[idz]}, {i, 1, imax}]
plnum0 = ListPlot[ttable, PlotStyle → {Thick, Orange, PointSize[0.008], Dashing[0.02]},
Frame → True, FrameLabel → {z, "w(z)"}];
hupar = 0.1;
dashpar = 0.001; thickpar = 0.007;
plf[ss1] = Plot[fsol, {t, ti, t0}, PlotStyle → {Hue[hupar], Dashing[dashpar], Thickness[thickpar]}, Frame
→ True, PlotRange → All, FrameLabel → {Style[t, FontSize → 10], Style["φ(t)", FontSize → 10]},
LabelStyle → {FontFamily → "Helvetica"}, Axes → False];
plfn[ss1] = Show[plf[ss1], Graphics[{Dashed, Line[{{tt, -11.6}, {tt, -10.7}}]}]];
pla[ss1] = Plot[Log[asol], {t, ti, t0}, PlotStyle → {Hue[hupar], Dashing[dashpar], Thickness[thickpar]},
Frame → True, FrameLabel → {Style[t, FontSize → 10], Style["ln[α(t)]", FontSize → 10]},
LabelStyle → {FontFamily → "Helvetica"}, Axes → False];
planl[ss1] = Plot[asol, {t, ti, t0}, PlotStyle → {Hue[hupar], Dashing[dashpar], Thickness[thickpar]},
Frame → True, FrameLabel → {t, "α(t)"}, LabelStyle → {FontFamily → "Helvetica"}, Axes → False];
plan[ss1] = Show[pla[ss1], Graphics[{Dashed, Line[{{tt, -1.5}, {tt, 1.5}}]}]];
plw[ss1] = Plot[wt, {t, ti, t0 - 3}, PlotStyle → {Hue[hupar], Dashing[dashpar], Thickness[thickpar]},
Frame → True, FrameLabel → {Style[t, FontSize → 10], Style["w(t)", FontSize → 10]},
```

```
LabelStyle → {FontFamily → "Helvetica"}, Axes → False];
plw1[ss1] = Plot[wt, {t, ti, 100tt}, PlotStyle → {Hue[hupar], Dashing[dashpar], Thickness[thickpar]},
Frame → True, FrameLabel → {t, "w(t)"}, LabelStyle → {FontFamily → "Helvetica"}, Axes → False];
plwn[ss1] = Show[plw[ss1], Graphics[{Dashed, Line[{{tt, -1}, {tt, -0.7}}]}]];
Clear[aa, fi, aad, aadd, tas, hht, hha];
fii = -6.95; fi0 = -2.08; ti = 0.035; t0 = 77.12;
aa = a[t]; fi = f[t];
aad = D[aa, t];
aadd = D[aa, {t, 2}];
fid = D[fi, t];
fidd = D[fi, {t, 2}];
ss = 0.1; (*V(φ) = -sφ,  s = 0.1*)
zem = 10^(-7);
om0m = 0.3;
om0r = 0.0001;
ω[fi] = 1;
eq1 = aadd/aa == (-om0m)/(2aa^3) (1+Abs[zem]E^(-2fi))/(1+Abs[zem]E^(-2fi0)) - om0r/aa^4 E^(-2(fi - fi0)) - 1/3 (ω[fi]fid^2 + ssfi);
eq2 = fidd + 3 fid(aad/aa) - ss/ω[fi] + D[ω,fi]fid^2/(2ω[fi]) == -(6zemom0mE^(-2fi))/(ω[fi]aa^3(1+Abs[zem]E^(-2fi0)));
eqb1 = f[ti]==fii;
eqb2 = f'[ti] == 0;
eqb3 = a[ti] == (4om0rE^(-2(fii - fi0)))^(1/4) ti^(1/2);
eqb4 = a'[ti] == (om0r/4 E^(-2(fii - fi0)))^(1/4) ti^(-1/2);
sol2 = NDSolve[{eq1, eq2, eqb1, eqb2, eqb3, eqb4}, {aa, fi}, {t, ti, t0}, MaxSteps → 1000000];
asol = Part[Evaluate[a[t]/.sol2], 1];
fsol = Part[Evaluate[f[t]/.sol2], 1];
as[t1_]:=asol/.t->t1;
tt = Part[FindRoot[as[t]==1, {t, 1}], 1, 2];
fis[t1_]:=fsol/.t → t1;
fis[tt];
tas[a_]:=Part[FindRoot[as[t] == a, {t, 1}], 1, 2];
hht[t1_]:=D[asol, t]/asol/.t->t1;
hha[a_]:=hht[tas[a]];
hhz[z_]:=hha[1/(z + 1)];
"=H(z=0)"hhz[0];
fi0n = fsol/.t → tt;
"=φ(z=0)"fi0n ;
dfsol = D[fsol, t];
enf0 = (ω[fi]dfsol^2/2 - ssfsol)/.t → tt;
"=Ω_0Φ"enf0;
"=t_0"tt;
dfsol/.t → tt;
asol/.t → tt;
om0r/asol^4 E^(-2(fsol - fi0))/.t → ti;
om0m/(2asol^3)/.t → ti;
asol/.t → t0;
dasol = D[asol, t];
Ht = dasol/asol;
dHt = D[Ht, t];
dfsol = D[fsol, t];
ddfsol = D[dfsol, t];
```

```
enf = (0.5dfsol^2 - ssfsol); (* (1/2 d\[Varphi]/dt - s\[Varphi]) *)
ppf = (0.5dfsol^2 + ssfsol); (* (1/2 d\[Varphi]/dt + s\[Varphi]) *);
wt = ppf/enf;
wt/.t -> ti;
wft[t1_]:=ppf/enf/.t -> t1;
wfa[a_]:=wft[tas[a]];
wfz[z_]:=wfa[1/(z + 1)];
w1 = Plot[wfz[z], {z, 0, 2}, Frame -> True, PlotStyle -> Blue, FrameLabel -> {z, "w(z)"}];
ddz = 0.00001;
wz[z_]:=((2/3)(1 + z)((Log[hhz[z + ddz]] - Log[hhz[z]])/ddz) - 1)/(1 - om0m(1 + z)^3/hhz[z]^2);
imax = 250; zmax = 2.0; dz = zmax/imax;
ttable = Table[{0, 0}, {i, 1, imax}];
Do[
ttable[[i]] = {idz, wfz[idz]}, {i, 1, imax}]
plnum1 = ListPlot[ttable, PlotStyle -> {Thick, Blue, PointSize[0.008], Dashing[0.03]}, Frame -> True,
FrameLabel -> {z, "w(z)"}];
hupar = 0.6;
dashpar = 0.001; thickpar = 0.007;
plf[ss2] = Plot[fsol, {t, ti, t0}, PlotStyle -> {Hue[hupar], Dashing[dashpar], Thickness[thickpar]},
Frame -> True, FrameLabel -> {Style[t, FontSize -> 10], Style["\[Phi](t)", FontSize -> 10]},
LabelStyle -> {FontFamily -> "Helvetica"}, Axes -> False];
plfn[ss2] = Show[plf[ss2], Graphics[{Dashed, Line[{{tt, -11.6}, {tt, -10.7}}]}]];
pla[ss2] = Plot[Log[asol], {t, ti, t0}, PlotStyle -> {Hue[hupar], Dashing[dashpar], Thickness[thickpar]},
Frame -> True, FrameLabel -> {Style[t, FontSize -> 10], Style["ln[\[Alpha](t)]", FontSize -> 10]},
LabelStyle -> {FontFamily -> "Helvetica"}, Axes -> False];
planl[ss2] = Plot[asol, {t, ti, t0}, PlotStyle -> {Hue[hupar], Dashing[dashpar], Thickness[thickpar]},
Frame -> True, FrameLabel -> {t, "\[Alpha](t)"}, LabelStyle -> {FontFamily -> "Helvetica"}, Axes -> False];
plan[ss2] = Show[pla[ss2], Graphics[{Dashed, Line[{{tt, -1.5}, {tt, 1.5}}]}]];
plw[ss2] = Plot[wt, {t, ti, t0 - 3}, PlotStyle -> {Hue[hupar], Dashing[dashpar], Thickness[thickpar]},
Frame -> True, FrameLabel -> {Style[t, FontSize -> 10], Style["w(t)", FontSize -> 10]},
LabelStyle -> {FontFamily -> "Helvetica"}, Axes -> False];
plw1[ss2] = Plot[wt, {t, ti, 100tt}, PlotStyle -> {Hue[hupar], Dashing[dashpar], Thickness[thickpar]},
Frame -> True, FrameLabel -> {t, "w(t)"}, LabelStyle -> {FontFamily -> "Helvetica"}, Axes -> False];
Clear[aa, fi, aad, aadd, tas, hht, hha];
fii = -6.77; fi0 = -1.1; ti = 0.035; t0 = 80.18;
aa = a[t]; fi = f[t];
aad = D[aa, t];
aadd = D[aa, {t, 2}];
fid = D[fi, t];
fidd = D[fi, {t, 2}];
ss = 0.1; (*V(\[Varphi]) = -s\[Varphi],  s = 0.1*)
zem = 10^(-6);
om0m = 0.3;
om0r = 0.0001;
\[Omega][fi] = 1;
eq1 = aadd/aa == (-om0m)/(2aa^3) (1+Abs[zem])/(1+Abs[zem]E^(-2fi0)) - om0r/aa^4 E^(-2(fi - fi0)) - 1/3(\[Omega][fi]fid^2 + ssfi);
eq2 = fidd + 3 fid(aad/aa) - ss/\[Omega][fi] + D[\[Omega],fi]fid^2/(2\[Omega][fi]) == -(6zemom0mE^(-2fi))/(\[Omega][fi]aa^3(1+Abs[zem])E^(-2fi0)) ;
eqb1 = f[ti]==fii;
eqb2 = f'[ti] == 0;
eqb3 = a[ti] == (4om0rE^(-2(fii - fi0)))^(1/4) ti^(1/2);
```

```
eqb4 = a'[ti] == (om0r/4 E^(-2(fii - fi0)))^(1/4) ti^(-1/2);
sol2 = NDSolve[{eq1, eq2, eqb1, eqb2, eqb3, eqb4}, {aa, fi}, {t, ti, t0}, MaxSteps -> 1000000];
asol = Part[Evaluate[a[t]/.sol2], 1];
fsol = Part[Evaluate[f[t]/.sol2], 1];
as[t1_]:=asol/.t->t1;
tt = Part[FindRoot[as[t]==1, {t, 1}], 1, 2];
fis[t1_]:=fsol/.t -> t1;
fis[tt];
tas[a_]:=Part[FindRoot[as[t] == a, {t, 1}], 1, 2];
hht[t1_]:=D[asol, t]/asol/.t->t1;
hha[a_]:=hht[tas[a]];
hhz[z_]:=hha[1/(z + 1)];
"=H(z=0)"hhz[0];
fi0n = fsol/.t -> tt;
"=φ(z=0)"fi0n;
dfsol = D[fsol, t];
enf0 = (ω[fi]dfsol^2/2 - ssfsol)/.t -> tt;
"=Ω_0Φ"enf0;
"=t_0"tt ;
dfsol/.t -> tt;
asol/.t -> tt;
om0r/asol^4 E^(-2(fsol - fi0))/.t -> ti;
om0m/(2asol^3)/.t -> ti;
asol/.t -> t0;
dasol = D[asol, t];
Ht = dasol/asol;
dHt = D[Ht, t];
dfsol = D[fsol, t];
ddfsol = D[dfsol, t];
enf = (0.5dfsol^2 - ssfsol); (* (1/2 dφ/dt - sφ) *)
ppf = (0.5dfsol^2 + ssfsol); (* (1/2 dφ/dt + sφ) *);
wt = ppf/enf;
wt/.t -> ti;
wft[t1_]:=ppf/enf/.t -> t1;
wfa[a_]:=wft[tas[a]];
wfz[z_]:=wfa[1/(z + 1)]
w2 = Plot[wfz[z], {z, 0, 2}, Frame -> True, PlotStyle -> Blue, FrameLabel -> {z, "w(z)"}];
ddz = 0.00001; imax = 250; zmax = 2; dz = zmax/imax;
ttable = Table[{0, 0}, {i, 1, imax}];
Do[
ttable[[i]] = {idz, wfz[idz]}, {i, 1, imax}]
plnum2 = ListPlot[ttable, PlotStyle -> {Thick, Gray, PointSize[0.008]}, Frame -> True,
FrameLabel -> {z, "w(z)"}]; hupar = 0.2;
dashpar = 0.001; thickpar = 0.007;
plf[ss3] = Plot[fsol, {t, ti, t0}, PlotStyle -> {Green, Dashing[dashpar], Thickness[thickpar]},
Frame -> True, FrameLabel -> {Style[t, FontSize -> 10], Style["φ(t)", FontSize -> 10]},
LabelStyle -> {FontFamily -> "Helvetica"}, Axes -> False];
plfn[ss3] = Show[plf[ss3], Graphics[{Dashed, Line[{{tt, -11.6}, {tt, -10.7}}]}]];
pla[ss3] = Plot[Log[asol], {t, ti, t0}, PlotStyle -> {Green, Dashing[dashpar], Thickness[thickpar]},
Frame -> True, FrameLabel -> {Style[t, FontSize -> 10], Style["ln[α(t)]", FontSize -> 10]},
```

```
LabelStyle → {FontFamily → "Helvetica"}, Axes → False];
planl[ss3] = Plot[asol, {t, ti, t0}, PlotStyle → {Green, Dashing[dashpar], Thickness[thickpar]}
, Frame → True, FrameLabel → {t, "α(t)"}, LabelStyle → {FontFamily → "Helvetica"}, Axes → False];
plan[ss3] = Show[pla[ss3], Graphics[{Dashed, Line[{{tt, -1.5}, {tt, 1.5}}]}]];
plw[ss3] = Plot[wt, {t, ti, t0 - 3}, PlotStyle → {Green, Dashing[dashpar], Thickness[thickpar]},
Frame → True, FrameLabel → {Style[t, FontSize → 10], Style["w(t)", FontSize → 10]},
LabelStyle → {FontFamily → "Helvetica"}, Axes → False];
plw1[ss3] = Plot[wt, {t, ti, 250tt}, PlotStyle → {Green, Dashing[dashpar], Thickness[thickpar]},
Frame → True, FrameLabel → {t, "w(t)"}, LabelStyle → {FontFamily → "Helvetica"}, Axes → False];
plwn[ss3] = Show[plw[ss3], Graphics[{Dashed, Line[{{tt, -1}, {tt, -0.7}}]}]];
Clear[aa, fi, aad, aadd, tas, hht, hha];
fii = -6.98; fi0 = -2.16; ti = 0.035; t0 = 75.77;
aa = a[t]; fi = f[t]; (* φ function*)
aad = D[aa, t];
aadd = D[aa, {t, 2}];
fid = D[fi, t];
fidd = D[fi, {t, 2}];
ss = 0.1; (*V(φ) = -sφ, s = 0.1*)
zem = 10^(-8);
om0m = 0.3; om0r = 0.0001; ω[fi] = 1;
eq1 = aadd/aa == (-om0m)/(2aa^3) (1+Abs[zem]E^(-2fi))/(1+Abs[zem]E^(-2fi0)) - om0r/aa^4 E^(-2(fi - fi0)) - 1/3 (ω[fi]fid^2 + ssfi);
eq2 = fidd + 3 fid(aad/aa) - ss/ω[fi] + D[ω,fi]fid^2/(2ω[fi]) == -(6zemom0mE^(-2fi))/(ω[fi]aa^3(1+Abs[zem]E^(-2fi0))) ;
eqb1 = f[ti]==fii;
eqb2 = f'[ti] == 0;
eqb3 = a[ti] == (4om0rE^(-2(fii - fi0)))^(1/4) ti^(1/2);
eqb4 = a'[ti] == (om0r/4 E^(-2(fii - fi0)))^(1/4) ti^(-1/2);
sol2 = NDSolve[{eq1, eq2, eqb1, eqb2, eqb3, eqb4}, {aa, fi}, {t, ti, t0}, MaxSteps → 1000000];
asol = Part[Evaluate[a[t]/.sol2], 1];
fsol = Part[Evaluate[f[t]/.sol2], 1];
as[t1_]:=asol/.t->t1;
tt = Part[FindRoot[as[t]==1, {t, 1}], 1, 2];
fis[t1_]:=fsol/.t → t1; fis[tt];
tas[a_]:=Part[FindRoot[as[t] == a, {t, 1}], 1, 2];
hht[t1_]:=D[asol, t]/asol/.t->t1;
hha[a_]:=hht[tas[a]];
hhz[z_]:=hha[1/(z + 1)]; "=H(z=0)"hhz[0];
fi0n = fsol/.t → tt; "=φ(z=0)"fi0n;
dfsol = D[fsol, t];
enf0 = (ω[fi]dfsol^2/2 - ssfsol)/.t → tt;
"=Ω_0Φ"enf0; "=t_0"tt;
dfsol/.t → tt;
asol/.t → tt;
om0r/asol^4 E^(-2(fsol - fi0))/.t → ti;
om0m/(2asol^3)/.t → ti;
dasol = D[asol, t];
Ht = dasol/asol;
dHt = D[Ht, t];
dfsol = D[fsol, t];
ddfsol = D[dfsol, t];
enf = (0.5dfsol^2 - ssfsol); (* (1/2 dφ/dt - sφ)  *)
```

```
ppf = (0.5dfsol^2 + ssfsol); (* (1/2 dφ/dt + sφ)  *);
wt = ppf/enf; wt/.t → ti; wft[t1_]:=ppf/enf/.t → t1;
wfa[a_]:=wft[tas[a]]; wfz[z_]:=wfa[1/(z + 1)]
w3 = Plot[wfz[z], {z, 0, 2}, Frame → True, PlotRange → All, PlotStyle → Blue,
FrameLabel → {z, "w(z)"}]; ddz = 0.00001; imax = 250; zmax = 2; dz = zmax/imax;
ttable = Table[{0, 0}, {i, 1, imax}];
Do[
ttable[[i]] = {idz, wfz[idz]}, {i, 1, imax}]
plnum3 = ListPlot[ttable, PlotStyle → {Thick, Magenta, PointSize[0.008]}, FrameLabel → {z, "w(z)"}];
hupar = 0.8;  dashpar = 0.001; thickpar = 0.007;
plf[ss4] = Plot[fsol, {t, ti, t0}, PlotStyle → {Hue[hupar], Dashing[dashpar], Thickness[thickpar]},
Frame → True, FrameLabel → {Style[t, FontSize → 10], Style["ϕ(t)", FontSize → 10]},
LabelStyle → {FontFamily → "Helvetica"}, Axes → False];
plfn[ss4] = Show[plf[ss4], Graphics[{Dashed, Line[{{tt, -11.6}, {tt, -10.7}}]}]];
pla[ss4] = Plot[Log[asol], {t, ti, t0}, PlotStyle → {Hue[hupar], Dashing[dashpar], Thickness[thickpar]},
Frame → True, FrameLabel → {Style[t, FontSize → 10], Style["ln[α(t)]", FontSize → 10]},
LabelStyle → {FontFamily → "Helvetica"}, Axes → False];
planl[ss4] = Plot[asol, {t, ti, t0}, PlotStyle → {Hue[hupar], Dashing[dashpar], Thickness[thickpar]},
Frame → True, FrameLabel → {t, "α(t)"}, LabelStyle → {FontFamily → "Helvetica"}, Axes → False];
plan[ss4] = Show[pla[ss4], Graphics[{Dashed, Line[{{tt, -1.5}, {tt, 1.5}}]}]];
plw[ss4] = Plot[wt, {t, ti, t0 - 3}, PlotStyle → {Hue[hupar], Dashing[dashpar], Thickness[thickpar]},
Frame → True, FrameLabel → {Style[t, FontSize → 10], Style["w(t)", FontSize → 10]},
LabelStyle → {FontFamily → "Helvetica"}, Axes → False];
plw1[ss4] = Plot[wt, {t, ti, 100tt}, PlotStyle → {Hue[hupar], Dashing[dashpar], Thickness[thickpar]},
Frame → True, FrameLabel → {t, "w(t)"}, LabelStyle → {FontFamily → "Helvetica"}, Axes → False];
plwn[ss4] = Show[plw[ss4], Graphics[{Dashed, Line[{{tt, -1}, {tt, -0.7}}]}]];
g0 = Graphics[{Orange, Line[{{15, 2}, {22, 2}}]}];
g1 = Graphics[{Magenta, Line[{{15, 0}, {22, 0}}]}];
g2 = Graphics[{Blue, Line[{{15, -2}, {22, -2}}]}];
g3 = Graphics[{Green, Line[{{15, -4}, {22, -4}}]}];
p3 = Show[plf[ss1], plf[ss2], plf[ss3], g0, g1, g2, g3, plf[ss4], PlotRange → {-7, 5},
Epilog → {Text["ζm=0", {10, 2}], Text["ζm = 10^-8", {10, 0}], Text["ζm = 10^-7", {10, -2}],
Text["ζm = 10^-6", {10, -4}], Text["V(φ)=-0.1φ", {40, 4.5}]}];
Export["p3.pdf", p3]
```

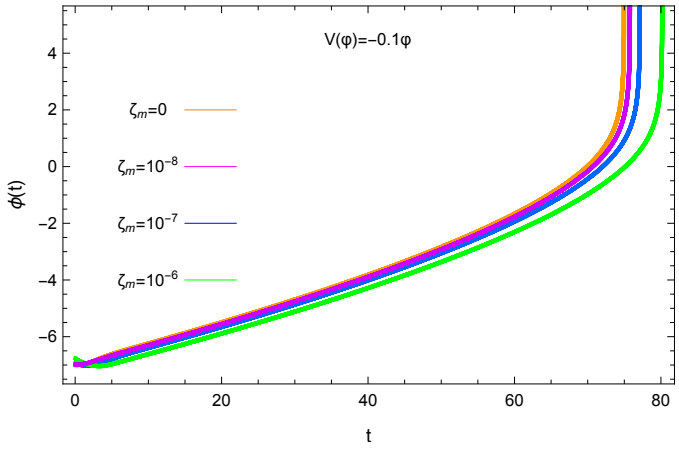

```
ga0 = Graphics[{Orange, Line[{{70, 10}, {78, 10}}]}];
ga1 = Graphics[{Magenta, Line[{{70, 7}, {78, 7}}]}];
ga2 = Graphics[{Blue, Line[{{70, 4}, {78, 4}}]}];
ga3 = Graphics[{Green, Line[{{70, 1}, {78, 1}}]}];
p4 = Show[pla[ss1], pla[ss2], pla[ss4], pla[ss3], ga0, ga1, ga2, ga3, PlotRange → {−1, 26},
Epilog → {Text["ζm=0", {65, 10}], Text["ζm = 10^−8", {65, 7}], Text["ζm = 10^−7", {65, 4}],
Text["ζm = 10^−6", {65, 1}], Text[“V(φ)=-0.1φ”, {40, 25}]}];
Export[“p4.pdf”, p4]
```

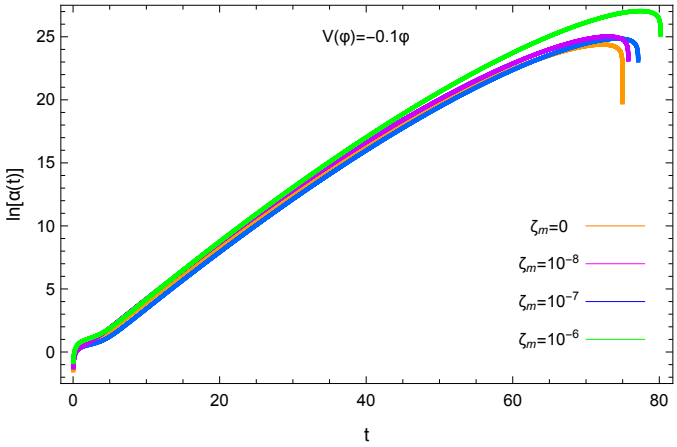


```
gb0 = Graphics[{Orange, Line[{{40, −0.991}, {44, −0.991}}]}];
gb1 = Graphics[{Magenta, Line[{{40, −0.994}, {44, −0.994}}]}];
gb2 = Graphics[{Blue, Line[{{40, −0.997}, {44, −0.997}}]}];
p5 = Show[plw1[ss1], plw1[ss2], plw1[ss4], gb0, gb1, gb2,
Epilog → {Text["ζm=0", {37, −0.991}], Text["ζm = 10^−8", {37, −0.994}],
Text["ζm = 10^−7", {37, −0.997}], Text[“V(φ)=-0.1φ”, {21, −0.978}]}];
Export[“p5.pdf”, p5]
```

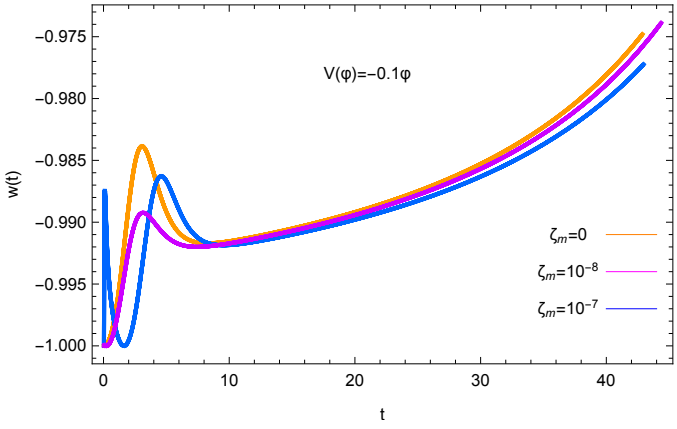

```
p1 = Show[plnum0, plnum3, Epilog → {Text["ζm=0", {0.4, −0.9998}],
Text["ζm = 10^−8", {1.1, −0.9999}], Text[“V(φ)=-0.1φ”, {1, −0.99973}]}];
Export[“p1.pdf”, p1]
```

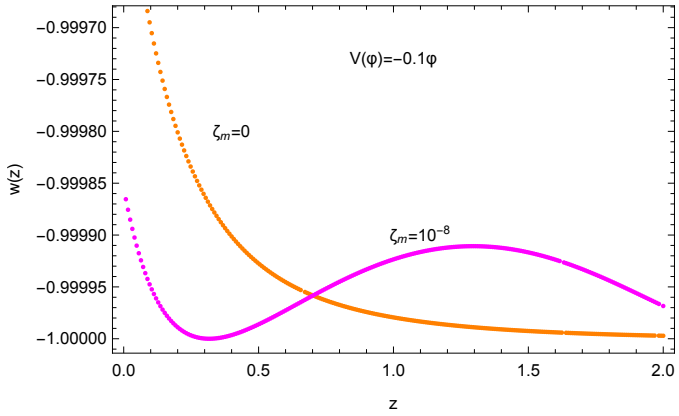


```
gc0 = Graphics[{Orange, Line[{{0.5, −0.994}, {0.7, −0.994}}]}];
gc1 = Graphics[{Magenta, Line[{{0.5, −0.996}, {0.7, −0.996}}]}];
gc2 = Graphics[{Blue, Line[{{0.5, −0.998}, {0.7, −0.998}}]}];
p2 = Show[plnum0, plnum1, plnum3, gc0, gc1, gc2, PlotRange → {−1, −0.9877},
Epilog → {Text["ζm=0", {0.35, −0.994}], Text["ζm = 10^−8", {0.35, −0.996}],
Text["ζm = 10^−7", {0.35, −0.998}], Text[“V(φ)=-0.1φ”, {1.7, −0.989}]}];
Export[“p2.pdf”,p2]
```

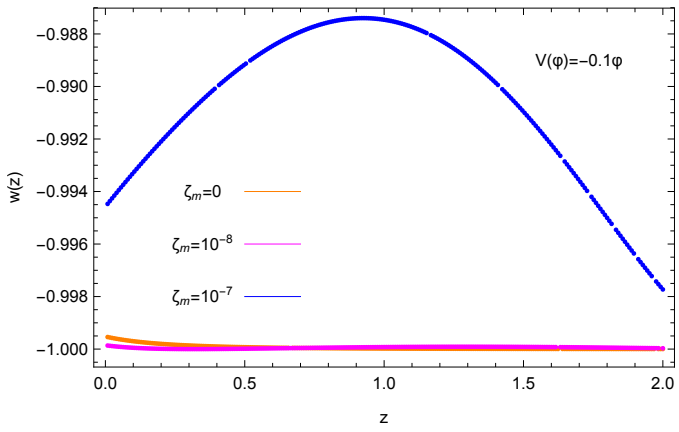

Appendix E

Numerical code for the calculation of the basic physical quantities in each spacetime

E.1 Physical quantities in a cosmological spacetime

When someone deals with a spacetime in Cosmology, it is necessary to calculate some quantities about the geometry of the spacetime, such as the Christoffel symbols, the Riemann tensor, geodesics and the field equations of GR, such as the components of the Einstein tensor. During my doctoral studies I have develop this code, which is useful and works in every spacetime.

```
Clear[coord, metric, inversemetric, affine, t, ρ, θ, φ]
n = 4;
coord = {t, ρ, θ, φ}; (*Defining a list of coordinates*)
metric = {{−(1 − 2M/(a[t]ρ)), 0, 0, 0}, {0, a[t]^2, 0, 0}, {0, 0, (a[t]^2ρ^2), 0},
{0, 0, 0, (a[t]^2ρ^2(sin[θ])^2)}}
(*Input the metric as a list of lists, i.e., as a matrix*)
metric//MatrixForm; inversemetric = Simplify[Inverse[metric]];
inversemetric//MatrixForm; (*The inverse metric is obtained through matrix inversion*)
(*Calculating the Christoffel symbols*)
affine:=
affine =
Simplify[
Table[(1/2) * Sum[(inversemetric[[i, s]]) * (D[metric[[s, j]], coord[[k]]] + D[metric[[s, k]], coord[[j]]]
−D[metric[[j, k]], coord[[s]]]), {s, 1, n}], {i, 1, n}, {j, 1, n}, {k, 1, n}]],
listaffine:=Table[If[UnsameQ[affine[[i, j, k]], 0], {ToString[Γ[i, j, k]], affine[[i, j, k]]}], {i, 1, n}, {j, 1, n},
{k, 1, j}], TableForm[Partition[DeleteCases[Flatten[listaffine], Null], 2], TableSpacing → {2, 2}];
(*Calculating the geodesic equations. The geodesic equations are calculated by asking Mathematica
to carry out the sum Γ^α_βγ u^β u^γ where u^α are the components of the four velocity. This gives the
derivative of u^α with respect to proper time t. This is replaced by s if the geodesics are spacelike.*)
geodesic:=geodesic = Simplify[Table[−Sum[affine[[i, j, k]]u[j]u[k], {j, 1, n}, {k, 1, n}], {i, 1, n}]]
listgeodesic:=Table[{"d/dt"ToString[u[i]], "=", geodesic[[i]]}, {i, 1, n}];
TableForm[listgeodesic, TableSpacing->{2}]; (*Calculating and displaying the Riemann tensor*)
riemann:=riemann = Simplify[Table[
D[affine[[i, j, l]], coord[[k]]] − D[affine[[i, j, k]], coord[[l]]]+
```

```
Sum[affine[[s, j, l]]affine[[i, k, s]] - affine[[s, j, k]]affine[[i, l, s]],
{s, 1, n}], {i, 1, n}, {j, 1, n}, {k, 1, n}, {l, 1, n}]]
(*Calculating and displaying the Riemann tensor*)
listriemann:=Table[If[UnsameQ[riemann[[i, j, k, l]], 0], {ToString[R[i, j, k, l]], riemann[[i, j, k, l]]}],
{i, 1, n}, {j, 1, n}, {k, 1, n}, {l, 1, k - 1}]
TableForm[Partition[DeleteCases[Flatten[listriemann], Null], 2], TableSpacing → {2, 2}]//FullSimplify;
(*Calculating and displaying the Ricci tensor*)
ricci:=ricci = Simplify[Table[Sum[riemann[[i, j, i, l]], {i, 1, n}], {j, 1, n}, {l, 1, n}]]
listricci:=Table[If[UnsameQ[ricci[[j, l]], 0], {ToString[R[j, l]], ricci[[j, l]]}], {j, 1, n}, {l, 1, j}]
TableForm[Partition[DeleteCases[Flatten[listricci], Null], 2], TableSpacing → {2, 2}];
(*Calculating the scalar curvature*)
scalar = Simplify[Sum[inversemetric[[i, j]]ricci[[i, j]], {i, 1, n}, {j, 1, n}]];
(*Calculating the Einstein tensor   G_μν = R_μν - 1/2 g_μν R   *)
einstein:=einstein = Simplify[ricci - (1/2)scalar * metric]
listeinstein:=Table[If[UnsameQ[einstein[[j, l]], 0], {ToString[G[j, l]], einstein[[j, l]]}], {j, 1, n}, {l, 1, j}]
TableForm[Partition[DeleteCases[Flatten[listeinstein], Null], 2], TableSpacing->{2, 2}];
(*A vanishing table means that the vacuum Einstein equation is satisfied!*)
```

Appendix F

Spinning particle in an expanding Universe

F.1 Christoffel symbols

In order to derive the system of equations (8.26) and (8.27), we need the Christoffel symbols of the metric (8.11). Assuming that $(R_s)^n = 0$ for $n > 1$, the non-vanishing components are

$$\begin{aligned}
\Gamma^0_{00} &= \frac{\dot{a}}{2a^2\rho}R_s + O(R_s^2) \\
\Gamma^1_{01} &= \frac{1}{2a\rho}R_s + O(R_s^2) \\
\Gamma^0_{11} &= a\dot{a} + \frac{3}{2\rho}\dot{a}R_s + O(R_s^2) \\
\Gamma^0_{22} &= \rho^2 a\dot{a} + \frac{3}{2}\rho\dot{a}R_s + O(R_s^2) \\
\Gamma^0_{33} &= a\dot{a}\rho^2\sin^2\theta + \frac{3}{2}\dot{a}\rho\sin^2\theta R_s + O(R_s^2) \\
\Gamma^1_{00} &= \frac{1}{2a^3\rho^2}R_s + O(R_s^2) \\
\Gamma^1_{01} &= \frac{\dot{a}}{a} - \frac{\dot{a}}{2a^2\rho}R_s + O(R_s^2) \\
\Gamma^1_{11} &= -\frac{1}{2\rho^2 a}R_s + O(R_s^2) \\
\Gamma^1_{22} &= -\rho + \frac{1}{2a}R_s + O(R_s^2) \\
\Gamma^1_{33} &= -\rho\sin^2\theta + \frac{\sin^2\theta}{2a}R_s + O(R_s^2) \\
\Gamma^2_{02} &= \frac{\dot{a}}{a} - \frac{\dot{a}}{2a^2\rho}R_s + O(R_s^2) \\
\Gamma^2_{12} &= \frac{1}{\rho} - \frac{1}{2a\rho^2}R_s + O(R_s^2) \\
\Gamma^2_{33} &= -\sin\theta\cos\theta \\
\Gamma^3_{03} &= \Gamma^2_{02} \\
\Gamma^3_{13} &= \Gamma^2_{12} \\
\Gamma^3_{23} &= \cot\theta
\end{aligned} \tag{F.1}$$

where $\dot{a} = \frac{da}{dt}$ and $R_s = \frac{2GM}{c^2}$ in normal units.

F.2 Riemann tensor

Similarly, we assume that $(R_s)^n = 0$ for $n > 1$ the non zero components of the Riemann tensor, which are necessary for the derivation of the equations of motion (8.26) and (8.27), are

$$\begin{aligned}
R^1_{001} &= \frac{\ddot{a}}{a} + \frac{1}{a^3\rho^3}(1 - \frac{1}{2}a\rho^2\ddot{a} - \frac{1}{2}\rho^2\dot{a}^2)R_s + O(R_s^2) \\
R^1_{313} &= \rho^2 \sin^2\theta\dot{a}^2 - \frac{\sin^2\theta}{2a\rho}(1 - 2\rho^2\dot{a}^2)R_s + O(R_s^2) \\
R^3_{003} &= \frac{\ddot{a}}{a} - \frac{1}{2a^3\rho^3}(1 + a\rho\ddot{a} + \rho^2\dot{a}^2)R_s + O(R_s^2) \\
R^3_{113} &= -\dot{a}^2 + \frac{1}{2a\rho^3}(1 - 2\rho^2\dot{a}^2)R_s + O(R_s^2)
\end{aligned} \tag{F.2}$$

Bibliography

[1] I. Antoniou and L. Perivolaropoulos, *Searching for a Cosmological Preferred Axis: Union2 Data Analysis and Comparison with Other Probes*, *JCAP* **1012** (2010) 012, [arXiv:1007.4347].

[2] N. Platis, I. Antoniou, and L. Perivolaropoulos, *Dilatonic Topological Defects in 3+1 Dimensions and their Embeddings*, *Phys. Rev.* **D89** (2014), no. 12 123510, [arXiv:1406.0639].

[3] I. Antoniou, *Constraints on scalar coupling to electromagnetism*, *Grav. Cosmol.* **23** (2017) 171, [arXiv:1508.00985].

[4] I. Antoniou and L. Perivolaropoulos, *Geodesics of McVittie Spacetime with a Phantom Cosmological Background*, *Phys. Rev.* **D93** (2016), no. 12 123520, [arXiv:1603.02569].

[5] I. Antoniou, D. Papadopoulos, and L. Perivolaropoulos, *Propagation of gravitational waves in an expanding background in the presence of a point mass*, *Phys. Rev.* **D94** (2016), no. 8 084018, [arXiv:1607.08103].

[6] I. Antoniou and L. Perivolaropoulos, *Constraints on spatially oscillating sub-mm forces from the Stanford Optically Levitated Microsphere Experiment data*, *Phys. Rev.* **D96** (2017), no. 10 104002, [arXiv:1708.02117].

[7] I. Antoniou, D. Papadopoulos, and L. Perivolaropoulos, *Spinning particle orbits around a black hole in an expanding background*, *Class. Quant. Grav.* **36** (2019), no. 8 085002, [arXiv:1903.03835].

[8] S. Dodelson, *Modern Cosmology*. Academic Press, Elsevier Science, 2003.

[9] E. Siegel, *Beyond the Galaxy: How Humanity Looked Beyond Our Milky Way and Discovered the Entire Universe*. World Scientific, 2015.

[10] M. Hobson, G. Efstathiou, and A. Lasenby, *General Relativity: An Introduction for Physicists*. Cambridge University Press, 2006.

[11] J. Khoury and A. Weltman, *Chameleon cosmology*, *Phys. Rev.* **D69** (2004) 044026, [astro-ph/0309411].

[12] **Planck** Collaboration, P. A. R. Ade et al., *Planck 2015 results. XIII. Cosmological parameters*, *Astron. Astrophys.* **594** (2016) A13, [arXiv:1502.01589].

[13] P. Astier and R. Pain, *Observational Evidence of the Accelerated Expansion of the Universe*, *Comptes Rendus Physique* **13** (2012) 521–538, [arXiv:1204.5493].

[14] D. W. Hogg, *Distance measures in cosmology*, astro-ph/9905116.

[15] L. Perivolaropoulos, *Cosmological Horizons, Uncertainty Principle and Maximum Length Quantum Mechanics*, *Phys. Rev.* **D95** (2017), no. 10 103523, [arXiv:1704.05681].

[16] **Supernova Search Team** Collaboration, A. G. Riess et al., *Observational evidence from supernovae for an accelerating universe and a cosmological constant*, *Astron. J.* **116** (1998) 1009–1038, [astro-ph/9805201].

[17] **Supernova Search Team** Collaboration, B. P. Schmidt et al., *The High Z supernova search: Measuring cosmic deceleration and global curvature of the universe using type Ia supernovae*, *Astrophys. J.* **507** (1998) 46–63, [astro-ph/9805200].

[18] D. H. Weinberg, M. J. Mortonson, D. J. Eisenstein, C. Hirata, A. G. Riess, and E. Rozo, *Observational Probes of Cosmic Acceleration*, *Phys. Rept.* **530** (2013) 87–255, [arXiv:1201.2434].

[19] D. Scott, *The Standard Model of Cosmology: A Skeptic's Guide*, 2018. arXiv:1804.01318.

[20] L. Perivolaropoulos, *Accelerating universe: observational status and theoretical implications*, *AIP Conf. Proc.* **848** (2006) 698–712, [astro-ph/0601014]. [,698(2006)].

[21] S. M. Carroll, *The Cosmological constant*, *Living Rev. Rel.* **4** (2001) 1, [astro-ph/0004075].

[22] T. Padmanabhan, *Cosmological constant: The Weight of the vacuum*, *Phys. Rept.* **380** (2003) 235–320, [hep-th/0212290].

[23] P. J. E. Peebles and B. Ratra, *The Cosmological constant and dark energy*, *Rev. Mod. Phys.* **75** (2003) 559–606, [astro-ph/0207347]. [,592(2002)].

[24] E. J. Copeland, M. Sami, and S. Tsujikawa, *Dynamics of dark energy*, *Int. J. Mod. Phys.* **D15** (2006) 1753–1936, [hep-th/0603057].

[25] J. Frieman, M. Turner, and D. Huterer, *Dark Energy and the Accelerating Universe*, *Ann. Rev. Astron. Astrophys.* **46** (2008) 385–432, [arXiv:0803.0982].

[26] **WMAP** Collaboration, E. Komatsu et al., *Seven-Year Wilkinson Microwave Anisotropy Probe (WMAP) Observations: Cosmological Interpretation*, *Astrophys. J. Suppl.* **192** (2011) 18, [arXiv:1001.4538].

[27] M. Tegmark, A. de Oliveira-Costa, and A. Hamilton, *A high resolution foreground cleaned CMB map from WMAP*, *Phys. Rev.* **D68** (2003) 123523, [astro-ph/0302496].

[28] C. J. Copi, D. Huterer, D. J. Schwarz, and G. D. Starkman, *Large angle anomalies in the CMB*, *Adv. Astron.* **2010** (2010) 847541, [arXiv:1004.5602].

[29] C. L. Bennett et al., *Seven-Year Wilkinson Microwave Anisotropy Probe (WMAP) Observations: Are There Cosmic Microwave Background Anomalies?*, *Astrophys. J. Suppl.* **192** (2011) 17, [arXiv:1001.4758].

[30] D. J. Schwarz, G. D. Starkman, D. Huterer, and C. J. Copi, *Is the low-l microwave background cosmic?*, *Phys. Rev. Lett.* **93** (2004) 221301, [astro-ph/0403353].

[31] K. Land and J. Magueijo, *The Axis of evil*, *Phys. Rev. Lett.* **95** (2005) 071301, [astro-ph/0502237].

[32] A. Gruppuso and K. M. Gorski, *Large scale directional anomalies in the WMAP 5yr ILC map*, *JCAP* **1003** (2010) 019, [arXiv:1002.3928].

[33] D. Sarkar, D. Huterer, C. J. Copi, G. D. Starkman, and D. J. Schwarz, *Missing Power vs low-l Alignments in the Cosmic Microwave Background: No Correlation in the Standard Cosmological Model*, *Astropart. Phys.* **34** (2011) 591–594, [arXiv:1004.3784].

[34] D. Hanson and A. Lewis, *Estimators for CMB Statistical Anisotropy*, *Phys. Rev.* **D80** (2009) 063004, [arXiv:0908.0963].

[35] K. M. Smith, L. Senatore, and M. Zaldarriaga, *Optimal limits on f_{NL}^{local} from WMAP 5-year data*, *JCAP* **0909** (2009) 006, [arXiv:0901.2572].

[36] R. Amanullah et al., *Spectra and Light Curves of Six Type Ia Supernovae at 0.511 < z < 1.12 and the Union2 Compilation*, *Astrophys. J.* **716** (2010) 712–738, [arXiv:1004.1711].

[37] J. C. B. Sanchez, S. Nesseris, and L. Perivolaropoulos, *Comparison of Recent SnIa datasets*, *JCAP* **0911** (2009) 029, [arXiv:0908.2636].

[38] S. Nesseris and L. Perivolaropoulos, *Testing Lambda CDM with the Growth Function delta(a): Current Constraints*, *Phys. Rev.* **D77** (2008) 023504, [arXiv:0710.1092].

[39] S. Trujillo-Gomez, A. Klypin, J. Primack, and A. J. Romanowsky, *Galaxies in LCDM with Halo Abundance Matching: luminosity-velocity relation, baryonic mass-velocity relation, velocity function and clustering*, *Astrophys. J.* **742** (2011) 16, [arXiv:1005.1289].

[40] B. A. Reid et al., *Cosmological Constraints from the Clustering of the Sloan Digital Sky Survey DR7 Luminous Red Galaxies*, *Mon. Not. Roy. Astron. Soc.* **404** (2010) 60–85, [arXiv:0907.1659].

[41] L. Perivolaropoulos, *Six Puzzles for LCDM Cosmology*, arXiv:0811.4684.

[42] R. Watkins, H. A. Feldman, and M. J. Hudson, *Consistently Large Cosmic Flows on Scales of 100 Mpc/h: a Challenge for the Standard LCDM Cosmology*, *Mon. Not. Roy. Astron. Soc.* **392** (2009) 743–756, [arXiv:0809.4041].

[43] G. Lavaux, R. B. Tully, R. Mohayaee, and S. Colombi, *Cosmic flow from 2MASS redshift survey: The origin of CMB dipole and implications for LCDM cosmology*, *Astrophys. J.* **709** (2010) 483–498, [arXiv:0810.3658].

[44] A. Kashlinsky, F. Atrio-Barandela, D. Kocevski, and H. Ebeling, *A measurement of large-scale peculiar velocities of clusters of galaxies: results and cosmological implications*, *Astrophys. J.* **686** (2009) L49–L52, [arXiv:0809.3734].

[45] C. G. Tsagas, *Large-scale peculiar motions and cosmic acceleration*, *Mon. Not. Roy. Astron. Soc.* **405** (2010) 503, [arXiv:0902.3232].

[46] P. Bielewicz, K. M. Gorski, and A. J. Banday, *Low order multipole maps of CMB anisotropy derived from WMAP*, *Mon. Not. Roy. Astron. Soc.* **355** (2004) 1283, [astro-ph/0405007].

[47] M. Frommert and T. A. Enßlin, *The axis of evil - a polarization perspective*, *PoS* **Cosmology2009** (2009) 015, [arXiv:0908.0453]. [Mon. Not. Roy. Astron. Soc.403,1739(2010)].

[48] C. H. Lineweaver, L. Tenorio, G. F. Smoot, P. Keegstra, A. J. Banday, and P. Lubin, *The dipole observed in the COBE DMR four-year data*, *Astrophys. J.* **470** (1996) 38–42, [astro-ph/9601151].

[49] E. D. Kovetz, A. Ben-David, and N. Itzhaki, *Giant Rings in the CMB Sky*, *Astrophys. J.* **724** (2010) 374–378, [arXiv:1005.3923].

[50] D. Hutsemekers, R. Cabanac, H. Lamy, and D. Sluse, *Mapping extreme-scale alignments of quasar polarization vectors*, *Astron. Astrophys.* **441** (2005) 915–930, [astro-ph/0507274].

[51] T. J. Broadhurst, M. Takada, K. Umetsu, X. Kong, N. Arimoto, M. Chiba, and T. Futamase, *The Surprisingly steep mass profile of Abell 1689, from a lensing analysis of Subaru images*, *Astrophys. J.* **619** (2005) L143, [astro-ph/0412192].

[52] K. Umetsu and T. Broadhurst, *Combining Lens Distortion and Depletion to Map the Mass Distribution of A1689*, *Astrophys. J.* **684** (2008) 177–203, [arXiv:0712.3441].

[53] C. Copi, D. Huterer, D. Schwarz, and G. Starkman, *The Uncorrelated Universe: Statistical Anisotropy and the Vanishing Angular Correlation Function in WMAP Years 1-3*, *Phys. Rev.* **D75** (2007) 023507, [astro-ph/0605135].

[54] A. A. Klypin, A. V. Kravtsov, O. Valenzuela, and F. Prada, *Where are the missing Galactic satellites?*, *Astrophys. J.* **522** (1999) 82–92, [astro-ph/9901240].

[55] B. Moore, *The dark matter crisis*, *AIP Conf. Proc.* **586** (2001) 73, [astro-ph/0103100].

[56] P. Madau, J. Diemand, and M. Kuhlen, *Dark matter subhalos and the dwarf satellites of the Milky Way*, *Astrophys. J.* **679** (2008) 1260, [arXiv:0802.2265].

[57] G. Gentile, P. Salucci, U. Klein, D. Vergani, and P. Kalberla, *The Cored distribution of dark matter in spiral galaxies*, *Mon. Not. Roy. Astron. Soc.* **351** (2004) 903, [astro-ph/0403154].

[58] G. Gentile, A. Burkert, P. Salucci, U. Klein, and F. Walter, *The dwarf galaxy DDO 47 as a dark matter laboratory: testing cusps hiding in triaxial halos*, *Astrophys. J. Lett.* **634** (2005) L145–L148, [astro-ph/0506538].

[59] J. D. Simon, A. D. Bolatto, A. Leroy, L. Blitz, and E. L. Gates, *High-resolution measurements of the halos of four dark matter-dominated galaxies: Deviations from a universal density profile*, *Astrophys. J.* **621** (2005) 757–776, [astro-ph/0412035].

[60] W. J. G. de Blok, *Halo mass profiles and low surface brightness galaxies rotation curves*, *Astrophys. J.* **634** (2005) 227–238, [astro-ph/0506753].

[61] A. Maeder, *An alternative to the ΛCDM model: The case of scale invariance*, *Astrophys. J.* **834** (2017), no. 2 194, [arXiv:1701.03964].

[62] D. Hutsemékers, L. Braibant, V. Pelgrims, and D. Sluse, *Alignment of quasar polarizations with large-scale structures*, *Astron. Astrophys.* **572** (2014) A18, [arXiv:1409.6098].

[63] H. V. Peiris and T. L. Smith, *CMB Isotropy Anomalies and the Local Kinetic Sunyaev-Zel'dovich Effect*, *Phys. Rev.* **D81** (2010) 123517, [arXiv:1002.0836].

[64] M. Zumalacarregui, T. S. Koivisto, D. F. Mota, and P. Ruiz-Lapuente, *Disformal Scalar Fields and the Dark Sector of the Universe*, *JCAP* **1005** (2010) 038, [arXiv:1004.2684].

[65] T. Koivisto and D. F. Mota, *Dark energy anisotropic stress and large scale structure formation*, *Phys. Rev.* **D73** (2006) 083502, [astro-ph/0512135].

[66] R. Battye and A. Moss, *Anisotropic dark energy and CMB anomalies*, *Phys. Rev.* **D80** (2009) 023531, [arXiv:0905.3403].

[67] C. Armendariz-Picon, *Could dark energy be vector-like?*, *JCAP* **0407** (2004) 007, [astro-ph/0405267].

[68] G. Esposito-Farese, C. Pitrou, and J.-P. Uzan, *Vector theories in cosmology*, *Phys. Rev.* **D81** (2010) 063519, [arXiv:0912.0481].

[69] D. C. Rodrigues, *Anisotropic Cosmological Constant and the CMB Quadrupole Anomaly*, *Phys. Rev.* **D77** (2008) 023534, [arXiv:0708.1168].

[70] J. Beltran Jimenez and A. L. Maroto, *Large-scale cosmic flows and moving dark energy*, *JCAP* **0903** (2009) 015, [arXiv:0811.3606].

[71] S. Alexander, T. Biswas, A. Notari, and D. Vaid, *Local Void vs Dark Energy: Confrontation with WMAP and Type Ia Supernovae*, *JCAP* **0909** (2009) 025, [arXiv:0712.0370].

[72] J. Garcia-Bellido and T. Haugboelle, *Confronting Lemaitre-Tolman-Bondi models with Observational Cosmology*, *JCAP* **0804** (2008) 003, [arXiv:0802.1523].

[73] T. Biswas, A. Notari, and W. Valkenburg, *Testing the Void against Cosmological data: fitting CMB, BAO, SN and H0*, *JCAP* **1011** (2010) 030, [arXiv:1007.3065].

[74] P. Dunsby, N. Goheer, B. Osano, and J.-P. Uzan, *How close can an Inhomogeneous Universe mimic the Concordance Model?*, *JCAP* **1006** (2010) 017, [arXiv:1002.2397].

[75] D. Garfinkle, *The Motion of galaxy clusters in inhomogeneous cosmologies*, *Class. Quant. Grav.* **27** (2010) 065002, [arXiv:0908.4102].

[76] J.-P. Luminet, *The Shape and Topology of the Universe*, arXiv:0802.2236.

[77] P. Bielewicz and A. Riazuelo, *The study of topology of the universe using multipole vectors*, *Mon. Not. Roy. Astron. Soc.* **396** (2009) 609, [arXiv:0804.2437].

[78] S. Carneiro and G. A. Mena Marugan, *Anisotropic cosmologies containing isotropic background radiation*, *Phys. Rev.* **D64** (2001) 083502, [gr-qc/0109039].

[79] E. Akofor, A. P. Balachandran, S. G. Jo, A. Joseph, and B. A. Qureshi, *Direction-Dependent CMB Power Spectrum and Statistical Anisotropy from Noncommutative Geometry*, *JHEP* **05** (2008) 092, [arXiv:0710.5897].

[80] T. S. Koivisto, D. F. Mota, M. Quartin, and T. G. Zlosnik, *On the Possibility of Anisotropic Curvature in Cosmology*, *Phys. Rev.* **D83** (2011) 023509, [arXiv:1006.3321].

[81] C. Armendariz-Picon, *Creating Statistically Anisotropic and Inhomogeneous Perturbations*, *JCAP* **0709** (2007) 014, [arXiv:0705.1167].

[82] A. R. Pullen and M. Kamionkowski, *Cosmic Microwave Background Statistics for a Direction-Dependent Primordial Power Spectrum*, *Phys. Rev.* **D76** (2007) 103529, [arXiv:0709.1144].

[83] L. Ackerman, S. M. Carroll, and M. B. Wise, *Imprints of a Primordial Preferred Direction on the Microwave Background*, *Phys. Rev.* **D75** (2007) 083502, [astro-ph/0701357]. [Erratum: Phys. Rev.D80,069901(2009)].

[84] K. Dimopoulos, M. Karciauskas, D. H. Lyth, and Y. Rodriguez, *Statistical anisotropy of the curvature perturbation from vector field perturbations*, *JCAP* **0905** (2009) 013, [arXiv:0809.1055].

[85] S. Yokoyama and J. Soda, *Primordial statistical anisotropy generated at the end of inflation*, *JCAP* **0808** (2008) 005, [arXiv:0805.4265].

[86] A. Golovnev and V. Vanchurin, *Cosmological perturbations from vector inflation*, *Phys. Rev.* **D79** (2009) 103524, [arXiv:0903.2977].

[87] N. Bartolo, E. Dimastrogiovanni, S. Matarrese, and A. Riotto, *Anisotropic bispectrum of curvature perturbations from primordial non-Abelian vector fields*, *JCAP* **0910** (2009) 015, [arXiv:0906.4944].

[88] B. Himmetoglu, C. R. Contaldi, and M. Peloso, *Instability of anisotropic cosmological solutions supported by vector fields*, *Phys. Rev. Lett.* **102** (2009) 111301, [arXiv:0809.2779].

[89] B. Himmetoglu, C. R. Contaldi, and M. Peloso, *Instability of the ACW model, and problems with massive vectors during inflation*, *Phys. Rev.* **D79** (2009) 063517, [arXiv:0812.1231].

[90] B. Himmetoglu, C. R. Contaldi, and M. Peloso, *Ghost instabilities of cosmological models with vector fields nonminimally coupled to the curvature*, *Phys. Rev.* **D80** (2009) 123530, [arXiv:0909.3524].

[91] T. Kahniashvili, G. Lavrelashvili, and B. Ratra, *CMB Temperature Anisotropy from Broken Spatial Isotropy due to an Homogeneous Cosmological Magnetic Field*, *Phys. Rev.* **D78** (2008) 063012, [arXiv:0807.4239].

[92] J. D. Barrow, P. G. Ferreira, and J. Silk, *Constraints on a primordial magnetic field*, *Phys. Rev. Lett.* **78** (1997) 3610–3613, [astro-ph/9701063].

[93] L. Campanelli, *A Model of Universe Anisotropization*, *Phys. Rev.* **D80** (2009) 063006, [arXiv:0907.3703].

[94] J. Kim and P. Naselsky, *Alfvén turbulence in the WMAP 5 year data and a forecast for the PLANCK*, *JCAP* **0907** (2009) 041, [arXiv:0903.1930].

[95] P. Brax, C. van de Bruck, A.-C. Davis, J. Khoury, and A. Weltman, *Detecting dark energy in orbit - The Cosmological chameleon*, *Phys. Rev.* **D70** (2004) 123518, [astro-ph/0408415].

[96] S. Nojiri and S. D. Odintsov, *Quantum effects and stability of chameleon cosmology*, *Mod. Phys. Lett.* **A19** (2004) 1273–1280, [hep-th/0310296].

[97] P. Brax and J. Martin, *Moduli Fields as Quintessence and the Chameleon*, *Phys. Lett.* **B647** (2007) 320–329, [hep-th/0612208].

[98] P. Brax, C. van de Bruck, A.-C. Davis, D. F. Mota, and D. J. Shaw, *Detecting chameleons through Casimir force measurements*, *Phys. Rev.* **D76** (2007) 124034, [arXiv:0709.2075].

[99] W. Nelson and M. Sakellariadou, *Cosmology and the Noncommutative approach to the Standard Model*, *Phys. Rev.* **D81** (2010) 085038, [arXiv:0812.1657].

[100] P. Brax, C. van de Bruck, and A.-C. Davis, *Compatibility of the chameleon-field model with fifth-force experiments, cosmology, and PVLAS and CAST results*, *Phys. Rev. Lett.* **99** (2007) 121103, [hep-ph/0703243].

[101] K. Hinterbichler, J. Khoury, and H. Nastase, *Towards a UV Completion for Chameleon Scalar Theories*, *JHEP* **03** (2011) 061, [arXiv:1012.4462]. [Erratum: JHEP06,072(2011)].

[102] P. Creminelli, J. Gleyzes, L. Hui, M. Simonović, and F. Vernizzi, *Single-Field Consistency Relations of Large Scale Structure. Part III: Test of the Equivalence Principle*, *JCAP* **1406** (2014) 009, [arXiv:1312.6074].

[103] A. Joyce, B. Jain, J. Khoury, and M. Trodden, *Beyond the Cosmological Standard Model*, *Phys. Rept.* **568** (2015) 1–98, [arXiv:1407.0059].

[104] B. Elder, J. Khoury, P. Haslinger, M. Jaffe, H. Müller, and P. Hamilton, *Chameleon Dark Energy and Atom Interferometry*, *Phys. Rev.* **D94** (2016), no. 4 044051, [arXiv:1603.06587].

[105] C. A. O. Schelpe, *Chameleon-Photon Mixing in a Primordial Magnetic Field*, *Phys. Rev.* **D82** (2010) 044033, [arXiv:1003.0232].

[106] J. Khoury and A. Weltman, *Chameleon fields: Awaiting surprises for tests of gravity in space*, *Phys. Rev. Lett.* **93** (2004) 171104, [astro-ph/0309300].

[107] R. R. Caldwell, R. Dave, and P. J. Steinhardt, *Cosmological imprint of an energy component with general equation of state*, *Phys. Rev. Lett.* **80** (1998) 1582–1585, [astro-ph/9708069].

[108] A. Einstein, *Approximative Integration of the Field Equations of Gravitation*, *Sitzungsber. Preuss. Akad. Wiss. Berlin (Math. Phys.)* **1916** (1916) 688–696.

[109] A. Einstein, *Über Gravitationswellen*, *Sitzungsber. Preuss. Akad. Wiss. Berlin (Math. Phys.)* **1918** (1918) 154–167.

[110] J. Ellis, N. E. Mavromatos, and D. V. Nanopoulos, *Comments on Graviton Propagation in Light of GW150914*, arXiv:1602.04764.

[111] A. Le Tiec and J. Novak, *Theory of Gravitational Waves*, arXiv:1607.04202.

[112] P. R. Saulson, *Josh Goldberg and the physical reality of gravitational waves*, *Gen. Rel. Grav.* **43** (2011) 3289–3299.

[113] R. A. Hulse and J. H. Taylor, *Discovery of a pulsar in a binary system*, *Astrophys. J.* **195** (1975) L51–L53.

[114] J. H. Taylor and J. M. Weisberg, *A new test of general relativity: Gravitational radiation and the binary pulsar PS R 1913+16*, *Astrophys. J.* **253** (1982) 908–920.

[115] W. H. Press and K. S. Thorne, *Gravitational-wave astronomy*, *Ann. Rev. Astron. Astrophys.* **10** (1972) 335–374.

[116] **Virgo, LIGO Scientific** Collaboration, B. P. Abbott et al., *GW150914: The Advanced LIGO Detectors in the Era of First Discoveries*, *Phys. Rev. Lett.* **116** (2016), no. 13 131103, [arXiv:1602.03838].

[117] **Virgo, LIGO Scientific** Collaboration, B. P. Abbott et al., *Observation of Gravitational Waves from a Binary Black Hole Merger*, *Phys. Rev. Lett.* **116** (2016), no. 6 061102, [arXiv:1602.03837].

[118] E. O. Kahya and S. Desai, *Constraints on frequency-dependent violations of Shapiro delay from GW150914*, *Phys. Lett.* **B756** (2016) 265–267, [arXiv:1602.04779].

[119] X.-F. Wu, H. Gao, J.-J. Wei, X.-L. Fan, P. Mészáros, B. Zhang, Z.-G. Dai, S.-N. Zhang, and Z.-H. Zhu, *Testing Einstein's Equivalence Principle With Gravitational Waves*, arXiv:1602.01566.

[120] M. Liu, Z. Zhao, X. You, J. Lu, and L. Xu, *Violation of Einstein's Equivalence Principle on Gravitational Wave Event GW150914 Associated with GBM Transient GW150914-GBM*, arXiv:1604.06668.

[121] N. Yunes, K. Yagi, and F. Pretorius, *Theoretical Physics Implications of the Binary Black-Hole Merger GW150914*, arXiv:1603.08955.

[122] V. Branchina and M. De Domenico, *Simultaneous observation of gravitational and electromagnetic waves*, arXiv:1604.08530.

[123] M. Schreck, *Looking for Lorentz violation with gravitational waves*, arXiv:1603.07452.

[124] M. Arzano and G. Calcagni, *What gravity waves are telling about quantum spacetime*, *Phys. Rev.* **D93** (2016), no. 12 124065, [arXiv:1604.00541].

[125] P. Bicudo, *Tighter bounds on a hypothetical graviton screening mass from the gravitational wave observation GW150914 at LIGO*, arXiv:1602.04337.

[126] T. E. Collett and D. Bacon, *Testing the speed of gravitational waves over cosmological distances with strong gravitational lensing*, arXiv:1602.05882.

[127] D. Blas, M. M. Ivanov, I. Sawicki, and S. Sibiryakov, *On constraining the speed of gravitational waves following GW150914*, arXiv:1602.04188.

[128] J. García-Bellido, S. Nesseris, and M. Trashorras, *Gravitational wave source counts at high redshift and in models with extra dimensions*, arXiv:1603.05616.

[129] R. Konoplya and A. Zhidenko, *Detection of gravitational waves from black holes: Is there a window for alternative theories?*, *Phys. Lett.* **B756** (2016) 350–353, [arXiv:1602.04738].

[130] J. W. Moffat, *LIGO GW 150914 Gravitational Wave Detection and Generalized Gravitation Theory (MOG)*, arXiv:1603.05225.

[131] J. Vainio and I. Vilja, *f(R) gravity constraints from gravitational waves*, arXiv:1603.09551.

[132] P. S. B. Dev and A. Mazumdar, *Probing the Scale of New Physics by Advanced LIGO/VIRGO*, *Phys. Rev.* **D93** (2016), no. 10 104001, [arXiv:1602.04203].

[133] J. Jaeckel, V. V. Khoze, and M. Spannowsky, *Hearing the smoke of dark sectors with gravitational wave detectors*, arXiv:1602.03901.

[134] S. B. Giddings, *Gravitational wave tests of quantum modifications to black hole structure – with post-GW150914 update*, arXiv:1602.03622.

[135] M. Sasaki, T. Suyama, T. Tanaka, and S. Yokoyama, *Primordial black hole scenario for the gravitational wave event GW150914*, arXiv:1603.08338.

[136] S. Bird, I. Cholis, J. B. Muñoz, Y. Ali-Haïmoud, M. Kamionkowski, E. D. Kovetz, A. Raccanelli, and A. G. Riess, *Did LIGO detect dark matter?*, *Phys. Rev. Lett.* **116** (2016), no. 20 201301, [arXiv:1603.00464].

[137] S. Clesse and J. García-Bellido, *The clustering of massive Primordial Black Holes as Dark Matter: measuring their mass distribution with Advanced LIGO*, arXiv:1603.05234.

[138] L. Amendola, M. Kunz, I. D. Saltas, and I. Sawicki, *Fate of Large-Scale Structure in Modified Gravity After GW170817 and GRB170817A*, *Phys. Rev. Lett.* **120** (2018), no. 13 131101, [arXiv:1711.04825].

[139] E. Bellini, A. J. Cuesta, R. Jimenez, and L. Verde, *Constraints on deviations from ΛCDM within Horndeski gravity*, *JCAP* **1602** (2016), no. 02 053, [arXiv:1509.07816]. [Erratum: JCAP1606,no.06,E01(2016)].

[140] **Planck** Collaboration, N. Aghanim et al., *Planck 2018 results. VI. Cosmological parameters*, arXiv:1807.06209.

[141] V. Poulin, T. L. Smith, T. Karwal, and M. Kamionkowski, *Early Dark Energy Can Resolve The Hubble Tension*, arXiv:1811.04083.

[142] A. G. Riess et al., *A 2.4% Determination of the Local Value of the Hubble Constant*, *Astrophys. J.* **826** (2016), no. 1 56, [arXiv:1604.01424].

[143] S. Birrer et al., *H0LiCOW - IX. Cosmographic analysis of the doubly imaged quasar SDSS 1206+4332 and a new measurement of the Hubble constant*, *Mon. Not. Roy. Astron. Soc.* **484** (2019) 4726, [arXiv:1809.01274].

[144] A. G. Riess, S. Casertano, W. Yuan, L. M. Macri, and D. Scolnic, *Large Magellanic Cloud Cepheid Standards Provide a 1% Foundation for the Determination of the Hubble Constant and Stronger Evidence for Physics Beyond LambdaCDM*, arXiv:1903.07603.

[145] **Planck** Collaboration, P. A. R. Ade et al., *Planck 2013 results. XXIII. Isotropy and statistics of the CMB*, *Astron. Astrophys.* **571** (2014) A23, [arXiv:1303.5083].

[146] F. K. Hansen, A. J. Banday, and K. M. Gorski, *Testing the cosmological principle of isotropy: Local power spectrum estimates of the WMAP data*, *Mon. Not. Roy. Astron. Soc.* **354** (2004) 641–665, [astro-ph/0404206].

[147] P. K. Samal, R. Saha, P. Jain, and J. P. Ralston, *Testing Isotropy of Cosmic Microwave Background Radiation*, *Mon. Not. Roy. Astron. Soc.* **385** (2008) 1718, [arXiv:0708.2816].

[148] L. Campanelli, P. Cea, G. L. Fogli, and A. Marrone, *Testing the Isotropy of the Universe with Type Ia Supernovae*, *Phys. Rev.* **D83** (2011) 103503, [arXiv:1012.5596].

[149] H.-N. Lin, S. Wang, Z. Chang, and X. Li, *Testing the isotropy of the Universe by using the JLA compilation of type-Ia supernovae*, *Mon. Not. Roy. Astron. Soc.* **456** (2016), no. 2 1881–1885, [arXiv:1504.03428].

[150] S. Sarkar, B. Pandey, and R. Khatri, *Testing isotropy in the Universe using photometric and spectroscopic data from the SDSS*, *Mon. Not. Roy. Astron. Soc.* **483** (2019), no. 2 2453–2464, [arXiv:1810.07410].

[151] **Pierre Auger** Collaboration, A. Aab et al., *Searches for Anisotropies in the Arrival Directions of the Highest Energy Cosmic Rays Detected by the Pierre Auger Observatory*, *Astrophys. J.* **804** (2015), no. 1 15, [arXiv:1411.6111].

[152] C. Gibelyou and D. Huterer, *Dipoles in the Sky*, *Mon. Not. Roy. Astron. Soc.* **427** (2012) 1994–2021, [arXiv:1205.6476].

[153] P. M. Sutter, G. Lavaux, B. D. Wandelt, and D. H. Weinberg, *A first application of the Alcock-Paczynski test to stacked cosmic voids*, *Astrophys. J.* **761** (2012) 187, [arXiv:1208.1058].

[154] P. K. Samal, R. Saha, P. Jain, and J. P. Ralston, *Signals of Statistical Anisotropy in WMAP Foreground-Cleaned Maps*, *Mon. Not. Roy. Astron. Soc.* **396** (2009) 511, [arXiv:0811.1639].

[155] C. J. Copi, D. Huterer, and G. D. Starkman, *Multipole vectors - A New representation of the CMB sky and evidence for statistical anisotropy or non-Gaussianity at 2 <= l <= 8*, *Phys. Rev.* **D70** (2004) 043515, [astro-ph/0310511].

[156] M. Blomqvist and E. Mortsell, *Supernovae as seen by off-center observers in a local void*, *JCAP* **1005** (2010) 006, [arXiv:0909.4723].

[157] M. Blomqvist, J. Enander, and E. Mortsell, *Constraining dark energy fluctuations with supernova correlations*, *JCAP* **1010** (2010) 018, [arXiv:1006.4638].

[158] K. Tomita, *Analyses of type Ia supernova data in cosmological models with a local void*, *Prog. Theor. Phys.* **106** (2001) 929–939, [astro-ph/0104141].

[159] R. Cooke and D. Lynden-Bell, *Does the Universe Accelerate Equally in all Directions?*, *Mon. Not. Roy. Astron. Soc.* **401** (2010) 1409–1414, [arXiv:0909.3861].

[160] T. S. Kolatt and O. Lahav, *Constraints on cosmological anisotropy out to z=1 from supernovae ia*, *Mon. Not. Roy. Astron. Soc.* **323** (2001) 859, [astro-ph/0008041].

[161] S. Gupta, T. D. Saini, and T. Laskar, *Direction Dependent Non-Gaussianity in High-z Supernova Data*, *Mon. Not. Roy. Astron. Soc.* **388** (2008) 242–246, [astro-ph/0701683].

[162] D. J. Schwarz and B. Weinhorst, *(An)isotropy of the Hubble diagram: Comparing hemispheres*, *Astron. Astrophys.* **474** (2007) 717–729, [arXiv:0706.0165].

[163] **Supernova Search Team** Collaboration, A. G. Riess et al., *Type Ia supernova discoveries at z > 1 from the Hubble Space Telescope: Evidence for past deceleration and constraints on dark energy evolution*, *Astrophys. J.* **607** (2004) 665–687, [astro-ph/0402512].

[164] **Supernova Cosmology Project** Collaboration, M. Kowalski et al., *Improved Cosmological Constraints from New, Old and Combined Supernova Datasets*, *Astrophys. J.* **686** (2008) 749–778, [arXiv:0804.4142].

[165] M. Hicken, W. M. Wood-Vasey, S. Blondin, P. Challis, S. Jha, P. L. Kelly, A. Rest, and R. P. Kirshner, *Improved Dark Energy Constraints from 100 New CfA Supernova Type Ia Light Curves*, *Astrophys. J.* **700** (2009) 1097–1140, [arXiv:0901.4804].

[166] **SDSS** Collaboration, J. A. Holtzman et al., *The Sloan Digital Sky Survey-II Photometry and Supernova IA Light Curves from the 2005 Data*, *Astron. J.* **136** (2008) 2306–2320, [arXiv:0908.4277].

[167] P. Duffett-Smith, *Practical Astronomy with your Calculator*. Cambridge University Press, 3 ed., 1989.

[168] K. M. Gorski, E. Hivon, A. J. Banday, B. D. Wandelt, F. K. Hansen, M. Reinecke, and M. Bartelman, *HEALPix - A Framework for high resolution discretization, and fast analysis of data distributed on the sphere*, *Astrophys. J.* **622** (2005) 759–771, [astro-ph/0409513].

[169] H. A. Feldman, R. Watkins, and M. J. Hudson, *Cosmic Flows on 100 Mpc/h Scales: Standardized Minimum Variance Bulk Flow, Shear and Octupole Moments*, *Mon. Not. Roy. Astron. Soc.* **407** (2010) 2328–2338, [arXiv:0911.5516].

[170] M. J. Longo, *Evidence for a Preferred Handedness of Spiral Galaxies*, arXiv:0904.2529.

[171] M. Quartin and L. Amendola, *Distinguishing Between Void Models and Dark Energy with Cosmic Parallax and Redshift Drift*, *Phys. Rev.* **D81** (2010) 043522, [arXiv:0909.4954].

[172] T. Damour, *The Equivalence Principle and the Constants of Nature*, *Space Sci. Rev.* **148** (2009) 191–199, [arXiv:0906.3174].

[173] J.-P. Uzan, *Varying Constants, Gravitation and Cosmology*, *Living Rev. Rel.* **14** (2011) 2, [arXiv:1009.5514].

[174] V. V. Flambaum, *Variation of fundamental constants: Theory and observations*, *Int. J. Mod. Phys.* **A22** (2007) 4937–4950, [arXiv:0705.3704].

[175] C. Brans and R. H. Dicke, *Mach's principle and a relativistic theory of gravitation*, *Phys. Rev.* **124** (1961) 925–935. [,142(1961)].

[176] E. Teller, *On the Change of Physical Constants*, *Phys. Rev.* **73** (1948) 801–802.

[177] J. D. Bekenstein, *Fine Structure Constant: Is It Really a Constant?*, *Phys. Rev.* **D25** (1982) 1527–1539.

[178] H. B. Sandvik, J. D. Barrow, and J. Magueijo, *A simple cosmology with a varying fine structure constant*, *Phys. Rev. Lett.* **88** (2002) 031302, [astro-ph/0107512].

[179] C. M. Will, *The Confrontation between general relativity and experiment*, *Living Rev. Rel.* **9** (2006) 3, [gr-qc/0510072].

[180] T. Chiba, *The Constancy of the Constants of Nature: Updates*, *Prog. Theor. Phys.* **126** (2011) 993–1019, [arXiv:1111.0092].

[181] F. Piazza and S. Tsujikawa, *Dilatonic ghost condensate as dark energy*, *JCAP* **0407** (2004) 004, [hep-th/0405054].

[182] T. Damour, F. Piazza, and G. Veneziano, *Violations of the equivalence principle in a dilaton runaway scenario*, *Phys. Rev.* **D66** (2002) 046007, [hep-th/0205111].

[183] H. Farajollahi and A. Salehi, *Varying alpha and cosmic acceleration in Brans-Dicke-BSBM theory: stability analysis and observational tests*, *JCAP* **1211** (2012) 002, [arXiv:1209.3763].

[184] L. Perivolaropoulos, *PPN Parameter gamma and Solar System Constraints of Massive Brans-Dicke Theories*, *Phys. Rev.* **D81** (2010) 047501, [arXiv:0911.3401].

[185] T. Chiba and K. Kohri, *Quintessence cosmology and varying alpha*, *Prog. Theor. Phys.* **107** (2002) 631–636, [hep-ph/0111086].

[186] J. D. Barrow and A. A. H. Graham, *General Dynamics of Varying-Alpha Universes*, *Phys. Rev.* **D88** (2013) 103513, [arXiv:1307.6816].

[187] E. J. Copeland, N. J. Nunes, and M. Pospelov, *Models of quintessence coupled to the electromagnetic field and the cosmological evolution of alpha*, *Phys. Rev.* **D69** (2004) 023501, [hep-ph/0307299].

[188] O. Bertolami, R. Lehnert, R. Potting, and A. Ribeiro, *Cosmological acceleration, varying couplings, and Lorentz breaking*, *Phys. Rev.* **D69** (2004) 083513, [astro-ph/0310344].

[189] S. Lee, K. A. Olive, and M. Pospelov, *Quintessence models and the cosmological evolution of alpha*, *Phys. Rev.* **D70** (2004) 083503, [astro-ph/0406039].

[190] E. Calabrese, M. Martinelli, S. Pandolfi, V. F. Cardone, C. J. A. P. Martins, S. Spiro, and P. E. Vielzeuf, *Dark Energy coupling with electromagnetism as seen from future low-medium redshift probes*, *Phys. Rev.* **D89** (2014), no. 8 083509, [arXiv:1311.5841].

[191] M. T. Murphy, J. K. Webb, V. V. Flambaum, V. A. Dzuba, C. W. Churchill, J. X. Prochaska, J. D. Barrow, and A. M. Wolfe, *Possible evidence for a variable fine structure constant from QSO absorption lines: Motivations, analysis and results*, *Mon. Not. Roy. Astron. Soc.* **327** (2001) 1208, [astro-ph/0012419].

[192] J. K. Webb, V. V. Flambaum, C. W. Churchill, M. J. Drinkwater, and J. D. Barrow, *Evidence for time variation of the fine structure constant*, *Phys. Rev. Lett.* **82** (1999) 884–887, [astro-ph/9803165].

[193] J. K. Webb, M. T. Murphy, V. V. Flambaum, V. A. Dzuba, J. D. Barrow, C. W. Churchill, J. X. Prochaska, and A. M. Wolfe, *Further evidence for cosmological evolution of the fine structure constant*, *Phys. Rev. Lett.* **87** (2001) 091301, [astro-ph/0012539].

[194] J. A. King, J. K. Webb, M. T. Murphy, V. V. Flambaum, R. F. Carswell, M. B. Bainbridge, M. R. Wilczynska, and F. E. Koch, *Spatial variation in the fine-structure constant – new results from VLT/UVES*, *Mon. Not. Roy. Astron. Soc.* **422** (2012) 3370–3413, [arXiv:1202.4758].

[195] A. Mariano and L. Perivolaropoulos, *Is there correlation between Fine Structure and Dark Energy Cosmic Dipoles?*, *Phys. Rev.* **D86** (2012) 083517, [arXiv:1206.4055].

[196] L. Perivolaropoulos, *Large Scale Cosmological Anomalies and Inhomogeneous Dark Energy*, *Galaxies* **2** (2014) 22–61, [arXiv:1401.5044].

[197] J. Grande and L. Perivolaropoulos, *Generalized LTB model with Inhomogeneous Isotropic Dark Energy: Observational Constraints*, *Phys. Rev.* **D84** (2011) 023514, [arXiv:1103.4143].

[198] L. Perivolaropoulos, *Topological quintessence: Generalizing Lambda CDM with inhomogeneous dark energy*, *Rom. J. Phys.* **57** (2012) 950–968.

[199] J. C. Bueno Sanchez and L. Perivolaropoulos, *Topological Quintessence*, *Phys. Rev.* **D84** (2011) 123516, [arXiv:1110.2587].

[200] A. Mariano and L. Perivolaropoulos, *CMB Maximum temperature asymmetry Axis: Alignment with other cosmic asymmetries*, *Phys. Rev.* **D87** (2013), no. 4 043511, [arXiv:1211.5915].

[201] K. A. Olive, M. Peloso, and J.-P. Uzan, *The Wall of Fundamental Constants*, *Phys. Rev.* **D83** (2011) 043509, [arXiv:1011.1504].

[202] J. Menezes da Silva, *Cosmological Consequences of Topological Defects: Dark Energy and Varying Fundamental Constants*. PhD thesis, Porto U., 2007. arXiv:0808.3274.

[203] J. Menezes, P. P. Avelino, and C. Santos, *Varying alpha monopoles*, *Phys. Rev.* **D72** (2005) 103504, [hep-ph/0509326].

[204] L. Perivolaropoulos and N. Platis, *Stabilizing the Semilocal String with a Dilatonic Coupling*, *Phys. Rev.* **D88** (2013), no. 6 065017, [arXiv:1307.3920].

[205] K. A. Olive, M. Peloso, and A. J. Peterson, *Where are the walls? Spatial variation in the fine-structure constant*, *Phys. Rev.* **D86** (2012) 043501, [arXiv:1204.4391].

[206] T. Vachaspati and A. Achucarro, *Semilocal cosmic strings*, *Phys. Rev.* **D44** (1991) 3067–3071.

[207] M. Hindmarsh, *Existence and stability of semilocal strings*, *Phys. Rev. Lett.* **68** (1992) 1263–1266.

[208] M. James, L. Perivolaropoulos, and T. Vachaspati, *Detailed stability analysis of electroweak strings*, *Nucl. Phys.* **B395** (1993) 534–546, [hep-ph/9212301].

[209] M. James, L. Perivolaropoulos, and T. Vachaspati, *Stability of electroweak strings*, *Phys. Rev.* **D46** (1992) R5232–R5235.

[210] M. Barriola, T. Vachaspati, and M. Bucher, *Embedded defects*, *Phys. Rev.* **D50** (1994) 2819–2825, [hep-th/9306120].

[211] A. Achucarro and T. Vachaspati, *Semilocal and electroweak strings*, *Phys. Rept.* **327** (2000) 347–426, [hep-ph/9904229]. [Phys. Rept.327,427(2000)].

[212] J. Preskill, *Semilocal defects*, *Phys. Rev.* **D46** (1992) 4218–4231, [hep-ph/9206216].

[213] G. 't Hooft, *Magnetic Monopoles in Unified Gauge Theories*, *Nucl. Phys.* **B79** (1974) 276–284. [,291(1974)].

[214] G. W. Gibbons, M. E. Ortiz, F. Ruiz Ruiz, and T. M. Samols, *Semilocal strings and monopoles*, *Nucl. Phys.* **B385** (1992) 127–144, [hep-th/9203023].

[215] T. Vachaspati, *Magnetic fields from cosmological phase transitions*, *Phys. Lett.* **B265** (1991) 258–261.

[216] T. Vachaspati and G. B. Field, *Electroweak string configurations with baryon number*, *Phys. Rev. Lett.* **73** (1994) 373–376, [hep-ph/9401220].

[217] M. Barriola, *Electroweak strings that produce baryons*, *Phys. Rev.* **D51** (1995) 300–304, [hep-ph/9403323].

[218] G. D. Starkman and T. Vachaspati, *Galactic cosmic strings as sources of primary anti-protons*, *Phys. Rev.* **D53** (1996) R6711–R6714, [astro-ph/9604007].

[219] Y. Nambu, *String-Like Configurations in the Weinberg-Salam Theory*, *Nucl. Phys.* **B130** (1977) 505. [,329(1977)].

[220] J. Sola, A. Gomez-Valent, and J. de Cruz Pérez, *Dynamical dark energy: scalar fields and running vacuum*, *Mod. Phys. Lett.* **A32** (2017), no. 9 1750054, [arXiv:1610.08965].

[221] J. Solà, A. Gómez-Valent, and J. de Cruz Pérez, *First evidence of running cosmic vacuum: challenging the concordance model*, *Astrophys. J.* **836** (2017), no. 1 43, [arXiv:1602.02103].

[222] J. K. Webb, J. A. King, M. T. Murphy, V. V. Flambaum, R. F. Carswell, and M. B. Bainbridge, *Indications of a spatial variation of the fine structure constant*, *Phys. Rev. Lett.* **107** (2011) 191101, [arXiv:1008.3907].

[223] M. T. Murphy, J. K. Webb, and V. V. Flambaum, *Further evidence for a variable fine-structure constant from Keck/HIRES QSO absorption spectra*, *Mon. Not. Roy. Astron. Soc.* **345** (2003) 609, [astro-ph/0306483].

[224] D. F. Mota and J. D. Barrow, *Local and global variations of the fine structure constant*, *Mon. Not. Roy. Astron. Soc.* **349** (2004) 291, [astro-ph/0309273].

[225] E. Reinhold, R. Buning, U. Hollenstein, A. Ivanchik, P. Petitjean, and W. Ubachs, *Indication of a Cosmological Variation of the Proton - Electron Mass Ratio Based on Laboratory Measurement and Reanalysis of H(2) Spectra*, *Phys. Rev. Lett.* **96** (2006) 151101.

[226] Y. Fenner, M. T. Murphy, and B. K. Gibson, *On variations in the fine-structure constant and limits on AGB pollution of quasar absorption systems*, *Mon. Not. Roy. Astron. Soc.* **358** (2005) 468–480, [astro-ph/0501168].

[227] P. Langacker, G. Segre, and M. J. Strassler, *Implications of gauge unification for time variation of the fine structure constant*, *Phys. Lett.* **B528** (2002) 121–128, [hep-ph/0112233].

[228] V. Marra and F. Rosati, *Cosmological evolution of alpha driven by a general coupling with quintessence*, *JCAP* **0505** (2005) 011, [astro-ph/0501515].

[229] S. Nesseris and L. Perivolaropoulos, *The Fate of bound systems in phantom and quintessence cosmologies*, *Phys. Rev.* **D70** (2004) 123529, [astro-ph/0410309].

[230] L. Anchordoqui and H. Goldberg, *Time variation of the fine structure constant driven by quintessence*, *Phys. Rev.* **D68** (2003) 083513, [hep-ph/0306084].

[231] S. Tsujikawa, *Quintessence: A Review*, *Class. Quant. Grav.* **30** (2013) 214003, [arXiv:1304.1961].

[232] L. Amendola, A. C. O. Leite, C. J. A. P. Martins, N. J. Nunes, P. O. J. Pedrosa, and A. Seganti, *Variation of fundamental parameters and dark energy. A principal component approach*, *Phys. Rev.* **D86** (2012) 063515, [arXiv:1109.6793].

[233] G. Raffelt and L. Stodolsky, *Mixing of the Photon with Low Mass Particles*, *Phys. Rev.* **D37** (1988) 1237.

[234] P. Arias, D. Cadamuro, M. Goodsell, J. Jaeckel, J. Redondo, and A. Ringwald, *WISPy Cold Dark Matter*, *JCAP* **1206** (2012) 013, [arXiv:1201.5902].

[235] D. Cadamuro, *Cosmological limits on axions and axion-like particles*. PhD thesis, Munich U., 2012. arXiv:1210.3196.

[236] L. D. Duffy and K. van Bibber, *Axions as Dark Matter Particles*, *New J. Phys.* **11** (2009) 105008, [arXiv:0904.3346].

[237] E. Calabrese, E. Menegoni, C. J. A. P. Martins, A. Melchiorri, and G. Rocha, *Constraining Variations in the Fine Structure Constant in the presence of Early Dark Energy*, *Phys. Rev.* **D84** (2011) 023518, [arXiv:1104.0760].

[238] **GammeV (T-969)** Collaboration, A. S. Chou, W. C. Wester, III, A. Baumbaugh, H. R. Gustafson, Y. Irizarry-Valle, P. O. Mazur, J. H. Steffen, R. Tomlin, X. Yang, and J. Yoo, *Search for axion-like particles using a variable baseline photon regeneration technique*, *Phys. Rev. Lett.* **100** (2008) 080402, [arXiv:0710.3783].

[239] E. Masso and R. Toldra, *On a light spinless particle coupled to photons*, *Phys. Rev.* **D52** (1995) 1755–1763, [hep-ph/9503293].

[240] M. P. Hertzberg, M. Tegmark, and F. Wilczek, *Axion Cosmology and the Energy Scale of Inflation*, *Phys. Rev.* **D78** (2008) 083507, [arXiv:0807.1726].

[241] **ADMX** Collaboration, S. J. Asztalos et al., *An Improved RF cavity search for halo axions*, *Phys. Rev.* **D69** (2004) 011101, [astro-ph/0310042].

[242] **CAST** Collaboration, K. Zioutas et al., *First results from the CERN Axion Solar Telescope (CAST)*, *Phys. Rev. Lett.* **94** (2005) 121301, [hep-ex/0411033].

[243] **PVLAS** Collaboration, E. Zavattini et al., *Experimental observation of optical rotation generated in vacuum by a magnetic field*, *Phys. Rev. Lett.* **96** (2006) 110406, [hep-ex/0507107]. [Erratum: Phys. Rev. Lett.99,129901(2007)].

[244] J. Redondo and A. Ringwald, *Light shining through walls*, *Contemp. Phys.* **52** (2011) 211–236, [arXiv:1011.3741].

[245] G. Ruoso et al., *Limits on light scalar and pseudoscalar particles from a photon regeneration experiment*, *Z. Phys.* **C56** (1992) 505–508.

[246] **OSQAR** Collaboration, P. Pugnat et al., *First results from the OSQAR photon regeneration experiment: No light shining through a wall*, *Phys. Rev.* **D78** (2008) 092003, [arXiv:0712.3362].

[247] F. Januschek, *Light-shining-through-walls with lasers*, in *10th Patras Workshop on Axions, WIMPs and WISPs (AXION-WIMP 2014) Geneva, Switzerland, June 29-July 4, 2014*, 2014. arXiv:1410.1633.

[248] G. G. Raffelt, *Stars as laboratories for fundamental physics*. 1996.

[249] M. Born, E. Wolf, and A. Bhatia, *Principles of Optics: Electromagnetic Theory of Propagation, Interference and Diffraction of Light*. Cambridge University Press, 1999.

[250] L. C. Garcia de Andrade, *Cosmic rotation axis, birefrigence and axions to detect primordial torsion fields*, hep-th/0110150.

[251] S. Villalba-Chávez, *Laser-driven search of axion-like particles including vacuum polarization effects*, *Nucl. Phys.* **B881** (2014) 391–413, [arXiv:1308.4033].

[252] A. Rubbia and A. Sakharov, *Polarization mesurements of gamma ray bursts and axion like particles*, in *Axions, WIMPs and WISPs. Proceedings, 4th Patras Workshop, PATRAS08, Hamburg, Germany, June 18-21, 2008*, pp. 65–68, 2008. arXiv:0809.0612.

[253] I. Antoniadis, A. Boyarsky, and O. Ruchayskiy, *Axion alternatives*, hep-ph/0606306.

[254] V. Dinu, T. Heinzl, A. Ilderton, M. Marklund, and G. Torgrimsson, *Photon polarization in light-by-light scattering: Finite size effects*, *Phys. Rev.* **D90** (2014), no. 4 045025, [arXiv:1405.7291].

[255] I. Antoniadis, A. Boyarsky, and O. Ruchayskiy, *Anomaly induced effects in a magnetic field*, *Nucl. Phys.* **B793** (2008) 246–259, [arXiv:0708.3001].

[256] M. Ahlers, H. Gies, J. Jaeckel, and A. Ringwald, *On the Particle Interpretation of the PVLAS Data: Neutral versus Charged Particles*, *Phys. Rev.* **D75** (2007) 035011, [hep-ph/0612098].

[257] A. Melchiorri, A. Polosa, and A. Strumia, *New bounds on millicharged particles from cosmology*, *Phys. Lett.* **B650** (2007) 416–420, [hep-ph/0703144].

[258] S. Davidson, S. Hannestad, and G. Raffelt, *Updated bounds on millicharged particles*, *JHEP* **05** (2000) 003, [hep-ph/0001179].

[259] **PVLAS** Collaboration, E. Zavattini et al., *New PVLAS results and limits on magnetically induced optical rotation and ellipticity in vacuum*, *Phys. Rev.* **D77** (2008) 032006, [arXiv:0706.3419].

[260] P. Brax, C. Burrage, and A.-C. Davis, *Shining Light on Modifications of Gravity*, *JCAP* **1210** (2012) 016, [arXiv:1206.1809].

[261] J. Jaeckel and A. Ringwald, *The Low-Energy Frontier of Particle Physics*, *Ann. Rev. Nucl. Part. Sci.* **60** (2010) 405–437, [arXiv:1002.0329].

[262] A. Dupays, E. Masso, J. Redondo, and C. Rizzo, *Light scalars coupled to photons and non-newtonian forces*, *Phys. Rev. Lett.* **98** (2007) 131802, [hep-ph/0610286].

[263] Y. Su, B. R. Heckel, E. G. Adelberger, J. H. Gundlach, M. Harris, G. L. Smith, and H. E. Swanson, *New tests of the universality of free fall*, *Phys. Rev.* **D50** (1994) 3614–3636.

[264] L. Perivolaropoulos, *Vacuum energy, the cosmological constant, and compact extra dimensions: Constraints from Casimir effect experiments*, *Phys. Rev.* **D77** (2008) 107301, [arXiv:0802.1531].

[265] G. Bressi, G. Carugno, R. Onofrio, and G. Ruoso, *Measurement of the Casimir force between parallel metallic surfaces*, *Phys. Rev. Lett.* **88** (2002) 041804, [quant-ph/0203002].

[266] C. D. Hoyle, D. J. Kapner, B. R. Heckel, E. G. Adelberger, J. H. Gundlach, U. Schmidt, and H. E. Swanson, *Sub-millimeter tests of the gravitational inverse-square law*, *Phys. Rev.* **D70** (2004) 042004, [hep-ph/0405262].

[267] E. G. Adelberger, B. R. Heckel, S. A. Hoedl, C. D. Hoyle, D. J. Kapner, and A. Upadhye, *Particle Physics Implications of a Recent Test of the Gravitational Inverse Sqaure Law*, *Phys. Rev. Lett.* **98** (2007) 131104, [hep-ph/0611223].

[268] S. M. Carroll, *Quintessence and the rest of the world*, *Phys. Rev. Lett.* **81** (1998) 3067–3070, [astro-ph/9806099].

[269] S. J. Landau and H. Vucetich, *Testing theories that predict time variation of fundamental constants*, *Astrophys. J.* **570** (2002) 463–469, [astro-ph/0005316].

[270] C. C. Davis, J. Harris, R. W. Gammon, I. I. Smolyaninov, and K. Cho, *Experimental Challenges Involved in Searches for Axion-Like Particles and Nonlinear Quantum Electrodynamic Effects by Sensitive Optical Techniques*, arXiv:0704.0748.

[271] J. Jaeckel, E. Masso, J. Redondo, A. Ringwald, and F. Takahashi, *The Need for purely laboratory-based axion-like particle searches*, *Phys. Rev.* **D75** (2007) 013004, [hep-ph/0610203].

[272] **OSQAR** Collaboration, M. Schott et al., *First Results of the Full-Scale OSQAR Photon Regeneration Experiment*, in *Photon 2011: International Conference On The Structure And Interactions Of The Photon and 19th International Workshop On Photon-Photon Collisions Spa, Belgium, May 22-27, 2011*, 2011. arXiv:1110.0774.

[273] R. Ballou et al., *Latest Results of the OSQAR Photon Regeneration Experiment for Axion-Like Particle Search*, in *10th Patras Workshop on Axions, WIMPs and WISPs (AXION-WIMP 2014) Geneva, Switzerland, June 29-July 4, 2014*, 2014. arXiv:1410.2566.

[274] **ALPS** Collaboration, K. Ehret et al., *Resonant laser power build-up in ALPS: A 'Light-shining-through-walls' experiment*, *Nucl. Instrum. Meth.* **A612** (2009) 83–96, [arXiv:0905.4159].

[275] **ALPS** Collaboration, K. Ehret, *The ALPS Light Shining Through a Wall Experiment - WISP Search in the Laboratory*, in *Proceedings, 45th Rencontres de Moriond on Electroweak Interactions and Unified Theories*, 2010. arXiv:1006.5741.

[276] K. Ehret et al., *New ALPS Results on Hidden-Sector Lightweights*, *Phys. Lett.* **B689** (2010) 149–155, [arXiv:1004.1313].

[277] A. Afanasev, O. K. Baker, K. B. Beard, G. Biallas, J. Boyce, M. Minarni, R. Ramdon, M. Shinn, and P. Slocum, *New Experimental limit on Optical Photon Coupling to Neutral, Scalar Bosons*, *Phys. Rev. Lett.* **101** (2008) 120401, [arXiv:0806.2631].

[278] **GammeV** Collaboration, A. S. Chou et al., *A Search for chameleon particles using a photon regeneration technique*, *Phys. Rev. Lett.* **102** (2009) 030402, [arXiv:0806.2438].

[279] M. Ahlers, A. Lindner, A. Ringwald, L. Schrempp, and C. Weniger, *Alpenglow - A Signature for Chameleons in Axion-Like Particle Search Experiments*, *Phys. Rev.* **D77** (2008) 015018, [arXiv:0710.1555].

[280] **GammeV** Collaboration, J. H. Steffen, *Constraints on chameleons and axion-like particles from the GammeV experiment*, *PoS* **IDM2008** (2008) 064, [arXiv:0810.5070].

[281] P. Brax, C. van de Bruck, A.-C. Davis, and D. Shaw, *Laboratory Tests of Chameleon Models*, in *Proceedings, 5th Patras Workshop on Axions, WIMPs and WISPs (AXION-WIMP 2009)*, pp. 151–154, 2009. arXiv:0911.1086.

[282] **ADMX** Collaboration, G. Rybka et al., *A Search for Scalar Chameleons with ADMX*, *Phys. Rev. Lett.* **105** (2010) 051801, [arXiv:1004.5160].

[283] **GammeV-CHASE** Collaboration, J. H. Steffen, *The CHASE laboratory search for chameleon dark energy*, *PoS* **ICHEP2010** (2010) 446, [arXiv:1011.3802].

[284] A. Upadhye, J. H. Steffen, and A. Weltman, *Constraining chameleon field theories using the GammeV afterglow experiments*, *Phys. Rev.* **D81** (2010) 015013, [arXiv:0911.3906].

[285] K. A. Bronnikov, V. N. Melnikov, S. G. Rubin, and I. V. Svadkovsky, *Nonlinear multidimensional gravity and the Australian dipole*, *Gen. Rel. Grav.* **45** (2013) 2509–2528, [arXiv:1301.3098].

[286] L. Perivolaropoulos, *Constraints on linear negative potentials in quintessence and phantom models from recent supernova data*, *Phys. Rev.* **D71** (2005) 063503, [astro-ph/0412308].

[287] R. Kallosh, J. Kratochvil, A. D. Linde, E. V. Linder, and M. Shmakova, *Observational bounds on cosmic doomsday*, *JCAP* **0310** (2003) 015, [astro-ph/0307185].

[288] A. Lykkas and L. Perivolaropoulos, *Scalar-Tensor Quintessence with a linear potential: Avoiding the Big Crunch cosmic doomsday*, *Phys. Rev.* **D93** (2016), no. 4 043513, [arXiv:1511.08732].

[289] K. A. Bronnikov, S. G. Rubin, and I. V. Svadkovsky, *Multidimensional world, inflation and modern acceleration*, *Phys. Rev.* **D81** (2010) 084010, [arXiv:0912.4862].

[290] K. A. Bronnikov and V. N. Melnikov, *Conformal frames and D-dimensional gravity*, in *International School of Cosmology and Gravitation: 18th Course: The Gravitational Constant: Generalized Gravitational Theories and Experiments: A NATO Advanced Study Institute Erice, Italy, April 30-May 10, 2003*, pp. 39–64, 2003. gr-qc/0310112.

[291] K. A. Bronnikov and V. N. Melnikov, *On observational predictions from multidimensional gravity*, *Gen. Rel. Grav.* **33** (2001) 1549–1578, [gr-qc/0103079].

[292] M. Pettini, A. E. Shapley, C. C. Steidel, J.-G. Cuby, M. Dickinson, A. F. M. Moorwood, K. L. Adelberger, and M. Giavalisco, *The Rest frame optical spectra of Lyman break galaxies: Star formation, extinction, abundances, and kinematics*, *Astrophys. J.* **554** (2001) 981–1000, [astro-ph/0102456].

[293] S. S. Vogt et al., *HIRES: the high-resolution echelle spectrometer on the Keck 10-m Telescope*, *Proc. SPIE Int. Soc. Opt. Eng.* **2198** (1994) 362.

[294] S. M. Faber et al., *The DEIMOS spectrograph for the Keck II Telescope: integration and testing*, *Proc. SPIE Int. Soc. Opt. Eng.* **4841** (1969) 1657–1669.

[295] M. Weber and W. de Boer, *Determination of the Local Dark Matter Density in our Galaxy*, *Astron. Astrophys.* **509** (2010) A25, [arXiv:0910.4272].

[296] **ADMX** Collaboration, S. J. Asztalos et al., *Experimental constraints on the axion dark matter halo density*, *Astrophys. J.* **571** (2002) L27–L30, [astro-ph/0104200].

[297] W. de Boer and M. Weber, *The Dark Matter Density in the Solar Neighborhood reconsidered*, *JCAP* **1104** (2011) 002, [arXiv:1011.6323].

[298] M. C. D. Marsh, *The Darkness of Spin-0 Dark Radiation*, *JCAP* **1501** (2015), no. 01 017, [arXiv:1407.2501].

[299] M. Giannotti, I. Irastorza, J. Redondo, and A. Ringwald, *Cool WISPs for stellar cooling excesses*, *JCAP* **1605** (2016), no. 05 057, [arXiv:1512.08108].

[300] **Particle Data Group** Collaboration, J. Beringer et al., *Review of Particle Physics (RPP)*, *Phys. Rev.* **D86** (2012) 010001.

[301] A. Payez, J. R. Cudell, and D. Hutsemekers, *Can axion-like particles explain the alignments of the polarisations of light from quasars?*, *Phys. Rev.* **D84** (2011) 085029, [arXiv:1107.2013].

[302] K. Zioutas et al., *Indirect signatures for axion(-like) particles*, *J. Phys. Conf. Ser.* **39** (2006) 103–106, [astro-ph/0603507].

[303] D. S. Gorbunov, G. G. Raffelt, and D. V. Semikoz, *Axion - like particles as ultrahigh-energy cosmic rays?*, *Phys. Rev.* **D64** (2001) 096005, [hep-ph/0103175].

[304] C. Burrage, A.-C. Davis, and D. J. Shaw, *Active Galactic Nuclei Shed Light on Axion-like-Particles*, *Phys. Rev. Lett.* **102** (2009) 201101, [arXiv:0902.2320].

[305] A. Payez, J. R. Cudell, and D. Hutsemekers, *Axions and polarisation of quasars*, *AIP Conf. Proc.* **1038** (2008) 211–219, [arXiv:0805.3946].

[306] K. Zioutas, M. Tsagri, Y. Semertzidis, T. Papaevangelou, T. Dafni, and V. Anastassopoulos, *Axion Searches with Helioscopes and astrophysical signatures for axion(-like) particles*, *New J. Phys.* **11** (2009) 105020, [arXiv:0903.1807].

[307] M. Fairbairn, T. Rashba, and S. V. Troitsky, *Photon-axion mixing and ultra-high-energy cosmic rays from BL Lac type objects - Shining light through the Universe*, *Phys. Rev.* **D84** (2011) 125019, [arXiv:0901.4085].

[308] K. A. Hochmuth and G. Sigl, *Effects of Axion-Photon Mixing on Gamma-Ray Spectra from Magnetized Astrophysical Sources*, *Phys. Rev.* **D76** (2007) 123011, [arXiv:0708.1144].

[309] P. Brax and C. Burrage, *Atomic Precision Tests and Light Scalar Couplings*, *Phys. Rev.* **D83** (2011) 035020, [arXiv:1010.5108].

[310] P. Brax and K. Zioutas, *Solar Chameleons*, *Phys. Rev.* **D82** (2010) 043007, [arXiv:1004.1846].

[311] A. Payez, C. Evoli, T. Fischer, M. Giannotti, A. Mirizzi, and A. Ringwald, *Revisiting the SN1987A gamma-ray limit on ultralight axion-like particles*, *JCAP* **1502** (2015), no. 02 006, [arXiv:1410.3747].

[312] C. Burrage, A.-C. Davis, and D. J. Shaw, *Detecting Chameleons: The Astronomical Polarization Produced by Chameleon-like Scalar Fields*, *Phys. Rev.* **D79** (2009) 044028, [arXiv:0809.1763].

[313] K. A. Olive and M. Pospelov, *Environmental dependence of masses and coupling constants*, *Phys. Rev.* **D77** (2008) 043524, [arXiv:0709.3825].

[314] K. Baker et al., *The quest for axions and other new light particles*, *Annalen Phys.* **525** (2013) A93–A99, [arXiv:1306.2841].

[315] A. Ringwald, *Axions and Axion-Like Particles*, in *Proceedings, 49th Rencontres de Moriond on Electroweak Interactions and Unified Theories*, pp. 223–230, 2014. arXiv:1407.0546.

[316] P. Hamilton, M. Jaffe, P. Haslinger, Q. Simmons, H. Müller, and J. Khoury, *Atom-interferometry constraints on dark energy*, *Science* **349** (2015) 849–851, [arXiv:1502.03888].

[317] L. Perivolaropoulos, *Sub-millimeter Spatial Oscillations of Newton's Constant: Theoretical Models and Laboratory Tests*, arXiv:1611.07293.

[318] C. P. L. Berry and J. R. Gair, *Linearized f(R) Gravity: Gravitational Radiation and Solar System Tests*, *Phys. Rev.* **D83** (2011) 104022, [arXiv:1104.0819]. [Erratum: Phys. Rev.D85,089906(2012)].

[319] S. Capozziello, A. Stabile, and A. Troisi, *A General solution in the Newtonian limit of f(R)-gravity*, *Mod. Phys. Lett.* **A24** (2009) 659–665, [arXiv:0901.0448].

[320] M. Hohmann, L. Jarv, P. Kuusk, and E. Randla, *Post-Newtonian parameters γ and β of scalar-tensor gravity with a general potential*, *Phys. Rev.* **D88** (2013), no. 8 084054, [arXiv:1309.0031]. [Erratum: Phys. Rev.D89,no.6,069901(2014)].

[321] L. Perivolaropoulos and C. Sourdis, *Cosmological effects of radion oscillations*, *Phys. Rev.* **D66** (2002) 084018, [hep-ph/0204155].

[322] A. Kehagias and K. Sfetsos, *Deviations from the 1/r**2 Newton law due to extra dimensions*, *Phys. Lett.* **B472** (2000) 39–44, [hep-ph/9905417].

[323] V. P. Frolov and A. Zelnikov, *Head-on collision of ultrarelativistic particles in ghost-free theories of gravity*, *Phys. Rev.* **D93** (2016), no. 6 064048, [arXiv:1509.03336].

[324] A. Kehagias and M. Maggiore, *Spherically symmetric static solutions in a nonlocal infrared modification of General Relativity*, *JHEP* **08** (2014) 029, [arXiv:1401.8289].

[325] A. D. Rider, D. C. Moore, C. P. Blakemore, M. Louis, M. Lu, and G. Gratta, *Search for Screened Interactions Associated with Dark Energy Below the 100 μm Length Scale*, *Phys. Rev. Lett.* **117** (2016), no. 10 101101, [arXiv:1604.04908].

[326] P. Brax, C. van de Bruck, A.-C. Davis, and D. J. Shaw, *f(R) Gravity and Chameleon Theories*, *Phys. Rev.* **D78** (2008) 104021, [arXiv:0806.3415].

[327] R. Gannouji, B. Moraes, D. F. Mota, D. Polarski, S. Tsujikawa, and H. A. Winther, *Chameleon dark energy models with characteristic signatures*, *Phys. Rev.* **D82** (2010) 124006, [arXiv:1010.3769].

[328] J. Khoury, *Chameleon Field Theories*, *Class. Quant. Grav.* **30** (2013) 214004, [arXiv:1306.4326].

[329] C. Burrage and J. Sakstein, *A Compendium of Chameleon Constraints*, *JCAP* **1611** (2016), no. 11 045, [arXiv:1609.01192].

[330] K. Koyama, *Cosmological Tests of Modified Gravity*, *Rept. Prog. Phys.* **79** (2016), no. 4 046902, [arXiv:1504.04623].

[331] S. Rahvar and B. Mashhoon, *Observational Tests of Nonlocal Gravity: Galaxy Rotation Curves and Clusters of Galaxies*, *Phys. Rev.* **D89** (2014) 104011, [arXiv:1401.4819].

[332] M. Bordag, U. Mohideen, and V. M. Mostepanenko, *New developments in the Casimir effect*, *Phys. Rept.* **353** (2001) 1–205, [quant-ph/0106045].

[333] G. L. Klimchitskaya, U. Mohideen, and V. M. Mostepanenko, *The Casimir force between real materials: Experiment and theory*, *Rev. Mod. Phys.* **81** (2009) 1827–1885, [arXiv:0902.4022].

[334] K. A. Milton, *The Casimir effect: Recent controversies and progress*, *J. Phys.* **A37** (2004) R209, [hep-th/0406024].

[335] D. J. Kapner, T. S. Cook, E. G. Adelberger, J. H. Gundlach, B. R. Heckel, C. D. Hoyle, and H. E. Swanson, *Tests of the gravitational inverse-square law below the dark-energy length scale*, *Phys. Rev. Lett.* **98** (2007) 021101, [hep-ph/0611184].

[336] E. Fischbach and C. L. Talmadge, *The search for nonNewtonian gravity*. 1999.

[337] E. G. Adelberger, B. R. Heckel, C. W. Stubbs, and W. F. Rogers, *Searches for new macroscopic forces*, *Ann. Rev. Nucl. Part. Sci.* **41** (1991) 269–320.

[338] E. G. Adelberger, B. R. Heckel, and A. E. Nelson, *Tests of the gravitational inverse square law*, *Ann. Rev. Nucl. Part. Sci.* **53** (2003) 77–121, [hep-ph/0307284].

[339] J. Chiaverini, S. J. Smullin, A. A. Geraci, D. M. Weld, and A. Kapitulnik, *New experimental constraints on nonNewtonian forces below 100 microns*, *Phys. Rev. Lett.* **90** (2003) 151101, [hep-ph/0209325].

[340] J. C. Long, H. W. Chan, A. B. Churnside, E. A. Gulbis, M. C. M. Varney, and J. C. Price, *Upper limits to submillimeter-range forces from extra space-time dimensions*, hep-ph/0210004. [Nature421,922(2003)].

[341] J. K. Hoskins, R. D. Newman, R. Spero, and J. Schultz, *Experimental tests of the gravitational inverse square law for mass separations from 2-cm to 105-cm*, *Phys. Rev.* **D32** (1985) 3084–3095.

[342] R. Spero, J. K. Hoskins, R. Newman, J. Pellam, and J. Schultz, *Test of the Gravitational Inverse-Square Law at Laboratory Distances*, *Phys. Rev. Lett.* **44** (1980) 1645–1648.

[343] M. V. Moody and H. J. Paik, *Gauss's law test of gravity at short range*, *Phys. Rev. Lett.* **70** (1993) 1195–1198.

[344] K. Kuroda and H. Hirakawa, *Experimental test of the law of gravitation*, *Phys. Rev.* **D32** (1985), no. 2 342.

[345] H. A. Chan, M. V. Moody, and H. J. Paik, *Null Test of the Gravitational Inverse Square Law*, *Phys. Rev. Lett.* **49** (1982) 1745–1748.

[346] E. G. Adelberger, J. H. Gundlach, B. R. Heckel, S. Hoedl, and S. Schlamminger, *Torsion balance experiments: A low-energy frontier of particle physics*, *Prog. Part. Nucl. Phys.* **62** (2009) 102–134.

[347] S. J. Smullin, A. A. Geraci, D. M. Weld, J. Chiaverini, S. P. Holmes, and A. Kapitulnik, *New constraints on Yukawa-type deviations from Newtonian gravity at 20 microns*, *Phys. Rev.* **D72** (2005) 122001, [hep-ph/0508204]. [Erratum: Phys. Rev.D72,129901(2005)].

[348] A. A. Geraci, S. J. Smullin, D. M. Weld, J. Chiaverini, and A. Kapitulnik, *Improved constraints on non-Newtonian forces at 10 microns*, *Phys. Rev.* **D78** (2008) 022002, [arXiv:0802.2350].

[349] S. K. Lamoreaux, *Demonstration of the Casimir force in the 0.6 to 6 micrometers range*, *Phys. Rev. Lett.* **78** (1997) 5–8. [Erratum: Phys. Rev. Lett.81,5475(1998)].

[350] A. O. Barvinsky, *Dark energy and dark matter from nonlocal ghost-free gravity theory*, *Phys. Lett.* **B710** (2012) 12–16, [arXiv:1107.1463].

[351] T. Li, S. Kheifets, and M. G. Raizen, *Millikelvin cooling of an optically trapped microsphere in vacuum*, *Nature Phys.* **7** (2011) 527–530, [arXiv:1101.1283].

[352] A. A. Geraci, S. B. Papp, and J. Kitching, *Short-range force detection using optically-cooled levitated microspheres*, *Phys. Rev. Lett.* **105** (2010) 101101, [arXiv:1006.0261].

[353] D. C. Moore, A. D. Rider, and G. Gratta, *Search for Millicharged Particles Using Optically Levitated Microspheres*, *Phys. Rev. Lett.* **113** (2014), no. 25 251801, [arXiv:1408.4396].

[354] L. Järv, P. Kuusk, M. Saal, and O. Vilson, *Invariant quantities in the scalar-tensor theories of gravitation*, *Phys. Rev.* **D91** (2015), no. 2 024041, [arXiv:1411.1947].

[355] S. Nojiri and S. D. Odintsov, *Newton potential in deSitter brane world*, *Phys. Lett.* **B548** (2002) 215–223, [hep-th/0209066].

[356] A. Donini and S. G. Marimón, *Micro-orbits in a many-brane model and deviations from Newton's $1/r^2$ law*, *Eur. Phys. J.* **C76** (2016), no. 12 696, [arXiv:1609.05654].

[357] R. Benichou and J. Estes, *The Fate of Newton's Law in Brane-World Scenarios*, *Phys. Lett.* **B712** (2012) 456–459, [arXiv:1112.0565].

[358] K. A. Bronnikov, S. A. Kononogov, and V. N. Melnikov, *Brane world corrections to Newton's law*, *Gen. Rel. Grav.* **38** (2006) 1215–1232, [gr-qc/0601114].

[359] B. Guo, Y.-X. Liu, and K. Yang, *Brane worlds in gravity with auxiliary fields*, *Eur. Phys. J.* **C75** (2015), no. 2 63, [arXiv:1405.0074].

[360] M. Kaminski, K. Landsteiner, J. Mas, J. P. Shock, and J. Tarrio, *Holographic Operator Mixing and Quasinormal Modes on the Brane*, *JHEP* **02** (2010) 021, [arXiv:0911.3610].

[361] G. O. Schellstede, *On the Newtonian limit of metric f(R) gravity*, *Gen. Rel. Grav.* **48** (2016), no. 9 118.

[362] N. Arkani-Hamed, S. Dimopoulos, and G. R. Dvali, *The Hierarchy problem and new dimensions at a millimeter*, *Phys. Lett.* **B429** (1998) 263–272, [hep-ph/9803315].

[363] N. Arkani-Hamed, S. Dimopoulos, and G. R. Dvali, *Phenomenology, astrophysics and cosmology of theories with submillimeter dimensions and TeV scale quantum gravity*, *Phys. Rev.* **D59** (1999) 086004, [hep-ph/9807344].

[364] I. Antoniadis, N. Arkani-Hamed, S. Dimopoulos, and G. R. Dvali, *New dimensions at a millimeter to a Fermi and superstrings at a TeV*, *Phys. Lett.* **B436** (1998) 257–263, [hep-ph/9804398].

[365] E. G. Floratos and G. K. Leontaris, *Low scale unification, Newton's law and extra dimensions*, *Phys. Lett.* **B465** (1999) 95–100, [hep-ph/9906238].

[366] D. F. Mota and D. J. Shaw, *Strongly coupled chameleon fields: New horizons in scalar field theory*, *Phys. Rev. Lett.* **97** (2006) 151102, [hep-ph/0606204].

[367] C. Burrage, E. J. Copeland, and E. A. Hinds, *Probing Dark Energy with Atom Interferometry*, *JCAP* **1503** (2015), no. 03 042, [arXiv:1408.1409].

[368] J. Edholm, A. S. Koshelev, and A. Mazumdar, *Behavior of the Newtonian potential for ghost-free gravity and singularity-free gravity*, *Phys. Rev.* **D94** (2016), no. 10 104033, [arXiv:1604.01989].

[369] A. Conroy, T. Koivisto, A. Mazumdar, and A. Teimouri, *Generalized quadratic curvature, non-local infrared modifications of gravity and Newtonian potentials*, *Class. Quant. Grav.* **32** (2015), no. 1 015024, [arXiv:1406.4998].

[370] A. Conroy and J. Edholm, *Newtonian Potential and Geodesic Completeness in Infinite Derivative Gravity*, arXiv:1705.02382.

[371] P. Burikham, T. Harko, and M. J. Lake, *The QCD mass gap and quark deconfinement scales as mass bounds in strong gravity*, arXiv:1705.11174.

[372] M. J. Lake, *Is there a connection between "dark" and "light" physics?*, in *IF-YITP GR+HEP+Cosmo International Symposium VI Phitsanulok, Thailand, August 3-5, 2016*, 2017. arXiv:1707.07563.

[373] L. Modesto and L. Rachwal, *Nonlocal quantum gravity: A review*, *Int. J. Mod. Phys.* **D26** (2017) 1730020.

[374] L. Amendola, N. Burzilla, and H. Nersisyan, *Quantum Gravity inspired nonlocal gravity model*, arXiv:1707.04628.

[375] A. Conroy, *Infinite Derivative Gravity: A Ghost and Singularity-free Theory*. PhD thesis, Lancaster U., 2017. arXiv:1704.07211.

[376] A. S. Koshelev and A. Mazumdar, *Absence of event horizon in massive compact objects in infinite derivative gravity*, arXiv:1707.00273.

[377] G. Calcagni and L. Modesto, *Stability of Schwarzschild singularity in non-local gravity*, arXiv:1707.01119.

[378] S. Talaganis and A. Teimouri, *Hamiltonian Analysis for Infinite Derivative Field Theories and Gravity*, arXiv:1701.01009.

[379] L. Buoninfante, *Ghost and singularity free theories of gravity*, arXiv:1610.08744.

[380] B. L. Giacchini, *On the cancellation of Newtonian singularities in higher-derivative gravity*, *Phys. Lett.* **B766** (2017) 306–311, [arXiv:1609.05432].

[381] A. Accioly, B. L. Giacchini, and I. L. Shapiro, *On the gravitational seesaw in higher-derivative gravity*, arXiv:1604.07348.

[382] Y. Dirian, S. Foffa, M. Kunz, M. Maggiore, and V. Pettorino, *Non-local gravity and comparison with observational datasets*, *JCAP* **1504** (2015), no. 04 044, [arXiv:1411.7692].

[383] Y. Dirian, S. Foffa, M. Kunz, M. Maggiore, and V. Pettorino, *Non-local gravity and comparison with observational datasets. II. Updated results and Bayesian model comparison with ΛCDM*, *JCAP* **1605** (2016), no. 05 068, [arXiv:1602.03558].

[384] M. Maggiore and M. Mancarella, *Nonlocal gravity and dark energy*, *Phys. Rev.* **D90** (2014), no. 2 023005, [arXiv:1402.0448].

[385] V. Vardanyan, Y. Akrami, L. Amendola, and A. Silvestri, *On nonlocally interacting metrics, and a simple proposal for cosmic acceleration*, arXiv:1702.08908.

[386] S. Park and A. Shafieloo, *Growth of perturbations in nonlocal gravity with non-ΛCDM background*, *Phys. Rev.* **D95** (2017), no. 6 064061, [arXiv:1608.02541].

[387] L. Feng, *Light bending in infinite derivative theories of gravity*, *Phys. Rev.* **D95** (2017), no. 8 084015, [arXiv:1703.06535].

[388] H.-N. Lin, J. Li, and X. Li, *Testing the anisotropy of the universe using the simulated gravitational wave events from advanced LIGO and Virgo*, *Eur. Phys. J.* **C78** (2018), no. 5 356, [arXiv:1802.00642].

[389] **LIGO Scientific, Virgo, 1M2H, Dark Energy Camera GW-E, DES, DLT40, Las Cumbres Observatory, VINROUGE, MASTER** Collaboration, B. P. Abbott et al., *A gravitational-wave standard siren measurement of the Hubble constant*, *Nature* **551** (2017), no. 7678 85–88, [arXiv:1710.05835].

[390] S. B. Giddings, S. Koren, and G. Treviño, *Exploring strong-field deviations from general relativity via gravitational waves*, arXiv:1904.04258.

[391] A. Maselli, S. Marassi, V. Ferrari, K. Kokkotas, and R. Schneider, *Constraining modified theories of gravity with gravitational wave stochastic background*, arXiv:1606.04996.

[392] M. Dominik, K. Belczynski, C. Fryer, D. Holz, E. Berti, T. Bulik, I. Mandel, and R. O'Shaughnessy, *Double Compact Objects I: The Significance of the Common Envelope on Merger Rates*, *Astrophys. J.* **759** (2012) 52, [arXiv:1202.4901].

[393] M. Dominik, E. Berti, R. O'Shaughnessy, I. Mandel, K. Belczynski, C. Fryer, D. Holz, T. Bulik, and F. Pannarale, *Double Compact Objects III: Gravitational Wave Detection Rates*, *Astrophys. J.* **806** (2015), no. 2 263, [arXiv:1405.7016].

[394] **Virgo, LIGO Scientific** Collaboration, B. P. Abbott et al., *GW150914: Implications for the stochastic gravitational wave background from binary black holes*, *Phys. Rev. Lett.* **116** (2016), no. 13 131102, [arXiv:1602.03847].

[395] **LIGO Scientific, Virgo** Collaboration, B. P. Abbott et al., *Searches for Continuous Gravitational Waves from Fifteen Supernova Remnants and Fomalhaut b with Advanced LIGO*, arXiv:1812.11656.

[396] T. Nakama and T. Suyama, *Primordial black holes as a novel probe of primordial gravitational waves*, *Phys. Rev.* **D92** (2015), no. 12 121304, [arXiv:1506.05228].

[397] T. Nakama and T. Suyama, *Primordial black holes as a novel probe of primordial gravitational waves II: detailed analysis*, arXiv:1605.04482.

[398] A. A. Starobinsky, *Spectrum of relict gravitational radiation and the early state of the universe*, *JETP Lett.* **30** (1979) 682–685. [Pisma Zh. Eksp. Teor. Fiz.30,719(1979)].

[399] L. F. Abbott and D. D. Harari, *Graviton Production in Inflationary Cosmology*, *Nucl. Phys.* **B264** (1986) 487–492.

[400] J. F. Dufaux, A. Bergman, G. N. Felder, L. Kofman, and J.-P. Uzan, *Theory and Numerics of Gravitational Waves from Preheating after Inflation*, *Phys. Rev.* **D76** (2007) 123517, [arXiv:0707.0875].

[401] B. Allen, *The Stochastic Gravity Wave Background in Inflationary Universe Models*, *Phys. Rev.* **D37** (1988) 2078.

[402] A. B. Henriques, *The stochastic gravitational - wave background and the inflation to radiation transition in the early universe*, *Class. Quant. Grav.* **21** (2004) 3057, [astro-ph/0309508]. [Erratum: Class. Quant. Grav.24,6431(2007)].

[403] **Supernova Cosmology Project** Collaboration, S. Perlmutter et al., *Measurements of Omega and Lambda from 42 high redshift supernovae*, *Astrophys. J.* **517** (1999) 565–586, [astro-ph/9812133].

[404] Y. Zhang, Y. Yuan, W. Zhao, and Y.-T. Chen, *Relic gravitational waves in the accelerating Universe*, *Class. Quant. Grav.* **22** (2005) 1383–1394, [astro-ph/0501329].

[405] G. Izquierdo and D. Pavon, *Relic gravitational waves and present accelerated expansion*, *Phys. Rev.* **D70** (2004) 084034, [astro-ph/0409364].

[406] L. P. Grishchuk, *Amplification of gravitational waves in an istropic universe*, *Sov. Phys. JETP* **40** (1975) 409–415. [Zh. Eksp. Teor. Fiz.67,825(1974)].

[407] W. Zhao, *Improved calculation of relic gravitational waves*, *Chin. Phys.* **16** (2007) 2894–2902, [gr-qc/0612041].

[408] M. L. Sosa Almazan and G. Izquierdo, *Late evolution of relic gravitational waves in coupled dark energy models*, *Gen. Rel. Grav.* **46** (2014) 1759, [arXiv:1312.0566].

[409] V. Balek and V. Polak, *Group velocity of gravitational waves in an expanding universe*, *Gen. Rel. Grav.* **41** (2009) 505–524, [arXiv:0707.1513].

[410] L.Brillouin, *Wave Propagation Group Velocity*. Academic,NY, 1960.

[411] J. C. Fabris and S. V. de Borba Goncalves, *Gravitational waves in an expanding universe*, gr-qc/9808007.

[412] G. A. Alekseev and J. B. Griffiths, *Propagation and interaction of gravitational waves in some expanding backgrounds*, *Phys. Rev.* **D52** (1995) 4497–4502.

[413] G. E. Tauber, *GRAVITATIONAL WAVES IN AN EXPANDING UNIVERSE*, *Found. Phys.* **14** (1984) 1169–1183.

[414] P. C. Waylen, *Gravitational Waves in an Expanding Universe*, *Proc. Roy. Soc. Lond.* **A362** (1978) 245–250.

[415] D. Tamayo, J. A. S. Lima, and D. F. A. Bessada, *Primordial Gravitational Waves Production in Running Vacuum Cosmologies*, arXiv:1503.06110.

[416] G. Izquierdo Saez, *Relic gravitational waves in the expanding Universe*. PhD thesis, Barcelona, Autonoma U., 2005. gr-qc/0601050.

[417] J. Hartnett and M. Tobar, *Properties of gravitational waves in an expanding universe*, in *In *Carmeli, M. (ed.): Relativity: Modern large-scale spacetime structure of the cosmos* 283-295*, 2008.

[418] J. C. Jackson, *Fingers of God: A critique of Rees' theory of primoridal gravitational radiation*, *Mon. Not. Roy. Astron. Soc.* **156** (1972) 1P–5P, [arXiv:0810.3908].

[419] T. Ikeda, C.-M. Yoo, and Y. Nambu, *Expanding universe with nonlinear gravitational waves*, *Phys. Rev.* **D92** (2015), no. 4 044041, [arXiv:1505.02959].

[420] D. Su and Y. Zhang, *Energy Momentum Pseudo-Tensor of Relic Gravitational Wave in Expanding Universe*, *Phys. Rev.* **D85** (2012) 104012, [arXiv:1204.0089].

[421] G. A. Alekseev, *Collision of strong gravitational and electromagnetic waves in the expanding universe*, *Phys. Rev.* **D93** (2016), no. 6 061501, [arXiv:1511.03335].

[422] J. P. Baptista and D. Gerbal, *DISPERSION RELATIONS FOR ZERO HELICITY GRAVITATIONAL WAVES IN A RELATIVISTIC EXPANDING MEDIUM*, *J. Phys.* **A15** (1982) 3351–3365.

[423] Ya. B. Zeldovich, *My universe: Selected reviews*. 1992.

[424] G. C. McVittie, *The mass-particle in an expanding universe*, *Mon. Not. Roy. Astron. Soc.* **93** (1933) 325–339.

[425] H. Stephani, D. Kramer, M. MacCallum, C. Hoenselaers, and E. Herlt, *Exact Solutions of Einstein's Field Equations*. Cambridge University Press, second ed., 2003. Cambridge Books Online.

[426] V. Faraoni and A. Jacques, *Cosmological expansion and local physics*, *Phys. Rev.* **D76** (2007) 063510, [arXiv:0707.1350].

[427] B. C. Nolan, *Particle and photon orbits in McVittie spacetimes*, *Class. Quant. Grav.* **31** (2014), no. 23 235008, [arXiv:1408.0044].

[428] E. Schluessel, *Propagation of gravitational waves in a universe with slowly-changing equation of state*, arXiv:1406.4526.

[429] Y. Zhang, X. Z. Er, T. Y. Xia, W. Zhao, and H. X. Miao, *Exact Analytic Spectrum of Relic Gravitational Waves in Accelerating Universe*, *Class. Quant. Grav.* **23** (2006) 3783–3800, [astro-ph/0604456].

[430] S. Nesseris and L. Perivolaropoulos, *A Comparison of cosmological models using recent supernova data*, *Phys. Rev.* **D70** (2004) 043531, [astro-ph/0401556].

[431] S. Koh, *Relic gravitational wave spectrum, the trans-Planckian physics and Horava-Lifshitz gravity*, *Class. Quant. Grav.* **27** (2010) 225015, [arXiv:0907.0850].

[432] C. Corda, *Information on the inflaton field from the spectrum of relic gravitational waves*, *Gen. Rel. Grav.* **42** (2010) 1323–1333, [arXiv:0909.4133]. [Erratum: Gen. Rel. Grav.42,1335(2010)].

[433] L. P. Grishchuk, *Discovering Relic Gravitational Waves in Cosmic Microwave Background Radiation*, arXiv:0707.3319.

[434] Y. Zhang, W. Zhao, T. Y. Xia, X. Z. Er, and H. X. Miao, *Relic Gravitational Waves And CMB Polarization In The Accelerating Universe*, *Int. J. Mod. Phys.* **D17** (2008) 1105–1123, [arXiv:0806.2243].

[435] G. Gogoberidze, T. Kahniashvili, and A. Kosowsky, *The Spectrum of Gravitational Radiation from Primordial Turbulence*, *Phys. Rev.* **D76** (2007) 083002, [arXiv:0705.1733].

[436] A. Buonanno, M. Maggiore, and C. Ungarelli, *Spectrum of relic gravitational waves in string cosmology*, *Phys. Rev.* **D55** (1997) 3330–3336, [gr-qc/9605072].

[437] N. Said, C. Baccigalupi, M. Martinelli, A. Melchiorri, and A. Silvestri, *New Constraints On The Dark Energy Equation of State*, *Phys. Rev.* **D88** (2013) 043515, [arXiv:1303.4353].

[438] **Planck** Collaboration, P. A. R. Ade et al., *Planck 2015 results. XIV. Dark energy and modified gravity*, *Astron. Astrophys.* **594** (2016) A14, [arXiv:1502.01590].

[439] W. Zheng, S.-Y. Li, H. Li, J.-Q. Xia, M. Li, and T. Lu, *Constraints on Dark Energy from New Observations including Pan-STARRS*, *JCAP* **1408** (2014) 030, [arXiv:1405.2724]. [Erratum: JCAP1409,E01(2014)].

[440] E. Piedipalumbo, E. Della Moglie, M. De Laurentis, and P. Scudellaro, *High Redshift Investigation On The Dark Energy Equation of State*, *Mon. Not. Roy. Astron. Soc.* **441** (2014), no. 4 3643–3655, [arXiv:1311.0995].

[441] V. B. Johri, *Phantom cosmologies*, *Phys. Rev.* **D70** (2004) 041303, [astro-ph/0311293].

[442] R. R. Caldwell, M. Kamionkowski, and N. N. Weinberg, *Phantom energy and cosmic doomsday*, *Phys. Rev. Lett.* **91** (2003) 071301, [astro-ph/0302506].

[443] S. Nojiri, S. D. Odintsov, and S. Tsujikawa, *Properties of singularities in (phantom) dark energy universe*, *Phys. Rev.* **D71** (2005) 063004, [hep-th/0501025].

[444] L. P. Chimento and R. Lazkoz, *On big rip singularities*, *Mod. Phys. Lett.* **A19** (2004) 2479–2484, [gr-qc/0405020].

[445] C. Cattoen and M. Visser, *Necessary and sufficient conditions for big bangs, bounces, crunches, rips, sudden singularities, and extremality events*, *Class. Quant. Grav.* **22** (2005) 4913–4930, [gr-qc/0508045].

[446] R. Nandra, A. Lasenby, and M. Hobson, *Dynamics of a spherical object of uniform density in an expanding universe*, *Phys. Rev.* **D88** (2013), no. 4 044041, [arXiv:1307.0526].

[447] C. Gao, X. Chen, Y.-G. Shen, and V. Faraoni, *Black Holes in the Universe: Generalized Lemaitre-Tolman-Bondi Solutions*, *Phys. Rev.* **D84** (2011) 104047, [arXiv:1110.6708].

[448] R. Nandra, A. N. Lasenby, and M. P. Hobson, *The effect of an expanding universe on massive objects*, *Mon. Not. Roy. Astron. Soc.* **422** (2012) 2945–2959, [arXiv:1104.4458].

[449] R. Moradi, J. T. Firouzjaee, and R. Mansouri, *Cosmological black holes: the spherical perfect fluid collapse with pressure in a FRW background*, *Class. Quant. Grav.* **32** (2015), no. 21 215001, [arXiv:1504.04746].

[450] A. Einstein and E. G. Straus, *The influence of the expansion of space on the gravitation fields surrounding the individual stars*, *Rev. Mod. Phys.* **17** (1945) 120–124.

[451] G. A. Baker, Jr., *Effects on the structure of the universe of an accelerating expansion*, astro-ph/0112320.

[452] J. E. Pringle, *Accretion discs in astrophysics*, *Ann. Rev. Astron. Astrophys.* **19** (1981) 137–160.

[453] M. A. Abramowicz and P. C. Fragile, *Foundations of Black Hole Accretion Disk Theory*, *Living Rev. Rel.* **16** (2013) 1, [arXiv:1104.5499].

[454] R. H. Price, *In an expanding universe, what doesn't expand?*, gr-qc/0508052.

[455] V. Pavlidou and T. N. Tomaras, *Where the world stands still: turnaround as a strong test of ΛCDM cosmology*, *JCAP* **1409** (2014) 020, [arXiv:1310.1920].

[456] M. D. Hartl, *Dynamics of spinning test particles in Kerr space-time*, *Phys. Rev.* **D67** (2003) 024005, [gr-qc/0210042].

[457] Y. N. Obukhov, A. J. Silenko, and O. V. Teryaev, *Spin in an arbitrary gravitational field*, *Phys. Rev.* **D88** (2013) 084014, [arXiv:1308.4552].

[458] K. P. Tod, F. de Felice, and M. Calvani, *Spinning test particles in the field of a black hole*, *Nuovo Cim.* **B34** (1976) 365.

[459] O. Semerak, *Spinning test particles in a Kerr field. 1.*, *Mon. Not. Roy. Astron. Soc.* **308** (1999) 863–875.

[460] I. B. Khriplovich, *Spinning Relativistic Particles in External Fields*, arXiv:0801.1881.

[461] G. Lukes-Gerakopoulos, *Spinning particles moving around black holes: integrability and chaos*, in *Proceedings, 14th Marcel Grossmann Meeting on Recent Developments in Theoretical and Experimental General Relativity, Astrophysics, and Relativistic Field Theories (MG14) (In 4 Volumes): Rome, Italy, July 12-18, 2015*, vol. 2, pp. 1960–1965, 2017. arXiv:1606.09430.

[462] L. F. O. Costa, J. Natário, and M. Zilhao, *Spacetime dynamics of spinning particles: Exact electromagnetic analogies*, *Phys. Rev.* **D93** (2016), no. 10 104006, [arXiv:1207.0470].

[463] L. M. Burko, *Orbital evolution of a particle around a black hole. 2. Comparison of contributions of spin orbit coupling and the selfforce*, *Phys. Rev.* **D69** (2004) 044011, [gr-qc/0308003].

[464] M. Shibata, *Gravitational waves induced by a particle orbiting around a rotating black hole: spin orbit interaction effect*, *Phys. Rev.* **D48** (1993) 663–666.

[465] W.-B. Han and S.-C. Yang, *Exotic orbits due to spin–spin coupling around Kerr black holes*, *Int. J. Mod. Phys.* **D27** (2017), no. 01 1750179, [arXiv:1610.01534].

[466] S. Suzuki and K.-i. Maeda, *Signature of chaos in gravitational waves from a spinning particle*, *Phys. Rev.* **D61** (2000) 024005, [gr-qc/9910064].

[467] D. Kubiznak and M. Cariglia, *On Integrability of spinning particle motion in higher-dimensional black hole spacetimes*, *Phys. Rev. Lett.* **108** (2012) 051104, [arXiv:1110.0495].

[468] J. K. Kao and H. T. Cho, *The Onset of chaotic motion of a spinning particle around the Schwarzchild black hole*, *Phys. Lett.* **A336** (2005) 159–166, [gr-qc/0406101].

[469] M. Saijo, K.-i. Maeda, M. Shibata, and Y. Mino, *Gravitational waves from a spinning particle plunging into a Kerr black hole*, *Phys. Rev.* **D58** (1998) 064005.

[470] T. Tanaka, Y. Mino, M. Sasaki, and M. Shibata, *Gravitational waves from a spinning particle in circular orbits around a rotating black hole*, *Phys. Rev.* **D54** (1996) 3762–3777, [gr-qc/9602038].

[471] Y. Mino, M. Shibata, and T. Tanaka, *Gravitational waves induced by a spinning particle falling into a rotating black hole*, *Phys. Rev.* **D53** (1996) 622–634. [Erratum: Phys. Rev.D59,047502(1999)].

[472] E. Harms, G. Lukes-Gerakopoulos, S. Bernuzzi, and A. Nagar, *Spinning test body orbiting around a Schwarzschild black hole: Circular dynamics and gravitational-wave fluxes*, *Phys. Rev.* **D94** (2016), no. 10 104010, [arXiv:1609.00356].

[473] N. Kaloper, M. Kleban, and D. Martin, *McVittie's Legacy: Black Holes in an Expanding Universe*, *Phys. Rev.* **D81** (2010) 104044, [arXiv:1003.4777].

[474] A. Papapetrou, *Spinning test particles in general relativity. 1.*, *Proc. Roy. Soc. Lond.* **A209** (1951) 248–258.

[475] M. Mathisson, *Neue mechanik materieller systemes*, *Acta Phys. Polon.* **6** (1937) 163–2900.

[476] W. G. Dixon, *A covariant multipole formalism for extended test bodies in general relativity*, *Il Nuovo Cimento (1955-1965)* **34** (Oct, 1964) 317–339.

[477] W. G. Dixon, *Dynamics of extended bodies in general relativity. I. Momentum and angular momentum*, *Proc. Roy. Soc. Lond.* **A314** (1970) 499–527.

[478] E. Barausse, E. Racine, and A. Buonanno, *Hamiltonian of a spinning test-particle in curved spacetime*, *Phys. Rev.* **D80** (2009) 104025, [arXiv:0907.4745]. [Erratum: Phys. Rev.D85,069904(2012)].

[479] D. Kunst, T. Ledvinka, G. Lukes-Gerakopoulos, and J. Seyrich, *Comparing Hamiltonians of a spinning test particle for different tetrad fields*, *Phys. Rev.* **D93** (2016), no. 4 044004, [arXiv:1506.01473].

[480] H. T. Cho, *PostNewtonian approximation for spinning particles*, *Class. Quant. Grav.* **15** (1998) 2465–2478, [gr-qc/9703071].

[481] R. A. Porto, *Post-Newtonian corrections to the motion of spinning bodies in NRGR*, *Phys. Rev.* **D73** (2006) 104031, [gr-qc/0511061].

[482] T. A. Apostolatos, *A spinning test body in the strong field of a schwarzschild black hole*, *Classical and Quantum Gravity* **13** (1996), no. 5 799.

[483] C. Chicone, B. Mashhoon, and B. Punsly, *Relativistic motion of spinning particles in a gravitational field*, *Phys. Lett.* **A343** (2005) 1–7, [gr-qc/0504146].

[484] J. Steinhoff, *Canonical formulation of spin in general relativity*, *Annalen Phys.* **523** (2011) 296–353, [arXiv:1106.4203].

[485] W. G. Dixon, *The definition of multipole moments for extended bodies*, *General Relativity and Gravitation* **4** (Jun, 1973) 199–209.

[486] B. Mashhoon and D. Singh, *Dynamics of Extended Spinning Masses in a Gravitational Field*, *Phys. Rev.* **D74** (2006) 124006, [astro-ph/0608278].

[487] J. Vines, D. Kunst, J. Steinhoff, and T. Hinderer, *Canonical Hamiltonian for an extended test body in curved spacetime: To quadratic order in spin*, *Phys. Rev.* **D93** (2016), no. 10 103008, [arXiv:1601.07529].

[488] M. Roshan, *Test particle motion in modified gravity theories*, *Phys. Rev.* **D87** (2013), no. 4 044005, [arXiv:1210.3136].

[489] R. Plyatsko and O. Stefanyshyn, *Mathisson Equations: Non-Oscillatory Solutions in a Schwarzschild Field*, *Acta Phys. Polon.* **B39** (2008) 23, [arXiv:0802.0652].

[490] R. Plyatsko and O. Stefanyshyn, *On common solutions of Mathisson equations under different conditions*, arXiv:0803.0121.

[491] R. Plyatsko, *Ultrarelativistic circular orbits of spinning particles in a Schwarzschild field*, *Class. Quant. Grav.* **22** (2005) 1545–1551, [gr-qc/0507023].

[492] R. Plyatsko and M. Fenyk, *Antigravity: Spin-gravity coupling in action*, *Phys. Rev.* **D94** (2016), no. 4 044047, [arXiv:1610.01545].

[493] S. Suzuki and K.-i. Maeda, *Chaos in Schwarzschild space-time: The motion of a spinning particle*, *Phys. Rev.* **D55** (1997) 4848–4859, [gr-qc/9604020].

[494] R. H. Rietdijk and J. W. van Holten, *Spinning particles in schwarzschild spacetime*, *Classical and Quantum Gravity* **10** (1993), no. 3 575.

[495] D. Bini, F. de Felice, A. Geralico, and R. T. Jantzen, *Spin precession in the Schwarzschild spacetime: Circular orbits*, *Class. Quant. Grav.* **22** (2005) 2947–2970, [gr-qc/0506017].

[496] R. Plyatsko, O. Stefanyshyn, and M. Fenyk, *Mathisson-Papapetrou-Dixon equations in the Schwarzschild and Kerr backgrounds*, *Class. Quant. Grav.* **28** (2011) 195025, [arXiv:1110.1967].

[497] R. Plyatsko and M. Fenyk, *Highly relativistic circular orbits of spinning particle in the Kerr field*, *Phys. Rev.* **D87** (2013), no. 4 044019, [arXiv:1303.4707].

[498] G. Lukes-Gerakopoulos, M. Katsanikas, P. A. Patsis, and J. Seyrich, *The dynamics of a spinning particle in a linear in spin Hamiltonian approximation*, *Phys. Rev.* **D94** (2016), no. 2 024024, [arXiv:1606.09171].

[499] D. Bini, A. Geralico, R. T. Jantzen, and F. de Felice, *Spin precession along circular orbits in the Kerr spacetime: the Frenet-Serret description*, *Class. Quant. Grav.* **23** (2006) 3287–3304, [arXiv:1408.4278].

[500] M. D. Hartl, *A Survey of spinning test particle orbits in Kerr space-time*, *Phys. Rev.* **D67** (2003) 104023, [gr-qc/0302103].

[501] S. Suzuki and K.-i. Maeda, *Innermost stable circular orbit of a spinning particle in Kerr space-time*, *Phys. Rev.* **D58** (1998) 023005, [gr-qc/9712095].

[502] W. Han, *Chaos and dynamics of spinning particles in Kerr spacetime*, *Gen. Rel. Grav.* **40** (2008) 1831–1847, [arXiv:1006.2229].

[503] E. Hackmann, C. Lämmerzahl, Y. N. Obukhov, D. Puetzfeld, and I. Schaffer, *Motion of spinning test bodies in Kerr spacetime*, *Phys. Rev.* **D90** (2014), no. 6 064035, [arXiv:1408.1773].

[504] M. Mohseni, *Stability of circular orbits of spinning particles in Schwarzschild-like space-times*, *Gen. Rel. Grav.* **42** (2010) 2477–2490, [arXiv:1005.3110].

[505] M. Mortazavimanesh and M. Mohseni, *Spinning particles in Schwarzschild-de Sitter space-time*, *Gen. Rel. Grav.* **41** (2009) 2697–2706, [arXiv:0904.1263].

[506] Y. N. Obukhov and D. Puetzfeld, *Dynamics of test bodies with spin in de Sitter spacetime*, *Phys. Rev.* **D83** (2011) 044024, [arXiv:1010.1451].

[507] Z. Stuchlik and P. Slany, *Equatorial circular orbits in the Kerr-de Sitter space-times*, *Phys. Rev.* **D69** (2004) 064001, [gr-qc/0307049].

[508] N. Zalaquett, S. A. Hojman, and F. A. Asenjo, *Spinning massive test particles in cosmological and general static spherically symmetric spacetimes*, *Class. Quant. Grav.* **31** (2014) 085011, [arXiv:1308.4435].

[509] R. Hojman and S. Hojman, *Spinning Charged Test Particles in a Kerr-Newman Background*, *Phys. Rev.* **D15** (1977) 2724.

[510] D. Bini, G. Gemelli, and R. Ruffini, *Spinning test particles in general relativity: Nongeodesic motion in the Reissner-Nordstrom space-time*, *Phys. Rev.* **D61** (2000) 064013.

[511] K. Nomura, T. Shirafuji, and K. Hayashi, *Spinning test particles in space-time with torsion*, *Prog. Theor. Phys.* **86** (1991) 1239–1258.

[512] D. Maity, S. SenGupta, and S. Sur, *Spinning test particle in Kalb-Ramond background*, *Eur. Phys. J.* **C42** (2005) 453–460, [hep-th/0409143].

[513] G. Lukes-Gerakopoulos, *Time parameterizations and spin supplementary conditions of the Mathisson-Papapetrou-Dixon equations*, *Phys. Rev.* **D96** (2017), no. 10 104023, [arXiv:1709.08942].

[514] F. Costa, C. A. R. Herdeiro, J. Natario, and M. Zilhao, *Mathisson's helical motions for a spinning particle: Are they unphysical?*, *Phys. Rev.* **D85** (2012) 024001, [arXiv:1109.1019].

[515] G. Lukes-Gerakopoulos, E. Harms, S. Bernuzzi, and A. Nagar, *Spinning test-body orbiting around a Kerr black hole: circular dynamics and gravitational-wave fluxes*, *Phys. Rev.* **D96** (2017), no. 6 064051, [arXiv:1707.07537].

[516] F. A. E. Pirani, *On the Physical significance of the Riemann tensor*, *Acta Phys. Polon.* **15** (1956) 389–405. [Gen. Rel. Grav.41,1215(2009)].

[517] G. Lukes-Gerakopoulos, J. Seyrich, and D. Kunst, *Investigating spinning test particles: spin supplementary conditions and the Hamiltonian formalism*, *Phys. Rev.* **D90** (2014), no. 10 104019, [arXiv:1409.4314].

[518] W. Tulczyjew, *Motion of multipole particles in general relativity theory*, *Acta Phys. Polon.* **18** (1959) 393.

[519] D. Bini, A. Geralico, and R. T. Jantzen, *Spin-geodesic deviations in the Schwarzschild spacetime*, *Gen. Rel. Grav.* **43** (2011) 959, [arXiv:1408.4946].

[520] F. A. Asenjo and S. A. Hojman, *Exact solutions for the motion of spinning massive particles in conformally flat spacetimes*, *J. Phys. Conf. Ser.* **720** (2016), no. 1 012011.

[521] K. Kyrian and O. Semerak, *Spinning test particles in a Kerr field*, *Mon. Not. Roy. Astron. Soc.* **382** (2007) 1922.

[522] L. F. O. Costa and J. Natário, *Center of mass, spin supplementary conditions, and the momentum of spinning particles*, *Fund. Theor. Phys.* **179** (2015) 215–258, [arXiv:1410.6443].

[523] L. F. O. Costa, G. Lukes-Gerakopoulos, and O. Semerák, *On spinning particles in general relativity: momentum-velocity relation for the Mathisson-Pirani spin condition*, arXiv:1712.07281.

[524] M. Carrera and D. Giulini, *On the generalization of McVittie's model for an inhomogeneity in a cosmological spacetime*, *Phys. Rev.* **D81** (2010) 043521, [arXiv:0908.3101].

[525] B. Schutz, *A First Course in General Relativity*. Cambridge University Press, 2nd ed., June, 2009.

[526] M. Carrera and D. Giulini, *On the influence of the global cosmological expansion on the local dynamics in the solar system*, gr-qc/0602098.

[527] S. A. Hojman and F. A. Asenjo, *Can gravitation accelerate neutrinos?*, *Class. Quant. Grav.* **30** (2013) 025008, [arXiv:1203.5008].

[528] C. Verhaaren and E. W. Hirschmann, *Chaotic orbits for spinning particles in Schwarzschild spacetime*, *Phys. Rev.* **D81** (2010) 124034, [arXiv:0912.0031].

[529] L. Barack and N. Sago, *Gravitational self-force correction to the innermost stable circular orbit of a Schwarzschild black hole*, *Phys. Rev. Lett.* **102** (2009) 191101, [arXiv:0902.0573].

[530] P. I. Jefremov, O. Yu. Tsupko, and G. S. Bisnovatyi-Kogan, *Innermost stable circular orbits of spinning test particles in Schwarzschild and Kerr space-times*, *Phys. Rev.* **D91** (2015), no. 12 124030, [arXiv:1503.07060].

[531] M. A. Abramowicz, M. Jaroszynski, S. Kato, J.-P. Lasota, A. Rozanska, and A. Sadowski, *Leaving the ISCO: the inner edge of a black-hole accretion disk at various luminosities*, *Astron. Astrophys.* **521** (2010) A15, [arXiv:1003.3887].

[532] J. T. Giblin, Jr., D. Marolf, and R. Garvey, *Space-time embedding diagrams for spherically symmetric black holes*, *Gen. Rel. Grav.* **36** (2004) 83–99, [gr-qc/0305102].

[533] A. de la Cruz-Dombriz, A. Dobado, and A. L. Maroto, *Black Holes in f(R) theories*, *Phys. Rev.* **D80** (2009) 124011, [arXiv:0907.3872]. [Erratum: Phys. Rev.D83,029903(2011)].

[534] T. Vachaspati, *Electroweak strings*, *Nucl. Phys.* **B397** (1993) 648–671.